

***“Impact of kinetics and flow path heterogeneity
on nanoparticle/radionuclide migration”***

***A Dissertation submitted to the “Fachbereich Geowissenschaften der Freien
Universität Berlin” for the Degree of Doctor of Science (Dr. rer. nat.)***

presented by

Dipl.-Geol. Florian M. Huber

Berlin/Karlsruhe 2011

Evaluators:

PD Dr. Thorsten Schäfer

Prof. Dr. Marco Dentz

Day of the Disputation:

29.11.2011

Declaration

I herewith declare that I autonomously carried out the PhD thesis entitled “Impact of kinetics and flow path heterogeneity on nanoparticle/radionuclide migration”.

The chapters 2 to 4 of my (cumulative) PhD thesis are publication-manuscripts which are either already published, in press or submitted to international journals, respectively. In the following the journal, status of the manuscript, co-authors and their contributions to the compilation of the manuscripts are listed:

Chapter 2:

- Schäfer, T.; Huber, F.; Seher, H.; Missana, T.; Alonso, U.; Kumke, M. U.; Eidner, S.; Claret, F.; Enzmann, F. (2011). *Nanoparticles and their influence on radionuclide mobility in deep geological formations.* Applied Geochemistry (2011), <http://dx.doi.org/10.1016/j.apgeochem.2011.09.009>

The goal of the manuscript was to provide a synopsis of the work delivered in the 6th framework project IP FUNMIG (Fundamental processes of radionuclide migration). The conception and preparation of the manuscript was done by Thorsten Schäfer and myself. I worked on the sorption reversibility and the modeling chapter. H. Seher, T. Missana and U. Alonso contributed to the bentonite erosion chapter. M. Kumke and S. Eidner provided data about the spectroscopic investigations on metal sorption onto organic material. F. Claret was involved in the chapter on the influence of organic material on radionuclide sorption. F. Enzmann conducted the μ CT measurements which served as basis for some of the modeling results presented.

Chapter 3: Influence of sorption and redox kinetics on radionuclide speciation

- Huber, F., Kunze, P., Geckeis, H. and Schäfer, T. (2011). *Sorption reversibility kinetics in the ternary system radionuclide - bentonite colloids/nanoparticles - granite fracture filling material.* Applied Geochemistry (2011), <http://dx.doi.org/10.1016/j.apgeochem.2011.08.005>

The conceptual design of the experiments evolved in discussion with Thorsten Schäfer and myself in the framework of the BMWi/PtKA project “KOLLORADO-I”. I conducted the experiments partly with the help of P. Kunze (student internship). The preparation of the manuscript was in my responsibility in close collaboration with H. Geckeis and T. Schäfer.

- Huber, F., Schild, D., Vitova, T., Rothe, J., Kirsch, R. & Schäfer, T. (2011). *U(VI) removal kinetics in the presence of synthetic magnetite nanoparticles.* Geochimica et Cosmochimica Acta (under review).

I was responsible for the conceptual design and preparation of the experimental program according to the agreement with T. Schäfer. D. Schild was responsible for the XPS analysis whereas T. Vitova, J.

Rothe and R. Kirsch made the XAS investigations and analysis. The preparation of the manuscript was done by myself in close collaboration with all co-authors.

- **Regenspurg, S., Schild, D., Schäfer, T., Huber, F. & Malmström, M. (2009).** *Removal of uranium(VI) from the aqueous phase by iron(II) minerals in the presence of bicarbonate.* **Applied Geochemistry (2009), <http://dx.doi.org/10.1016/j.apgeochem.2009.04.029>**

The conception and design of the experiments were done by S. Regenspurg and T. Schäfer in the framework of an FP6 ACTINET joint research proposal. I contributed in both the characterization of the solid phases and in the accomplishment of the experiments. The manuscript was prepared by S. Regenspurg in close collaboration with all co-authors. The co-author M. Malmström was the supervisor of R. Regenspurg at KTH (Stockholm)

Chapter 4: Retardation by flow path heterogeneity: experiments versus modeling

- **Huber, F., Enzmann, F., Wenka, A., Dentz, M. & Schäfer, T. (2011).** *Natural micro-scale heterogeneity induced solute and nanoparticle retardation in fractured crystalline rock.* **Journal of Contaminant Hydrology (under review).**

The conception and the preparation of the migration experiments were done after discussion with T. Schäfer by myself. Furthermore, I was responsible for the modeling task. F. Enzmann conducted the μ CT measurements. In discussions with A. Wenka and M. Dentz the strategy of the modeling procedure was established. The manuscript was written by myself in close collaboration with all co-authors.

I did not receive any assistance in return for payment by consulting agencies or any other person. No one received any kind of payment for direct or indirect assistance in correlation to the content of the submitted thesis.

The thesis was conducted at the Karlsruhe Institute of Technology (KIT)/ Institute for Nuclear Waste Disposal (INE).

The thesis has not been submitted elsewhere for an exam, as thesis or for evaluation in a similar context.

I hereby affirm the above statements to be complete and true to the best of my knowledge.

Florian M. Huber

In loving memory of my parents....

“I was like a boy playing on the sea-shore, and diverting myself now and then finding a smoother pebble or a prettier shell than ordinary, whilst the great ocean of truth lay all undiscovered before me.”

(Isaac Newton)

Acknowledgments

The prevailing work would not have been possible without the support of a lot of people. Especially,

- my superb supervisor and doctoral advisor, **PD Dr. Thorsten Schäfer**, for all his guidance, help, patience and constant motivation (even late night).
- **Prof Dr. Michael Schneider** for taking the chair of the examination board.
- my second advisor, **Prof. Dr. Marco Dentz** for his refreshing way of thinking opening my eyes when it comes down to reflect upon my modeling results. Beyond, I have to thank for some very nice evenings in Barcelona and San Francisco.
- **Dr. Dieter Schild** for the numerous XPS measurements and his explanations significantly extending my knowledge in the field of spectroscopic techniques.
- **Dipl. Phys. Alexandra Pudewills** for teaching me the mysteries of ADINA-F.
- **Dipl. Ing. Achim Wenka** for spending hours with me in front of the PC illuminating my understanding for FLUENT and serious CFD modeling. Despite the frequent drawbacks we had to suffer in the beginning, it was always a pleasure for me.
- **Dr. Frieder Enzmann** for the μ CT data of (our beloved) core#8 and his willingness in explaining me any question concerning modeling and CT measurements.
- **Prof. Dr. Horst Geckeis** for several constructive discussions and questions which greatly improved my knowledge, understanding and work.
- **Dr. Johannes Lützenkirchen** who had and still always has an open ear for all my (hopefully sometimes not too annoying) questions.
- The **INE Analytic team** for dozens of measurements.
- The **INE EXAFS group**, namely **Dr. Melissa A. Denecke**, **Dr. Kathy Dardenne**, **Dr. Tonya Vitova** and **Dr. Jörg Rothe**, for the XAS measurements and analysis of some tricky samples.
- The INE workshop team, especially **Volker Krepper** and **Erwin Schmitt**, for all the technical advices and ideas.
- My colleagues in the room 108, **Stephanie Heck**, **Dipl. Chem. Tomas Kupcik**, **Dipl. Math. Michael Trumm** and **Dipl. Chem. David Fellhauer** for all the discussions (regardless of the topic), help and last but not least, for your friendship.
- The **SKB “colloid” project** and the **BMW/PTKA projects “Kollorado-I and Kollorado-II”** are gratefully acknowledged for financial support.
- My brother, **Christian Huber**, for simply everything.
- Dipl.-Geol. **Stefan Gutekunst** for being such a good friend in all the years
- Last but not least, some other not explicitly mentioned good friends and people.

Abstract

The issue of a safe disposal of nuclear waste in a deep underground repository fuses *inter alia* state of the art knowledge of different scientific fields like e.g. radiochemistry, geochemistry and hydrogeology. Mechanistically process understanding is required of numerous interdependent chemical and physical processes governing radionuclide migration like e.g. sorption/desorption, reduction, precipitation, diffusion, hydrodynamic dispersion and/or colloid-facilitated transport. These processes, often kinetically controlled, may lead to effective retention and retardation of radionuclides in the geosphere. Moreover, spatial geochemical and hydraulic heterogeneities/perturbations in crystalline rock are known to have a strong impact on radionuclide migration independent of the observation scale.

Therefore, the prevailing PhD thesis experimentally investigates the impact of both sorption/desorption (reversibility) and reduction kinetics on radionuclide migration in synthetic and natural systems from the nano- to the centimeter scale. Furthermore, the impact of fracture heterogeneity on flow and solute/nanoparticle transport as a potential additional retardation mechanism is examined both on an experimental and numerical basis.

Sorption and reduction kinetics of uranium in presence of synthetic nanoparticulate magnetite ($(\text{Fe}^{\text{III}}\text{Fe}^{\text{III}})_2\text{O}_4$) and maghemite ($\gamma\text{-Fe}_2\text{O}_3$), respectively have been investigated by classical batch experiments in conjunction with spectroscopic techniques (XPS and XAS) to probe for the valence state of uranium on the iron oxide surface. As accessory mineral, magnetite occurs naturally in crystalline rocks but moreover, as corrosion product of the stainless steel canisters used as engineered barrier in a nuclear waste repository. The structural bound Fe(II) in the magnetite may reduce the mobile dissolved hexavalent uranium to its low soluble tetravalent valence state representing an effective retention mechanism. Beside a freshly prepared (non-oxidized) magnetite, a partly oxidized magnetite was applied in the experiments comparing the redox capacity of both mineral phases in terms of available Fe(II) content. In contrast, maghemite does not possess Fe(II) therefore no reduction is expected and sorption may be the only retardation mechanism possible. The experimental program comprised both short term (<90 d contact time) experiments and long term (550 d contact time) experiments, respectively. Total uranium concentrations applied in the experiments were $3 \cdot 10^{-5}$ M (short and long term experiments) and $1 \cdot 10^{-7}$ M (only long term experiments), enabling spectroscopic investigations of selected samples in case of the higher uranium concentrations used. Short term kinetic experiments for 4 different pH values (2.5, 5, 8 and 11) revealed a fast kinetic within the first 24 h. That is, no (or only slight) sorption was observed in case of pH 2.5 over the whole experimental duration whereas at higher pH > 90 % magnetite associated uranium was detected after 24 h. Similar results were found for the long term pH-edge sorption experiments for both total uranium concentrations applied. No magnetite associated uranium was found below pH ~ 3 after 550 d contact time. The pH sorption edges are located between pH 3-4 and pH 4-5 for uranium concentrations of $1 \cdot 10^{-7}$ M and $3 \cdot 10^{-5}$ M, respectively. The sorption rises up and remains at ~ 100 % above the sorption edges corroborating the absence of dissolved carbonate. XPS investigations confirmed the presence of reduced uranium on the magnetite surface after 24 h, thus verifying a fast reduction kinetic. Moreover, the amount of tetravalent uranium clearly correlates to the available Fe(II) content of the magnetite, that is, increasing Fe(II) content leads to an increase in tetravalent uranium. The presence of U(V), as recently reported in the literature, was also examined. However, U(V) could not be verified due to low signal-to-noise ratio in the XPS spectra. In line with XPS, XAS investigations corroborate the presence of U(IV) on the surface of magnetite. Regarding U(V), the presence of minor contributions of U(V) cannot be verified but not excluded.

One of the reference scenarios in the Swedish safety case is the possible occurrence of dilute groundwaters during glacial conditions down to repository depth potentially causing erosion of the bentonite buffer/backfill and generation of bentonite colloids, respectively. The potential role of

these generated colloids enhancing radionuclide (RN) mobility is *inter alia* depending on the RN sorption reversibility and the colloid attachment probability. To investigate the consequences of such a hydro-geochemical disturbance to the far-field environment and the potential impact on the long term safety of the deep geological repository, a detailed laboratory program was conducted. Sorption and reversibility studies on the interaction of strong and weakly sorbing radionuclides (Np^(V), Pu^(IV), Am^(III), U^(VI), Th^(IV), Tc^(VII), Cs^(I), Ba^(II) and Na^(I)) with Febex bentonite colloids under Grimsel groundwater conditions (pH 9.6; I = 1.2·10⁻³M) in the presence of Äspö Fracture Filling Material (FFM) (0.25 – 2 mm) have been performed. Grimsel groundwater was taken to mimic the influence of low mineralized glacial melt water. All studies were made under Ar-atmosphere. These results are compared to identical studies substituting the Äspö FFM by Grimsel FFM in order to evaluate the effect of mineralogical differences. Furthermore, the effect of different FFM size fractions (surface area) was investigated. Bentonite colloids remained stable, as identified by the ICP-MS Al signal, and showed no attachment to the FFM within the analytical uncertainty. From a comparison of ultra-centrifuged and not ultra-centrifuged samples it is obvious that Tc, U and Np are not colloid associated. The concentrations of Tc and U remain constant over 1000 h, indicating an absence of sorption to fracture filling material or reduction in both investigated systems. Regarding long term contact times of 312 d, both U and Tc concentrations slightly decreased which may be referred to reduction processes. Np concentration decreases after ~ 300 h in both systems which could either be explained by sorption to the FFM or by a slow reduction to Np(IV). In contrast, the tri- and tetravalent elements Th, Pu and Am are initially clearly colloid associated. After ~ 100 h however, actinide concentrations significantly decrease indicating desorption from colloids and sorption to FFM. Th and Pu data yield a slower dissociation from colloids compared to Am indicating stronger RN-colloid interaction. The driving force for the observed metal ion desorption from colloids is binding to fracture filling material surfaces being in excess of the available colloid surface area (76:1, 55:1 and 44:1 for the 0.25-0.5 mm, 0.5-1 mm and 1-2 mm size fraction of the FFM, respectively). Overall, the results show that the desorption kinetics of bentonite colloids are rather independent from the FFM used in this study and also of the grain size of the investigated material, at least in the size fraction range 0.25 – 2 mm.

Beside static batch experiments, dynamic core migration studies on bentonite colloid and radionuclide mobility in a natural single fracture under variation of the residence time (flow velocity) have been conducted. The diorite drill core (core#8) with spatial dimensions of 13.5 cm in length and 5.04 cm width comes from the hard rock laboratory (HRL) in Äspö, Sweden. The same radionuclide cocktail as applied in the reversibility experiments has been used for the column experiments. The results of the migration experiments show bentonite nanoparticle immobility and thus very low recoveries (< 5 %) of associated radionuclides (Am(III), Pu(IV) and Th(IV)) under geochemical conditions expected to favour bentonite stability. Np(V) and Tc(VII) show a partly retarded breakthrough with Np recoveries of ~72-76 % and Tc recoveries ~79-100 %. Thermodynamic calculations indicate the stability of Np(IV) under the established geochemical conditions whereas for Tc, the heptavalent valence state as initially spiked to the cocktail predominates explaining the high mobility. The unexpected low nanoparticle recovery is referred to the critical coagulation concentration (Ca-CCC ~1mmol·L⁻¹) found in the eluent. It is likely that the core matrix still possesses the signature of the former higher mineralized Äspö groundwater and that Ca²⁺ is still leaching from this matrix into the water conducting fracture. It is hypothesized that this higher Ca²⁺ concentration in the vicinity of the fracture surface is responsible for the higher attachment probability of the colloids to the fracture surface.

In crystalline rock, fractures are the only pathways for significant groundwater flow and for solute and colloid transport to take place. The impact of natural fracture geometry on fluid flow and mass transport is investigated by means of 3D computational fluid dynamics (CFD) simulations in comparison to HTO and engineered nanoparticle (quantum dots (QD)) migration experiments. Therefore, the drill core (core#8) used in the migration experiments was scanned using μ -computed tomography (μ CT) with a voxel resolution of 80 μ m. On basis of the full resolution μ CT data a 3D

model was generated with a total of 10.5 Mio. elements capturing the complete complex fracture geometry. To solely examine the impact of fracture geometry on mass transport no chemical processes besides diffusion have been included in the CFD simulations. The transport of the nanoparticles has been simulated using the calculated diffusion coefficient based on the measured hydrodynamic diameter of the QD by AsFIFFF. Concerning fluid flow, a complex flow field evolves reflecting the strong impact of spatial fracture heterogeneity and geometrical features like asperities and/or microscale roughness. In consequence, zones of high flow velocity develop near asperities due to narrowing of the fracture cross-sectional area. In conjunction with low flow zones, typical flow characteristics of fractures like flow channelling are visible. Since mass transport is strongly coupled to the flow field, simulated breakthrough curves (BTCs) show pronounced late time arrivals (tailing) indicating non-Fickian transport behaviour. These findings tally well with the experimental HTO and QD BTCs also showing heavy tailings. Discrepancies between experimental and simulated results are referred to uncertainties in the μ CT measurements, experimental and simulation boundary conditions, respectively. Overall, the investigation clearly verifies the importance of complex natural fracture geometry as an additional retardation mechanism.

In summary, the prevailing work highlights the importance of (i) kinetically controlled processes like radionuclide sorption/desorption (reversibility) and reduction, (ii) the impact of nanoparticles and (iii) the effect of hydraulic (flow path) heterogeneities on radionuclide migration on different observation scales (nano- micro to mesoscale). The approach of combining (i) classical batch experiments to state-of-the-art spectroscopic techniques (XPS and XAS) and (ii) μ -computed tomography to 3D CFD calculations provide detailed chemical and physical information facilitating a deepened mechanistically process understanding of radionuclide migration behaviour.

Zusammenfassung

Die Aufgabe der sicheren Entsorgung von radioaktiven Abfällen in einer tiefen geologischen Formation bedarf der Kombination modernster wissenschaftlicher Erkenntnisse auf verschiedenen Fachgebieten wie z.B. der Radiochemie, Geochemie und Hydrogeologie. Dabei wird ein mechanistisches Prozessverständnis einer Vielzahl von wechselseitig abhängigen chemischen und physikalischen Prozessen benötigt, welche die Radionuklidmigration beeinflussen (z.B. Sorption/Desorption, Reduktion, Präzipitation, Diffusion, hydrodynamische Dispersion und/oder kolloidgetragenem Transport). Diese, oft kinetisch kontrollierten Prozesse, können zu einer effektiven Radionuklid-Retention und -Retardation in der Geosphäre führen. Weiterhin ist bekannt, dass, unabhängig vom Beobachtungsmaßstab, räumliche geochemische und hydraulische Heterogenitäten in kristallinen Gesteinen einen großen Einfluss auf die Radionuklidmigration haben können.

Die vorliegende Doktorarbeit untersucht sowohl den Einfluss von Sorptions-/Desorptionkinetiken (Reversibilität), als auch von Reduktionskinetiken auf die Radionuklidmigration in synthetischen und natürlichen Systemen im nm- bis cm-Maßstab. Daneben wird, auf experimenteller und numerischer Basis, der Einfluss räumlicher Kluftheterogenität auf die Strömung und den Stoff-/Kolloidtransport untersucht, welcher als potenzieller Retardationsmechanismus in Frage kommt.

Sorptions- und Reduktionskinetiken von Uran in Anwesenheit von synthetischem nanopartikulärem Magnetit ($\text{Fe}^{\text{III}}\text{Fe}^{\text{III}}_2\text{O}_4$) und Maghemit ($\gamma\text{-Fe}_2\text{O}_3$) wurden mittels klassischen Batchexperimenten untersucht. Magnetit tritt in der Natur als akzessorisches Gemengteil in kristallinen Gesteinen auf. Darüber hinaus entsteht er auch im Nahfeld eines geologischen Endlagers als Korrosionsprodukt der Edelstahlbehälter (technische Barriere). Ein effektiver Retentionsmechanismus für Uran ist die Reduktion von gelöstem, mobilem Uran(VI) in schwerlöslicheres, weniger mobiles Uran(IV) durch das in Magnetit strukturell gebundene Fe(II). Um die Redoxkapazität von Magnetit hinsichtlich des verfügbaren Fe(II) Gehalts zu untersuchen, wurden die Batchuntersuchungen an einem frisch synthetisierten („nicht oxidierten“), sowie an einem partiell oxidierten Magnetit durchgeführt. Als zusätzliche Mineralphase wurde Maghemit ($\gamma\text{-Fe}_2\text{O}_3$) verwendet, welches im Gegensatz zu Magnetit kein strukturelles Fe(II) besitzt. Damit kann eine Reduktion von U(VI) vernachlässigt werden, und die Sorption an die Mineralphase stellt den einzig möglichen Retardierungsmechanismus dar. Neben Kurzzeitexperimenten (< 90 Tage Kontaktzeit) umfasst das experimentelle Programm auch Langzeitversuche (550 Tage Kontaktzeit). Die Untersuchungen wurden mit zwei Urankonzentrationen durchgeführt: $c = 3 \cdot 10^{-5}$ M (Kurzzeit- und Langzeitexperimente) und $1 \cdot 10^{-7}$ M (nur Langzeitexperimente). Die höhere Urankonzentration ermöglicht dabei eine Kopplung der Batchexperimente an spektroskopische Techniken (XPS und XAS), aus welchen der Valenzzustand von oberflächensorbiertem Uran bestimmt werden kann. Kurzzeitkinetik-Experimente zur Wechselwirkung von U(VI) mit Magnetit bei vier verschiedenen pH-Werten (2.5, 5, 8 und 11) belegen eine U(VI)-Abnahme innerhalb der ersten 24 Stunden. Während für pH 2.5 nur eine sehr geringe U(VI)-Abnahme beobachtet wurde, zeigen die Ergebnisse für höhere pH-Werte eine Sorption von ~100 % des eingesetzten Uran an. Ähnliche Resultate wurden auch in den Langzeitexperimenten für beide verwendeten Urangesamtkonzentrationen erhalten. In diesen Untersuchungen konnte für pH < 3 nach einer Kontaktzeit von 550 Tagen kein Magnetit-assoziiertes Uran beobachtet werden. Die Sorptionskante liegt im Falle der niedrigen Urankonzentration ($1 \cdot 10^{-7}$ M) zwischen pH 3 und 4. Eine Erhöhung der Metallionenkonzentration ($3 \cdot 10^{-5}$ M) führt zu einer Verschiebung der Sorptionskante zu höheren pH-Werten (pH 4 – 5). Für pH > ~5.5 liegt Uran vollständig sorbiert vor. Ein Rückgang der Sorption kann nicht beobachtet werden, was auf die Abwesenheit von gelösten Karbonatkomplexen hindeutet. XPS Untersuchungen bestätigen durch die Anwesenheit von oberflächensorbiertem U(IV) die schnelle Sorptions-/Reduktionskinetik ($t = 24$ h). Dabei korreliert die Menge an reduziertem Uran mit dem Fe(II)-Anteil im Magnetit. Neben vierwertigem ist auch die Existenz von fünfwertigem Uran auf der Magnetitoberfläche möglich. Dieses konnte jedoch in XPS Untersuchungen aufgrund eines

niedrigen Signal-zu-Rausch-Verhältnisses nicht bestätigt werden. In Übereinstimmung mit den XPS Ergebnissen, unterstützen auch XAS Untersuchungen die Anwesenheit von vierwertigem Uran auf der Magnetitoberfläche, jedoch kann die Anwesenheit von geringen Anteilen an U(V) mittels XAS nicht vollständig ausgeschlossen werden.

Ein Referenzszenario in den Sicherheitsanalysen im schwedischen Programm zur Endlagerung nuklearer Abfälle ist ein Auftreten von gering mineralisierten, glazialen Grundwässern während zukünftigen Eiszeiten bis in die Tiefen des Endlagers. Ins Endlager eindringende Grundwässer können zu einer Erosion von Bentonit und anderen Versatzmaterialien (technische Barriere) führen, wodurch Bentonitkolloide generiert und freigesetzt werden können. Um die Auswirkungen solch einer hydrogeochemischen Störung auf das Fernfeld eines Endlagers sowie den möglichen Einfluss auf die Langzeitsicherheit des Endlagers zu untersuchen wurden Sorptions- und Reversibilitätsstudien zur Wechselwirkung von stark und schwach sorbierenden Radionukliden ($\text{Np}^{(\text{V})}$, $\text{Pu}^{(\text{IV})}$, $\text{Am}^{(\text{III})}$, $\text{U}^{(\text{VI})}$, $\text{Th}^{(\text{IV})}$, $\text{Tc}^{(\text{VII})}$, $\text{Cs}^{(\text{I})}$, $\text{Ba}^{(\text{II})}$ and $\text{Na}^{(\text{I})}$) mit FEBEX Bentonitkolloiden unter Grimsel Grundwasserbedingungen ($\text{pH} \sim 9.6$; $I = 1.2 \cdot 10^{-3} \text{ M}$) in Anwesenheit von Kluftfüllmaterial (KFM) (0.25 – 2 mm Korngrößen) aus Äspö, Schweden durchgeführt. Die Verwendung von Grimsel Grundwasser bietet dabei die Möglichkeit, den Einfluss von gering mineralisiertem, glazialen Schmelzwasser zu simulieren. Um einen Effekt von mineralogischen Unterschieden der verschiedenen Kluftfüllmaterialien zu untersuchen wurde in vergleichenden Experimenten das Äspö- durch Grimsel-Kluftfüllmaterial ausgetauscht. Alle Experimente wurden unter identischen Bedingungen und Inertgasatmosphäre (Ar) durchgeführt. Desweiteren wurde der Einfluss verschiedener Korngrößenfraktionen (bzw. unterschiedlichen spezifischen Oberflächen) auf die Metallionensorption untersucht. In Al-ICP-MS Untersuchungen konnte (im Rahmen der analytischen Genauigkeit) keine Anlagerung der Kolloide an das Kluftfüllmaterial beobachtet werden, was die Stabilität der Bentonitkolloide unter den experimentellen Bedingungen bestätigt. Ein Vergleich der Proben mit und ohne Phasentrennung (Ultrazentrifugation; $\sim 694000 \text{ g}$) belegt, dass U, Tc und Np nicht kolloidal assoziiert vorliegen. Die $\text{Tc}^{(\text{VII})}$ und $\text{U}^{(\text{VI})}$ Konzentrationen blieben für beide untersuchten Systeme (Äspö- bzw. Grimsel-Kluftfüllmaterial) innerhalb der ersten 1000 Stunden konstant, was auf die Abwesenheit von Sorptions- und Redoxreaktionen (Reduktion von $\text{Tc}^{(\text{VII})}$ und $\text{U}^{(\text{VI})}$) hindeutet. Für eine Kontaktzeit von 312 Tagen zeigten die ICP-MS Daten einen leichten Abfall an gelöstem $\text{Tc}^{(\text{VII})}$ und $\text{U}^{(\text{VI})}$. Dies deutet Reduktionsprozesse der genannten Metallionen nach dieser Kontaktzeit an. Im Fall von Np wird eine Abnahme der gelösten $\text{Np}^{(\text{V})}$ Konzentration nach ~ 300 Stunden beobachtet, was einerseits mit einer Sorption an das Kluftfüllmaterial, andererseits mit einer langsamen Reduktion von $\text{Np}^{(\text{V})}$ zu $\text{Np}^{(\text{IV})}$ erklärt werden kann. Im Gegensatz zu Tc, U und Np sind die drei- und vierwertigen Radionuklide Th, Pu und Am initial an die Bentonitkolloide assoziiert. Nach ~ 100 Stunden Kontaktzeit wird eine Desorption der Metallionen von den Bentonitkolloiden beobachtet. Gleichzeitig nimmt die Konzentration an Th, Pu und Am in den Proben ohne Phasentrennung deutlich ab, was auf eine Sorption an das Kluftfüllmaterial hindeutet. Dabei zeigen die ICP-MS Ergebnisse eine langsamere Desorption von $\text{Th}^{(\text{IV})}$ und $\text{Pu}^{(\text{IV})}$ im Vergleich zu $\text{Am}^{(\text{III})}$, was auf eine stärkere Wechselwirkung von $\text{Th}^{(\text{IV})}$ und $\text{Pu}^{(\text{IV})}$ mit den Kolloiden hindeutet. Die Triebkraft für die beobachtete Desorption der Metallionen von den Kolloiden in Richtung des Kluftfüllmaterials ist dessen höhere spezifische Oberfläche mit einem Verhältnis von $A(\text{KFM})/A(\text{K}) = 76:1$; $55:1$ und $44:1$ für die 0.25-0.5 mm, 0.5-1 mm und 1-2 mm Korngrößenfraktionen. Weiter belegen die Resultate, dass die Desorptionskinetik unabhängig von der Art des Kluftfüllmaterials, sowie der verwendeten Korngröße (im Korngrößenbereich von 0.25 – 2 mm) ist.

Neben den statischen Batchexperimenten wurden Migrationsversuche zur Bentonitkolloid- und Radionuklidmigration in einer natürlichen Einzelkluft unter Variation der Verweilzeit (Fließgeschwindigkeit) durchgeführt. Die Untersuchungen wurden an einem Diorit-Bohrkern (core#8) mit den räumlichen Abmessungen $l = 13.5 \text{ cm}$ und $d = 5.04 \text{ cm}$ durchgeführt, welcher aus dem Felslabor in Äspö, Schweden erhalten wurde. Als Radionuklide kamen die in den oben angeführten Reversibilitätsversuchen verwendeten Radioisotope zum Einsatz ($\text{Np}^{(\text{V})}$, $\text{Pu}^{(\text{IV})}$, $\text{Am}^{(\text{III})}$, $\text{U}^{(\text{VI})}$, $\text{Th}^{(\text{IV})}$, $\text{Tc}^{(\text{VII})}$, $\text{Cs}^{(\text{I})}$, $\text{Ba}^{(\text{II})}$ und $\text{Na}^{(\text{I})}$). Die Ergebnisse zeigen einen Wiedererhalt von $< 5 \%$ der kolloidassoziierten

Radionuklide (Am, Th und Pu). Dieses Ergebnis deutet einerseits auf eine Erhöhung der Kolloidstabilität unter Einsatz von Am, Th und Pu hin, und belegt andererseits eine Immobilität der Kolloide unter den experimentellen Bedingungen. Der unerwartet geringe Kolloid-Wiedererhalt kann dabei mit der kritischen Koagulationskonzentration ($Ca\text{-CCC} \sim 1\text{mM}$) im Eluat erklärt werden. Die erhöhte Ca^{2+} Konzentration resultiert wahrscheinlich aus der Matrix des Bohrkerns, welche noch immer die Signatur des ehemaligen, höher mineralisierten Äspö Grundwasser aufweist. Dadurch gelangt weiterhin Ca^{2+} aus der Matrix in die wasserführende Kluft und führt zu einer höheren Ca^{2+} Konzentration, die für eine höhere Anlagerungswahrscheinlichkeit der Kolloide an die Kluftoberfläche verantwortlich ist. Np und, in geringerem Ausmaße, Tc zeigen einen teilweise retardierten Durchbruch mit Wiedererhalten von $\sim 72\text{-}76\%$ für Np und $\sim 79\text{-}100\%$ für Tc. Dabei weisen thermodynamische Berechnungen auf die Stabilität von Np(IV) unter den vorherrschenden geochemischen Bedingungen hin, während Tc in der Oxidationsstufe +7 vorliegt und damit nur leicht retardiert wird.

Klüfte stellen die einzigen verfügbaren Wegsamkeiten für signifikante Grundwasserströmung und Stofftransport (gelöste Stoffe und Kolloide) in Kristallingestein dar. Der Einfluss der natürlichen Kluftgeometrie auf die Grundwasserströmung und den Stofftransport wurde mittels 3-dimensionalen strömungsmechanischen Simulationen im Vergleich zu Migrationsversuchen mit HTO und Nanopartikeln (Quantum dots (QD)) untersucht. Für die Simulationen wurde der in den Migrationsversuchen verwendete Bohrkern (core#8) mittels Computertomographie (CT) mit einer Auflösung von $80\ \mu\text{m}$ gescannt. Auf Basis dieses CT-Datensatzes wurde ein 3-dimensionales Computermodell (10.5 Mio. Elemente) der Einzelkluft generiert, um die komplexe natürliche Geometrie der Kluft detailliert zu erfassen. Um ausschließlich den Einfluss der Kluftgeometrie auf den Stofftransport zu untersuchen, wurden weder Matrixdiffusion noch chemische Prozesse in den Simulationen berücksichtigt. Der Transport der Kolloide wurde mittels des berechneten Diffusionskoeffizienten auf Basis des hydrodynamischen Durchmessers der QD modelliert. Der hydrodynamische Durchmesser konnte durch die AsFFFF Messungen bestimmt werden. Die Simulation der Strömung in der Kluft ergab aufgrund der heterogenen Kluftgeometrie und weiteren geometrischen Eigenschaften (z.B. Asperitäten und/oder mikroskalige Rauigkeit) ein komplexes Fließfeld. In der Nähe der Asperitäten entstehen aufgrund der Verringerung des Kluftquerschnittes Bereiche hoher Fließgeschwindigkeit. Daneben wurden weitere typische Charakteristika von Kluftströmungen wie z.B. eine Kanalisierung der Strömung beobachtet. Aufgrund der engen Kopplung von Stofftransport an die Strömung weisen die simulierten Durchbruchkurven ein ausgeprägtes „tailing“ auf, welches auf ein Nicht-Fick'sches Transportverhalten hindeutet. Die Simulationsergebnisse sind in guter Übereinstimmung mit den experimentellen Durchbruchkurven für HTO und QD, welche ebenfalls ein stark ausgeprägtes „tailing“ besitzen. Unterschiede zwischen den Experimenten und den Simulationen können auf Unsicherheiten in den CT Messungen, sowie auf die unterschiedlichen Randbedingungen der Experimente und Simulationen zurückgeführt werden. Zusammenfassend belegen die Untersuchungen die Relevanz von der natürlichen Kluftgeometrie als ein zusätzlicher Retardationsmechanismus für gelöste Stoffe und Nanopartikel/Kolloide.

Die Ergebnisse der vorliegenden Arbeit verdeutlichen die Bedeutung von (i) kinetisch kontrollierten Prozessen wie Sorption/Desorption (Reversibilität) und Reduktion, (ii) den Einfluss von Nanopartikeln und (iii) den Effekt von hydraulischer (Fließpfad) Heterogenität auf die Radionuklidmigration für verschiedene Beobachtungsskalen (nm bis cm Maßstab). Der gewählte Ansatz einer Kombination von (i) klassischen Batchexperimenten in Verbindung mit modernen spektroskopischen Analysemethoden (XPS und XAS) und (ii) der Computertomographie mit 3-dimensionalen Strömungs- und Stofftransportsimulationen liefert detaillierte chemische und physikalische Informationen, die zu einem vertieftem Verständnis des Migrationsverhalten von stark sorbierende und redoxsensitiven Radionukliden im Nah- und Fernfeld eines nuklearen Endlagers führen.

Table of Contents

1	GENERAL INTRODUCTION.....	1
1.1	RADIONUCLIDE MIGRATION IN NATURAL SYSTEMS	1
1.2	MOTIVATION AND SCOPE OF THE WORK	5
1.3	STRUCTURE OF THIS THESIS	7
2	NANOPARTICLES AND THEIR EFFECT ON RADIONUCLIDE MOBILITY.....	9
2.1	INTRODUCTION	11
2.2	BACKGROUND NANOPARTICLE CHARACTERIZATION IN DEEP GEOLOGICAL FAR-FIELD SYSTEMS	13
2.2.1	<i>Inorganic nanoparticles</i>	13
2.2.2	<i>Organic nanoparticles</i>	13
2.3	ADDITIONAL NANOPARTICLE SOURCES FROM THE REPOSITORY NEAR-FIELD?	14
2.3.1	<i>Canister and glass corrosion</i>	14
2.3.2	<i>Bentonite backfill and buffer erosion</i>	15
2.4	STABILITY OF NANOPARTICLES IN FAR-FIELD ENVIRONMENTS?	16
2.5	MOBILITY OF NANOPARTICLES	18
2.5.1	<i>Advection controlled systems</i>	18
2.5.2	<i>Diffusion controlled system</i>	19
2.6	INTERACTION OF RADIONUCLIDES WITH NANOPARTICLES.....	20
2.6.1	<i>Inorganic nanoparticles</i>	20
2.6.2	<i>Organic nanoparticles</i>	20
2.7	REVERSIBILITY OF RADIONUCLIDE SORPTION	21
2.8	NANOPARTICLE MODELING APPROACHES	22
2.8.1	<i>Nanoparticle stability</i>	22
2.8.2	<i>Bentonite buffer erosion and nanoparticle generation</i>	23
2.8.3	<i>Nanoparticle transport modeling</i>	24
2.9	CONCLUSIONS AND FUTURE DIRECTION OF STUDIES	25
3	INFLUENCE OF SORPTION AND REDOX KINETICS ON RADIONUCLIDE SPECIATION	29
3.1	SORPTION REVERSIBILITY KINETICS IN THE TERNARY SYSTEM RADIONUCLIDE - BENTONITE COLLOIDS/NANOPARTICLES - GRANITE FRACTURE FILLING MATERIAL.....	29
3.1.1	<i>Introduction</i>	31
3.1.2	<i>Materials and Methods</i>	32
3.1.2.1	Fracture Filling Material (FFM) characterization	32
3.1.2.2	FEBEX bentonite colloid characterization.....	33
3.1.2.3	Grimsel groundwater (GGW) characterization	34
3.1.2.4	Radionuclide cocktail characterization	34
3.1.2.5	Experimental conditions and procedure	35
3.1.3	<i>Results and Discussion</i>	35
3.1.3.1	Redox and pH evolution of the experiments.....	35
3.1.3.2	Thermodynamic calculations.....	36
3.1.3.3	RN-colloid-FFM interaction	38
3.1.3.3.1	The case of tri- and tetravalent actinides (Am, Pu and Th).....	40
3.1.3.3.2	²⁴³ Am(III)	41
3.1.3.3.3	²⁴² Pu(IV) and ²³² Th(IV).....	41
3.1.3.4	The case of ²³⁷ Np(V), ²³³ U(VI) and ⁹⁹ Tc(VII).....	44
3.1.3.4.1	²³⁷ Np(V).....	44
3.1.3.4.2	⁹⁹ Tc(VII) and ²³³ U(VI)	45
3.1.3.5	Effect of available surface area on sorption reversibility of Np, Am and Pu	46
3.1.4	<i>Conclusions</i>	47

3.2	U(VI) REMOVAL KINETICS IN PRESENCE OF SYNTHETIC MAGNETITE PARTICLES	51
3.2.1	<i>Introduction</i>	53
3.2.2	<i>Materials and Methods</i>	54
3.2.2.1	Solid Phase Synthesis and Characterization	54
3.2.2.2	Batch Experiments.....	55
3.2.2.2.1	Magnetite Samples (Series#1-3).....	55
3.2.2.2.2	Maghemite Samples (Series#4)	56
3.2.2.3	Spectroscopic Techniques	56
3.2.2.3.1	X-ray Photoelectron Spectroscopy (XPS)	56
3.2.2.3.2	X-ray Absorption Spectroscopy (XAS)	57
3.2.2.4	Thermodynamic Calculations	57
3.2.3	<i>Results and Discussion</i>	58
3.2.3.1	Solid Phase Characterization	58
3.2.3.2	Thermodynamic modeling results and redox potential measurements.....	59
3.2.3.2.1	U Speciation.....	59
3.2.3.2.2	Redox Potential (Eh) Measurements	60
3.2.3.3	Batch Experiment Results.....	61
3.2.3.3.1	Series#1 (Short Term (kinetic) studies).....	61
3.2.3.3.2	Series#2 (Long Term Studies)	64
3.2.3.4	Spectroscopic Results	65
3.2.3.4.1	XPS.....	67
3.2.3.4.1.1	Fe(II) speciation	67
3.2.3.4.1.2	U speciation.....	67
3.2.3.4.1.3	Comparison to literature data.....	72
3.2.3.4.2	XAS.....	72
3.2.4	<i>Conclusion</i>	74
3.3	REMOVAL OF URANIUM(VI) FROM THE AQUEOUS PHASE BY IRON(II) MINERALS IN PRESENCE OF BICARBONATE	79
3.3.1	<i>Introduction</i>	81
3.3.2	<i>Materials and Methods</i>	82
3.3.2.1	XPS analysis	83
3.3.3	<i>Results and discussion</i>	83
3.3.3.1	Uranium immobilization – quantitative analysis	83
3.3.3.1.1	Effect of initial uranium concentration.....	84
3.3.3.1.2	Effect of pH values and redox conditions	85
3.3.3.1.2.1	Acidification to pH 4.....	86
3.3.3.1.3	Effect of bicarbonate	87
3.3.3.1.4	Effect of Fe(II) source.....	87
3.3.3.2	Surface analysis by XPS.....	88
3.3.3.2.1	Total elemental composition	88
3.3.3.2.2	Redox state of uranium	89
3.3.3.2.3	Redox state of iron	91
3.3.3.3	Uranium reduction processes.....	91
4	RETARDATION BY FLOW PATH HETEROGENEITY: EXPERIMENTS VERSUS MODELING.....	97
4.1	INTRODUCTION	99
4.2	MATERIALS AND METHOD.....	100
4.2.1	<i>X-ray computed tomography</i>	100
4.2.2	<i>Quantum dots</i>	100
4.2.3	<i>Core migration experiments</i>	101
4.2.4	<i>CFD modeling</i>	101
4.3	RESULTS AND DISCUSSION	103
4.3.1	<i>Core analysis by x-ray computed tomography</i>	103
4.3.2	<i>Quantum dots characterization by AsFIFFF</i>	104
4.3.3	<i>Flow modeling</i>	104

4.3.4	<i>Core migration experiment</i>	106
4.3.4.1	Run#1	106
4.3.4.2	Run#2	106
4.3.5	<i>Transport modeling (Run#1 & Run#2)</i>	107
4.3.6	<i>Uncertainties in μCT analysis and boundary conditions</i>	108
4.4	CONCLUSIONS.....	109
5	MAJOR CONCLUSIONS	111
6	OPEN QUESTIONS AND FUTURE DIRECTIONS OF RESEARCH	113
7	REFERENCES	117
8	APPENDIX A: SORPTION REVERSIBILITY KINETICS: THE ÄSPÖ SYSTEM	133
9	APPENDIX B: CORE MIGRATION EXPERIMENTS	143

List of Figures

Figure 1.1: Generic scheme of adsorption processes. a) adsorption b) ion exchange.	2
Figure 1.2: Schematic representation of the processes governing radionuclide migration in fractured rock.	4
Figure 2.1: (a) Processes controlling the mobility of nanoparticles in water-saturated porous media: (1) release of colloids, (2) aggregation of colloids, (3) immobilization by gravitational settling of aggregates, (4) immobilization by straining of aggregates or single nanoparticles, (5) immobilization by nanoparticle deposition on solid–water interfaces, (6) transport of dispersed nanoparticles over long distances by flowing water. (b) In unsaturated porous media, additional mechanisms of nanoparticle retardation may occur: (7) immobilization by film straining and (8) immobilization by deposition on air–water interfaces (figure taken from Kretzschmar and Schäfer (2005))......	12
Figure 2.2: Critical coagulation concentration (CCC) as a function of the pH value determined for the calcium (Ca-CCC) and the sodium (Na-CCC) system for different montmorillonites are represented as different data points. The red dash-dotted line indicates the onset of purely diffusion controlled coagulation. In addition, the pH- cation concentration regions for the different geological formations studied within IP FUNMIG are inserted as shaded areas (data with reference) is given in Table 2.1.	17
Figure 2.3: (a) Rendered 3D image of the real fracture geometry used for the migration experiments derived from μ CT data showing the surface morphology and the very irregular shaped boundary on one side of the fracture, for details see (Huber et al., 2009). (b) Data points represent two independent measured HTO breakthrough curves showing the reproducibility of the migration experiments. Modeling results using the finite-element code ADINA-F (Bathe et al., 1999) are additionally presented. The semi-2D model captures the peak maximum but fails in predicting the experimentally observed tailing. The 2D line and point model differ by assuming either point or line injection, but use both the midplane of the fracture ignoring all aperture information implementing only the influence of fracture side walls.	25
Figure 3.1: (a) $E_{h(SHE)}$ measurement for a single point plotted in the left figure showing the response time of the redox electrode reaching asymptotically a constant plateau value after several hours. (b) Measured final pH and $E_{h(SHE)}$ values in the batch-type studies after various contact times.	36
Figure 3.2: Calculated predominance diagram for ^{237}Np based on thermodynamic constants from the NEA database.....	37
Figure 3.3: Comparison of the Al concentration in the ultra-centrifuged (UC) and non ultra-centrifuged (not UC) samples for all sizes fractions investigated. Dashed line represents the FEBEX colloid concentration derived by ICP-MS Al signal. Dotted line gives the Al background concentration in natural Grimsel groundwater.	38
Figure 3.4: Time dependent radionuclide concentration change in the ternary system RN-fracture filling material (FFM)- bentonite colloids. The time-dependent concentration margins given in red squares (filled or open) represent predictions of the ternary system based on the binary system sorption data: (i) bentonite colloids – RN and (ii) fracture filling material – RN as published in (Missana and Geckeis, 2006). (a) Initial Am(III) concentrations $8 \cdot 10^{-9} \text{ mol} \cdot \text{L}^{-1}$ (filled circles) and $1.4 \cdot 10^{-9} \text{ mol} \cdot \text{L}^{-1}$ (open black squares). The dashed lines are first order rate law fitting curves using a desorption rate k_3 of 0.009 h^{-1} as presented in Flügge et al. (2010) and the desorption rate $k_{3,average}$ of 0.0037 h^{-1} as determined for the long-term desorption data (note the break in the X axis). (b) Initial Pu(IV) concentrations $1.3 \cdot 10^{-8} \text{ mol} \cdot \text{L}^{-1}$ (filled circles) and $7.7 \cdot 10^{-11} \text{ mol} \cdot \text{L}^{-1}$ (open black squares). The dashed lines are first order rate law fitting curves using a desorption rate k_3 of 0.0085 h^{-1} as presented in Flügge et al. (2010) and the desorption rate $k_{3,average}$ of 0.0014 h^{-1} as determined for the long-term desorption data averaged from the Pu(IV) and Th(IV) desorption experiments. Additionally inserted are the back calculated Pu(IV) solution concentrations based on the ternary Rd values published in (Missana and Geckeis, 2006) (blue stars) (note the break in the X axis).	42
Figure 3.5: Residence time dependent recovery based on the batch experiment determined desorption rate (Figure 4).	43
Figure 3.6: (a) Time dependent Np concentration change in the ternary system Np-fracture filling material (FFM)- bentonite colloids for two different initial Np(V) concentrations $1.8 \cdot 10^{-6} \text{ mol} \cdot \text{L}^{-1}$ (filled squares) and $2 \cdot 10^{-8} \text{ mol} \cdot \text{L}^{-1}$ (open black squares). The time-dependent concentration margins given in red squares (filled or open) represent predictions of the ternary system based on the binary system sorption data: (i) bentonite colloids – Np(V) and (ii) fracture filling material – Np(V) as published in (Missana and Geckeis, 2006). The dashed lines are first order rate law fitting curves (Note the break in the x axis) (b) pe/pH diagram showing the experimental pe/pH range and the pe borderline for 50 % and 95 % Np reduction (note the break in the X axis).	44

- Figure 3.7:** Time dependent evolution of radionuclide concentration for (a) $^{99}\text{Tc(VII)}$ and (b) $^{233}\text{U(VI)}$ for the 1-2 mm experiments (SET4). Values are given both for ultra-centrifuged (UC) samples and for non ultra-centrifuged (not UC) samples. 45
- Figure 3.8:** Surface normalized $\log(R_d)$ values for (a) $^{237}\text{Np(V)}$ (b) $^{242}\text{Pu(IV)}$ and (c) $^{243}\text{Am(III)}$. The N_2 BET surface area taken for the calculation is: Grimsel FFM (1-2 mm): $0.15 \text{ m}^2 \cdot \text{g}^{-1}$; Grimsel FFM (0.5-1 mm): $0.19 \text{ m}^2 \cdot \text{g}^{-1}$; Grimsel FFM (0.25-0.5 mm): $0.24 \text{ m}^2 \cdot \text{g}^{-1}$. Dashed lines visualize the range of uncertainties. 46
- Figure 3.9:** XRD patterns in conjunction with SEM pictures for all three solid phases used in the experiments. Scale bar 300 nm. a) Partly oxidized magnetite (po-mag b) Non-oxidized magnetite (fmag) and c) Maghemite (mgh); enhanced view: max. peak intensity 1400 (-). 58
- Figure 3.10:** Predominance plots for the speciation of U calculated with the Hydra/Medusa code using NEA constants. a) $[\text{U}]_{\text{TOT}}: 1 \cdot 10^{-7} \text{ M}$. Additionally inserted are redox potentials obtained in this study. b) $[\text{U}]_{\text{TOT}}: 3 \cdot 10^{-5} \text{ M}$. Additionally inserted are redox potentials obtained in this study in comparison to literature data by Regenspurg et al. (2009) and Missana et al. (2003a). c) $[\text{U}]_{\text{TOT}}: 3 \cdot 10^{-5} \text{ M}$. Only samples measured by XPS are shown. d) $[\text{U}]_{\text{TOT}}: 1.8 \cdot 10^{-4} \text{ M}$ as used in the experiments from Ilton et al. (2010). 59
- Figure 3.11:** Results of the short term kinetic batch experiments using po-mag as solid phase. a) Aqueous U concentrations. The error bars for the sample series at pH 2.5 are in the order of the symbol size. b) Aqueous $\text{Fe}_{\text{(TOT)}}$ concentrations. 62
- Figure 3.12:** a) U pH edges (550 d contact time) of Series#2a ($3 \cdot 10^{-5} \text{ M U}$) and Series#2b ($1 \cdot 10^{-7} \text{ M U}$). b) Surface normalized $\log K_d$ values of Series#2a and Series#2b in comparison to literature data from Missana et al. (2003a). Regarding the aqueous concentrations applied, they used slightly higher amounts of U ($4.4 \cdot 10^{-7} \text{ M}$) as our lower concentration series. 64
- Figure 3.13:** a) XPS $\text{Fe } 2p_{3/2}$ spectra for the magnetite reference, sample fmag#3, hematite reference and maghemite reference showing the amount of Fe(II) and Fe(III). B) XPS U 4f spectra of the UO_x -Pd film with U(IV,V), fmag#1 and fmag#3 samples. Additionally, the peak position of U(VI), U(V) and U(IV) are indicated in conjunction with their corresponding satellites of the U 4f peaks. 68
- Figure 3.14:** XPS U 4f spectra for Series#4 samples (maghemite; 13 d contact time) showing small portions of U(IV) in case of magh#2 and magh#3. 69
- Figure 3.15:** U speciation as function of $\text{Fe(II)}/\text{Fe}_{\text{TOT}}$ content for all samples measured by XPS in the experiments. Note the trend in increasing U(IV) with increasing $\text{Fe(II)}/\text{Fe}_{\text{TOT}}$ content and vice versa, the trend of decreasing U(V) and U(VI) with increasing $\text{Fe(II)}/\text{Fe}_{\text{TOT}}$ content, respectively in case of Series#1 and Series#3. a) Series#1 (po-mag; $\leq 90\text{d}$ contact time) b) Series#2a (grey area; po-mag; 550 d contact time) and Series#3 (fmag; 13 d contact time). 71
- Figure 3.16:** a) XANES spectra of the reference samples and the po-mag#42 sample. b) and c) EXAFS spectra of the po-mag#42 sample (in R (a) and k (b) space, the best fit and the used theoretical single scattering paths 73
- Figure 3.17:** Left: Predominance diagram for uranium-mineral suspensions in 10 mM NaCl as calculated with Hydra/Medusa software (Puigdomenech, 2004). Data points represent measured values of pH and uranium concentration in different magnetite suspensions. Initial values (open symbols) are at pH 6, 8, 10 and at uranium concentration of $2.9 \cdot 10^{-5} \text{ M}$ (triangles), $8.9 \cdot 10^{-6} \text{ M}$ (diamonds) and $9.9 \cdot 10^{-8} \text{ M}$ (squares). Filled symbols represent final measured data. Right: Predominance diagram for uranium-mineral suspensions containing 10 mM NaCl and 1 mM CO_3^{2-} as calculated with Hydra/Medusa software (Puigdomenech, 2004). Data points are measured values of pH and uranium concentration. Initial data (crosses) are at pH 6, 8, 10 and at uranium concentration of $2.9 \cdot 10^{-5} \text{ M}$. Filled symbols represent final concentration of uranium in corundum-Fe(II) amended suspensions (squares) and in magnetite suspensions (triangles). 86
- Figure 3.18:** Left: Eh/pH diagram for the iron equilibrium system. Open diamonds represent corundum and black diamonds represent magnetite suspensions. Long-dashed lines give the stability line of H_2 and O_2 , respectively. The short-dashed line shows the equilibrium area of a solid Fe(II)/Fe(III) buffer (Felmy et al., 1989; Rai et al., 2002). Other lines represent predominance areas of Fe(II) and Fe(III) species as calculated with Hydra/Medusa software with 1 mM CO_3^{2-} and a 0.01 mM Fe concentration. ("c" in the diagram indicates a solid phase. Right: Predominance diagram for Fe(II) species in a carbonate solution (1 mM). Data points represent measured iron concentrations and pH values of solutions reacted with corundum (open diamonds) and magnetite (black diamonds). 87
- Figure 3.19:** Left: Uranium concentration in solutions containing magnetite, magnetite amended with 1 mM HCO_3^- , corundum amended with 1 mM Fe(II) and corundum amended with each 1 mM Fe(II) and HCO_3^- , measured after the experiment at pH 8 (Table 1 and 2 indicate the final pH values) and after re-acidification to pH 4. Initial uranium concentration was $2.95 \cdot 10^{-5} \text{ M}$. Right: Uranium concentration in

- solutions containing magnetite, magnetite amended with 1 mM HCO_3^- , corundum amended with 1 mM Fe(II) and corundum amended with Fe(II) and HCO_3^- (each 1 mM), measured after the experiment at pH 8 and 10. Values above the columns indicate final pH values. 88
- Figure 3.20:** Left: XPS uranium 4f spectra on the surface of Al_2O_3 at various conditions: a) Corundum reacted with U(VI) at pH 8. b) Corundum reacted with U(VI) at pH 8 in presence of 1 mM Fe(II). c) Sample b) which was later acidified to pH 4. d) Corundum reacted with U(VI) at pH 8 in presence of each 1 mM HCO_3^- and Fe(II). e) Sample d) which was later acidified to pH 4. The dashed lines indicate the reference binding energies of U 4f_{7/2} for U(IV) in UO_2 and U(VI) in UO_3 , respectively. Right: XPS uranium 4f spectra on the surface of Fe_3O_4 at various conditions: a) Magnetite reacted with U(VI) at pH 8. b) Sample a) which was later acidified to pH 4. c) Magnetite reacted with U(VI) at pH 8 in presence of 1 mM HCO_3^- . d) Sample c) which was later acidified to pH 4. The dashed lines indicate the reference binding energies of U 4f_{7/2} for U(IV) in UO_2 and U(VI) in UO_3 , respectively. 91
- Figure 3.21:** Left: XPS Fe 2p spectra on the surface of Fe_3O_4 at various conditions: a) Magnetite reacted with U(VI) at pH 8. b) Sample a) which was later acidified to pH 4. c) Magnetite reacted with U(VI) at pH 8 in presence of 1 mM HCO_3^- . d) Sample c) which was later acidified to pH 4. The dashed line indicates the reference binding energy of Fe 2p_{3/2} for Fe(III) and Fe(II). Right: XPS O 1s spectra on the surface of Fe_3O_4 at various conditions: a) Magnetite reacted with U(VI) at pH 8. b) Sample a) which was later acidified to pH 4. c) Magnetite reacted with U(VI) at pH 8 in presence of 1 mM HCO_3^- . d) Sample c) which was later acidified to pH 4. Positions of oxygen in oxides, water, carbonate and hydroxide are marked. 92
- Figure 4.1:** a) Drill core as installed in the laboratory. In red, the fracture suture is marked. b) A schematically sketch of the set-up as installed in the laboratory for use in the migration experiments. 100
- Figure 4.2:** a) Absorbance and ICP-MS fractograms obtained after injection of 100 μL of a QD solution diluted at $1 \text{ mg}\cdot\text{L}^{-1}$ in the AsFIFFF eluent (ultrapure water + NaOH; pH 9.3). The system is calibrated prior to the QD size measurements by injection of a mixture of polystyrene sulfonate standard (PSS) salt and carboxylated polystyrene nanoparticles. b) Size distribution analysis via ultrafiltration (UF) of the QD in comparison to ^{14}C -labelled Gorleben humic acid (GoHy-573 HA) (Mansel and Kupsch, 2007). 101
- Figure 4.3:** a) Rendered view of the fracture on basis of the μXCT data set showing the complex fracture geometry and morphology together with the spatial dimensions. b) Fracture aperture distribution in conjunction with a histogram of aperture and several statistical parameters of the fracture. 104
- Figure 4.4:** a) Normalized volume rendering plot of the flow field as calculated on basis of the μCT data. b) Particle traces snapshots showing the heterogeneous particle spreading due to flow velocity variability. c) Normalized histogram of the flow velocities for both Re numbers. Number of bins are 1000. Frequency is normalized to total number of frequencies; velocity magnitude normalized by the maximum velocity magnitude. 105
- Figure 4.5:** Experimentally derived BTCs (open stars) in comparison to simulated BTCs (black lines). a) HTO BTCs for Run#1 b) QD BTCs for Run#1 c) HTO BTCs for Run#2 and d) QD BTCs for Run#2. Red lines in a) and b) represents the empirical power law for matrix diffusion ($t^{-3/2}$), respectively. 107
- Figure A1:** Comparison of (a) the ^{22}Na , (b) ^{137}Cs and (c) ^{133}Ba concentration in the ultracentrifugated (UC) and not ultracentrifugated (not UC) samples for the Äspö FFM and Grimsel FFM system. The additional inserted straight dashed line illustrates the $t^{-3/2}$ -dependency which is indicative for matrix diffusion. 134
- Figure A2:** Comparison of the Al concentration in the ultracentrifugated (UC) and not ultracentrifugated (not UC) samples for the Äspö FFM and Grimsel FFM system. 135
- Figure A3:** Time dependent radionuclide concentration change in the ternary system RN-fracture filling material (FFM)- bentonite colloids. The time-dependent concentration margins given in red squares (filled or open) represent predictions of the ternary system based on the binary system sorption data: (i) bentonite colloids – RN and (ii) fracture filling material – RN as published in (Nagra, 2006). (a) Initial Am(III) concentrations $8\cdot 10^{-9} \text{ mol}\cdot\text{L}^{-1}$ (filled circles) and $1.4\cdot 10^{-9} \text{ mol}\cdot\text{L}^{-1}$ (open black squares). The dashed lines are first order rate law fitting curves using a desorption rate k_3 of 0.009 h^{-1} as presented in (Flügge et al., 2010) and the desorption rate $k_{3,\text{average}}$ of 0.0037 h^{-1} as determined for the long-term desorption data. (b) Initial Pu(IV) concentrations $1.3\cdot 10^{-8} \text{ mol}\cdot\text{L}^{-1}$ (filled circles) and $7.7\cdot 10^{-11} \text{ mol}\cdot\text{L}^{-1}$ (open black squares). The dashed lines are first order rate law fitting curves using a desorption rate k_3 of 0.0085 h^{-1} as presented in (Flügge et al., 2010) and the desorption rate $k_{3,\text{average}}$ of 0.0014 h^{-1} as determined for the long-term desorption data averaged from the Pu(IV) and Th(IV) desorption experiments. Additionally inserted are the back calculated Pu(IV) solution concentrations based on the ternary Rd values published in (Nagra, 2006) (blue stars). 136

Figure A4: Time dependent ^{232}Th evolution of radionuclide concentration for the Äspö (red symbols) and Grimsel FFM (black symbols) experiments. Values are given both for ultracentrifugated (UC) samples and for not ultracentrifugated (not UC) samples.	138
Figure A5: Time dependent ^{99}Tc (a), ^{233}U (b) and ^{237}Np (c) evolution of radionuclide concentration for the Äspö (red symbols) and Grimsel FFM (black symbols) experiments. Values are given both for ultracentrifugated (UC) samples and for not ultracentrifugated (not UC) samples.	139
Figure A 6: pe/pH diagram for the batch experiments showing the experimental pe/pH range and the pe borderline for 50% Np reduction. (black: Grimsel FFM; red: Äspö FFM).....	140
Figure A7: Surface normalized $\log(K_d)$ values for (a) ^{237}Np (b) ^{242}Pu and (c) ^{243}Am . Data of this study are shown as filled symbols. The N_2 BET- surface area taken for the calculation is: Äspö FFM: $0.2 \text{ m}^2 \cdot \text{g}^{-1}$. Grimsel FFM (1-2mm): $0.15 \text{ m}^2 \cdot \text{g}^{-1}$; Grimsel FFM (0.5-1mm): $0.19 \text{ m}^2 \cdot \text{g}^{-1}$, Grimsel FFM (0.25-0.5mm): $0.24 \text{ m}^2 \cdot \text{g}^{-1}$, respectively.....	141
Figure B1: (left) Picture taken from white precipitate observed after stagnant phase in core #8. (right) SEM-EDX characterization of the white precipitate observed during the change from Äspö GW to Grimsel GW.	143
Figure B2: Breakthrough curves of conservative tracer HTO (dashed line) and a) Am, Pu b) U and c) Np in the Äspö core after equilibration with Grimsel GW (flowrate $50 \mu\text{L} \cdot \text{min}^{-1}$).....	145
Figure B3: Breakthrough curves of Tc and Np (Run#2 & Run#3) together with the conservative tracer HTO...	146

List of Tables

Table 2.1: Nanoparticle stability determining chemical parameters for the different host rock formations investigated within IP FUNMIG.	17
Table 3.1: XRF results of Grimsel FFM (1-2 mm size fraction).	33
Table 3.2: Chemical composition of the original Grimsel groundwater (GGW) and after different contact times (24 h and 500 h) with Grimsel FFM in the batch experiments.....	34
Table 3.3: Time-dependent sorption data of various elements in the ternary system fracture filling material (FFM) – bentonite colloids – metal; V/m: 4 mL·g ⁻¹ ; Specific surface area (N ₂ BET): 0.238 m ² ·g ⁻¹ , 0.187 m ² ·g ⁻¹ and 0.153-0.166 m ² ·g ⁻¹ for 0.25-0.5 mm, 0.5-1 mm and 1-2 mm FFM size fraction, respectively.	39
Table 3.4: Thermodynamic constants used in the calculation of the predominance diagrams in Figure 3.10. Consistently, only thermodynamic constants from the actual NEA database (Guillaumont et al. 2003) have been used.	57
Table 3.5: Results of the short term kinetic batch experiments (Series#1).....	63
Table 3.6: Results of the long term batch experiments (Series#2) and the batch samples of Series#3 (fmag) and Series#4 (magh).	66
Table 3.7: Overview of all samples measured by XPS.....	70
Table 3.8: Results from the fit of the po-mag#41 EXAFS spectra.	74
Table 3.9: Chemical properties of different mineral suspensions before (initial) and after (final) the reaction with U(VI) solution over 27 days. Fe(II) source (mineral), pH (6-10), HCO ₃ ⁻ , and U(VI) concentration is indicated. Background electrolyte of all solutions was 10 mM NaCl.....	84
Table 3.10: Chemical properties of different mineral suspensions originally adjusted to pH 8 with highest initial uranium concentration (2.8·10 ⁻⁵ - 2.9·10 ⁻⁵ M; Table 3.9) measured 48 h after acidification to pH 4.....	89
Table 3.11: Elements determined by XPS (in at.%) in different samples. Initially, 2.95·10 ⁻⁵ M U(VI) was added to all samples. Relative atomic concentrations results are typically within 10-20% error. Hydrogen is not measured by XPS.....	90
Table 4.1: Conditions and results from migration experiments and CFD simulations.	108
Table B1: Chemical composition of the Äspö groundwater (TRUE-1 site. Feature A. KXTT4), the Grimsel groundwater (GGW) as well as the chemical evolution of GGW during contact with Äspö core #8 and after stop-flow (to observe the influence of matrix porewater).	144
Table B2: Summary of the radionuclide migration studies in presence of Febex bentonite colloids in the Äspö drill core under Grimsel groundwater conditions. Colloid associated elements are given in bold letters.	146

1 General Introduction

1.1 Radionuclide migration in natural systems

Deep geological formations are nowadays the preferred option for the disposal of high-level nuclear waste produced mainly by energy generation in nuclear power plants. Possible host rock formations currently discussed in different nations are crystalline rocks (i.e. granite, gneiss), evaporates (rock salt) and sedimentary rocks (indurated or plastic clays/claystones). Regarding crystalline rocks in e.g. Sweden, nowadays the multi-barrier system is the preferred option to ensure an isolation or retardation of the radioactive waste from the biosphere (SKB, 2006a). The vitrified waste or spent fuel will be encapsulated in stainless steel or copper canisters representing the first so-called technical barrier. Secondly, as geotechnical barrier the cavities around the canisters and the shafts/drifts will be backfilled with clays, like e.g. Febex bentonite. The third and last barrier, the so-called geological barrier, is the host rock formation itself.

One of the reference evolution scenarios of the deep geological repository considers a glaciation with the intrusion of low mineralized waters to repository depth causing a potential erosion of the bentonite buffer/backfill. Subsequently, migration of colloid associated radionuclides out of the nuclear waste repository near-field into the geological formation and biosphere might be a transport pathway. Such a migration process might be a potential threat to nature and mankind due to the radio- and chemotoxicity of the waste derived radionuclides even in trace concentrations. It is therefore of paramount importance to gain fundamental insights into the various chemical and physical processes governing the migration behaviour to assure the development of sound risk assessment strategies. Much effort has been spent in the past and is still ongoing today to shed light on the various interdependent geochemical and hydrogeological processes and their impact on the radionuclide migration (Kim et al., 1984; Kersting et al., 1999; Artinger et al., 2000; Möri et al., 2003; Schäfer et al., 2004; Schäfer et al., 2009). Generally speaking, radionuclide mobility, retardation and retention are prone to the following processes (Figure 1.1 and Figure 1.2):

- Sorption:

The accumulation of matter (dissolved, gaseous or solid phases like e.g. nanoparticles/colloids) at the solid-water interface is known as (ad)sorption whereas the opposite process, desorption, denotes the release of matter off the surface into the surrounding bulk phase (Stumm and Morgan, 1996). Beside ionic species (cations, anions and/or charged nanoparticles/colloids), uncharged inorganic species and a variety of organic phases may as well be prone to adsorption processes. The sorption process can be described, on the one hand, by electrostatic interaction between charged species and a charged surface (dipole-dipole, ion-dipole-, van-der-Waals-interaction or ion-bonding), where the metal ion maintain its full hydration sphere (outer-sphere complexation). On the other hand, the metal ion can be bound by inner-sphere complexation where part of the water molecules in the first coordination sphere is removed.

Besides, replacement of sorbed ions at the solid-water interface for dissolved ions in the bulk water phase is called ion exchange. This type of adsorption process is often considered in case of clay minerals like e.g. montmorillonite possessing a permanent negative surface charge due to isomorphic substitution of Si by Al in the crystal lattice. This leads to sorption of counter-ions like e.g. Na^+ or Ca^{2+} on the charged mineral surface and in the clay interlayer space (Appelo and Postma, 1996).

Generally speaking, the amount and type of sorption depends on:

- The chemical properties of the dissolved species, that is concentration, speciation, valence state and charge

1 General Introduction

- Properties of the adsorbing surface, e.g. mineralogy, morphology, surface charge, solid-solution ratio, type of sorption sites (strong/ weak sites)
- (Geo)chemical conditions like pH, $E_{h(SHE)}$, ionic strength, temperature, pressure, concentration of competing ligands in solution

A possibility to quantitatively evaluate adsorption processes are batch type experiments, where a defined amount of solid material is given to a solution with a defined concentration of a solute. After equilibration between the solid material and the solute, a distribution coefficient (K_d) can be derived, which is the ratio between the amount of adsorbed solute on the solid material (q) and the concentration of the solute in solution (c). It can be expressed by the following equation 1.1 (e.g. (Appelo and Postma, 1996):

$$K_d = q/c \quad (1.1)$$

If no sorption occurs, $K_d = 0$. The K_d is a very simplified approach and is sensitive regarding changes of system parameters like e.g. pH or ionic strength. It is only valid under the experimental conditions for which it has been determined. Beyond, it has to be stated that this approach requires (i) a full established equilibrium between the sorbed mass and the sorbing surface and (ii) a full reversibility of the sorption reaction.

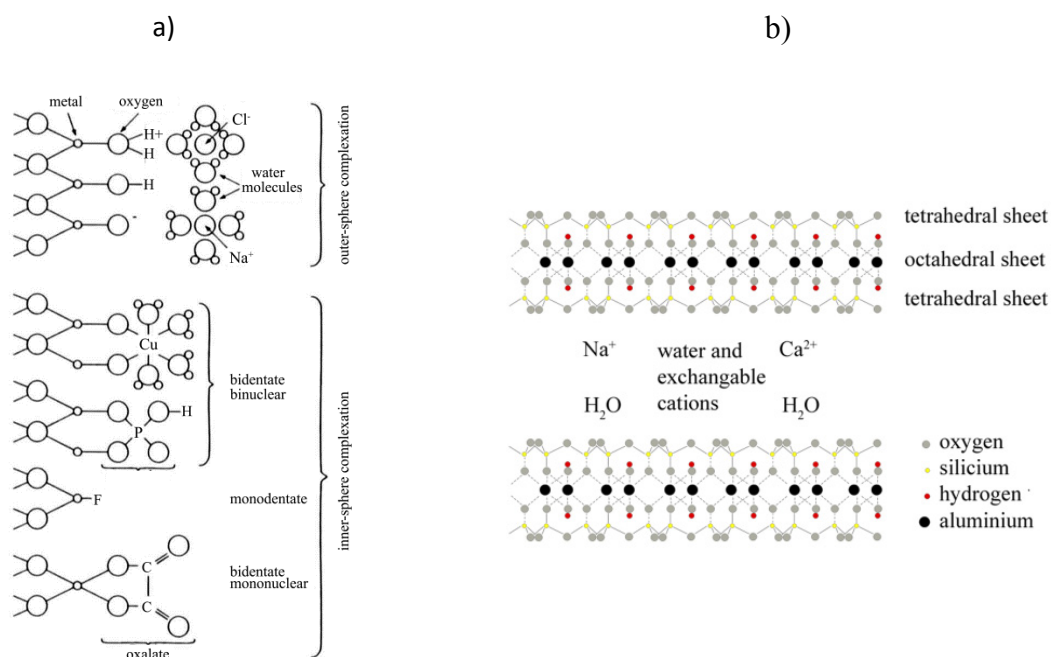


Figure 1.1: Generic scheme of adsorption processes. a) adsorption b) ion exchange.

A more sophisticated framework to describe adsorption is surface complexation where the adsorption of a dissolved species is described as a chemical reaction on the surface including surface sites in analogy to complexation reactions between aqueous species with organic/inorganic ligands in solution. The adsorbed species is bond to functional groups on the surfaces in different modes (e.g. edge-sharing, corner sharing) and number of involved binding sites (e.g. monodentate, bidentate, tridentate), which are charged due to their acid-base properties (Appelo and Postma, 1996).

Depending on the geochemical conditions prevailing, metal sorption to mineral surfaces represents one of the most important retention processes. Especially the tri- and tetravalent actinides like e.g. Am, Th and/or Pu are known to sorb strongly (Geckeis and Rabung, 2008). In contrast, pentavalent

Np, hexavalent U and/or heptavalent Tc show a less pronounced sorption behaviour and therefore possess a higher mobility in the environment.

- Reduction:

The migration behaviour of redox sensitive radionuclides like e.g. Tc, U, Np, and/or Pu is strongly determined by the geochemical conditions (i.e. pH/Eh) prevailing. The reduced oxidation states of radionuclides, e.g. Np(IV) in contrast to Np(V), most often show considerably lower solubilities (Neck and Kim, 2001). Thus, reduction of e.g. hexavalent U to its low soluble tetravalent oxidation state means an effective retention mechanism. Though, it has to be mentioned that changes in the geochemical conditions can cause a re-oxidization leading to radionuclide remobilization as it was observed e.g. in the Swedish site investigation program for Oskarshamn (SKB, 2008).

The redox potential of a given system is specified as normal potential E_h against the standard hydrogen electrode or in logarithmic units as electron activity a_{e^-} ($pe = -\log a_{e^-}$) in analogy to the definition of the pH ($pH = -\log a_{H^+}$). The relationship between Eh and pe is governed by the following equation (1.2):

$$E_h = - (RT/F) \ln a_{e^-} = (RT \ln(10) / F) pe \quad (1.2)$$

whereas R is the gas constant [$J \cdot mol^{-1} \cdot K^{-1}$], T the absolute temperature [K] and F the Faraday constant [$C \cdot mol^{-1}$]. For $T = 25^\circ C$, the following equation holds: $pe = 16.9 E_h [V]$.

The redox state of a solution is conveniently depicted in a, so-called, Pourbaix-diagrams (pe-pH diagram) (see for example Figure 3.2).

- Matrix diffusion:

Flow of groundwater in highly impermeable crystalline rocks takes place almost exclusively in fracture zones. This mobile water is connected with immobile water located in the porous matrix of the bedrock. Dissolved elements (to a lesser extent also colloids/nanoparticles) like e.g. radionuclides can penetrate the stagnant groundwater in the porous matrix by molecular diffusion. This process is known as matrix diffusion and leads to retardation of solutes by transferring them out of the main flow paths into areas with very little flow considerably increasing the residence time (Neretnieks, 1980). Beyond, the solutes in the porous matrix of the bedrock are accessed to a much higher surface area where geochemical reactions like sorption, reduction or precipitation can take place leading to a further increase in residence time. Additionally, once entrapped in the porous matrix, the solute exhibits much lower effective diffusion coefficients compared to the free diffusion coefficient in water making it more difficult for the solute to diffuse back in the main flow paths. The pore diffusion coefficient can be expressed as follows (Alonso et al., 2007b):

$$D_p = D_o \frac{\delta}{\tau^2} \quad (1.3)$$

where D_p is the diffusivity in the pores [$m \cdot s^{-2}$], D_o is the free diffusion coefficient in water [$m \cdot s^{-2}$], δ = constrictivity [-] and τ is the tortuosity [-]. The ratio between the constrictivity and tortuosity is always smaller than one, rendering the pore diffusion to become smaller than the free diffusion in water (Alonso et al., 2007b).

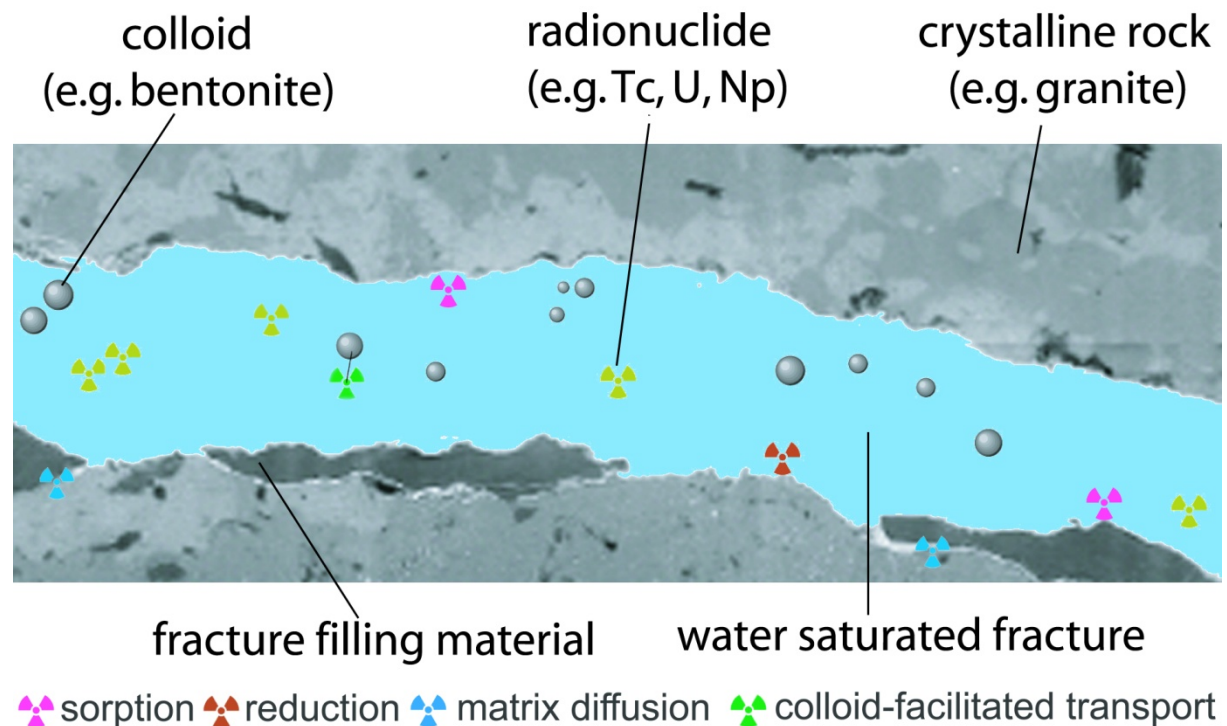


Figure 1.2: Schematic representation of the processes governing radionuclide migration in fractured rock.

- Colloid-facilitated transport:

Rock forming mineral fragments, humic and fulvic acids, mineral precipitates and microorganisms in the size range of 1 nm to 1000 nm are typically termed colloids/nanoparticles (McCarthy and Zachara, 1989). They occur ubiquitous in all kind of natural water systems like e.g. lakes, rivers or groundwater. Their composition often resembles chemically the composition of the corresponding host rock formation. When sorbed to colloids/nanoparticles the migration behaviour of radionuclides is superimposed by the transport properties of the colloids drastically altering the migration behaviour of the radionuclide itself. Several field studies and laboratory experiments could verify the importance of colloid-facilitated transport of contaminants, e.g. the colloid and radionuclide retardation (CRR) experiment conducted at the Grimsel Test Site in Switzerland (Möri et al., 2003; Geckeis et al., 2004). Here, it could be observed, that especially the transport of tri- and tetravalent radionuclides is facilitated in presence of colloidal phases. As another example, Pu migration at the Nevada Test Site (USA) was considerably influenced due to radionuclide colloid interaction leading to higher travel distances as expected (Kersting et al., 1999).

- Flow path heterogeneity

Fluid flow and solute transport in single fractures are of concern for several decades due to its importance in both industrial and scientific fields. Typically, natural fractures feature irregular spatial geometries and/or asperities imposing a heterogeneous flow field with recirculation zones (low flow zones) and/or “highways” (higher flow velocities in open zones) causing complex mass residence time distributions with e.g. pronounced tailings (late time arrival of the solutes/colloids) (e.g. Kosakowski, 2004; Boutt et al, 2006). The complex interdependency between hydrodynamic solute/colloid dispersion and matrix diffusion both causing heavy tailings in breakthrough curves thus providing pathways to solute/colloid retardation often hampers the clear differentiation between both mechanisms hindering the exact determination of the predominant retardation process.

Unfortunately, in most laboratory and in-situ field migration studies the spatial characterisation of the fracture/ fracture network is lacking and therefore a clear estimation of the effect on fluid flow and solute transport cannot be made. Here, coupling of spatial tomography data with flow and transport modelling tools provides a promising way to isolate the impact of flow path heterogeneity from matrix diffusion.

1.2 Motivation and scope of the work

It is well established in the scientific community, that mineralogical and geochemical heterogeneities can strongly influence the migration of radionuclides through the geosphere. Nevertheless, the effect of spatial geochemical and hydraulic (e.g. flowpath) heterogeneity in fractured crystalline rock on radionuclide migration still lacks fundamental process understanding. The most common approach in studying the mechanism of radionuclide migration are laboratory experiments like batch-type or column experiments on well defined but simplified systems. Disadvantage of experimentally obtained results in the laboratory is the uncertainty in view of a spatial and temporal upscaling to natural systems. This circumstance still remains an open question and needs further investigations.

Therefore, a bottom-up approach has been used in this PhD thesis:

- Studies with well-defined synthetic mineral phases and their interaction with radionuclides on a nm- to μm -level have been conducted by means of laboratory batch experiments. The kinetically controlled reduction of hexavalent uranium in presence of dissolved as well as structural bound ferrous iron in magnetite (Fe_3O_4) has been examined on an atomistic scale using XPS and XAS.
- On a μm - to mm-scale the kinetics of the sorption reversibility of colloid-associated radionuclides in presence of different types of fracture filling material (FFM), representing a natural mineral assemblage, have been studied. Systematic investigations concerning kinetically controlled desorption processes have not been paid much attention in the research community compared to adsorption processes. It must be assumed that desorption of colloid-bound radionuclides and a possible subsequent sorption onto the rock matrix exhibits a strong impact regarding the transport of radionuclides in groundwater causing retardation depending on the groundwater flow velocity / fracture residence times. Therefore data about desorption rates needs to be determined by laboratory and in-situ experiments as basis for the modeling of colloid-facilitated radionuclide transport to obtain more precise and reliable predictions. Ignoring radionuclide reversibility kinetics can lead to an over-estimation of the radionuclide mobility.
- In contrast to the static batch type experiments, real system analysis via laboratory core migration experiments using a fractured drill core from Äspö (Sweden) have been performed representing a natural system on a cm-scale. Besides, the application of a meteoric, low mineralized groundwater from Grimsel offers the possibility to mimic a possible melt-water intrusion scenario in the Äspö system. Colloid-facilitated radionuclide transport has been examined by use of the same cocktail as in the fracture filling material batch type experiments.
- The effect of fracture geometry/flow path heterogeneity on radionuclide and nanoparticle (quantum dots) migration has been studied by use of computational fluid dynamics (CFD) using μCT data of the drill core mentioned above. This spatial information served as direct input in the CFD code FLUENT to simulate fluid flow and mass transport in 3D.

1.3 Structure of this thesis

The prevailing thesis is based on 5 papers published in or submitted to peer-reviewed international scientific journals. Additional work which is not yet published is presented in the Appendix A and B. For a consistent layout, the papers have been re-edited. The thesis is outlined in the following way:

Chapter 1 provides a short general introduction on the fundamental processes impacting radionuclide migration in natural environments. Secondly, a brief overview of the aims and motivations of the PhD thesis is presented.

Chapter 2, 3 and 4 comprise the results of the research conducted within the thesis. Each chapter represents either a published paper or a manuscript submitted for peer-review in international journals, respectively. That is, each chapter is a self-contained piece of work and can be read individually. They are as follows:

Chapter 2: Nanoparticles and their effect on radionuclide mobility

- I. **Schäfer, T.; Huber, F.; Seher, H.; Missana, T.; Alonso, U.; Kumke, M. U.; Eidner, S.; Claret, F.; Enzmann, F. (2011).** *Nanoparticles and their influence on radionuclide mobility in deep geological formations.* **Applied Geochemistry (2011),** <http://dx.doi.org/10.1016/j.apgeochem.2011.09.009>

Chapter 3: Influence of sorption and redox kinetics on radionuclide speciation

- II. **Huber, F., Kunze, P., Geckeis, H. and Schäfer, T. (2011).** *Sorption reversibility kinetics in the ternary system radionuclide - bentonite colloids/nanoparticles - granite fracture filling material.* **Applied Geochemistry (2011),** <http://dx.doi.org/10.1016/j.apgeochem.2011.08.005>
- III. **Huber, F., Schild, D., Vitova, T., Rothe, J., Kirsch, R. & Schäfer, T. (2011).** *U(VI) removal kinetics in the presence of synthetic magnetite nanoparticles.* **Geochimica Cosmochimica Acta (under review).**
- IV. **Regenspurg, S., Schild, D., Schäfer, T., Huber, F. & Malmström, M. (2009).** *Removal of uranium(VI) from the aqueous phase by iron(II) minerals in the presence of bicarbonate.* **Applied Geochemistry (2009),** <http://dx.doi.org/10.1016/j.apgeochem.2009-04.029>

Chapter 4: Retardation by flow path heterogeneity: experiments versus modeling

- V. **Huber, F., Enzmann, F., Wenka, A., Dentz, M. & Schäfer, T. (2011).** *Natural micro-scale heterogeneity induced solute and nanoparticle retardation in fractured crystalline rock.* **Journal of Contaminant Hydrology (under review).**

Chapter 5 draws the major conclusion of the thesis and gives an outlook for future research.

Appendix A and B summarizes results of (i) further bentonite sorption reversibility studies using fracture filling material from Äspö, Sweden and (ii) radionuclide migration experiments on a diorite drill core, respectively.

2 Nanoparticles and their effect on radionuclide mobility

This article gives an overview of the current status of knowledge concerning the role of nanoparticles (inorganic and organic) in deep geological host rocks and the potential influence of these nanoparticles on radionuclide migration in far-field systems. The manuscript is not intended to be a full review paper or overview paper concerning nanoparticles, here we intend to refer to recent publications (Kretzschmar and Schäfer, 2005; Lead and Wilkinson, 2006; Tushar and Khilar, 2006; Wigginton et al., 2007; Hochella et al., 2008) but will highlight the progress made in the 6th framework project IP FUNMIG (Fundamental processes of radionuclide migration) and the open literature over the past five years concerning the process understanding of nanoparticle related issues in the three host rock formations investigated, namely claystones, crystalline rocks and salt rock overburden. The results show *inter alia* that the inorganic nanoparticle concentration in deep geological groundwaters of advection dominated systems rarely exceeds $1 \text{ mg}\cdot\text{L}^{-1}$ and is expected in the $\text{ng}\cdot\text{L}^{-1}$ range in diffusion controlled systems. For organic nanoparticles DOC concentrations up to tens of milligram in diffusion-controlled indurated clays with molecular sizes mostly $< 500 \text{ Da}$ were found. Fulvic acid type organics were identified in crystalline environments and plastic clay formations (Boom Clay) with molecular sizes $\leq 300 \text{ kDa}$. Additional sources of inorganic nanoparticles from the repository near-field (compacted bentonite) could be identified and the erosion rates were determined. The results indicate under stagnant conditions $\sim 38 \text{ mg}\cdot\text{cm}^{-2}\cdot\text{a}^{-1}$ for bi-distilled water, $\sim 20 \text{ mg}\cdot\text{cm}^{-2}\cdot\text{a}^{-1}$ for glacial melt water (Grimsel groundwater) and very low rates $\sim 0.02 \text{ mg}\cdot\text{cm}^{-2}\cdot\text{a}^{-1}$ for 5 mM CaCl_2 contact water. The low critical coagulation concentration (CCC) indicative for purely diffusion controlled coagulation of $1 \text{ mM}\cdot\text{L}^{-1} \text{ Ca}^{2+}$ found in bentonite nanoparticle stability analysis matches the low nanoparticle mobilization from compacted bentonite found in these systems.

Schäfer, T.; Huber, F.; Seher, H.; Missana, T.; Alonso, U.; Kumke, M. U.; Eidner, S.; Claret, F.; Enzmann, F. (2011) Nanoparticles and their influence on radionuclide mobility in deep geological formations. Applied Geochemistry (2011), <http://dx.doi.org/10.1016/j.apgeochem.2011.09.009>

2.1 Introduction

There is no universally accepted definition for the term nanoparticle, but frequently this notion is used for particles having one or more dimensions of the order of ≤ 100 nm. The upper size range of nanominerals or mineral nanoparticles is likely to be quite variable, depending on the mineral itself (Hochella et al., 2008). The upper size limit should be defined as the size, above which the properties of the particles are indistinguishable from those of the bulk material. In most cases for natural occurring nanoparticles it is clearly not known, below which size the chemical, electrical, optical, mechanical or thermodynamic properties will begin to vary, because, to date, few measurements of this type have been made (Madden and Hochella Jr, 2005; Chernyshova et al., 2007). However, this length scale of transition, where properties differ substantially from those of bulk materials of the same composition is the target of newly developed and designed so-called engineered nanomaterials (ENP) in the broad field of nanoscience (Lieber, 2003). Possible undesirable results of these ENP capabilities are harmful interactions with biological systems and the environment, with the potential to generate toxicity are a new field of research (Nel et al., 2006; Nowack and Bucheli, 2007) not dealt with in this article.

The term “colloid” is frequently used in the field of environmental sciences (geochemistry, hydrogeology) and colloids can be defined as nanoscopic solids of organic or inorganic nature in the size range from ~ 1 nm to ~ 1 μ m (upper size limit depending on their density) that remain suspended in water (Honeyman, 1999). Based on several observations made in groundwater systems (Vilks and Bachinski, 1996b; Hauser et al., 2002; Novikov et al., 2006) the majority of mobile colloids relevant for contaminant migration are with at least one dimension of less than 100 nm. Therefore, we use in this article the term nanoparticle, although in *sensu stricto* the change in properties from the bulk mineral has not been proven.

Inorganic nanoparticles are formed by alteration or physical erosion of minerals, or by direct precipitation from groundwater, and typically comprise of silica, clay minerals, calcite or Fe-oxyhydroxides. Two types of inorganic nanoparticles are usually distinguished. The so-called intrinsic-nanoparticles or eigencolloids consist essentially of polymerized complexes of a particular element (e.g. Pu(IV)-polymer, formed by condensation of hydrolysed actinide ions and consisting of actinide cations linked by anions). The carrier- or pseudo- nanoparticles consist of mineral fragments of crystalline or amorphous solids to which a particular element/radionuclide may be attached. Organic nanoparticles may comprise fragments of degrading organic material, or they may be organic macromolecules (i.e. humic or fulvic acids) or microbes that are stabilized by hydrophilic coatings on their surfaces. Organic materials, especially humic and fulvic acids may form coatings on inorganic nanoparticles, increasing their electrostatic stability.

Numerous publications have demonstrated, that the classical two phase flow concept of transport (stationary phase: sediment; mobile phase: groundwater) has to be expanded by a third phase, namely the nanoparticles, which are ubiquitous in aquifer systems (McCarthy and Zachara, 1989; Wilkinson and Lead, 2006). Neglecting the nanoparticulate phase in groundwater systems can drastically underestimate the mobility of strong sorbing contaminants (e.g. Plutonium) (Kim et al., 1984; Kim, 1994; Kersting et al., 1999). Especially geochemically or hydraulically disturbed systems might generate a high concentration of colloidal phases and therefore can enhance the mobility of strong sorbing contaminants (Ryan and Gschwend, 1994). However, colloid destabilization via aggregation can also lead to an additional retention mechanism for strong sorbing contaminants.

A more recently made review considering twelve performance assessment (PA) programs for deep geological storage of high-level nuclear waste in nine countries (Belgium, Canada, Finland, Japan, Netherlands, Sweden, Switzerland, UK, USA) showed that all programs include colloid formation in their features, events and processes (FEP) list (Wickham et al., 2000) and discuss colloids/nanoparticles in performance assessment (PA), but not commonly model colloids/nanoparticles in PA (SKB, 2005b).

Transport in far-field environments/geological formations has to take into account saturated and unsaturated flow regimes (Robinson et al., 2003). Nanoparticle mobilization and transport in the unsaturated host rocks and from soils to the groundwater table (vadose zone) is an important research topic, which changes nanoparticle migration mechanism (DeNovio et al., 2004) and has to be considered in the far-field system of the U.S. Department of Energy (DOE) Yucca Mountain (Nevada) site and the underground waste tank leakages at the U.S. DOE Washington State Hanford Site (Zhuang et al., 2007). Understanding colloid transport in unsaturated media is complicated by the presence of dynamic air–water interfaces and the increasing discontinuity of water-filled pores with decreasing water content. Additional mechanisms of nanoparticle retention have been suggested, such as film-straining and deposition of nanoparticles on the air–water interface (Figure 2.1). In this work transport phenomena in the unsaturated zone are not discussed in detail.

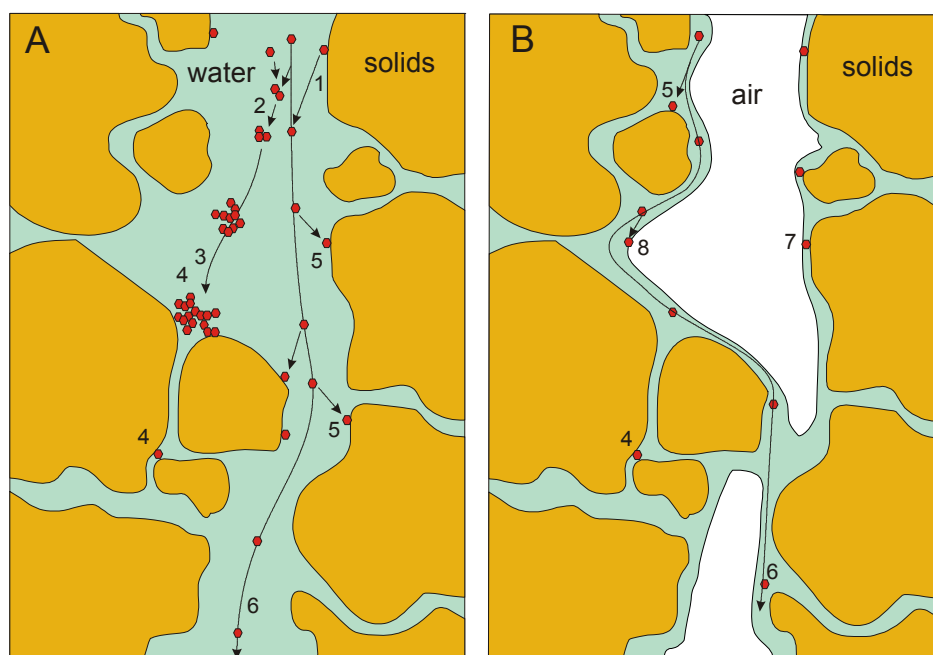


Figure 2.1: (a) Processes controlling the mobility of nanoparticles in water-saturated porous media: (1) release of colloids, (2) aggregation of colloids, (3) immobilization by gravitational settling of aggregates, (4) immobilization by straining of aggregates or single nanoparticles, (5) immobilization by nanoparticle deposition on solid–water interfaces, (6) transport of dispersed nanoparticles over long distances by flowing water. (b) In unsaturated porous media, additional mechanisms of nanoparticle retardation may occur: (7) immobilization by film straining and (8) immobilization by deposition on air–water interfaces (figure taken from Kretzschmar and Schäfer (2005)).

In general, the importance of colloidal phases or nanoparticles on transport processes depends on (a) the presence, (b) the mobility and stability and (c) the slow reversibility or “irreversibility” of metal/radionuclide interaction with these nanoparticles. Therefore, the discussion is structured on the basis of the following key questions to be addressed:

- Are nanoparticles present in deep geological far-field environments?
- Additional nanoparticle sources from the repository near-field?
- Are nanoparticles stable under the conditions of far-field environments?
- Are nanoparticles mobile in far-field environments?
- Do radionuclides interact with nanoparticles? and
- Is this radionuclide interaction reversible or irreversible?

2.2 Background nanoparticle characterization in deep geological far-field systems

The sampling of nanoparticles in groundwater systems is not a trivial issue and a number of artefacts can bias the sampling procedure and therefore the reliable measurements of background nanoparticle concentration. The exact determination of nanoparticle background concentration is motivated by the fact, that this concentration will give an estimation of the maximum transport enhancement for strongly sorbing tracers. In fractured rocks it can be clearly benefited from the experience made in the “colloid community” and this experience is well documented (Backhus et al., 1993; Degueldre et al., 1996; Barcelona et al., 2005). A general procedure for low-flow passive sampling technique has been established for different geological formations as documented in e.g. a workshop summary by Puls (1995). Discussions on the advantages of different analytical techniques that can be used for background nanoparticle sampling are also found elsewhere (Barcelona et al., 2005; Nilsson et al., 2008). A lot of progress has also been made in the field of analytic development concerning the detection of nanoparticles. The community clearly benefitted from developments made especially in the field of nanoparticle size distribution analysis (e.g. via laser-induced breakdown detection s-curve analysis) and the possibility to detect size dispersion/chromatography effects in nanoparticle migration experiments (Walther et al., 2006; Delos et al., 2008).

2.2.1 Inorganic nanoparticles

Taking the mobile equipment of laser-induced breakdown detection (LIBD) (Hauser et al., 2002) applied within the framework of IP FUNMIG, field investigations at the Grimsel Test Site and in the Swedish site investigation program as well as the Ruprechtov site (salt rock overburden) detailed informations on the inorganic nanoparticle concentration were obtained in several observation boreholes and correlated to geochemical parameters. The data shows that inorganic nanoparticle concentration is limited in advective transport dominated far-field environments (crystalline and rock salt overburden) mostly to concentrations $< 1 \text{ mg}\cdot\text{L}^{-1}$ and strongly depends on the ionic strength of the groundwater. Lower concentrations of inorganic nanoparticles are expected if the groundwater composition exceeds an ionic strength of 0.1 M, where a decrease of nanoparticle concentrations down to the detection limit of the LIBD system (~ 10 ppt) could be observed (SKB, 2005a). In the SR-Can report (SKB, 2006b) the highest nanoparticle concentration in groundwaters is expected during a glacial period, especially during the advance and retreat of an ice sheet when groundwater velocities are highest. The concentration is set to the highest measured nanoparticle concentrations in groundwaters at repository depths, $\approx 1 \text{ mg}\cdot\text{L}^{-1}$. The new data collected within IP FUNMIG confirms this highest concentration limit observed in natural groundwater systems and gives therefore further confidence on this nanoparticle concentration value.

2.2.2 Organic nanoparticles

For far-field environments in diffusion controlled claystone systems model calculations based on the pore size distribution and connectivity argue for nanoparticles $\ll 10$ nm to fit through pore necks and model calculations indicate that nanoparticle-related transport is negligible (Nagra, 2002). Several in-situ collected water samples from the Opalinus Clay (Mont Terri) were studied with focus on the size range 1-10 nm and a very low concentration of inorganic nanoparticles around 10-20 ppt was derived with organic nanoparticles (humic substances) below the detection limit (Degueldre et al., 1998). Detailed studies on the organic inventory in indurated clays (Opalinus and Callovo-Oxfordian) porewater have shown rather high dissolved organic carbon (DOC) concentrations of $56.7 \text{ mg}\cdot\text{L}^{-1}$ in the Callovo-Oxfordian (Courdouan et al., 2007b) and from 1.2 to $15.8 \pm 0.5 \text{ mg}\cdot\text{L}^{-1}$ in the Opalinus Clay porewater (Courdouan et al., 2007a). However, a significant fraction of DOC belongs to low molecular weight compounds, with a molecular size < 500 Da, and not nanoparticles (Courdouan et al., 2007b; Courdouan et al., 2007a). For plastic clays (Boom Clay formation) the real porewater

contains $\sim 100 \text{ mg}\cdot\text{L}^{-1}$ DOC (Maes et al., 2006; Liu et al., 2008) and comparison between batch-type studies bringing the whole organic inventory in suspension and the pore water sampled in the HADES underground laboratory (Ionescu et al., 2008) gives indications that the pore-size cut-off of the mobile fraction is $\leq \sim 300 \text{ kD}$. Further support has been obtained within IP FUNMIG using Asymmetrical Flow-Field Flow Fractionation (AsFFFF) (unpublished project internal document PID2.2.17).

Concerning the potential role of organic nanoparticles in crystalline environments studies on groundwaters of the Äspö have shown that fulvic acids represent in the investigated groundwaters a significant fraction of the DOC inventory (Buckau, 2005; SKB, 2005a). In general, for the Grimsel Test Site, Switzerland a DOC concentration of around $1 \text{ mg}\cdot\text{L}^{-1}$ is determined, ranging from $0.24 \text{ mg}\cdot\text{L}^{-1}$ found by Degueldre et al. (1996) and $1.2 \pm 0.2 \text{ mg}\cdot\text{L}^{-1}$ quantified by Schäfer et al. (2004). The groundwater of the shallow region (70 m below surface) in the Äspö underground laboratory (Sweden) has a higher DOC content of $10 - 22 \text{ mg}\cdot\text{L}^{-1}$ (Tullborg and Gustafsson, 1999), with maximum values found by Kienzler et al. (2003) in the CHEMLAB2 borehole of $42.3 \text{ mg}\cdot\text{L}^{-1}$ at $\sim 270 \text{ m}$ depth below surface. For the Whiteshell Research Area (Canada) Vilks and Bachinski (1996a) reported an average DOC concentration of $0.5 \text{ mg}\cdot\text{L}^{-1}$.

2.3 Additional nanoparticle sources from the repository near-field?

2.3.1 Canister and glass corrosion

Although the IP FUNMIG was a far-field project a brief status should be given in this manuscript concerning the potential presence of nanoparticles in the near-field. Early work by Bates and co-workers (Bates et al., 1992) already identified insoluble Pu- and Am-bearing nanoparticles formed during simulated weathering of a high-level nuclear waste glass and pointed to a nanoparticle-trapping mechanism necessary for a waste repository to meet long-term performance specifications. Buck and co-workers identified by analytical transmission electron microscopy plutonium enriched layers on corroded spent uranium oxide fuel which might be an increased potential for the generation of Pu-bearing colloids (Buck et al., 2004). UO_2 nanoparticles were identified as corrosion products of metallic uranium nuclear fuel (Kaminski et al., 2005a) and predominantly clay nanoparticles were released from corroded uranium-aluminium fuels (Kaminski et al., 2005b) and identified in glass corrosion products (Buck and Bates, 1999) which shows the dependency of the colloid source term on the corroded waste forms.

Within IP FUNMIG a couple of research activities focused on the generation mechanism of nanoparticulate phases as e.g. hydroxyl-aluminosilicates (HAS), which can be seen as precursor phases of clay minerals that will be formed as an interstage product. The spectroscopic results of trivalent actinide HAS interaction show a structural incorporation (Kim et al., 2005; Panak et al., 2005; Kim et al., 2007), which in turn can be seen as a further near-field retardation or mobilisation process depending on the mobility of these nanoparticulate phases. Other work include classical thermodynamic data generation by measuring solubility limits of tetravalent elements through the onset of nanoparticle formation (Neck et al., 2007b) which indicate that especially tetravalent actinides form nanoparticles in the near-field. Here, also within the FUNMIG project data has been generated e.g. on the formation of U(IV) nanoparticles (Opel et al., 2007) and U(VI) mineral species as boltwoodite and compreignacite (Arnold and Baumann, 2009).

As a consequence of these near-field nanoparticle observations mentioned above the bentonite buffer as repository component in the e.g. KBS-3 disposal system has to filter nanoparticles as a safety function (SKB, 2006b). As a quantitative limit or safety function indicator criterion to fulfil the role of nanoparticle filtration a buffer density $> 1,650 \text{ kg}\cdot\text{m}^{-3}$ is required. This requirement is put on the buffer so that it is dense enough to immobilize fuel nanoparticles escaped from a defective

canister. Thereby, the release of several key radionuclides will be limited purely by their solubility. The criterion is based on 15 nm gold nanoparticle transport experiments showing that the bentonite microstructure with a dry density of $1,000 \text{ kg}\cdot\text{m}^{-3}$ (saturated clay density of about $1,640 \text{ kg}\cdot\text{m}^{-3}$) effectively filter these nanoparticles (Kurosawa and Ueta, 2001). Homogenization analysis indicates that interstitial pores sizes of $< 1 \text{ nm}$ may be achieved for montmorillonite partial densities in excess of $1,200 \text{ kg}\cdot\text{m}^{-3}$ (Kurosawa et al., 2006).

2.3.2 Bentonite backfill and buffer erosion

Bentonite as backfill and buffer material is an important component of engineered-barrier systems (Gates et al., 2009) and will be used in its pure form or as bentonite/sand mixture in different repository concepts for spent fuel/high level waste (Hummel, 2008). A number of groups within the FUNMIG consortium have investigated parameters influencing the erosion behaviour of compacted bentonite (Alonso et al., 2008; Seher et al., 2009). These parameters included *inter alia* the dry density of compacted bentonite, the exchangeable cation composition, the clay type, the surface area exposed to hydration, the pore size of the extrusion contact and the contact water solution chemistry (pH, ionic strength, cation composition). The investigations have shown that for an ionic strength below the critical coagulation concentration (CCC) determined in bentonite nanoparticle stability studies a colloid/nanoparticle generation can be confirmed. The strong pH dependency of colloid stability in the sodium system observed in coagulation experiments was confirmed in the colloid generation experiments. Furthermore, the exchangeable cation composition of the starting clay material clearly controls the bentonite erosion rates with Na-exchanged bentonite being more sensitive than Ca-exchanged bentonite to erosion, as expected. A filter pore size dependent colloid generation mechanism could not be observed in the course of the experimental period (two years). Flow rate dependent nanoparticle generation was also investigated outside the FUNMIG consortium and e.g. Baik and co-workers (Baik et al., 2007) could observe the release of particulate material (542-1363 nm diameter) under advective flow conditions (4.7 to $473 \text{ m}\cdot\text{a}^{-1}$). In all experiments mentioned above the colloid concentration reaches with water contact time a plateau value indicating a steady-state of the nanoparticle generation process. Higher dry densities of compacted bentonite yielded a higher colloid concentration plateau value. The exchange of the contact water leads to a rapid neo-formation of nanoparticles reaching again a plateau value, sometimes below the first concentration plateau. The reason for these observations (a) dynamic generation/ aggregation equilibrium and/or (b) depletion of the colloid source could not be clarified within the project. The internal erosion of the sand- bentonite mixtures was not focus of IP FUNMIG and here we refer to published data (Kaoser et al., 2006). Kaoser et al. found that internal erosion is mainly influenced by porosity, which can be reduced by properly selecting the sand particle size distribution and the bentonite admixture percentage. An empirical expression to predict the risk of internal erosion in the sand-bentonite mixtures has been proposed which can be used for designing compacted bentonite.

In the following the erosion rates determined by different experimental groups within FUNMIG and data available in the open literature will be summarized by normalizing the released bentonite mass to the contact area (cm^2) and the contact time (s) of the different experiments. Data for compaction densities of $\geq 1.6 \text{ g}\cdot\text{cm}^{-3}$ reveal maximum erosion rates (assuming linear erosion progress) under stagnant conditions for bi-distilled contact water of $1.2\cdot 10^{-6} \text{ mg}\cdot\text{cm}^{-2}\cdot\text{s}^{-1}$ and of $6.3\cdot 10^{-7} \text{ mg}\cdot\text{cm}^{-2}\cdot\text{s}^{-1}$ in Grimsel groundwater. Lowest bentonite erosion rates were found in contact with 5 mM CaCl_2 solution with $4\cdot 10^{-10} \text{ mg}\cdot\text{cm}^{-2}\cdot\text{s}^{-1}$. Increase in flow rate to $3.3\cdot 10^{-6} \text{ m}\cdot\text{s}^{-1}$ resulted in bentonite erosion rates of $1\text{-}4\cdot 10^{-7} \text{ mg}\cdot\text{cm}^{-2}\cdot\text{s}^{-1}$ (Seher et al., 2009) and investigations of Baik et al. in groundwater from the Yuseong Site revealed highest erosion rates of $6.8\cdot 10^{-7} \text{ mg}\cdot\text{cm}^{-2}\cdot\text{s}^{-1}$ for a flow velocity of $1.5\cdot 10^{-5} \text{ m}\cdot\text{s}^{-1}$. It has to be noted that the observed time- dependent bentonite erosion rate changes with the formation of a plateau value are overestimated due to the linear regression used. Using a simplified zero order model to predict the erosion rates (fracture aperture $\delta = 1\cdot 10^{-4} \text{ m}$; outer periphery of the intruding bentonite as circular boundary with a diameter $d = 2 \text{ m}$) three stages of the glacial melt

water intrusion can be differentiated (Liu and Neretnieks, 2006). In the initial stage of glacial water intrusion lasting a few years, when the bentonite becomes equilibrated with typical fresh glacial groundwater as Grimsel groundwater (Geckeis et al., 2004) without re-supply of calcium erosion rates of $4.7 \cdot 10^{-4}$ - $6.6 \cdot 10^{-2}$ $\text{mg} \cdot \text{cm}^{-2} \cdot \text{s}^{-1}$ are predicted. In the intermediate stage the bentonite erosion rate is dependent on the presence or absence of readily soluble calcium phases such as gypsum/anhydrite to provide a calcium supply. In the presence of gypsum erosion rates of $4.7 \cdot 10^{-5}$ - $6.8 \cdot 10^{-3}$ $\text{mg} \cdot \text{cm}^{-2} \cdot \text{s}^{-1}$ are predicted, whereas in the absence of gypsum erosion rates of $8.5 \cdot 10^{-3}$ - 1.2 $\text{mg} \cdot \text{cm}^{-2} \cdot \text{s}^{-1}$ are calculated. Taking the highest erosion rates determined in the FUNMIG laboratory program of $1.2 \cdot 10^{-6}$ $\text{mg} \cdot \text{cm}^{-2} \cdot \text{s}^{-1}$ even the lowest modelled erosion rates overestimate the experimental determined bentonite erosion rate by more than one order of magnitude. The data generated within FUNMIG gives the experimental basis for improved models on bentonite erosion to be developed in the near future.

Nanoparticles might also be generated through local oversaturation by mixing of bentonite pore water with granite groundwater. Studies on the neo-formation of nanoparticles in synthetic Febex porewater resembling the saturated bentonite state with natural groundwater from the Grimsel Test Site (GTS) revealed a limited nanoparticle concentration increase (~ 100 ppt, average diameter ~ 30 nm) but showed an influence on trivalent actinide speciation most likely polysilicic acid nanoparticles (Kunze et al., 2008a; Kunze et al., 2008b).

2.4 Stability of nanoparticles in far-field environments?

Based on long-term safety for KBS-3 repositories at Forsmark and Laxemar evaluation (SKB, 2006b) the stability of suspended nanoparticles is much decreased as well as the stability of the buffer and backfill is enhanced if the concentration of divalent cations exceeds 1 mM. The criterion for the safety function indicator is $[M^{2+}] > 1$ $\text{mmol} \cdot \text{L}^{-1}$, as available experimental data suggests that montmorillonite nanoparticles are not stable at concentrations above this limit (SKB, 2006b). The stability of Febex bentonite nanoparticles was determined by coagulation studies under variation of pH, electrolyte concentration and fulvic acid (GoHy-573FA) content. For CaCl_2 electrolyte solutions, a pH independent critical coagulation concentration Ca-CCC of 1 $\text{mmol} \cdot \text{L}^{-1}$ was found and supports the above mentioned safety function indicator. In the case of NaCl background electrolyte a pH dependent Na-CCC could be determined with 15 ± 5 $\text{mmol} \cdot \text{L}^{-1}$ at pH 6, 20 ± 5 $\text{mmol} \cdot \text{L}^{-1}$ at pH 7, 200 ± 50 $\text{mmol} \cdot \text{L}^{-1}$ at pH 8, 250 ± 50 $\text{mmol} \cdot \text{L}^{-1}$ at pH 9 and 350 ± 100 $\text{mmol} \cdot \text{L}^{-1}$ at pH 10, respectively. The determined Na-CCC values for pH 6 and pH 7 are in quite good agreement with published Na-CCC data for SWy-1 and the beidelite from Hetzel and Doner (1993), Lagaly and Ziesmer (2003) for pH 6.5 and Chheda et al. (1992) for pH 6.8. Tombácz and Szekeres (2004) however determined Na-CCC values at pH 6 for Wyoming montmorillonite SWy-1 & SWy-2 of 52 $\text{mmol} \cdot \text{L}^{-1}$, which are considerably higher than the Na-CCC values observed in this study for Febex bentonite. Theoretical calculations by Liu et al. (2009b) predict based on the Febex bentonite nanoparticle size of 185 nm and a calculated particle surface area S_p of $8.2 \cdot 10^4$ nm^2 (particle thickness δ_p 2.4 nm) a Na-CCC of 20-30 $\text{mmol} \cdot \text{L}^{-1}$ for pH 5 to ~ 6.5 , which is slightly above the measured values for pH 6.

The observed increase in Na-CCC above the isoelectrical point pH_{iep} of the montmorillonite edges might be explained by a full delamination of the montmorillonite platelets based on the approach of Liu et al. (2009b). Asymmetrical Flow Field Flow Fractionation (AsFFFF) studies of fully delaminated Febex bentonite by Bouby and co-workers (Bouby et al., 2009) have shown a bimodal size distribution varying from 15-300 nm with peak maxima at 40 nm and 150 nm. Taking a particle thickness δ_p of 1.2 nm for fully delaminated platelets and the AsFFFF derived smaller colloid size peak maxima of 40 nm a Na-CCC of approx. 200 $\text{mmol} \cdot \text{L}^{-1}$ would be predicted, which is in fairly good agreement with the measurements made at pH 8-10. However, it has to be noted that published Na-CCC data in the pH range 8-10 scatter considerably with highest values found by Tombácz et al. (1990) of 350-400 $\text{mmol} \cdot \text{L}^{-1}$ at pH 8 and lowest values of 18-40 $\text{mmol} \cdot \text{L}^{-1}$ at pH 8-10 for SWy-1 (Hetzel and Doner, 1993).

2 Nanoparticles and their effect on radionuclide mobility

The addition of $1 \text{ mg}\cdot\text{L}^{-1}$ DOC FA increases the Ca/FA-CCC to $2 \text{ mmol}\cdot\text{L}^{-1}$. Scanning Transmission X-Ray Microscopy (STXM), a technique to map carbon functionality under high resolution (Schäfer et al., 2007) showed an FA association with Febex bentonite colloids as surface coating and specific hot spots.

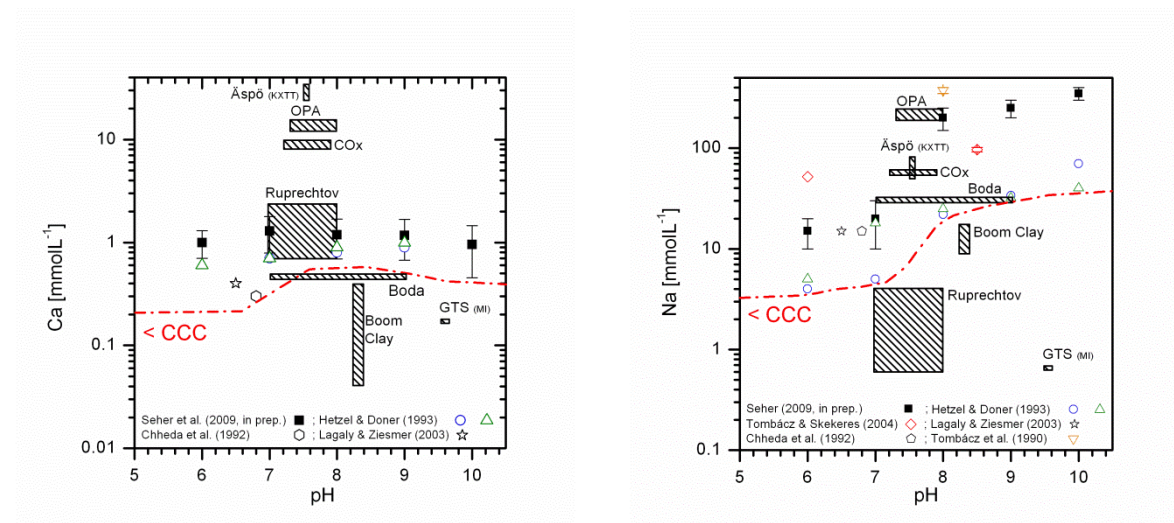


Figure 2.2: Critical coagulation concentration (CCC) as a function of the pH value determined for the calcium (Ca-CCC) and the sodium (Na-CCC) system for different montmorillonites are represented as different data points. The red dash-dotted line indicates the onset of purely diffusion controlled coagulation. In addition, the pH- cation concentration regions for the different geological formations studied within IP FUNMIG are inserted as shaded areas (data with reference) is given in Table 2.1.

Table 2.1: Nanoparticle stability determining chemical parameters for the different host rock formations investigated within IP FUNMIG.

Formation	pH	Na [mmol·L ⁻¹]	Ca [mmol·L ⁻¹]
Grimsel Test Site (MI Shearzone) ¹	9.5 - 9.6	0.64	0.13
Äspö groundwater ¹ (TRUE-1 site, KXTT4)	7.5 - 7.6	52.2 – 76.6	24.2 – 33.9
Boom Clay ²	8.2 - 8.4	8.7 - 17.7	0.04 - 0.4
Callovo-Oxfordian Argillite (COx) ²	7.2 - 7.9	56 – 57	7.6 - 9.6
Opalinus Clay (OPA) ²	7.3 – 8.0	187 – 245	11.3 - 15.2
Boda Claystone ²	7.0 – 9.2	30	0.45
Ruprechtov Site Rock-salt overburden ³	6.15 - 8.0	0.58 – 4.0	0.65 – 2.2

¹(Bouby et al., 2010); ²(Altmann, 2009); ³(Noseck et al., 2009)

In Figure 2.2 the experimentally determined Ca-CCC and Na-CCC values for bentonite derived montmorillonite nanoparticles (Tombácz et al., 1990; Chheda et al., 1992; Hetzel and Doner, 1993; Lagaly and Ziesmer, 2003; Tombácz and Szekeres, 2004) and the water chemistry of the fractured rocks (Grimsel Test Site, Migration shearzone; Äspö Hard rock Laboratory, water KXTT), indurated and plastic clay formations (Boom Clay, Callovo- Oxfordian argillite, Opalinus Clay and Boda Claystone), and the Ruprechtov Natural Analogue Site investigated within the FUNMIG project are

compiled. Based on this comparison montmorillonite nanoparticle stability is not expected for the CO_x, OPA, Boda claystones and the Äspö system both from the Ca and Na porewater concentrations under the current groundwater geochemistry. Furthermore, based on the Ca concentration montmorillonite nanoparticles should coagulate at the Ruprechtov site. However, for the Boom Clay system, based on the Ca and Na concentrations and also considering the elevated dissolved organic carbon concentrations additionally stabilizing clay colloids nanoparticle stability can be expected. The strongest colloid/nanoparticle stabilizing geochemical conditions are clearly found in the Grimsel granite groundwater, as expected.

2.5 Mobility of nanoparticles

The mobility of nanoparticles is mainly driven by their stability and retardation processes during transport (attachment, matrix diffusion, size cut-off), which are usually lump together in the term *filtration* and will be discussed in the following for an advection or diffusion dominated system.

2.5.1 Advection controlled systems

There are a number of field investigations published concerning nanoparticle sampling and characterization of associated radionuclides at different contaminated sites like Nevada Test Site, Mayak etc. (Kersting et al., 1999; Novikov et al., 2006; Utsunomiya et al., 2009) and a fair amount of publications is also available on laboratory column investigations. Furthermore, migration tests have been performed at underground research laboratories to investigate the influence of bentonite nanoparticles on the radionuclide mobility (Möri et al., 2003; Geckeis et al., 2004). Especially under long residence times it became obvious that in order to reliably quantify the mobile nanoparticle fraction or “source term” (a) the natural background concentration and their fluctuation has to be quantified and (b) sampling artefacts have to be minimized (Missana et al., 2008a).

Nanoparticle filtration will control the transport of nanoparticle associated strongly sorbing radionuclides in water conduction features. In most laboratory transport studies performed on over-cored natural fractures, the nanoparticle breakthrough curve maximum arrives slightly earlier (retardation factor $R_f < 1$) or similar to that of the conservative tracer ($R_f = 1$) with the later usually observed under near-natural flow conditions. Even in Grimsel water, where the chemical conditions favour colloidal stability and “unfavourable” electrostatic conditions for colloid-rock attachment exist, a mass recovery reduction with increasing residence time indicating filtration and a nanoparticle attachment to fracture surfaces was observed (Schäfer et al., 2004; Albarran et al., 2009; Schäfer et al., 2009). Similar results of decreasing nanoparticle recovery were obtained when the roughness of the fracture surface was increased as predicted by microscale modelling approaches implementing surface roughness (Boutt et al., 2006) and known from membrane fouling (Hoek et al., 2003; Hoek and Agarwal, 2006).

The quantification of nanoparticle retention under conditions unfavorable and favorable to electrostatic attachment was analyzed within FUNMIG by μ PIXE using gold nanoparticles from 2-100 nm diameter (Alonso et al., 2009), fluorescence microscopy using 25 nm carboxylated latex microspheres (Filby et al., 2008) and AFM force spectroscopy using the so-called “colloid probe” technique (Filby et al., 2009a). Under favorable conditions, electrostatic attraction prevailed: strong adsorption of negatively charged colloids was in fact observed at pH values close or below the point of zero charge (pH_{PZC}) of the respective mineral surface. The adsorption of polyvalent cations as Eu^{3+} ($10^{-5} \text{ mol}\cdot\text{L}^{-1}$ concentration) increased nanoparticle attachment to minerals (Filby et al., 2008).

Under unfavourable conditions nanoparticle attachment was still observed (Alonso et al., 2009) and even in the alkaline regime typical for the Grimsel groundwaters (Filby, 2009). In this case, nanoparticle (carboxylated microspheres) adsorption can only be expected on apatite in presence of Ca(II) or with Grimsel groundwater. Overall, nanoparticle retention on granite was found to be

strongly dependent on small scale chemical effects, roughness or non-uniform distribution of charge sites or even the combination of effects mentioned above. Consequently, detailed mechanistic understanding on the nanoparticle retention mechanisms under “unfavourable” conditions and especially the implementation into model approaches is still pending after the closure of FUNMIG (see discussion in chapter 2.8).

Beside the above mentioned surface retention on fracture walls the possible matrix diffusion is an additional process that can retain or eliminate nanoparticles from the mobile aqueous phase. Studies within FUNMIG focused on the precise determination of bentonite nanoparticle diffusion coefficient in the granite rock matrix. The results obtained by Rutherford backscattering spectrometry (RBS) revealed diffusion coefficients of $10^{-17} \text{ m}^2\cdot\text{s}^{-1}$ for $250 \pm 50 \text{ nm}$ diameter bentonite nanoparticles (Alonso et al., 2007a). Surprisingly, studies on the size dependency of the diffusion coefficient performed with gold nanoparticles in the size range from 2 nm up to 100 nm by the same group revealed lower D_{max} values of $8\cdot 10^{-18} \text{ m}^2\cdot\text{s}^{-1}$ and D_{min} values of $8\cdot 10^{-19} \text{ m}^2\cdot\text{s}^{-1}$, respectively, which might indicate additional sorption taking place (Alonso et al., 2007b). Taking the diffusion length dependence over time in a diffusion-controlled system $x = \sqrt{D \cdot t}$ with D diffusion coefficients ($\text{m}^2\cdot\text{s}^{-1}$), x the diffusion length (m) and t the residence time in (s) assuming an average groundwater velocity of $1 \text{ m}\cdot\text{a}^{-1}$ and a observation period of one year the bentonite nanoparticles would travel by advection 1 m, while they enter the matrix porosity to a maximum distance of $1.8 \text{ }\mu\text{m}$ for the investigated granite. It has to be stated clearly in this context that the molecular diffusion coefficient in water D_w is a real physical parameter, while the effective diffusion coefficient in the rock matrix D_e is linked to D_w via an empirical correlation (Archie’s Law) including the porosity ε and a cementation factor m ; $D_e = D_w \cdot \varepsilon^m$. From this point of view the effective diffusion coefficient D_e is host rock formation dependent and it could be e.g. shown that the cementation factor m varies between 2 and 3 for HTO and Cl^- in clays and shales (NEA, 2009).

This data can be implemented in transport models taking into account matrix porosity/diffusion as potential retention process, but the effect for nanoparticle retention based on the matrix diffusion coefficients determined should be minor.

2.5.2 Diffusion controlled system

For nanoparticle mobility in claystone formations or compacted bentonite mostly indirect information is available. Diffusion experiments with lignosulfonate and humic acid nanoparticles through MX-80 bentonite (dry densities from 600 to $1,800 \text{ kg}\cdot\text{m}^{-3}$) with an average size of 80 and $< 10 \text{ nm}$, respectively showed diffusivities of these organic nanoparticles to be in the same range as negatively charged ions like Cl^- and I^- , which was very unexpected. The effect of humic nanoparticles on both Co and Eu sorption as well as on diffusion was significant. The apparent diffusivity (D_a) increased significantly for both Co(II) and Eu(III) when humic nanoparticles were present and the distribution coefficient (K_d) values decreased (Wold and Eriksen, 2003; SKB, 2006a; Wold and Eriksen, 2007). Explanations for the lack of nanoparticle filtration could be the presence of larger pores in the compacted bentonite, or transformation of the molecules during course of the experiment.

The results mentioned above are somehow in contradiction to the findings of the Kurosawa group (Kurosawa and Ueta, 2001; Kurosawa et al., 2006) who found effective nanoparticle filtration at a saturated clay density of about $1,640 \text{ kg}\cdot\text{m}^{-3}$ and interstitial pores sizes of $< 1 \text{ nm}$ for montmorillonite partial densities in excess of $1,200 \text{ kg}\cdot\text{m}^{-3}$.

For diffusion controlled claystone far-field environments model calculations are made. The model calculations indicate that based on the pore size distribution and connectivity it can be argued for nanoparticles $\ll 10 \text{ nm}$ fitting through pore necks and nanoparticle related transport can be negligible (Nagra, 2002). Several in-situ collected water samples from the Opalinus Clay (Mont Terri)

were studied with focus on the size range 1-10 nm. A concentration of inorganic colloids around 10-20 ppt was derived and humic colloids below the detection limit (Degueldre et al., 1998). New detailed studies on the organic inventory of the Opalinus and Callovo-Oxfordian porewater performed outside the FUNMIG consortium have shown that a significant fraction of dissolved organic carbon (DOC) belongs to low molecular weight compounds with a molecular size < 500 Da and not nanoparticles (Courdouan et al., 2007b; Courdouan et al., 2007a). For plastic clays (Boom Clay formation) comparison performed between batch-type studies bringing the whole organic inventory in suspension and the pore water sampled in the HADES underground laboratory gives indications to a pore-size cut-off of ~300 kD. Further support has been obtained within FUNMIG using Asymmetrical Flow-Field Flow Fractionation (AsFIFFF). Taking the size distribution of humic and fulvic acids analyzed from the Gorleben aquifer system as reference (Kim et al., 1990; Buckau, 2004) one has to assume that both humic and fulvic acids can be mobile in the Boom Clay system.

Concerning the mobility of organic nanoparticles (humic and fulvic acids) and metals the prediction of metal distribution in the ternary system (mineral surface - organic matter – metal) using the linear additive model (LAM) approach based on the binary systems often fails (Heidmann et al., 2005). Spectroscopic investigations performed within the FUNMIG project probing both the metal environment (Eu(III)-TRLFS) and the organic functionality (carbon K-edge XANES) could show that fractionation can occur depending on the mineral surface site occupancy (Claret et al., 2008) and developments were made on the ligand charge distribution (LCD) model to explain the differences in sorption behaviour of different humic substance size fractions to overcome the limitations of LAM models (Weng et al., 2007).

2.6 Interaction of radionuclides with nanoparticles

2.6.1 Inorganic nanoparticles

The sorption behaviour of a whole suite of metals has been studied within FUNMIG including monovalent (Cs), divalent (Ni, Sr, Co), trivalent (Am, Cm, Nd, Eu, Gd, Lu, Y), tetravalent (Th, Pu, Se) and hexavalent (U, Se) ions. Also the solid material varied from well defined model systems (gibbsite, bayerite, α -Alumina, amorphous silica, quartz, ferrihydrite, magnetite, synthetic hectorite) to purified natural clays (Febex Na-smectite, Illite du Puy Na-form) and micas (biotite) and additionally work on rock samples from host rocks investigated within FUNMIG. For details on metal adsorption work performed within FUNMIG and the development of models it is referred to (Lützenkirchen, (this issue)). Outside the project *inter alia* a compilation of data for a high-level waste repository in Korea including pseudo-colloid formation constants or radionuclide- nanoparticle sorption coefficients for Am, Sr, and U are given (Baik et al., 2008). Another example was the experimental and modeling study on U(VI)-Na-smectite interaction, where reasonable model fits could be obtained by taking 15% of the BET surface area as edge site surface (Korichi and Bensmaili, 2009).

2.6.2 Organic nanoparticles

A couple of publications appeared in the last years on the characterization and role of organics found in porewaters or extracted by different procedures from claystones. To compare the published studies the conditions chosen for the complexation studies have to be carefully compared. Laboratory experiments by Glaus and co-workers (Glaus et al., 2005) indicated that sorption characteristics of nickel, europium and thorium were independent of the presence or absence of organic nanoparticles in synthetic porewater or aquatic OPA extracts with total inorganic carbon concentrations (TIC) ranging from $2.84 - 8.34 \cdot 10^{-3}$ M. Cm^{3+} complexation studies on extracted organic matter from the COx host rock isolated clay fraction using 0.2M NaClO_4 at pH 5.7 - 6.0 revealed in absence of inorganic carbon a brown coal derived fulvic acids comparable $\log(\beta)$ values of 5.5 to 6.5

and for the OPA of 6.0 (Claret et al., 2005). Calculated Eu-speciation under in-situ conditions taking into account the carbonate content, concentration of all known inorganic compounds, the low molecular weight organic acids (LMWOA) and using the additional found strong organic ligand (DOM) binding L_{Eu} with a binding constant $\log(\beta)$ of 6.50 determined by differential pulse voltametry (DPV) revealed for the OPA porewater up to 54 % $EuCO_3^-$ and 29 % Eu-DOM complexes (Courdouan et al., 2008). The presence of DOM may therefore enhance the Eu solubility in OPA porewater by a maximum surplus of $\sim 5 \cdot 10^{-8}$ M.

The majority of work conducted within FUNMIG focused *inter alia* on (a) the actinide complexation behaviour of organics, (b) the potential role of kinetics on metal ion humic substance interaction, (c) the development and application of spectroscopic methods to gain insights into the complexation mechanism and the influence of humic substances on the metal redox state. A brief summary on a topical session concerning the above mentioned topics held within a FUNMIG Annual workshop in 2007 is available and gives also some views on how we can account for organics in a safety case (Schäfer and Reiller, 2008). The FUNMIG experimental program on humic acid complexation focused mainly on tri- and tetravalent actinides (Szabo et al., 2006; Konstantinou et al., 2009) and variation of metal loading and pH (Rabung and Geckeis, 2009) and the compilation and interpretation of actinide (IV) – humic acid data available (Reiller et al., 2008). A further aspect investigated within FUNMIG was the competition between trivalent actinides or their chemical homologues (REE), alkaline earth and d-transition metals for organic matter binding sites and analysis of the chemical environment by advanced spectroscopic methods (Kumke et al., 2005). Comparison of humic substance extracts from “terrestrial” and “aquatic” origin was performed to link molecule structure differences to metal complexation changes. A similar chemical environment for Eu(III) complexation in terms of crystal ligand splitting and luminescence decay was found for the ‘terrestrial’ samples, whereas ‘aquatic’ originating extracts do provide a somewhat different but also inner consistent chemical environment with slightly less symmetric fluorescence spectra compared to ‘terrestrial’ samples (Brevet et al., 2009). Further work is in progress in order to verify the potential wider applicability of these spectroscopic observations. Due to the presence of other metal ions in natural environments a competition for organic molecule binding sites can be expected. The effect of Ca(II) and Cu(II) on the binding of Eu(III) was evaluated using time-resolved luminescence spectroscopy and showed for Cu(II) a stronger competition with Eu(III) inducing its release into the Donnan phase, and into the bulk solution as free Eu^{3+} . This could be evidenced by both the shape of the spectra and by the decrease in the luminescence decay times. In contrast, Ca(II) induces a modification of the HA structure, which enhances the luminescence of humic-bound Eu(III), and causes a minor modification of the chemical environment of the complexed rare earth ion. In other words this study shows that Eu(III) and Ca(II) do not share the same binding sites whereas Eu(III) and Cu(II) are actually in direct competition (Marang et al., 2006; Marang et al., 2008; Marang et al., 2009).

As pointed out by Reiller and co-workers (Reiller et al., 2008) especially the data for the redox sensitive elements U, Np and Pu cannot be interpreted by a complexation- only mechanism and redox processes have to be included. Here, investigations focused mainly on the Se and Tc humic substance interaction (Bruggeman et al., 2005; Bruggeman et al., 2007) and will be discussed in detail in a separate chapter within this special issue.

2.7 Reversibility of radionuclide sorption

Application of thermodynamic equilibrium approaches require the detailed knowledge of the residence time and the desorption kinetics, otherwise the assumption of local equilibrium will fail to describe metal ion transport in nanoparticle containing groundwater (Artinger et al., 2002). Although desorption kinetics or the reversibility of metal sorption on nanoparticles is a key issue to quantify the role of nanoparticle-facilitated transport in far-field environments especially for future performance assessment periods and has been pointed out by a number of publications developing

colloid/nanoparticle transport models (Turner et al., 2006; Bekhit and Hassan, 2007; Bouby et al., 2010), the laboratory and field data basis is rather limited.

The elucidation of underlying processes which are responsible for the observed kinetics and notably the possible existence of long term kinetics (close to “irreversibility”) are a key point and have to be a focus as documented below in further studies on actinide nanoparticle interaction.

Probably one of the most extensively investigated systems concerning reversibility is the caesium sorption onto clay (especially illite) (Comans, 1987; Comans et al., 1991; de Koning and Comans, 2004). Reversibility of trace metal sorption in batch-type studies has often been found to be incomplete, which is interpreted by some authors as partially “irreversible” binding (e.g. (Bellenger and Staunton, 2008; Galunin et al., 2009) after 1 day desorption time). Isotopic exchange studies on Sm and Yb (Coppin et al., 2003) and spectroscopic work using time-resolved laser fluorescence spectroscopy (TRLFS) (Rabung et al., 2005) however indicates the formation of inner-sphere surface complexes at pH > 5 for Eu(III)/Cm(III) in the form $\equiv\text{S-O-Eu/Cm(OH)}_x^{(2-x)}(\text{H}_2\text{O})_{5-x}$ which are expected to be slow but fully reversible. Also work of Latrille & Herbette on Sn(IV) and Pu(IV) sorption reversibility on Callovo-Oxfordian argillite has revealed sorption reversibility (Latrille et al., 2006). The apparent lack of reversibility found in some studies might therefore be due to the short desorption experiment duration in comparison to the slow desorption kinetics as found e.g. for Cd (Comans, 1987) or in the case of Eu and especially Th (Bouby et al., 2009). Especially in the later work conducted in the framework of FUNMIG, humic acid was used as a competing ligand to initiate and force desorption of Eu and Th initially bound to bentonite colloids. Even after shortest Th bentonite contact times of 24 hours prior to humic acid addition, 30-50 % of the Th remains bentonite colloid bound over a 3 years observation period.

The slow desorption kinetics of colloid-bound radionuclides and a possible subsequent sorption onto the rock matrix might have a strong impact on the colloid-facilitated transport depending on the rate of advection (residence time) as discussed later (Turner et al., 2006).

Concerning reversibility kinetics of humic substances and their effect on the radionuclide mobility it is referred to the chapter of Bryan and co-workers within this special issue and no further details will be given here.

2.8 Nanoparticle modeling approaches

2.8.1 Nanoparticle stability

Reliable models for colloid/nanoparticle stability determination of monodisperse size distributions used in various commercial applications exist for decades. Transferring this expertise to the real (natural) world has been performed quite often and was in many cases successful. The nanoparticle stability and collision efficiency prediction often relies on the classical approach of the DLVO theory (Derjaguin and Landau, 1941; Verwey and Overbeek, 1948) summing up electrostatic and dispersive interactions. The suspending phase water is treated thereby as a force transmitting medium. However, the structure of water and other moieties (sorbed or dissolved) may have non-DLVO effects. Significant progress has been made to implement these non-DLVO forces as hydrogen bonding and the hydrophobic effect, hydration pressure, non-charge transfer Lewis acid base interactions, and steric interactions to describe nanoparticle stability (Grasso et al., 2002). The experimental bentonite stability results presented in Figure 2.2 were described by means of an approach summing up the DLVO short-range Born repulsion, van der Waals attraction and electrical double layer repulsion as well as the non-DLVO hydration forces based on the geometrical assumptions published in (Mahmood et al., 2001). The measured zeta (ζ)-potential of the bentonite colloids was used as platelet face charge and the edge charge is estimated by the combination of silica and alumina ζ -

potential data in the ratio given by the Febex bentonite structural formula (Villar et al., 1998). Adjusting the montmorillonite face charge by a maximum of ± 12 mV was sufficient to successfully reproduce the measured stability ratios W . The Na-CCC values, however, could only be reasonably predicted using solely the calculated edge-face interaction energy. The strong deviations of the model predictions and the experimentally determined Na-CCC values found at low electrolyte concentrations, are explained by the spill-over of the platelet face electrical double layer (EDL) shielding the positive platelet edge charge (Seher et al., 2006; Seher et al., 2010, in prep.) points to the significance of the aspect ratio for the prediction of clay nanoparticle stability and the CCC as demonstrated also by other groups (Liu et al., 2009b).

A bottleneck in testing new models for nanoparticle interaction forces has been the absence of reliable force measurement techniques and data for environmental relevant systems. AFM force distance measurement is one direction to overcome the data gap. Using latex microsphere as nanoparticle probe and different granite rock forming minerals as “collector” surface within FUNMIG have shown the sensitivity of nanoparticle attachment to the Ca solution concentration, the presence of Ca-bearing mineral phases and pH (Filby, 2009). Work outside the FUNMIG consortium has used successfully the extended DLVO-theory including non-DLVO forces to explain interaction forces measured by AFM for rather complicated (bitumen-silica-illite-montmorillonite used as nanoparticle probe) natural systems (Liu et al., 2004; Liu et al., 2005). Another approach, called particle force light scattering (PFLS), combines the techniques of differential electrophoresis and intensity light scattering to measure the critical force required to separate spheres and has been recently used to measure forces between Brownian, nearly touching particles down to 85 nm (Velegol et al., 2007). The forces, some less than 0.1 pN matched within a factor of 2 with predictions from depletion (Walz and Sharma, 1994) and DLVO theory (Velegol et al., 2007). Interestingly, these depletion forces can explain the effect of low DOC concentrations on the potential stability increase of montmorillonite nanoparticles observed (Seher et al., 2010, in prep.).

A model for the stability predictions of near field nanoparticles generated from the nuclear waste forms has also been published (Buck and Wittman, 2009), but there is considerable discussion e.g. for Yucca Mountain, if the reference smectite or iron-oxy-hydroxide colloids and their surface properties used in these analysis/model reports (AMRs) will behave similar to the nanoparticulate phases found in corrosion studies (Traexler et al., 2004).

2.8.2 Bentonite buffer erosion and nanoparticle generation

Bentonite erosion is a well known problem in civil geology and mining engineering (Chapuis, 2002) and has also been discussed as a method for retrieval of canisters in disposal of spent nuclear fuel even after these canisters have been deposited and the surrounding bentonite has absorbed water to the saturation point (Sjöblom et al., 1999). An experimental and numerical study investigating the hydromechanical behaviour of the rock-bentonite interface has demonstrated that bentonite is very sensitive to hydraulic erosion and the induced variation of transmissivity has to be taken into account in model approaches (Buzzi et al., 2008).

New models for the upward expansion of compacted bentonite under variation of contact water chemistry have been developed and tested in laboratory “glass tube” systems (Liu et al., 2009a) as well as a mathematical model to describe the evolution of a nanoparticle suspension above a compacted bentonite has been published (Degueldre et al., 2009). Within the FUNMIG consortium as documented in chapter 2.3.2 several parameters and their influence on bentonite erosion and bentonite nanoparticle generation have been gathered and compared to the zero order model predictions (Liu and Neretnieks, 2006), but the timeframe of the project was insufficient to develop a new model or implement this data into one of the above mentioned recent published model approaches.

2.8.3 Nanoparticle transport modeling

A couple of transport codes, based on the advection-dispersion equation, are available usually for modeling the transport of nanoparticulate phases (Sen and Khilar, 2006). Most of the model studies found in the literature have assumed equilibrium interactions between the nanoparticulate phase and the contaminant in the dissolved phase (Chrysikopoulos and Abdel-Salam, 1997) analogous to the model developed by Corapcioglu and co-workers (Corapcioglu and Jiang, 1993). Another step in the model development was to implement the influence of reversible and irreversible radionuclide sorption processes showing that slow desorption kinetics of the contaminant from the nanoparticles is an essential prerequisite in order for nanoparticle-facilitated contaminant transport to become significant (Ibaraki and Sudicky, 1995; Contardi et al., 2001; Artinger et al., 2002; Bekhit and Hassan, 2007; Bouby et al., 2010). Colloids/ nanoparticles interaction with the stationary phase (porous media, fracture surface) is classically implemented via correlation equations to calculate the theoretical single-collector efficiencies (based on the filter theory), either classical (Rajagopalan and Tien, 1976) or with the more recently published Tufenkji and Elimelech correlation (Tufenkji and Elimelech, 2004a; Tufenkji and Elimelech, 2004b; Tufenkji and Elimelech, 2005), where the overall reaction can be formulated as first-order kinetics. Recent advances included *inter alia* the implementation of physical and chemical heterogeneity (Bekhit and Hassan, 2005; Severino et al., 2007) which remains a key challenge in describing nanoparticle transport and retention (McCarthy and McKay, 2004). The FUNMIG project used a twofold approach to tackle the issue of nanoparticle transport, namely (a) programming an object oriented code (CHEPROO, CHEmical PRocesses Object-Oriented) that is capable to simulate complex hydrobiogeochemical processes and is open to include more complex chemical systems as e.g. solid solutions, nanoparticle transport without loss in the handling of simple problems (Bea et al., 2009) and (b) to characterize and monitor by integrating the analytical tools available within the FUNMIG consortium to a maximum extent the heterogeneity of natural systems observed in nanoparticle transport experiments. The methods included *inter alia* μ CT (computer tomography) to characterize the fracture geometry (Enzmann and Kersten, 2006), C-14 PMMA impregnation (Kelokaski et al., 2006; Sardini et al., 2006; Leskinen et al., 2007; Voutilainen et al., 2009) and application of positron-emission-tomography (PET) to direct visualisation of the solute transport and nanoparticle transport in this natural rock fracture (Kulenkampff et al., 2008). Based on the geometrical data available a comparison of four model types generated with different degree of geometrical complexity have been realized purely implementing the fracture surface heterogeneity without considering matrix diffusion in the models (Figure 2.3). The semi-2D model using only the mean values of the aperture for every CT slice captures the peak maximum but fails in predicting the experimentally observed tailing indicating clearly an oversimplified geometry assumption. The 2D (point or line) model predicts both the experimental peak maximum and the tailing quite well and demonstrates the influence of the rough fracture side walls, which seems to have a bigger influence compared to the aperture. Furthermore, the 2D model shows recirculation zones (not presented) in which solute can be trapped and retarded leading to a pronounced tailing. Both, in the 2D and 3D model (not shown) preferential flowpaths due to the complex fracture geometry (including asperities) can be observed. The implementation of a nanoparticle transport code was not completed within FUNMIG, but recently a Lagrangian particle tracking model (PTM) was proposed for predicting colloid/nanoparticle transport near a rough surface by embedding protruding spherical asperities in a planar surface (Kemps and Bhattacharjee, 2009).

In summary, the model results show that asperities protruding from the planar surface can act as additional collectors, either directly or indirectly through changing the flow field. All the observations made in this study indicate that physical surface heterogeneity has a far reaching influence on particle deposition and it is important to accurately determine the flow field near roughness features in nanoparticle deposition models in order to reliably predict deposition efficiencies or deposit morphologies.

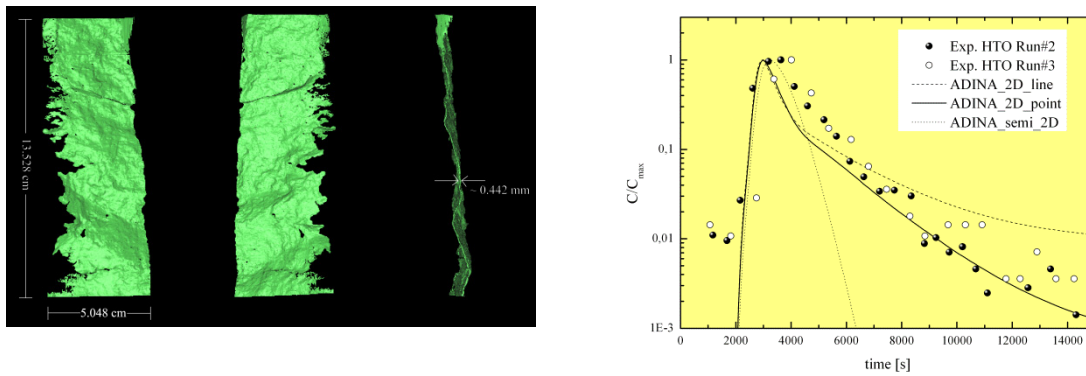


Figure 2.3: (a) Rendered 3D image of the real fracture geometry used for the migration experiments derived from μ CT data showing the surface morphology and the very irregular shaped boundary on one side of the fracture, for details see (Huber et al., 2009). (b) Data points represent two independent measured HTO breakthrough curves showing the reproducibility of the migration experiments. Modeling results using the finite-element code ADINA-F (Bathe et al., 1999) are additionally presented. The semi-2D model captures the peak maximum but fails in predicting the experimentally observed tailing. The 2D line and point model differ by assuming either point or line injection, but use both the midplane of the fracture ignoring all aperture information implementing only the influence of fracture side walls.

2.9 Conclusions and future direction of studies

The paper focused on summarizing the results obtained within the FUNMIG project on the colloid/nanoparticle research related to a deep geological repository far-field in indurated/plastic clay host rocks, granite host rocks and rock salt overburden (sedimentary porous media sequences). In addition, research results outside the project published within the project period in the open literature are mentioned, without intending to be a full review paper. The data obtained within the past five years indicate *inter alia* that:

- The background concentration of inorganic nanoparticles in far-field groundwaters of advection dominated systems rarely exceeds $1 \text{ mg}\cdot\text{L}^{-1}$ and is expected in the $\text{ng}\cdot\text{L}^{-1}$ range in diffusion controlled systems. For organic nanoparticles DOC concentrations up to tens of milligram in diffusion-controlled indurated clays (Callovo-Oxfordian, Opanilus Clay) as well as crystalline environments were found. Small molecular sizes mostly $< 500 \text{ Da}$ were identified in indurated clay porewaters, whereas larger molecular sizes of fulvic acids were mobile in crystalline environments. Plastic Clay formations (Boom Clay) show higher concentrations $\sim 100 \text{ mg}\cdot\text{L}^{-1}$ with molecular sizes $\leq 300 \text{ kDa}$.
- Additional sources of inorganic nanoparticles from the repository near-field (compacted bentonite) could be identified and the erosion rates were determined. The results indicate under stagnant conditions $\sim 38 \text{ mg}\cdot\text{cm}^{-2}\cdot\text{a}^{-1}$ for bi- distilled water, $\sim 20 \text{ mg}\cdot\text{cm}^{-2}\cdot\text{a}^{-1}$ for glacial melt water (Grimsel groundwater) and very low rates $\sim 0.02 \text{ mg}\cdot\text{cm}^{-2}\cdot\text{a}^{-1}$ for 5 mM CaCl_2 contact water. A few dynamic experiments are published and highest bentonite erosion rates of $\sim 22 \text{ mg}\cdot\text{cm}^{-2}\cdot\text{a}^{-1}$ under a flowrate of $1.5 \text{ m}\cdot\text{s}^{-1}$ could be determined.
- The low mobilization of bentonite nanoparticles from compacted bentonite observed in the presence of Ca^{2+} ions matches the low critical coagulation concentration (CCC) indicative for purely diffusion controlled coagulation of $1 \text{ mM}\cdot\text{L}^{-1} \text{ Ca}^{2+}$ found in bentonite nanoparticle stability analysis in the pH range 6 to 10. All these observations together with the higher nanoparticle attachment found in AFM force distance measurements in presence of calcium indicate the importance of divalent cations for clay mineral nanoparticle mobility.

However, the paper has also addressed some of the open questions remaining in order to reliably predict colloid/nanoparticle transport, *inter alia*:

- The problem of physical and chemical heterogeneity remains a key challenge. Using a bottom-up approach from micro- to macroscale it could be shown by AFM force distance

measurements on natural granite fracture surfaces and rock forming minerals that the divalent exchangeable cation composition and the divalent cations in the contact water are a key to nanoparticle attachment. Similar effects have been observed for the clay-bitumen system (Liu et al., 2004; Liu et al., 2005). Interestingly, macroscopic experiments on granite core material from the Äspö site initially in equilibrium with Ca-dominated groundwater flushed with low ionic strength groundwater to mimic glacial melt water intrusion have shown unexpected high bentonite nanoparticle attachment factors. Here, slow diffusive exchange processes as already observed in fractured shales (McCarthy et al., 2002) might be the mobility controlling mechanism. Implementing surface complexation models in nanoparticle transport models might be an appropriate way to predict surface charge changes and therefore attachment probabilities.

- Another aspect is the size cut-off of the mobile nanoparticle fraction in clay formations as the Boom Clay. Well defined experiments on the size exclusion in combination with microimaging tools as the 3D microstructural analysis using synchrotron based computer tomography and/or cryo-SEM with FIB-nanotomography (Desbois et al., 2009; Holzer and Münch, 2009; Holzer et al., 2010, in press) could be a way forward to link directly pore connectivity to the mobile nanoparticle size fraction in compacted bentonite.
- The hydraulic conditions and fracture residence times used in most laboratory, but predominantly field migration studies are orders of magnitude above the natural flow fields (see e.g. (Vilks et al. (1997); Möri et al. (2004))), but have been chosen to capture the tracer in the extraction borehole with a reasonable recovery to be detectable. The transferability of this data to real site conditions is heavily discussed. New experiments in the Grimsel Test Site (GTS) in the framework of the Colloid Formation and Migration (CFM) project aim *inter alia* on performing experiments under near-natural flow conditions to close this data gap. Therefore, a shear zone was sealed-off at the tunnel surface with a tunnel mega-packer to create a no flow boundary and to reduce the gradient in the groundwater heads from the rock towards the tunnel (for details see <http://www.grimsel.com>).

In conclusion, the FUNMIG project has clearly helped to increase our fundamental understanding of colloid/nanoparticle processes leading to mobility/retention of radionuclides in repository far-field environments and a huge dataset is available to be implemented in new and/or already established modeling approaches.

3 Influence of sorption and redox kinetics on radionuclide speciation

3.1 Sorption reversibility kinetics in the ternary system radionuclide - bentonite colloids/nanoparticles - granite fracture filling material

The kinetics of radionuclide desorption from bentonite colloids and subsequent sorption onto fracture filling material can influence colloid-facilitated radionuclide migration in groundwater. To shed light on the significance of these issues batch-type experiments using a cocktail of strong and weak sorbing radionuclides as well as FEBEX bentonite colloids in the presence of fracture filling material from Grimsel (Switzerland) under Grimsel groundwater conditions have been conducted. Results show that tri- and tetravalent radionuclides, $^{232}\text{Th(IV)}$, $^{242}\text{Pu(IV)}$ and $^{243}\text{Am(III)}$ are clearly colloid associated in contrast to $^{233}\text{U(VI)}$, $^{237}\text{Np(V)}$ and $^{99}\text{Tc(VII)}$. Concentrations of colloid-borne $^{232}\text{Th(IV)}$, $^{242}\text{Pu(IV)}$ and $^{243}\text{Am(III)}$ decrease after ~ 100 h showing desorption from bentonite colloids while $^{233}\text{U(VI)}$ and $^{99}\text{Tc(VII)}$ concentrations remain constant over the entire experimental time of 7500 h thus showing no interaction neither to colloids nor to the fracture filling material. $^{232}\text{Th(IV)}$ and $^{242}\text{Pu(IV)}$ data yield a slower dissociation from colloids compared to $^{243}\text{Am(III)}$ indicating stronger RN-colloid interaction. In the case of $^{237}\text{Np(V)}$, a decrease in concentration after ~ 300 h is observed which can be explained either by slow reduction to Np(IV) and subsequent sorption to mineral surfaces in accordance with the evolution of pe/pH and/or by a slow sorption onto the fracture filling material. No influence of the different fracture filling material size fractions (0.25-0.5 mm, 0.5-1 mm and 1-2 mm) can be observed implying reaction independence of the mineral surface area and mineralogical composition. The driving force of the observed metal ion desorption from colloids is binding to fracture filling material surfaces being in excess of the available colloid surface area (76:1, 55:1 and 44:1 for the 0.25-0.5 mm, 0.5-1 mm and 1-2 mm size fraction of the FFM, respectively).

Huber, F., Kunze, P., Geckeis, H. and Schäfer, T. Sorption reversibility kinetics in the ternary system radionuclide - bentonite colloids/nanoparticles - granite fracture filling material. *Applied Geochemistry* (2011), <http://dx.doi.org/10.1016/j.apgeochem.2011.08.005>

3.1.1 Introduction

The migration of radionuclides out of a nuclear waste disposal into the environment is a potential threat to nature and mankind due to their radio- and chemotoxicity even in trace concentrations. It is therefore of great importance to gain insight in the various chemical and physical processes including colloid generation, stability and mobility governing RN migration behaviour to assure the development of sound risk assessment strategies (Schäfer & Noseck, 2010). Much effort has been spent in the past and is still ongoing today to shed light on the various complex geochemical processes and their impact on the RN mobility, among them, sorption of radionuclides onto colloids/nanoparticles. For detailed discussion on the current knowledge gaps concerning montmorillonite colloid- radionuclide interaction, including *inter alia* radionuclide desorption rates we refer to Wold (2010) and Schäfer & Noseck (2010). In general colloids/nanoparticles range between 1 nm and 1000 nm in size consisting of a huge ensemble of various inorganic and/or organic matter such as e.g. mineral precipitates, rock forming mineral fragments, humic and fulvic acids and microorganisms (McCarthy and Zachara, 1989). Colloids/nanoparticles are ubiquitous in natural surface and subsurface waters and their mineralogy often is closely related to the host rock formation. Furthermore, some radionuclides, especially the tri- and tetravalent actinides (Th, Pu, Am) show strong hydrolysis and subsequent polymerization therefore prone to the formation so-called “eigencolloids” (Kim et al., 1984).

The importance of colloids for migration of contaminants has been proven by various laboratory and field studies carried out in the past (Kersting et al., 1999), among them the colloid and radionuclide retardation (CRR) experiments conducted at the Grimsel Test Site (Möri et al., 2003; Geckeis et al., 2004). These experiments revealed under the given hydrogeochemical conditions (mean fracture residence time of 88 min) that especially the transport of tri- and tetravalent radionuclides, Am(III) and Pu(IV), is facilitated in presence of colloidal phases leading to an un-retarded breakthrough whereas not colloidal-associated radionuclides like U(VI) or Np(V) exhibit slight retardation due to fracture surface interaction. In parallel, a laboratory program focused on short-term desorption kinetics to link this data to the field experiments. Therefore, these studies focused on desorption times ≤ 340 h (Geckeis et al., 2004).

Variation of groundwater flow rates in laboratory column migration experiments revealed an attachment/filtration of colloids/nanoparticles onto the rock matrix even under geochemical/electrostatic conditions favouring the stability of colloids in the bulk solution (Schäfer et al., 2004; Missana et al., 2008b). Reasons for the latter findings were attributed to chemical and physical heterogeneity of the fracture surface or flow path geometry. Overall, the results mentioned above clearly show the complexity of the ternary system RN-nanoparticle-collector (fracture filling/surface).

Another key aspect regarding the potential influence of colloids/nanoparticles on contaminant mobility is sorption reversibility/irreversibility and kinetics involved. Probably one of the most extensively investigated systems is the cesium sorption reversibility onto clay (especially illite) (Comans, 1987; Comans et al., 1991; de Koning and Comans, 2004). Reversibility of trace metal sorption in batch-type studies has often been found to be incomplete, which is interpreted by some authors as partially “irreversible” binding (e.g. Galunin et al. (2009); Bellenger and Staunton, 2008) after 1 day desorption time). Isotopic exchange studies on Sm(III) and Yb(III) (Coppin et al., 2003) and spectroscopic work using time-resolved laser fluorescence spectroscopy (TRLFS) (Rabung et al., 2005) however indicate the formation of inner-sphere surface complexes at $\text{pH} > 5$ for Eu(III)/Cm(III) in the form $\equiv\text{S-O-Eu/Cm}(\text{OH})_x^{(2-x)}(\text{H}_2\text{O})_{5-x}$ which are expected to be slow but fully reversible. Also work of Latrille & Herbette on Sn(IV) and Pu(IV) with Callovo-Oxfordian argillite has revealed sorption reversibility (Latrille et al., 2006). The apparent lack of reversibility might therefore be due to the short desorption experiment duration in comparison to the slow desorption kinetics as found e.g. for Cd(II) (Comans, 1987) or Th(IV) (Bouby et al., 2009). The desorption kinetics of colloid-bound radionuclides and a possible subsequent sorption onto the rock matrix might have a strong impact on

the colloid-facilitated transport depending on the rate of advection (residence time) (Turner et al., 2006). Therefore reliable data on radionuclide desorption rates are needed to be included in reactive transport models. Ignoring reversibility kinetics can lead to an over-estimation of the radionuclide mobility and travel distances in groundwater systems.

The aim of this study is to investigate the sorption and desorption process of $^{99}\text{Tc(VII)}$, $^{232}\text{Th(IV)}$, $^{233}\text{U(VI)}$, $^{237}\text{Np(V)}$, $^{242}\text{Pu(IV)}$ and $^{243}\text{Am(III)}$ onto FEBEX bentonite colloids under Grimsel groundwater conditions in the presence of Fracture Filling Material (FFM) from the Grimsel Test Site (GTS) for long (weeks-months) equilibrium time to extend the already existing datasets for short contact times (Missana & Geckeis, 2006). The selected radionuclides and their oxidation states provide a good representation of nuclear waste constituents and their possible forms. Therefore batch-type studies were conducted regarding the following aspects: Impact of (i) $^{237}\text{Np(V)}$, $^{242}\text{Pu(IV)}$ and $^{243}\text{Am(III)}$ concentration, (ii) influence of available surface area and (iii) contact time on RN sorption and reversibility processes.

3.1.2 Materials and Methods

3.1.2.1 Fracture Filling Material (FFM) characterization

Fracture filling material separated in different grain sizes originates from the Grimsel Test Site (GTS), Switzerland. The so-called Grimsel granodiorite represents a medium to coarse grained crystalline rock possessing several joint and fracture systems induced by a relatively cold and therefore brittle deformation history (Nagra, in press). The Grimsel materials consist mainly of plagioclase (29–33 vol. %), quartz (27–28 vol.%), K-feldspar (12–24 vol.%) and biotite (7–11 vol.%). As accessory minerals muscovite/sericite, apatite, sphene, epidote, zircon, chlorite, calcite and opaque minerals were identified (Nagra, in press). For the batch type sorption studies fracture filling material (FFM) was crushed, sieved and freeze dried under atmospheric conditions. Three different size fractions, namely 0.25-0.5 mm, 0.5-1 mm and 1-2 mm of the Grimsel FFM have been separated. The main part of the batch-type experiments is on the 1-2 mm size fraction. Fracture filling material has been characterized by powder x-ray diffraction (XRD), scanning electron microscopy (SEM), energy dispersive x-ray microanalysis (EDX), specific surface area analysis (N_2 -BET) and x-ray fluorescence analysis (XFR) prior to the experiments.

Powder X-ray diffraction was applied to examine the mineral composition of the three different FFM size fractions applied in this study. XRD pattern were recorded from $5^\circ 2\theta$ to $100^\circ 2\theta$, using $0.01^\circ 2\theta$ steps, and 2 s counting time per step with a Bruker AXS D8 powder diffractometer equipped with a BSI (Baltic Scientific Instrument) Si(Li) solid detector and $\text{Cu K}\alpha$ radiation. For evaluation of the spectra the software DiffacPlus from Bruker-AXS was used in combination with the database of the International Centre for Diffraction Data (PDF). All spectra show a very similar mineralogical composition independent of the grain size. Prevailing mineral phases are quartz, plagioclase (anorthite/albite), k-feldspar, biotite and muscovite.

Scanning electron microscopy (SEM) of the Grimsel FFM grains show an angular morphology with rough heterogeneous grain surfaces. Grain sizes for the three different size fractions, namely 0.25-0.5 mm, 0.5-1 mm and 1-2 mm can be validated by SEM. Energy dispersive x-ray microanalysis (EDX) spectra yield mainly k-feldspar, quartz and element signatures for sheet-silicates, most likely of biotite-type. The specific surface areas of the different FFM size fractions were determined by BET N_2 -adsorption. The samples were heated to 300°C and degassed for 6 h. The determination of the surface was done via multiple point analysis and a subsequent fit with the BET isotherm. In all BET measurements care was taken to have sufficient total surface ($> 1\text{ m}^2$) for reliable measurements. Specific surface area measurements (BET) of the three Grimsel size fractions yielded values of $0.238\text{ m}^2\cdot\text{g}^{-1}$, $0.187\text{ m}^2\cdot\text{g}^{-1}$ and $0.153\text{--}0.166\text{ m}^2\cdot\text{g}^{-1}$ for 0.25-0.5 mm, 0.5-1 mm and 1-2 mm size fraction, respectively. Full adsorption isotherms of the particles have been measured to detect a possible

micro-porosity. The observed hysteresis in the isotherms corroborates the presence of a meso-/macro-porosity potentially offering additional surface area for sorption of the radionuclides accessible via diffusion processes. Pore sizes are heterogeneously distributed covering a broad range between ~1.5 to ~210 nm with a slight predominance between ~3 to ~10 nm.

Chemical rock composition analysis by x-ray fluorescence (XRF) has been conducted to determine the bulk major and trace elemental distribution in the fracture filling material (Table 3.1). As expected for a granodiorite, major elemental composition is dominated by SiO₂, Al₂O₃, Na₂O and K₂O representing the main mineral elements quartz and k-feldspar/albite which is in accordance to the EDX analysis. Interestingly, the total iron content (2.96 wt% Fe₂O_{3(t)}) is mainly composed of ferrous iron with 1.87 wt% FeO) which gives hint to minor oxidation effects through the separation and preparation of the FFM size fractions.

Table 3.1: XRF results of Grimsel FFM (1-2 mm size fraction).

Major elements		Trace elements	
	[%]		[ppm]
SiO ₂	68.18	Sc	7
Al ₂ O ₃	15.47	V	24
Fe ₂ O _{3(t)}	2.96	Cr	3
MnO	0.05	Co	5
MgO	1.61	Ni	0
CaO	1.23	Cu	0
Na ₂ O	4.42	Zn	47
K ₂ O	4.23	Ga	17
TiO ₂	0.45	Rb	176
P ₂ O ₅	0.12	Sr	153
SO ₃	0.008	Y	37
Cr ₂ O ₃	0.0003	Zr	244
NiO	0.0004	Nb	21
LOI	1.12	Cs	8
Sum	99.84	Ba	859
FeO	1.87	W	5
		Pb	19
		Th	13.6
		U	1.9

3.1.2.2 FEBEX bentonite colloid characterization

For the experiments FEBEX (full-scale engineered barrier experiment) bentonite from the deposit of Cabo de Gata, Almería (Spain) is used (Villar et al., 1998). It is described as a smectite-rich bentonite. The bentonite was sieved to obtain the < 63 µm size fraction and equilibrated with 1 mol·L⁻¹ NaCl to transfer the bentonite to its mono-ionic Na-form. The sodium exchanged bentonite is washed with de-ionized (Milli-Q) water to remove excess salt after one week equilibration time. The suspension is centrifuged at 4,000 rpm (3360 g) for 40 min. Subsequently the supernatant is discarded and the centrifugate re-suspended in Milli-Q water. This washing cycle is repeated three times. Each washing step is checked by electrical conductivity measurements and the final electrical conductivity after all washing cycles was 1.9 µS·cm⁻¹. The final supernatant, containing bentonite colloids, is taken as a colloid stock dispersion and stored in a refrigerator until experiments were performed. The extracted colloidal fraction consists totally of montmorillonite as proved by XRD analysis. The bentonite colloid concentration is determined via Al ICP-MS measurements. Taking into account the structural formula of FEBEX bentonite given in (Villar et al., 1998), the bentonite colloid concentration of the stock solution could be calculated to be 640 mg·L⁻¹. Specific surface area of the FEBEX bentonite colloids

3 Influence of sorption and redox kinetics on radionuclide speciation

have been measured by Missana et al. (2008) yielding a value of $33 \text{ m}^2 \cdot \text{g}^{-1}$. The morphology and size of the FEBEX bentonite colloids was probed by Scanning Electron Microscopy (SEM), Atomic Force Microscopy (AFM), Laser-induced Breakdown Detection (LIBD), Flow Field Flow Fractionation (AsFIFFF) and Photon Correlation Spectroscopy (PCS). Mean particle sizes range between 73 nm (AFM), 67 +/- 13 nm (LIBD), ~ 70 nm (AsFIFFF) and >200 nm (PCS) with a rather broad size distribution from 25 to 500 nm (see Plaschke et al., 2001 for further details).

3.1.2.3 Grimsel groundwater (GGW) characterization

In the present investigations Grimsel groundwater was used which was stored in Teflon coated 50 L Al barrels under Ar atmosphere until the experiments were launched. Water chemistry was analyzed via ICP-MS, ICP-AES and ion chromatography. Colloid concentrations were determined by laser-induced breakdown detection (LIBD). The Grimsel groundwater represents a low mineralized, meteoric, Na-Ca-HCO₃⁻-type groundwater which possesses a low ionic strength of $I \approx 1 \text{ mmol} \cdot \text{L}^{-1}$. Both $E_{h(\text{SHE})}$ and pH measurements were conducted prior to cocktail preparation, yielding a value of +37 mV and 9.6, respectively. Background colloidal concentration was determined to be around ~ 20 ppb. The chemical composition of the original sampled groundwater and at different contact times in the batch experiments is listed in Table 3.2.

Table 3.2: Chemical composition of the original Grimsel groundwater (GGW) and after different contact times (24 h and 500 h) with Grimsel FFM in the batch experiments.

	Grimsel GW (MI shearzone) initial	After contact with Grimsel FFM	After contact with Grimsel FFM
Contact time	12.2.08*	24 h	500 h
pH	9.67	9.72	9.68
$E_{h(\text{SHE})}$	n.d.	62mV	35mV
[Mg ²⁺]	12.6 $\mu\text{g} \cdot \text{L}^{-1}$	42.2 $\mu\text{g} \cdot \text{L}^{-1}$	35.6 $\mu\text{g} \cdot \text{L}^{-1}$
[Ca ²⁺]	5.3 $\text{mg} \cdot \text{L}^{-1}$	5.3 $\text{mg} \cdot \text{L}^{-1}$	6.5 $\text{mg} \cdot \text{L}^{-1}$
[Fe ^{2+,3+}]	< D.L.	< D.L.	< D.L.
[Mn ²⁺]	< D.L.	0.17 $\mu\text{g} \cdot \text{L}^{-1}$	0.17 $\mu\text{g} \cdot \text{L}^{-1}$
[Sr ²⁺]	182 $\mu\text{g} \cdot \text{L}^{-1}$	157 $\mu\text{g} \cdot \text{L}^{-1}$	214 $\mu\text{g} \cdot \text{L}^{-1}$
[Cs ⁺]	0.79 $\mu\text{g} \cdot \text{L}^{-1}$	0.02 $\mu\text{g} \cdot \text{L}^{-1}$	0.03 $\mu\text{g} \cdot \text{L}^{-1}$
[La ³⁺]	< D.L.	0.03 $\mu\text{g} \cdot \text{L}^{-1}$	0.02 $\mu\text{g} \cdot \text{L}^{-1}$
[U]	0.028 $\mu\text{g} \cdot \text{L}^{-1}$	0.55 $\mu\text{g} \cdot \text{L}^{-1}$	0.47 $\mu\text{g} \cdot \text{L}^{-1}$
[Th]	0.00136 $\mu\text{g} \cdot \text{L}^{-1}$	0.085 $\mu\text{g} \cdot \text{L}^{-1}$	0.058 $\mu\text{g} \cdot \text{L}^{-1}$
[Al ³⁺]	42.9 $\mu\text{g} \cdot \text{L}^{-1}$	90.5 $\mu\text{g} \cdot \text{L}^{-1}$	70.9 $\mu\text{g} \cdot \text{L}^{-1}$
[Na ⁺]	14.7 $\text{mg} \cdot \text{L}^{-1}$	17.2 $\text{mg} \cdot \text{L}^{-1}$	17.2 $\text{mg} \cdot \text{L}^{-1}$
[Cl ⁻]	6.7 $\text{mg} \cdot \text{L}^{-1}$	7.12 $\text{mg} \cdot \text{L}^{-1}$	31.53 $\text{mg} \cdot \text{L}^{-1}$
[Si]	5.6 $\text{mg} \cdot \text{L}^{-1}$	4.9 $\text{mg} \cdot \text{L}^{-1}$	4.9 $\text{mg} \cdot \text{L}^{-1}$
[SO ₄ ²⁻]	5.8 $\text{mg} \cdot \text{L}^{-1}$	7.11 $\text{mg} \cdot \text{L}^{-1}$	7.17 $\text{mg} \cdot \text{L}^{-1}$
[F ⁻]	6.3 $\text{mg} \cdot \text{L}^{-1}$	6.60 $\text{mg} \cdot \text{L}^{-1}$	6.61 $\text{mg} \cdot \text{L}^{-1}$
[Br ⁻]	n.d.	n.d.	n.d.
[NO ₃ ²⁻]	< D.L.	< D.L.	< D.L.
[HCO ₃ ⁻]	3.0 $\text{mg} \cdot \text{L}^{-1}$	n.d.	n.d.

*: sampling date; n.d.: not determined; < D.L.: below detection limit

3.1.2.4 Radionuclide cocktail characterization

The radionuclide cocktail was prepared in a glove box under Ar atmosphere by spiking radionuclides to Grimsel groundwater containing bentonite colloids ($25.56 \text{ mg} \cdot \text{L}^{-1}$). After spiking of the

radionuclides only a slight pH decrease to a lower value of 9.1 was measured, likely due to buffering capabilities of the bentonite colloids. Subsequently, pH was readjusted using CO₂-free NaOH. The prepared cocktail was stored for 24 h before aliquots of the radionuclide cocktail were spiked to the sample batches containing fracture filling material giving the sorption rate K_3 . The following radiotracers in their respective oxidation states have been used: ⁹⁹Tc(VII), ²³²Th(IV), ²³³U(VI), ²³⁷Np(V), ²⁴²Pu(IV), and ²⁴³Am(III). ²⁴²Pu was added as ²⁴²Pu(III) after electrochemical reduction and totally transferred to ²⁴²Pu(IV) through pH adjustment of the cocktail. Table 3.3 gives an overview of the applied RN concentrations used in the different experiments. An aliquot of every sample was ultra-centrifuged to remove colloid associated radionuclides. Aliquots for ultra-centrifugation were pipetted in ultra-centrifugation vials, sealed by welding inside an Ar glove box and subsequently centrifuged for 1 h at 90,000 rpm (ca. 5·10⁵ g). Afterwards aliquots of the ultra-centrifuged supernatant were taken and analyzed by ICP-MS. As shown in Table 3.3 ²³²Th(IV) and ²⁴³Am(III) are almost totally bound to the bentonite colloids and for ²⁴²Pu(IV) ~ 15 % are not colloid associated. In contrast, ²³³U(VI), ⁹⁹Tc(VII) and ²³⁷Np(V) the colloid bound fraction yielded values below 2 % of the initial concentration C_0 .

3.1.2.5 Experimental conditions and procedure

All experiments were conducted at room temperature (~ 21 °C) in a glove box under Ar atmosphere (< 1 ppm O₂). The pH measurements were undertaken using a semi-micro Ross electrode (81-03, Orion Co.) in combination with a digital pH meter (720A, Orion Co.). The set-up was calibrated using at least 4 commercial buffer solutions (Merck). All FFM materials were contacted prior to the batch-type experiments with fresh Grimsel groundwater in Zinsser vials (20 mL, HDPE) over a period of six weeks, exchanging the solution at least 5 times within this period. Aliquots of supernatant solution were taken for analysis monitoring the equilibration process. The solid to liquid ratio is 1:4 (g·mL⁻¹) for all experiments. After this equilibration phase the supernatant was exchanged with the radionuclide cocktail. The influence of the FFM on the initial Grimsel groundwater element concentrations is monitored by ICP-MS measurements (Table 3.2). Triplicates of every sample were prepared: two of the three identical samples with 2 g solid and 8 ml of cocktail solution and one sample with 4 g solid and 16 ml of solution. First aliquots were taken 1 h after spiking of the samples. The next aliquots after 24 h, 48 h, 120 h, 336 h, 504 h, 700 h, 1000 h and 7500 h, respectively. An aliquot of every sample (~ 4 ml) was ultra-centrifuged (Beckman XL-90, rotor type 90Ti) at 90,000 rpm (centrifugal force of about 5·10⁵ g) for 60 min to remove colloid associated radionuclides. This ultra-centrifugation procedure has been proven to be suitable to effectively remove bentonite colloids as well as Th(IV) "eigencolloids" from solution (Altmaier et al., 2004). The remaining supernatant was subsequently analyzed by ICP-MS as described in detail above.

3.1.3 Results and Discussion

3.1.3.1 Redox and pH evolution of the experiments

Since the radionuclide cocktail included several redox sensitive radionuclides, i.e. ⁹⁹Tc(VII), ²³³U(VI), ²³⁷Np(V) and ²⁴²Pu(IV) it was mandatory to monitor the contact time dependent evolution of pH and $E_{h(SHE)}$ values. The response time for the pH electrode was rather uncritical, whereas for the E_h measurements the criterion to accept the measured value is not well documented and established in the literature (for discussion on redox measurements see Grenthe et al. (1992)). In this study we monitored the time dependent change in the redox value although the automatic slope analysis of the Orion instrument already indicated a constant value after < 1 h. The $E_{h(SHE)}$ drifted over several hours and we took the value when a plateau was reached. In Figure 3.1a a typical redox

measurement is shown. As depicted in Figure 3.1b the measured pH dropped from pH 9.6 originally found in the Grimsel groundwater to pH 9.0 after 7500 h most probably due to mineral dissolution processes. Meanwhile, the $E_{h(SHE)}$ values dropped from ~ 50 mV to ~ 0 mV within the first two days and remained between ~ 0 mV and ~ 20 mV until 624 h. Afterwards the redox potential started to decrease again to ~ -15 mV after 7500 h (Figure 2b). It has to be stated that our measured $E_{h(SHE)}$ values are higher than values found in the literature. Mörri et al. (2003) determined in-situ $E_{h(SHE)}$ values below ~ -300 mV. These discrepancies reflect on one hand the complex hydrogeological environment prevailing in natural groundwaters where spatial and temporal changes give rise to slightly different geochemical conditions and on the other hand the uncertainties in determining Eh values in general as stated above.

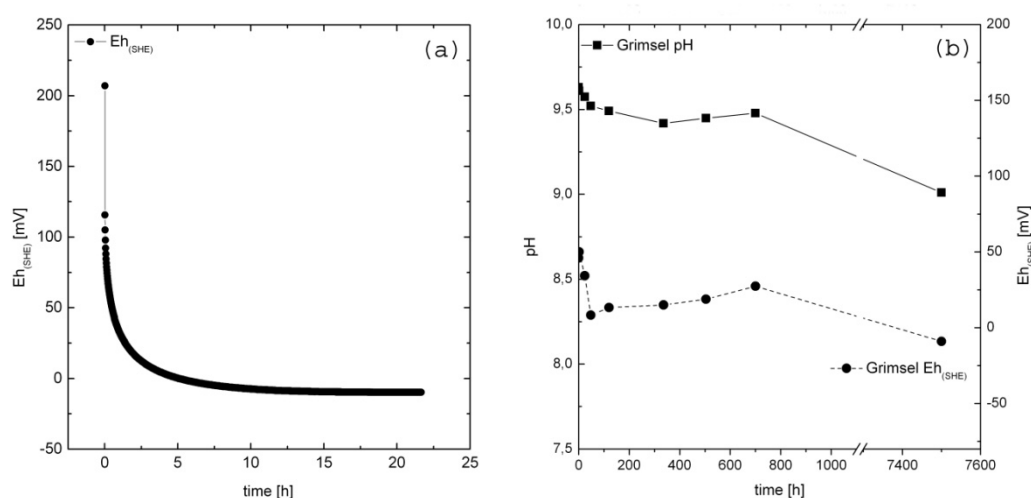


Figure 3.1: (a) $E_{h(SHE)}$ measurement for a single point plotted in the left figure showing the response time of the redox electrode reaching asymptotically a constant plateau value after several hours. (b) Measured final pH and $E_{h(SHE)}$ values in the batch-type studies after various contact times.

3.1.3.2 Thermodynamic calculations

Knowledge about the radionuclide equilibrium speciation and redox state is a prerequisite for a thorough analysis, interpretation and understanding of the experimental results. Therefore, thermodynamic calculations have been performed to model the aqueous speciation of the radionuclide cocktail. Consistently, only thermodynamic data from the actual NEA database (Guillaumont et al., 2003; Rand et al., 2009) have been used in the simulations. Total concentrations for the radionuclides used in the calculations for the predominance diagrams are exactly the same as added to the cocktail. As ligands, CO_3^{2-} , SO_4^{2-} , $Si(OH)_4(aq)$, Cl^- and F^- have been considered. In the case of CO_3^{2-} , a fixed concentration is used as constraint. The modeling procedure was a stepwise process. Firstly, we calculated the predominant oxidation state for each radionuclide separately using the thermodynamic constants for all oxidation states and taking into account the experimentally determined $E_{h(SHE)}$ value after 7500 h. Secondly, the speciation and solubility for each radionuclide was calculated applying only NEA constants for the calculated dominating valence state, respectively. The Hydra/Medusa code (Puigdomenech, 2004) has been applied for the modeling task. The following points should be noted: (i) the presence of bentonite colloids and the potential surface complexation by this additional surface is disregarded in the following discussion and (ii) the analysis and interpretation of the speciation results are based on the assumption that the selected oxidation state dominates the geochemical behaviour and minor fractions of differing valence states can be neglected. It should be noted that uncertainties in the thermodynamic data (Denison & Garnier-Laplace (2005)) have been disregarded in this study as for a sound uncertainty analysis correlations

between the uncertainties in the thermodynamic data need to be known, which is beyond the scope of this paper.

^{99}Tc is mainly present as pertechnetate $(\text{Tc(VII)O})_4^-$ under the experimental conditions. A reduction to the tetravalent TcO_2 begins at values below ~ -100 mV for a pH around 9.7 which is in good agreement to calculations published in Neck et al. (1999). As solubility limiting solid phase $\text{TcO}_2(\text{cr})$ was selected which possesses a solubility in the range of $\log(c) \sim -5$ to -4 between pH 9 to 10, respectively. As the initial Tc concentration is at $\log(c) = -8$ no precipitation of $\text{TcO}_2(\text{cr})$ is expected in our experiments.

The redox stable ^{232}Th occurs in the tetravalent form in natural aquatic systems. Thermodynamic calculations yield $\text{Th}(\text{OH})_4(\text{aq})$ as the predominant solution species over a broad pH range including pH 9.7 and the solution is under-saturated with respect to $\text{Th}(\text{OH})_4(\text{am})$ under the experimental conditions.

Results for uranium yield the uranyl-hydroxo-complex $\text{UO}_2(\text{OH})_3^-$ as dominant species under the prevailing pH/Eh conditions. Reduction of hexavalent uranium to amorphous U(IV)O_2 is thermodynamic feasible only at Eh values lower than -210 mV between pH 9 to 10. As solubility limiting solid phases both $\text{UO}_2(\text{OH})_2(\text{am})$ and $\text{UO}_2\text{CO}_3(\text{cr})$ have been chosen yielding no over-saturation, respectively. The recently discovered $\text{Ca}_2\text{UO}_2(\text{CO}_3)_3$ (Bernhard et al., 2001) complex is not included in the thermodynamic calculations since this complex has not yet been selected by the NEA review.

Concerning ^{237}Np , tetra- and pentavalent oxidation states have been considered in the present calculations. A predominance diagram for Np is shown in Figure 3.2. It can be stated that under the prevailing experimental conditions a reduction of Np(V) to the sparingly soluble $\text{Np(IV)O}_2(\text{am})$ can be expected. Solubility calculations predict a precipitation of $\text{NpO}_2(\text{am})$. Applying the solubility constant for colloidal NpO_2 (Volker Neck, personal communication) which is a precursor for the precipitation of $\text{NpO}_2(\text{am})$, a significant higher solubility is predicted.

Calculations for $^{243}\text{Am(III)}$ predict the hydroxo complex $\text{Am}(\text{OH})_2^+$ as major species followed to a lesser extent ($< 10\%$) by $\text{Am}(\text{OH})_3(\text{aq})$ and the bi-carbonato complex $\text{Am}(\text{CO}_3)_2^-$. Precipitation of amorphous $\text{Am}(\text{OH})_3$ is not expected under the experimental Eh/pH conditions and americium concentrations applied.

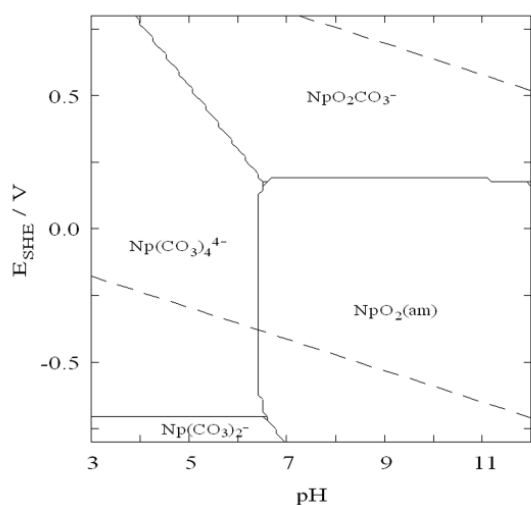


Figure 3.2: Calculated predominance diagram for ^{237}Np based on thermodynamic constants from the NEA database.

Pu(IV) solubility is calculated to be around $1.5 \cdot 10^{-9}$ M. According to this calculation $\text{Pu(IV)}(\text{OH})_4(\text{am})$ should precipitate and only about 10 % of the totally added Pu exists as $\text{Pu}(\text{OH})_4(\text{aq})$ in solution. The implications of this result are discussed in chapter 3.3.1.2. Speciation calculations for various metal ions in Grimsel groundwater including surface complexation reactions with clay colloids ($20 \text{ mg} \cdot \text{L}^{-1}$)

3 Influence of sorption and redox kinetics on radionuclide speciation

Table 3.3: Time-dependent sorption data of various elements in the ternary system fracture filling material (FFM) – bentonite colloids – metal; V/m: 4 mL·g⁻¹; Specific surface area (N₂ BET): 0.238 m²·g⁻¹, 0.187 m²·g⁻¹ and 0.153-0.166 m²·g⁻¹ for 0.25-0.5 mm, 0.5-1 mm and 1-2 mm FFM size fraction, respectively.

Time	Al	⁹⁹ Tc	²³² Th	²³³ U	²³⁷ Np	²⁴² Pu	²⁴³ Am
h	mol·L ⁻¹	mol·L ⁻¹	mol·L ⁻¹	mol·L ⁻¹	mol·L ⁻¹	mol·L ⁻¹	mol·L ⁻¹
SET 1: FFM 0.25-0.5 mm							
Colloid bound concentration [%]	~ 95				~ 30	~ 93	~ 97
0 (initial)	4.72·10 ⁻⁵				2.96·10 ⁻⁸	7.68·10 ⁻¹¹	1.54·10 ⁻⁰⁹
	6.51±				2.06 ±	5.48 ±	1.01±
4	0.57·10 ⁻⁵				0.065·10 ⁻⁸	1.02·10 ⁻¹¹	0.03·10 ⁻⁹
	5.72 ±				1.83 ±	5.02 ±	9.79±
24	0.52·10 ⁻⁵				0.053·10 ⁻⁸	1.99·10 ⁻¹¹	0.97·10 ⁻¹⁰
72	5.46·10 ⁻⁵				1.78·10 ⁻⁸	4.96·10 ⁻¹¹	9.64·10 ⁻¹⁰
	5.26±				8.2 ±	4.78 ±	7.55±
144	0.25·10 ⁻⁵				0.64·10 ⁻⁹	1.94·10 ⁻¹¹	0.84·10 ⁻¹⁰
	6.17±				4.05 ±	1.11 ±	3.01±
312	0.26·10 ⁻⁵				0.49·10 ⁻⁹	0.16·10 ⁻¹¹	0.79·10 ⁻¹⁰
	1.48±				5.82 ±	1.25 ±	1.35±
624	0.02·10 ⁻⁵				0.68·10 ⁻⁹	0.55·10 ⁻¹¹	0.12·10 ⁻¹⁰
SET 2: FFM 0.5-1 mm							
Colloid bound concentration [%]	~ 96				~ 28	~ 98	~ 95
0 (initial)	4.72·10 ⁻⁵				2.96·10 ⁻⁸	7.68·10 ⁻¹¹	1.54·10 ⁻⁰⁹
	6.06 ±				2.11 ±	7.04 ±	9.98±
4	0.28·10 ⁻⁵				0.03·10 ⁻⁸	0.76·10 ⁻¹¹	0.58·10 ⁻¹⁰
	4.90 ±				1.94 ±	6.43 ±	9.82±
24	0.08·10 ⁻⁵				0.18·10 ⁻⁸	1.05·10 ⁻¹¹	0.64·10 ⁻¹⁰
72	5.43·10 ⁻⁵				1.72·10 ⁻⁸	5.00·10 ⁻¹¹	8.75·10 ⁻¹⁰
	5.19 ±				8.32 ±	4.83 ±	6.13±
144	0.13·10 ⁻⁵				0.24·10 ⁻⁹	1.29·10 ⁻¹¹	1.81·10 ⁻¹⁰
	5.85 ±				2.65 ±	1.87 ±	2.56±
312	0.27·10 ⁻⁵				0.16·10 ⁻⁹	0.59·10 ⁻¹¹	0.43·10 ⁻¹⁰
	1.23 ±				5.44 ±	4.82 ±	8.98±
624	0.8·10 ⁻⁵				0.62·10 ⁻⁹	2.73·10 ⁻¹²	3.66·10 ⁻¹¹
SET 3: FFM 1-2 mm (Low concentration series)							
Colloid bound concentration [%]	~ 96				~ 28	~ 98	~ 98
0 (initial)	4.72·10 ⁻⁵				2.96·10 ⁻⁸	7.68·10 ⁻¹¹	1.54·10 ⁻⁰⁹
	6.25 ±				2.12 ±	6.74 ±	1.05±
4	0.25·10 ⁻⁵				0.095·10 ⁻⁸	1.18·10 ⁻¹¹	0.072·10 ⁻⁹
	5.63 ±				1.94 ±		9.0±
24	0.30·10 ⁻⁵				0.075·10 ⁻⁸	6.65·10 ⁻¹¹	0.04·10 ⁻¹⁰
						5.15 ±	
72	5.46·10 ⁻⁵				1.72·10 ⁻⁸	1.57·10 ⁻¹¹	7.8±·10 ⁻¹⁰
	5.18 ±				8.32 ±	4.78 ±	5.97±
144	0.22·10 ⁻⁵				0.38·10 ⁻⁹	0.74·10 ⁻¹¹	1.63·10 ⁻¹⁰
	5.94 ±				8.79 ±	1.6 ± 7·10 ⁻¹¹	2.4±
312	0.03·10 ⁻⁵				0.001·10 ⁻⁹		0.33·10 ⁻¹⁰
	1.46 ±				6.52 ±	1.21 ±	1.14±
624	0.19·10 ⁻⁵				0.36·10 ⁻⁹	0.41·10 ⁻¹¹	0.26·10 ⁻¹⁰

3 Influence of sorption and redox kinetics on radionuclide speciation

Time	Al	⁹⁹ Tc	²³² Th	²³³ U	²³⁷ Np	²⁴² Pu	²⁴³ Am
SET 4: FFM 1-2 mm (High concentration series)							
Colloid bound concentration [%]	~ 97	~ 1	~ 99	~ 1.6	~ 0.1	~ 84	~ 94
0 (initial)	6.21 ± 0.68·10 ⁻⁵	1.0 ± 0.2·10 ⁻⁸	7.3 ± 0.44·10 ⁻⁹	4.3 ± 0.9·10 ⁻⁷	1.8 ± 0.36·10 ⁻⁶	1.3 ± 0.004·10 ⁻⁸	8.0 ± 0.24·10 ⁻⁹
24	1.75 ± 0.59·10 ⁻⁴	1.26 ± 0.091·10 ⁻⁸	6.15 ± 0.086·10 ⁻⁸	4.81 ± 0.2·10 ⁻⁷	1.66 ± 0.05·10 ⁻⁶	1.08 ± 0.093·10 ⁻⁸	6.05 ± 0.28·10 ⁻⁹
48	2.06 ± 0.63·10 ⁻⁴	1.47 ± 0.017·10 ⁻⁸	8.56 ± 0.084·10 ⁻⁸	5.5 ± 0.2·10 ⁻⁷	1.86 ± 0.04·10 ⁻⁶	1.26 ± 0.02·10 ⁻⁸	6.23 ± 0.26·10 ⁻⁹
120	1.26 ± 1.82 ± 1.15·10 ⁻⁴	0.14·10 ⁻⁸ 1.35 ± 0.042·10 ⁻⁸	0.81·10 ⁻⁹ 7.01 ± 0.26·10 ⁻⁹	0.27·10 ⁻⁷ 5.0 ± 0.67·10 ⁻⁷	0.067·10 ⁻⁶ 1.34 ± 0.01·10 ⁻⁶	0.79·10 ⁻⁸ 7.83 ± 2·10 ⁻⁹	2.82·10 ⁻⁹ 2.94 ± 0.72·10 ⁻⁹
336	1.52 ± 0.48·10 ⁻⁴	1.31 ± 0.079·10 ⁻⁸	3.97 ± 3.6·10 ⁻⁹	4.86 ± 0.12·10 ⁻⁷	1.11 ± 0.015·10 ⁻⁶	3.43 ± 2.57·10 ⁻⁹	1.21 ± 0.97·10 ⁻⁹
504	0.48·10 ⁻⁴	1.29 ± 0.011·10 ⁻⁸	3.92 ± 3.7·10 ⁻⁹	4.88 ± 0.6·10 ⁻⁷	1.09 ± 0.2·10 ⁻⁶	4.54 ± 3.39·10 ⁻⁹	1.66 ± 1.27·10 ⁻⁹
700	1.46·10 ⁻⁴	0.011·10 ⁻⁸	4.87 ± 4.87 ± 1.16·10 ⁻⁹	4.91 ± 4.91 ± 0.25·10 ⁻⁷	7.02 ± 7.02 ± 0.34·10 ⁻⁷	2.86 ± 0.56·10 ⁻⁹	1.0 ± 0.18·10 ⁻⁹
1000	2.15·10 ⁻⁴	1.19·10 ⁻⁸	1.16·10 ⁻⁹	0.25·10 ⁻⁷	0.34·10 ⁻⁷	0.56·10 ⁻⁹	0.18·10 ⁻⁹
7500	3.01 ± 0.87·10 ⁻⁴	9.59 ± 1.35·10 ⁻⁹	6.28 ± 10 ⁻¹⁰	4.51 ± 0.01·10 ⁻⁷	1.16 ± 1.5·10 ⁻⁷	2.19 ± 1.05·10 ⁻⁹	6.16 ± 3.08·10 ⁻¹⁰

3.1.3.3.1 The case of tri- and tetravalent actinides (Am, Pu and Th)

To study the influence of RN concentration on sorption and reversibility two series with the 1-2 mm FFM size fraction have been prepared applying two different ²³⁷Np(V), ²⁴²Pu(IV) and ²⁴³Am(III) concentrations. In both sample sets the same solid to solution ratio (1:4 g·mL⁻¹) has been used. For the experiments with higher radionuclide concentration two samples have been prepared for long term measurements after 7500 h. In addition to Pu(IV), Th(IV) was chosen as a homologue for tetravalent actinides. Figure 3.4 shows the results of ²³²Th(IV), ²⁴²Pu(IV) and ²⁴³Am(III) concentrations with time. Further details will be discussed in the following sections. Additionally inserted in Figure 3.4 are calculated concentration margins for the ternary system based on batch sorption data derived partitioning coefficients of the binary systems “bentonite colloids – radionuclide” ($K_{d, coll}$) and “FFM – radionuclide” ($K_{d, FFM}$) (published in Tab. 4.7 and 4.9 in Missana and Geckeis (2006)). The fairly stable aluminium concentration measured throughout the experimental period (Figure 3.3) infers that the interaction of colloids with the fracture filling material can be neglected ($K_{d, coll-FFM} = 0$) and therefore the following equation (3.1) can be applied for the determination of the ternary $R_{d, tot}$ (Lührmann, 1999):

$$R_{d, tot} = \frac{K_{d, FFM}}{1 + C_C \cdot K_{d, coll}} \quad (3.1)$$

where C_C is the bentonite colloid concentration in solution [mol·L⁻¹]; $K_{d, FFM}$ is the distribution coefficient for the interaction of radionuclides with the fracture filling material (FFM) [L·g⁻¹]; $K_{d, coll}$ is the distribution coefficient for the interaction of radionuclides with the bentonite colloids [L·g⁻¹]. From the calculated distribution coefficient $R_{d, tot}$ the solution concentration for individual radionuclides in the ternary system C_f is derived by (3.2):

$$C_f = \frac{C_0}{\left(\frac{m}{V} \cdot R_{d,tot} + 1\right)} \quad (3.2)$$

With C_0 = initial aqueous radionuclide concentration [$\text{mol}\cdot\text{L}^{-1}$]; m = total mass of fracture filling material [g]; V = total solution volume [L]; $R_{d,tot}$ represents the distribution coefficient for the ternary system “radionuclide – bentonite colloids – fracture filling material”.

3.1.3.3.2 $^{243}\text{Am(III)}$

Results for the $^{243}\text{Am(III)}$ ternary system as a function of concentration ($1.4\cdot 10^{-9}$ $\text{mol}\cdot\text{L}^{-1}$ and $8\cdot 10^{-9}$ $\text{mol}\cdot\text{L}^{-1}$) feature an exponential concentration decrease in the log-linear visualization (Figure 3.4a). The time-dependent concentration margins are given in red squares (filled or open) of $K_{d,\text{coll}}$ and $K_{d,\text{FFM}}$. The additionally inserted dashed lines are first order rate law best-fit curves using a desorption rate k_3 of 0.009 h^{-1} as taken in Flügge et al. (2010) under the assumption that equilibrium in the sorption systems has been reached after 624 h. The long-term desorption experiment however yielded a significantly lower desorption rate $k_{3,\text{average}}$ of 0.0037 h^{-1} . The desorption rate k_3 is calculated based on the following equation (3.3):

$$C(t) = C_0 \cdot e^{-k \cdot t} \quad (3.3)$$

where $C(t)$ = time dependent concentration in solution [$\text{mol}\cdot\text{L}^{-1}$], C_0 = RN concentration in solution [$\text{mol}\cdot\text{L}^{-1}$], k_3 = desorption rate [h^{-1}] and t = time [h] (Lührmann, 1999))

Comparison of the predicted solution concentration based on the binary systems with those of the ternary system data shows a systematically lower predicted solution concentration (Figure 3.4). The reason is the clear difference between the bentonite colloid – radionuclide desorption rate k_3 and the bentonite colloid – radionuclide sorption rate K_3 of 0.123 h^{-1} as determined after 24 h contact time (Table 3.3). Therefore, Am(III) desorption from the initially almost totally bentonite colloid associated Am(III) (94 %) is the overall rate limiting step in our ternary system and clearly determines the radionuclide solution concentration. Between 1000 h and 7500 h desorption time only a small decrease in $^{243}\text{Am(III)}$ concentration can be detected, indicating that either the system has reached equilibrium conditions or the kinetics of the reversibility process are becoming very slow. Further samplings at longer observation periods are in work to elucidate this open issue.

3.1.3.3.3 $^{242}\text{Pu(IV)}$ and $^{232}\text{Th(IV)}$

$^{242}\text{Pu(IV)}$ is initially colloidal associated to 84 % (analytical uncertainty of colloid bound concentrations ca. +/- 5 %), whereas $^{232}\text{Th(IV)}$ is strongly colloidal associated (99 %) after spiking to the groundwater with bentonite colloids and 24 h equilibration time (Table 3). ^{242}Pu samples with $7.0\cdot 10^{-11}$ $\text{mol}\cdot\text{L}^{-1}$ and $1.3\cdot 10^{-8}$ $\text{mol}\cdot\text{L}^{-1}$ have been prepared. Geochemical calculations show that Pu is in the tetravalent oxidation state under the given conditions. Figure 3.4b shows the time dependent concentration decrease for both Pu sample sets. The series with the lower $^{242}\text{Pu(IV)}$ concentration shows a slightly steeper decrease in concentration starting after ~ 125 h compared to the set with higher $^{242}\text{Pu(IV)}$ concentration. Final Pu(IV) concentrations after 624 h (equilibrium assumption in Flügge et al. (2010)) for the high and the low Pu(IV) concentration series are $1.21\cdot 10^{-11}$ $\text{mol}\cdot\text{L}^{-1}$ and $4.53\cdot 10^{-9}$ $\text{mol}\cdot\text{L}^{-1}$, respectively. Pu(IV) concentration for the long term sample after 7500 h is $2.18\cdot 10^{-9}$ $\text{mol}\cdot\text{L}^{-1}$. Like $^{242}\text{Pu(IV)}$, a time dependent concentration decrease (from initially $7.3\cdot 10^{-9}$ $\text{mol}\cdot\text{L}^{-1}$ to

$6.2 \cdot 10^{-10} \text{ mol} \cdot \text{L}^{-1}$) has been observed for $^{232}\text{Th(IV)}$. The additionally inserted dashed lines in Figure 4b are again first order rate law best-fit curves using a desorption rate k_3 of 0.0085 h^{-1} as taken in Flügge et al. (2010) under the assumption that equilibrium in the sorption systems has been reached after 624 h. The long-term desorption experiment however yielded a significantly lower desorption rate averaged over both the Pu(IV) and Th(IV) data sets with $k_{3,\text{average}}$ of 0.0014 h^{-1} . In comparison to $^{243}\text{Am(III)}$, both $^{242}\text{Pu(IV)}$ and $^{232}\text{Th(IV)}$ obviously exhibits a slower reversibility kinetic.

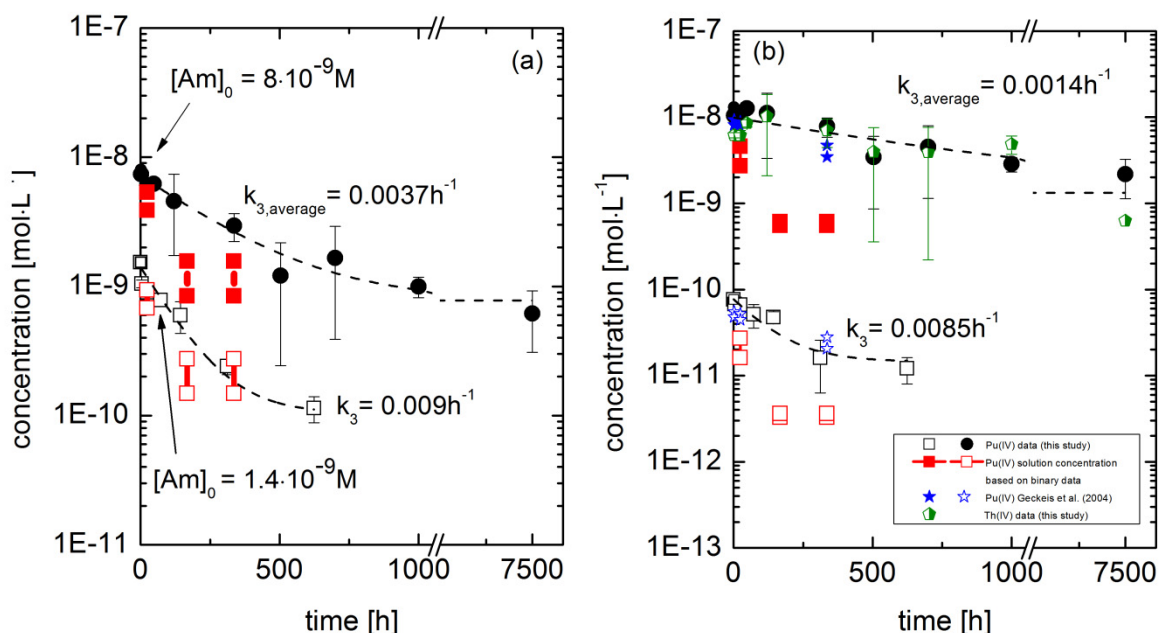


Figure 3.4: Time dependent radionuclide concentration change in the ternary system RN-fracture filling material (FFM)-bentonite colloids. The time-dependent concentration margins given in red squares (filled or open) represent predictions of the ternary system based on the binary system sorption data: (i) bentonite colloids – RN and (ii) fracture filling material – RN as published in (Missana and Geckeis, 2006). (a) Initial Am(III) concentrations $8 \cdot 10^{-9} \text{ mol} \cdot \text{L}^{-1}$ (filled circles) and $1.4 \cdot 10^{-9} \text{ mol} \cdot \text{L}^{-1}$ (open black squares). The dashed lines are first order rate law fitting curves using a desorption rate k_3 of 0.009 h^{-1} as presented in Flügge et al. (2010) and the desorption rate $k_{3,\text{average}}$ of 0.0037 h^{-1} as determined for the long-term desorption data (note the break in the X axis). (b) Initial Pu(IV) concentrations $1.3 \cdot 10^{-8} \text{ mol} \cdot \text{L}^{-1}$ (filled circles) and $7.7 \cdot 10^{-11} \text{ mol} \cdot \text{L}^{-1}$ (open black squares). The dashed lines are first order rate law fitting curves using a desorption rate k_3 of 0.0085 h^{-1} as presented in Flügge et al. (2010) and the desorption rate $k_{3,\text{average}}$ of 0.0014 h^{-1} as determined for the long-term desorption data averaged from the Pu(IV) and Th(IV) desorption experiments. Additionally inserted are the back calculated Pu(IV) solution concentrations based on the ternary Rd values published in (Missana and Geckeis, 2006) (blue stars) (note the break in the X axis).

Similar slow desorption kinetics from bentonite colloids have been observed by Schäfer and Noseck (2010). A straightforward interpretation of the presented Plutonium results is hindered by the complex Pu(IV) aquatic chemistry and the fact that due to low metal concentrations used no spectroscopic technique can be applied to gain further insights into the prevailing Pu(IV) speciation. Therefore, the following discussion is based on macroscopic/phenomenological observations and supporting thermodynamic calculations. Recalling the results from the thermodynamic calculations presented above, the $\text{Pu(OH)}_4(\text{am})$ solid phase (also termed $\text{PuO}_2 \cdot x\text{H}_2\text{O}(\text{am})$ or $\text{PuO}_2(\text{am,hyd})$) is oversaturated in case of the high Pu(IV) concentration series (but not in case of the low Pu(IV) concentrations series) and the $\text{Th(OH)}_4(\text{am})$ is undersaturated in the experiments presented. However, no immediate removal of Pu(IV) from solution due to precipitation can be observed in the experimental data, since the $^{242}\text{Pu(IV)}$ (and Th(IV)) concentration remains constant for more than 100 hours after spiking to the radionuclide cocktail and the sample batches, respectively. Under the given experimental conditions the precipitation of a Pu(IV) solid phase starts with the formation of nanocrystalline Pu(IV) oxyhydroxide species, also called polymeric $\text{Pu(IV)O}_n(\text{OH})_{4-2n}$ “eigencolloids”. Colloidal Pu(IV) species are known to be quite stable in aqueous solution and considered part of the

overall thermodynamic equilibrium system (Neck et al, 2007). It is reasonable to assume that the neutrally charged polymeric $\text{Pu(IV)O}_n(\text{OH})_{4-2n}$ "eigencolloids" possess very similar chemical and sorption properties like the neutrally charged monomeric aquatic Pu(IV) hydrolysis complex $\text{Pu(IV)OH}_4(\text{aq})$. Therefore, it is not possible on the basis of the available experimental evidences to differentiate if Pu(IV) is present as a monomeric hydrolysis complex or an "eigencolloid" species. Following this line of reasoning, both types of Pu(IV)/Th(IV) species should be equally prone to sorption onto the bentonite colloids. A similar chemical behaviour of both types of Pu(IV)/Th(IV) species would also corroborate the observation of the quite likewise desorption kinetics for both Pu(IV) concentrations series (due to the absence of Pu(IV) "eigencolloids" for the low concentration series expected from calculations). The results presented by Geckeis et al. (2004) under similar experimental conditions to the prevailing study reported a Pu(IV) colloidal fraction between 5 to 55 % (in absence of bentonite colloids) for Pu(IV) concentrations of $9.94 \cdot 10^{-9} \text{ mol} \cdot \text{L}^{-1}$ and approximately 84 % colloid associated Pu(IV) in presence of $20 \text{ mg} \cdot \text{L}^{-1}$ bentonite colloids for Pu(IV) concentrations of $6.7 \cdot 10^{-9} \text{ mol} \cdot \text{L}^{-1}$. Thus, the concentration decrease is explainable by desorption of colloid bound $^{242}\text{Pu(IV)}/^{232}\text{Th(IV)}$, either as a monomeric or an "eigencolloid" species and subsequent sorption on the FFM.

Taking the observed differences in long-term sorption reversibility kinetics of the batch sorption data presented in Figure 3.4 one can predict the residence time dependent recovery of the tri- and tetravalent radionuclides under the assumption of negligible colloid attachment as important for the in-situ migration studies in the framework of the CFM (Colloid Formation & Migration project) (Figure 3.5).

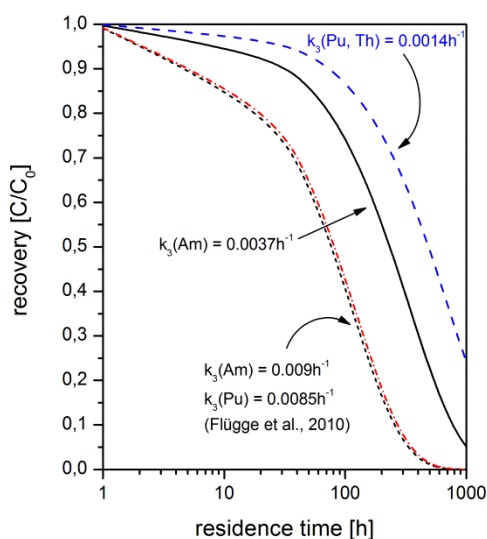


Figure 3.5: Residence time dependent recovery based on the batch experiment determined desorption rate (Figure 4).

Flügge et al. made an attempt to assess the order of magnitude of rate values for Pu(IV) desorption from colloids in absence of colloid filtration, which may have an impact for the colloid mediated Pu migration from a repository over relevant long time scales. They found from a performance assessment perspective rates must be lower than about $2 \cdot 10^{-5} \text{ h}^{-1}$, which is about 2 orders of magnitude lower than our experimentally obtained data. However, it has to be clearly stated that these interpretations are based on the assumption of complete RN sorption reversibility. As it was observed e.g. by Bouby et al. (2009), one has to be aware of the fact that sorption is not at all fully reversible, that is, a fraction of the RN still remains associated to the colloids and can contribute to a long term colloid facilitated radionuclide transport. Indirect evidence is also given by our results presented showing significantly lower fitted k_3 desorption rates of the long-term experimental data up to 7500 h contact time.

3.1.3.4 The case of $^{237}\text{Np(V)}$, $^{233}\text{U(VI)}$ and $^{99}\text{Tc(VII)}$

3.1.3.4.1 $^{237}\text{Np(V)}$

Regarding $^{237}\text{Np(V)}$, samples with $2.0 \cdot 10^{-8} \text{ mol}\cdot\text{L}^{-1}$ and $1.8 \cdot 10^{-6} \text{ mol}\cdot\text{L}^{-1}$ $^{237}\text{Np(V)}$ concentration have been prepared. As shown in Figure 6a a time dependent decrease in solution concentration can be detected for both concentrations. The observed $^{237}\text{Np(V)}$ concentration decrease can either be explained by a slow reduction kinetic to Np(IV) in accordance with the evolution of experimental pe/pH conditions and/or with a slow sorption kinetic on the fracture filling material. Approximately 95 % of the initial $^{237}\text{Np(V)}$ concentration is removed from solution after 7500 h. The time-dependent concentration margins given in red squares (filled or open) of Figure 3.6a represent predictions of the ternary system based on the binary system sorption data $K_{d,\text{coll}}$ and $K_{d,\text{FFM}}$ and fit, in contrary to the data presented for the tri- and tetravalent radionuclides, the experimental data quite well. Based on

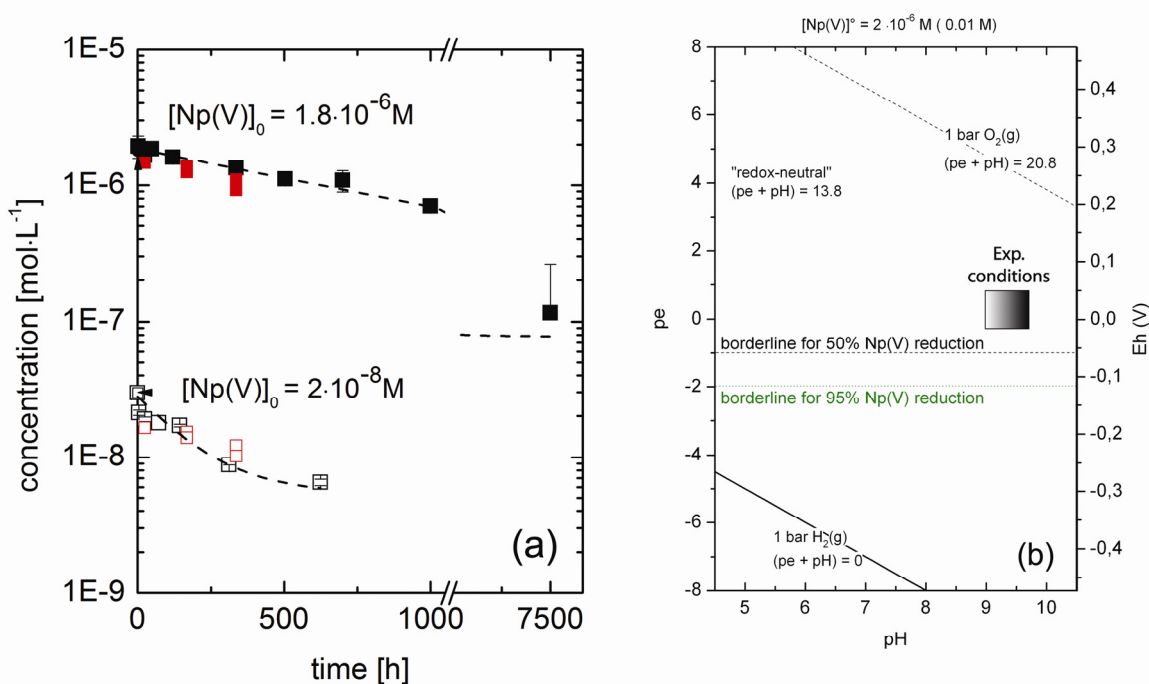


Figure 3.6: (a) Time dependent Np concentration change in the ternary system Np-fracture filling material (FFM)- bentonite colloids for two different initial Np(V) concentrations $1.8 \cdot 10^{-6} \text{ mol}\cdot\text{L}^{-1}$ (filled squares) and $2 \cdot 10^{-8} \text{ mol}\cdot\text{L}^{-1}$ (open black squares). The time-dependent concentration margins given in red squares (filled or open) represent predictions of the ternary system based on the binary system sorption data: (i) bentonite colloids – Np(V) and (ii) fracture filling material – Np(V) as published in (Missana and Geckeis, 2006). The dashed lines are first order rate law fitting curves (Note the break in the x axis) (b) pe/pH diagram showing the experimental pe/pH range and the pe borderline for 50 % and 95 % Np reduction (note the break in the X axis).

the low initial bentonite colloid association found for the Np system (0.1 % initially colloid associated) this observation is not surprising as the bentonite colloid desorption kinetics are not the rate limiting step. The borderline of $^{237}\text{Np(V)}$ reduction is at $E_{h(\text{SHE})}$ around -60 mV (50 % reduced Np), which is slightly lower than our measured $E_{h(\text{SHE})}$ values of -15 mV in the Grimsel system. Due to serious uncertainties in redox measurements, especially in natural groundwater with low concentrations of redox sensitive species like e.g. (Fe(II)/Fe(III)) (Grenthe et al., 1992), we cannot exclude redox potentials lying in the range of the borderline for reduction. It is well established in the literature that many redox couples are far from equilibrium conditions showing slow reaction kinetics (Stumm and Morgan, 1996). The experimental data obtained so far show that the time frame is insufficient to reach equilibrium conditions. A partial reduction at shorter contact times might occur, but cannot be

resolved within the analytical uncertainties. Calculations based on equation 3.4 (Neck et al., 2009) can be used to estimate the amount of reduced ^{237}Np .

$$pe = \log K_{V-IVcoll} + \log[\text{Np}]_{\text{tot}} - \log(2) + \log \gamma \text{NpO}_2^{2+} - \left\{1 + \sum \beta' n, L[\text{Lz-}]n\right\} \quad (3.4)$$

with $\log K_{V-IVcoll}$ = equilibration constant for the redox reaction $\text{Np(V)} \Rightarrow \text{Np(IV)}$, $[\text{Np}]_{\text{tot}}$ = total Np concentration in the system [$\text{mol}\cdot\text{L}^{-1}$], γ = activity coefficient (calculated with SIT) and β' = conditional complex formation constant. Under the experimental conditions of pH 5 to 10 and $I \leq 0.1 \text{ mol}\cdot\text{L}^{-1}$ background electrolytes and Ar atmosphere the following simplifications of eq. 3.4 can be made: (i) Formation of hydrolysis species and other complexes can be neglected and the term $\{1 + \sum \beta' n, L[\text{Lz-}]n\}$ can be omitted. (ii) Concerning the $^{237}\text{Np(V)}$ total concentration ($[\text{Np}]_{\text{tot}} = [\text{Np(V)}] = (1.8 \pm 0.2) \cdot 10^{-6} \text{ mol}\cdot\text{L}^{-1}$) the SIT calculated activity coefficient for NpO_2^+ in $0.1 \text{ mol}\cdot\text{L}^{-1}$ NaCl ($\log \gamma \text{NpO}_2^+ = -0.10$) is constant.

With $pe = 0.15 \pm 0.35$ the following equilibrium constant for $I = 0$ can be obtained: $\log K_{V-IVcoll}^{\circ} = 5.0 \pm 0.4$. Calculating the pe based on the values given above results in the borderline for 50 % Np(V) reduction at $pe \approx -1$ as given in Figure 3.6b. This calculated pe is not far away from the measured pe values in the batch experiments, therefore a partial reduction of Np(V) on the FFM surface is plausible.

3.1.3.4.2 $^{99}\text{Tc(VII)}$ and $^{233}\text{U(VI)}$

The concentrations of $^{99}\text{Tc(VII)}$ and $^{233}\text{U(VI)}$ remain constant over the experimental period with $1.3 \cdot 10^{-8} \pm 1.4 \cdot 10^{-9} \text{ mol}\cdot\text{L}^{-1}$ and $5 \cdot 10^{-7} \pm 3 \cdot 10^{-8} \text{ mol}\cdot\text{L}^{-1}$, respectively indicating the absence of sorption to fracture filling material or reduction within the analytical uncertainty in both investigated systems. Both elements show no interaction with the FEBEX colloids which is evidenced by the comparison between UC and not UC samples in Figure 3.7. A K_d value [$\text{L}\cdot\text{kg}^{-1}$] of $\sim 0.67 \pm 0.78$ for

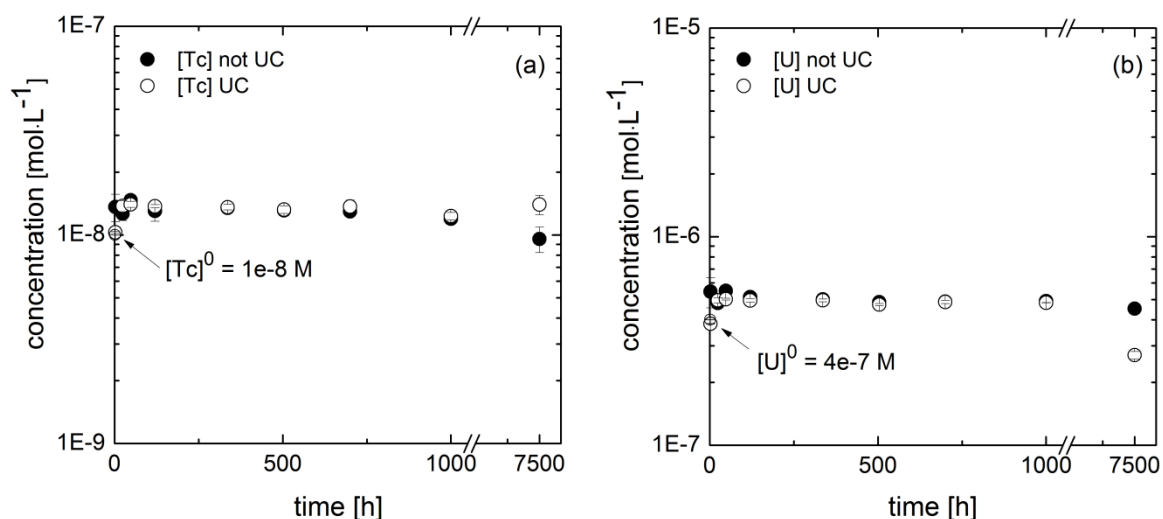


Figure 3.7: Time dependent evolution of radionuclide concentration for (a) $^{99}\text{Tc(VII)}$ and (b) $^{233}\text{U(VI)}$ for the 1-2 mm experiments (SET4). Values are given both for ultra-centrifuged (UC) samples and for non ultra-centrifuged (not UC) samples.

3 Influence of sorption and redox kinetics on radionuclide speciation

$^{232}\text{Th(IV)}$ in-situ K_d show even higher values with $\sim 1.6 \cdot 10^5$. But again these so-called in-situ K_d values do not provide information on “sorption” behaviour. They rather reflect a general measure for element mobilities in the geosphere. It is well known that U mobility is higher than Th mobility mainly due to its redox chemistry.

3.1.3.5 Effect of available surface area on sorption reversibility of Np, Am and Pu

Three different FFM grain sizes have been used to study the influence of available surface area on sorption reversibility for $^{237}\text{Np(V)}$, $^{242}\text{Pu(IV)}$ and $^{243}\text{Am(III)}$, namely 0.25-0.5 mm, 0.5-1 mm and 1-2 mm. Specific surface area measurements (BET) of the three Grimsel size fractions yielded values of $0.238 \text{ m}^2 \cdot \text{g}^{-1}$, $0.187 \text{ m}^2 \cdot \text{g}^{-1}$ and $0.153\text{-}0.166 \text{ m}^2 \cdot \text{g}^{-1}$ for 0.25-0.5 mm, 0.5-1 mm and 1-2 mm size fraction, respectively. Concerning the 1-2 mm size fraction, sample sets with two different RN concentrations have been examined.

Results are depicted in Figure 3.8 and presented as surface area normalized distribution coefficients, calculated according to equation 3.5:

$$R_d = \frac{\Gamma_{RN}}{[RN]} = \frac{TOTRN - [RN]}{[RN]} / \varphi m = \left(\frac{TOTRN}{[RN]} - 1 \right) / \varphi m \quad (3.5)$$

with R_d = distribution coefficient [$\text{L} \cdot \text{m}^{-2}$]; Γ_{RN} = surface excess of [RN] [$\text{mol} \cdot \text{m}^{-2}$]; [RN] = dissolved [RN] concentration [$\text{mol} \cdot \text{L}^{-1}$]; $TOTRN$ = total [RN] concentration [$\text{mol} \cdot \text{L}^{-1}$]; φ = surface area [$\text{m}^2 \cdot \text{g}^{-1}$]; m = solid concentration [$\text{g} \cdot \text{L}^{-1}$].

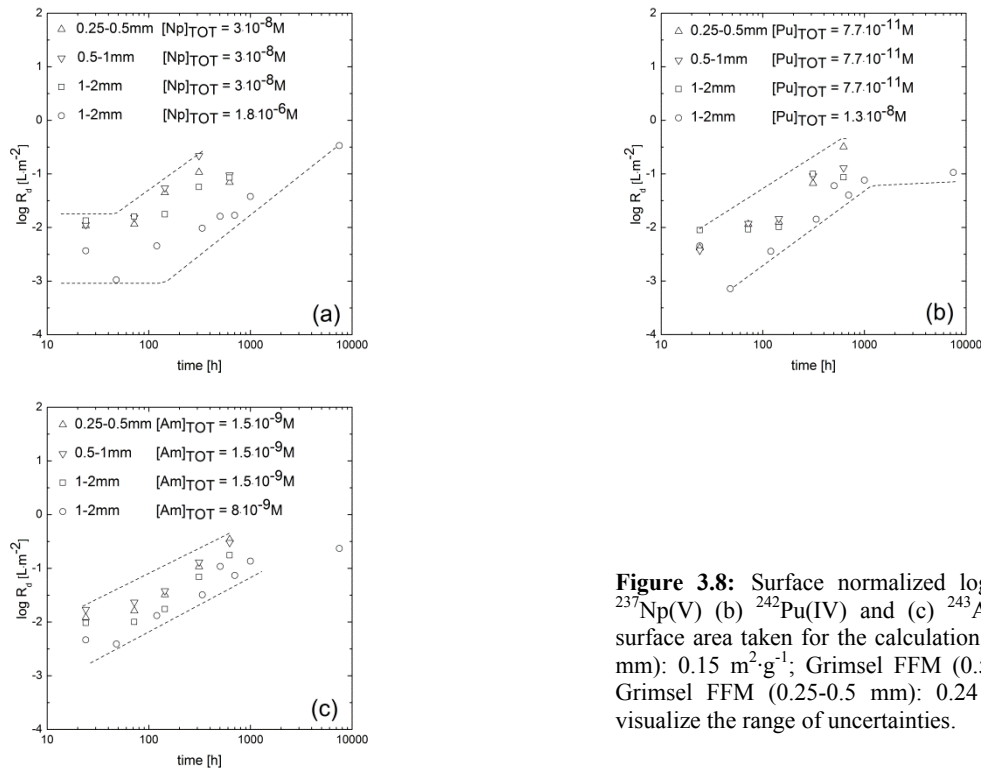


Figure 3.8: Surface normalized $\log(R_d)$ values for (a) $^{237}\text{Np(V)}$ (b) $^{242}\text{Pu(IV)}$ and (c) $^{243}\text{Am(III)}$. The N_2 BET surface area taken for the calculation is: Grimsel FFM (1-2 mm): $0.15 \text{ m}^2 \cdot \text{g}^{-1}$, Grimsel FFM (0.5-1 mm): $0.19 \text{ m}^2 \cdot \text{g}^{-1}$, Grimsel FFM (0.25-0.5 mm): $0.24 \text{ m}^2 \cdot \text{g}^{-1}$. Dashed lines visualize the range of uncertainties.

$^{99}\text{Tc(VII)}$ and $\sim 0.13 \pm 0.71$ for $^{233}\text{U(VI)}$ could be determined. The $^{99}\text{Tc(VII)}$ K_d value is comparable to data of K_d $^{99}\text{Tc(VII)} = 0.38 \pm 0.10$ obtained after one week contact time for fracture filling material

fraction < 1160 μm published in (Nagra, in press), but significantly lower than $K_d^{99}\text{Tc(VII)} = 2.5 \pm 0.10$ obtained after five weeks contact time. Concerning our K_d value for $^{233}\text{U(VI)}$, it is lower than the K_d values obtained by Missana and Geckeis (2006) of 1.81 ± 0.19 and $^{233}\text{U(VI)} = 10.4 \pm 0.10$ for contact times of one week and five weeks, respectively. Interestingly, the uranium in-situ K_d simply calculated based on the given FFM uranium concentration (Table 3.1) and the groundwater uranium concentration (Table 3.2) is orders of magnitude higher with $K_d \approx 3800$ which clearly indicates that a large part of the natural uranium pool present in the FFM does not interact with the groundwater.

$^{237}\text{Np(V)}$ shows lower R_d values (~ 0.5 orders of magnitude) for the 1-2 mm system with higher $^{237}\text{Np(V)}$ concentration compared to the same size fraction with lower concentrations. All data sets show an increase in R_d values of about one order of magnitude with time. This time dependent trend of increasing $^{237}\text{Np(V)}$ R_d values was not observed in earlier studies (Geckeis et al., 2004).

R_d values for $^{242}\text{Pu(IV)}$ and $^{243}\text{Am(III)}$ show a rise from $R_d \sim -2.5$ up to $-0.5 \text{ L}\cdot\text{m}^{-2}$. This increase in R_d can be explained by the kinetics of desorption and the subsequent sorption to the fracture filling material, whereas the observed trend in the $^{237}\text{Np(V)}$ R_d values reflects most likely a combined effect of reduction and sorption. In general, R_d values for the three samples series with higher metal concentration are always lower than R_d values for the three samples series with lower metal concentration. This observation may be a commonly observed non-linear sorption behaviour. R_d values often increase at decreasing metal concentrations which is usually assigned to a weak and strong sorption process. The envelope curves given in Figure 3.8 give an uncertainty margin for the kinetics of actinide dissociation from FEBEX bentonite colloid that can be used in reactive transport modeling (Noseck and Klotz, 2002). The surface normalized R_d values reflect no systematic trend in terms of the available surface area and/or the mineralogy of the FFM. The latter observation is expected since the mineralogical composition of the three different FFM size fractions is very similar to each other based on the XRD results stated above.

3.1.4 Conclusions

Batch type experiments studying the reversibility of radionuclide binding to bentonite colloids in presence of fracture filling material with different grain sizes spanning a range from 0.25 to 2 mm from Grimsel have been conducted using a cocktail of radionuclides spiked to natural groundwater from the Grimsel test site. $^{99}\text{Tc(VII)}$, $^{233}\text{U(VI)}$ and $^{237}\text{Np(V)}$ are not colloidal associated under our experimental conditions. Concentrations of $^{99}\text{Tc(VII)}$ and $^{233}\text{U(VI)}$ remain constant over the whole experimental duration (7500 h) showing both no interaction with the fracture filling material due to sorption effects and no reduction to sparingly soluble phases. In contrast, the tri- and tetravalent radionuclides $^{243}\text{Am(III)}$, $^{232}\text{Th(IV)}$ and $^{242}\text{Pu(IV)}$ are almost totally associated to bentonite colloids. The three colloid associated RNs show slow desorption from colloids which becomes detectable after about 100 h contact time with the fracture filling material and proceeds up to at least 7500 h. The reason for the observed desorption of $^{232}\text{Th(IV)}$, $^{242}\text{Pu(IV)}$ and $^{243}\text{Am(III)}$ in the presence of FFM could be attributed to the higher surface area of the FFM available for radionuclide sorption compared to the bentonite surface area under the given experimental conditions. Results for $^{243}\text{Am(III)}$ slightly differ from $^{242}\text{Pu(IV)}$ and $^{232}\text{Th(IV)}$ in terms of slower desorption kinetics. Overall, it has to be stated that the experimental duration of almost 1 year was not sufficiently long to fully establish sorption equilibrium unequivocally. Further studies at longer time scales are in progress to shed light on this issue.

In the case of $^{237}\text{Np(V)}$ a decrease in concentration could be explained by both slow sorption to fracture filling material and, more likely, by reduction to $^{237}\text{Np(IV)}$. The latter assumption is corroborated by means of geochemical modeling yielding also in agreement with the experimental results no reduced species of $^{233}\text{U(VI)}$ and $^{99}\text{Tc(VII)}$ under prevailing geochemical conditions of the experiments. Overall, the results show that the RN desorption kinetics from bentonite colloids are rather independent from (i) the grain size or respective surface area of the investigated material, at

3 Influence of sorption and redox kinetics on radionuclide speciation

least in the size fraction range 0.25-2 mm and (ii) the concentration in case of $^{237}\text{Np(V)}$, $^{242}\text{Pu(IV)}$ and $^{243}\text{Am(III)}$.

Our findings imply the importance of kinetics of RN-colloid binding for colloid facilitated radionuclide migration. These results need to be included in codes for simulating colloid-facilitated radionuclide transport to reduce the degree of uncertainties in input parameters leading to an improvement in the quality of the simulation results. RN dissociation from colloids has to be considered when results from migration experiments performed in the laboratory and in the field are transferred to assess the long-term colloid impact on radionuclide mobility in a nuclear waste repository.

3.2 *U(VI) removal kinetics in presence of synthetic magnetite particles*

The interaction of hexavalent U with a freshly synthesized nanoparticulate magnetite ($\text{Fe}^{\text{II}}\text{Fe}^{\text{III}}\text{O}_4$) (stoichiometric ratio $x(\text{Fe}(\text{II})/\text{Fe}_{\text{TOT}}) = 0.25 - 0.33$), a partly oxidized synthetic nanoparticulate magnetite ($x = 0.11 - 0.27$) and maghemite nanoparticles ($x = 0$) under anoxic conditions and exclusion of CO_2 as function of pH, contact time and total U concentration ($3 \cdot 10^{-5}$ M and $1 \cdot 10^{-7}$ M) has been examined. Short term kinetic batch experiments (contact time of 90 d) for four different pH values have been conducted. Moreover, classical batch pH sorption edges have been prepared for two different uranium concentrations for a contact time of 550 d. Spectroscopic techniques (XPS, XAS) were applied to probe for the presence and amount of reduced U on the magnetite surface. Batch kinetic studies revealed a fast initial U removal from aqueous solution with > 90% magnetite associated U after 24 hours within the pH range 5-11. Long term contact time batch experiments (550 d) showed neither a U removal below pH < 3 nor a decrease in the magnetite associated U at pH ≥ 9 . Redox speciation by XPS verifies the presence of tetravalent U on the magnetite surface up to a contact time of 550 d. A clear correlation of the amount of available Fe(II) on the magnetite surface and the amount of tetravalent U is observed. XANES investigations confirm the presence of tetravalent U, but cannot resolve the occurrence of pentavalent U doubtlessly. EXAFS results indicate the formation of a U(IV)-oxide-species coordinated to Fe. Thermodynamic calculations based on the experimentally determined redox potentials corroborate the spectroscopic findings of U oxidation states. Overall, the results reflect the importance of magnetite bond structural bound Fe(II) as redox partner for uranyl reduction.

3.2.1 Introduction

The release of U into the environment through anthropogenic induced geochemical perturbations (e.g. migration out of a nuclear waste repository; use of depleted U for military devices; U exploration and acid mine drainage) is a potential threat to mankind and biosphere due to U chemotoxicity. In this regard, the uptake of U by humans is mostly due to water and food (see e.g. (Bosshard et al., 1992)). Therefore, drinking water limits have been proposed e.g. 15 ppb (WHO, 2004) or 30 ppb (EPA, 2011). This range of values reflects the uncertainties about tolerable doses for humans and their impact on health (see e.g. (EFSA, 2009)). To develop sound risk assessment strategies and U remediation concepts a mechanistically process understanding of the behaviour of U in natural environments and its interaction with geologic materials is of crucial necessity. Various processes occurring in the subsurface environment (adsorption onto minerals (see e.g. (Waite et al., 1994; Duff and Amrhein, 1996; Barnett et al., 2000; Davis et al., 2004; Huber and Lützenkirchen, 2009)) or abiotical and microbial induced redox processes causing precipitation of sparingly soluble U phases under anoxic conditions (see e.g. (Lovley et al., 1991; Liger et al., 1999; Wall and Krumholz, 2006)) influence the migration of U leading to retardation/retention. Most important redox partners are Fe(II), sulfide (Wersin et al., 1994) and/or organic matter (Lovley et al., 1991). Fe(II) occurs frequently in a variety of natural environments either as aqueous species produced by mineral dissolution or structural bound in different mineral phases like e.g. pyrite, biotite or magnetite. The mixed-valent iron oxide magnetite, $\text{Fe}^{(III)}[\text{Fe}^{(II)}\text{Fe}^{(III)}]\text{O}_4$ possesses an inverse spinel crystal structure and a stoichiometric ratio $x(\text{Fe(II)}/\text{Fe}_{\text{TOT}}) = 0.33$ (Cornell and Schwertmann, 1996). Magnetite occurs naturally in e.g. igneous and plutonic rocks as accessory mineral phase. Furthermore, it can be found as corrosion product of stainless steel, e.g. canisters in the framework of the multi-barrier concept of deep geological waste disposals (Grambow et al., 1996) representing an important Fe(II) source for redox reactions with radionuclides.

Experimental studies on sorption and/or reduction of U(VI) in presence of magnetite are still accumulating, mostly motivated by the importance of elucidating effective immobilization processes of (U(VI) => U(IV)) and the role of aqueous, surface sorbed or structural bound Fe(II). U data of sorption and reduction studies with magnetite in presence of carbonate at pH values representative for granitic ground-waters (pH 8-9) for contact times up to 150 days were presented by (El Aamrani, 1999). These authors applied X-ray photoelectron spectroscopy (XPS) to identify the U surface species on magnetite and found evidences for a coupled reduction-oxidation process of U(VI) and Fe(II), respectively, in the presence of bicarbonate. Though, they found no U(IV) at slightly acidic pH (4.81) in the absence of carbonate. XPS results presented by Missana et al. (2003a,b) and Scott et al. (2003) indicate U reduction in the presence of structural bound Fe(II) on mineral phases. U(VI) reduction is also feasible by means of sorbed ferrous iron in presence of an Fe(III) containing solid phase (nanoparticulate hematite) as shown by (Liger et al., 1999). Here, a surface-catalyzed process for the U reduction by sorbed Fe(II) is proposed. The influence of bicarbonate in the system uranyl-magnetite for pH 6, 8 and 10 with contact times of 42 days using XPS was investigated by (Regenspurg et al., 2009). A facilitated U(VI) reduction attributed to the formation of siderite representing an additional Fe(II) pool was found. Most recently, Ilton and co-workers presented spectroscopic indications (XPS) of the formation of U(V) in the presence of magnetite and explained the stability of U(V) by sorption/incorporation/precipitation in either secondary iron phases or mixed valent U phases (Ilton et al., 2010). No evidences of U(IV) on basis of XPS and X-ray absorption spectroscopy (XAS) measurements were found by these authors. However, no Eh measurements of the XPS samples were given to link the experimental findings to thermodynamic calculations and other data published.

The motivation of the prevailing study is the following:

- Deliver long-term contact time data (550 d) for the system U-magnetite covering a pH range from 3 to 11 for two different total U concentrations.

- Provide kinetic data about removal processes for different pH values from 1 day up to 90 days contact time.
- Compare the redox capacity of a partly oxidized magnetite with a freshly prepared magnetite mineral phase.
- Probe for the presence of U(V) on the surface of magnetite, as recently reported in the literature, using XPS and XAS for near natural U concentrations.
- Examine if thermodynamic calculations based on independent measured Eh-pH conditions are consistent with spectroscopically determined U redox states.

3.2.2 Materials and Methods

Three nanoparticulate solid phases have been applied in the experiments, namely a freshly prepared magnetite suspension (hereafter called, fmag), a maghemite suspension prepared using the fmag suspension (hereafter called mgh) and an older magnetite suspension which was stored over more than 2 years in a Ar glove box showing partly oxidization due to repeated exposure to low oxygen contents in the glove box (hereafter called, partly-oxidized magnetite (po-mag)).

3.2.2.1 Solid Phase Synthesis and Characterization

Synthesis. The magnetite mineral phases were prepared by reaction of 0.3 M FeSO₄ with 3.33 M KOH and 0.27 M KNO₃ (Schwertmann and Cornell, 1991) under Ar atmosphere in a glove box. Since the mineral synthesis involved a strong base the mineral suspension was dialyzed against de-ionized water which was exchanged every day until the electric conductivity was < 10 µS/cm. The magnetite suspensions yield concentrations of 11.4 g/L and 35.34 g/L for the po-mag and fmag, respectively and were stored in polyethylene bottles in a glove box under Ar atmosphere.

Maghemite was obtained by heating the fresh synthetic magnetite suspension at 250°C for 2 hours (Schwertmann and Cornell, 1991) under ambient atmosphere.

X-ray diffraction (XRD). Powder x-ray diffraction was applied to verify the mineral compositions. XRD patterns for all three mineral phases were recorded from 5° to 80° 2θ using 0.01° 2θ steps and a 2 s accumulation time per step with a Bruker AXS D8 powder diffractometer equipped with a BSI (Baltic Scientific Instrument) Si(Li) solid detector and a Cu K_α X-ray source. Care was taken to minimize oxidization of the samples by using a special X-ray transparent cap on the sample holder.

Scanning electron microscopy (SEM) and energy dispersive X-ray spectroscopy (EDX). Sample material was dried under room temperature in the glove box and transferred into the SEM device (CS44FE Field Emission SEM (CamScan, Cambridge, UK)). The EDX detector system is a silicon drift detector with Peltier cooling (ultra-dry detector system NS 6, Thermo-Fisher, Madison, Wisconsin, USA).

Specific surface area (BET). Specific surface area of the solid phases was determined by BET N₂-adsorption (AUTOSORB-1, Quantachrome Corporation). The samples were heated under anoxic conditions to 80 °C and degassed for 60 min. The determination of the surface area was done via the multiple-point-method at different pressures and a subsequent fit with the BET isotherm.

Electrokinetic measurements. The isoelectrical point (pH_{iep}) of the fmag and po-mag suspensions was determined in 0.001 M NaCl by means of electrophoretic measurements (Zeta Plus, Zeta Potential Analyser, Brookhaven Instruments Corporation).

3.2.2.2 Batch Experiments

The batch type experiments were conducted at room temperature ($\sim 21\text{ }^{\circ}\text{C}$) in a glove box under Ar atmosphere ($< 1\text{ ppm O}_2$). All chemicals used were reagent grade (ultra pure).

Batch samples have been prepared in polyethylene vials (Zinsser, 20 mL) in all experiments. Both the magnetite and maghemite suspensions were applied for the experiments by dilution of the stock solutions with Milli-Q water ($18.2\text{ M}\Omega$), purged with Ar before use, to strip out dissolved carbonate and oxygen. An ionic strength of 0.01 M was set by using NaCl as background electrolyte. The pH was adjusted by addition of HCl and NaOH (Backer, CO_2 free). Finally, U was spiked to the samples from a 1 g/L stock solution of $\text{UO}_2(\text{NO}_3)_2$ (ICP-MS reference standard) to achieve the desired concentrations. If necessary, pH was readjusted slowly by addition of NaOH or HCl immediately after the addition of U. Determination of pH was done applying a semi-micro Ross electrode (81-03, Orion Co.) in combination with a digital pH meter (720A, Orion Co.). The set-up was calibrated using at least 4 commercial buffer solutions (Merck). Besides pH, the redox potential of the samples was measured using a Pt combined electrode (Metrohm) coupled to the Orion pH meter. We measured the redox potential of our samples in contact with the suspension without stirring of the samples. We consistently online monitored (read out every 60 s) the evolution of the redox potential and stopped the measurement when a plateau value was reached. That is, the measurement sometimes took several hours up to one day (for details see (Huber et al., 2010, in review)).

In course of the experiments, pH was frequently measured and readjusted several times if necessary. After the desired contact time, samples were ultra-centrifuged at 694000 g (Beckman XL-90, rotor type 90Ti) in sealed vials for one hour to separate the solid phase and possible colloidal Fe phases. After centrifugation, the samples were immediately transferred back into the glove box and an aliquot of the supernatant was taken using a syringe. This intricate procedure was necessary since preliminary tests using filtration (10 kD; Microsep, Pall Life Science) of the suspension to remove the solid phase indicated a possible U sorption and/or a sorption of U associated colloidal phases on the filter material. Aliquots of the ultra-centrifuged supernatant have been analyzed by inductively coupled plasma mass-spectrometry (ICP-MS) for determination of U and $\text{Fe}_{(\text{TOT})}$ concentrations.

3.2.2.2.1 Magnetite Samples (Series#1-3)

Both magnetite suspensions have been applied in the experiments. The po-mag suspension was stored over a period of approximately 2 years in a Ar glove box before used in the experiments exhibiting partly oxidization ($\text{Fe(II)}/\text{Fe}_{\text{TOT}} = 0.2$ in average as verified by XPS) due to the repeated exposure to the glove box atmosphere which always contains trace amounts of oxygen ($\text{O}_2 \approx 1\text{-}2\text{ ppm}$). The fmag suspension was prepared immediately before the start of the experiments assuring that no or minor oxidization had occurred.

Po-mag sample series (Series #1 and Series#2). Two sample series have been prepared: short term (1 d up to 90 d) kinetic (hereafter called Series#1) and long term (550 d) experiments (hereafter called Series#2), respectively. For Series#1, 4 sample series at 4 different pH values ($\sim 2.5, 5, 8$ and 11) with a U concentration of $3 \cdot 10^{-5}\text{ M}$ have been prepared. Samples have been taken after 1, 2, 3, 6, 14, 48, 57 and 90 d, respectively (Table 3.5). Regarding Series#2, both $3 \cdot 10^{-5}\text{ M}$ (Series#2a) and $1 \cdot 10^{-7}\text{ M}$ (Series#2b) U concentrations have been used and pH of the samples was adjusted between pH ~ 2 to 11 to obtain pH sorption edges (Table 3.6). XPS and XAS measurements of both series have been conducted subsequently after the desired contact times of 1d and 550d, respectively.

Fmag sample series (Series#3). Batch experiments with the freshly prepared magnetite using the same conditions as in Series#1 and Series#2 have been conducted (hereafter called Series#3) but with a different contact time (13 days). Here, three different pH values have been adjusted (pH $\sim 5, 8, 11$) (Table 3.6). Again, XPS measurements have been carried out after the end of the experiments

to probe for the valence state of U. The results are compared to the results obtained in Series#1 and Series#2 to evaluate the influence of a slightly oxidized magnetite in relation to a freshly prepared magnetite in terms of U reduction, respectively.

3.2.2.2 Maghemite Samples (Series#4)

Experiments using maghemite (hereafter called Series#4) have been conducted using the same conditions as for the two magnetite series ($[U]_{TOT} = 3 \cdot 10^{-5}$ M and ionic strength $I = 0.01$ M NaCl). As it was the case for Series#3, three pH values have been adjusted (pH ~ 5 , ~ 8 and ~ 11) and a contact time of 13 d has been applied (Table 3.6).

3.2.2.3 Spectroscopic Techniques

3.2.2.3.1 X-ray Photoelectron Spectroscopy (XPS)

XPS provides an effective surface sensitive method for determination of the valence state of Fe and U at the magnetite surface. After ultra-centrifugation of the samples, the supernatant was separated from the solid magnetite phase. Subsequently, preparation of the samples for XPS measurements was done in the glove box under Ar atmosphere. The separated solid phase was dried at room temperature, pressed on In foil and mounted on the sample holder. Transfer of the prepared samples under Ar atmosphere to the XP spectrometer was achieved by means of an O-ring sealed vacuum transfer vessel (PHI model 04-110). XPS measurements at room temperature were carried out by using a Physical Electronics Inc. (PHI) model 5600ci instrument equipped with a standard dual anode X-ray source, Mg K_{α} (1253.6 eV) and Al K_{α} (1486.6 eV), and with a monochromatized Al K_{α} source operating at 100 W source power. The spectrometer has a hemispherical capacitor analyzer and a detector consisting of a microchannel plate with 16 anodes.

Elemental lines of pure and Ar⁺ beam sputter cleaned metals (Mg K_{α} : Cu 2p_{3/2} at 932.62 eV, Ag 3d_{5/2} at 368.22 eV, Au 4f_{7/2} at 83.95 eV) with well-established binding energies are used to calibrate the binding energy scale of the spectrometer (Seah et al., 1998). Standard deviation of binding energies is within ± 0.1 eV for conductors and within ± 0.2 eV for non-conducting samples.

Spectra were collected with monochromatic Al K_{α} x-ray excitation at a take-off angle of 65° (angle between sample surface and analyzer). During analysis, the pressure inside the spectrometer was about 10^{-7} Pa. Elemental surface composition was analyzed by survey spectra recorded from an analysis area of about 0.8 mm in diameter with a pass energy of 187.85 eV at the hemispherical capacitor analyzer. The narrow scan spectra, used to obtain chemical state information of U and iron, were recorded at a pass energy of 11.75 eV. The XP spectrometer results a FWHM of 0.62 eV for the Ag 3d_{5/2} line at this pass energy. The magnetite powder samples were almost conductive, thus only a small shift for charge referencing (< 0.3 eV) to the O 1s elemental line of magnetite at 530.0 eV (Moulder et al., 1992) was applied. Charge referencing to the C 1s elemental line of adventitious hydrocarbon commonly used was not practical since the C 1s spectra exhibited noisy spectra at low intensity. Narrow scan spectra of elemental lines were analyzed using the program PHI MultiPak, Version 9.2. Curve fitting of the elemental lines was performed by using a nonlinear least-squares optimization procedure with Gaussian-Lorentzian sum functions after subtraction of a Shirley background. Surface species and oxidation states were identified by comparison of the binding energies of the elemental lines with previous results in literature.

3.2.2.3.2 X-ray Absorption Spectroscopy (XAS)

X-ray absorption spectroscopy experiments were performed at the INE-Beamline for actinide research at the ANKA 2.5 GeV synchrotron radiation facility, KIT, Karlsruhe, Germany. For details about the instrumentation at this beamline see (Denecke et al., 2005). A Lemonnier-type (Lemonnier et al., 1978) double-crystal monochromator equipped with a set of Ge(422) crystals was employed for energy monochromatization. For energy calibration of the U L3-edge spectra a photon energy of 17179 eV was assigned to the maximum of the most intense absorption resonance (white line, WL) of the L3-edge X-ray absorption near edge structure (XANES) spectrum of a $(\text{UO}_2)_4\text{O}(\text{OH})_6(\text{H}_2\text{O})_6$ (schoepite) reference sample simultaneously measured with all samples and references. The $[\text{UO}_2(\text{CO}_3)_3]^{4-}$ (U(VI)), $[\text{UO}_2(\text{CO}_3)_3]^{5-}$ (U(V)), and $\text{UO}_2(\text{s})$ (U(IV)), schoepite(s) (U(VI)) reference samples were measured as solutions in fluorescence mode and as solid pellets in transmission mode, respectively. UO_2 or schoepite (20 mg) powders were mixed with cellulose and pressed in the form of pellets. A magnetite sample from Series#2a (po-mag#42) was measured in fluorescence mode. A five-element Ge solid state detector (Canberra LGe type) was used for all measurements in fluorescence mode. At least five X-ray absorption fine structure (XAFS) spectra, including XANES and extended X-ray absorption fine structure (EXAFS) energy regions, were collected from each sample measured in fluorescence mode, in order to check for reproducibility of the spectral features and to improve the counting statistics.

3.2.2.4 Thermodynamic Calculations

Knowledge about the U equilibrium speciation and redox state under the experimental conditions facilitates a thorough analysis, interpretation and understanding of the results. Therefore, thermodynamic calculations have been performed to model the aqueous speciation of the system. Consistently, only thermodynamic data for U from the actual NEA database (Guillaumont et al., 2003) have been used (Table 3.4). Total concentrations for U and NaCl used in the calculations for the speciation plots and the predominance diagrams are the same as applied in the batch experiments.

Table 3.4: Thermodynamic constants used in the calculation of the predominance diagrams in Figure 3.10. Consistently, only thermodynamic constants from the actual NEA database (Guillaumont et al. 2003) have been used.

Species	Reaction	$\text{Log}_{10} K^0$
U^{4+}	$4\text{H}^+ + \text{UO}_2^{2+} + 2\text{e}^- \leftrightarrow \text{H}_2\text{O} + \text{U}^{4+}$	9.038
$\text{UO}_2(\text{am})$	$\text{U}^{4+} + 4\text{OH}^- \leftrightarrow 2\text{H}_2\text{O} + \text{UO}_2(\text{am})$	54.500
UO_2^+	$\text{UO}_2^{2+} + \text{e}^- \leftrightarrow \text{UO}_2^+$	1.484
UOH^{3+}	$\text{H}_2\text{O} + \text{U}^{4+} \leftrightarrow \text{H}^+ + \text{UOH}^{3+}$	-0.540
UO_2OH^+	$\text{H}_2\text{O} + \text{UO}_2^{2+} \leftrightarrow \text{H}^+ + \text{UO}_2\text{OH}^+$	-5.250
$\text{UO}_2(\text{OH})_2(\text{aq})$	$2\text{H}_2\text{O} + \text{UO}_2^{2+} \leftrightarrow 2\text{H}^+ + \text{UO}_2(\text{OH})_2(\text{aq})$	-12.150
$\text{U}(\text{OH})_4(\text{aq})$	$4\text{OH}^- + \text{U}^{4+} \leftrightarrow \text{U}(\text{OH})_4(\text{aq})$	46.000
$\text{UO}_2(\text{OH})_3^-$	$3\text{H}_2\text{O} + \text{UO}_2^{2+} \leftrightarrow 3\text{H}^+ + \text{UO}_2(\text{OH})_3^-(\text{aq})$	-20.250
$\text{UO}_2(\text{OH})_4^{2-}$	$4\text{H}_2\text{O} + \text{UO}_2^{2+} \leftrightarrow 4\text{H}^+ + \text{UO}_2(\text{OH})_4^{2-}(\text{aq})$	-32.400
$(\text{UO}_2)_2\text{OH}^{3+}$	$\text{H}_2\text{O} + 2\text{UO}_2^{2+} \leftrightarrow (\text{UO}_2)_2\text{OH}^{3+} + \text{H}^+$	-2.700
$(\text{UO}_2)_2(\text{OH})_2^{2+}$	$2\text{H}_2\text{O} + 2\text{UO}_2^{2+} \leftrightarrow (\text{UO}_2)_2(\text{OH})_2^{2+} + 2\text{H}^+$	-5.620
$(\text{UO}_2)_3(\text{OH})_4^{2+}$	$4\text{H}_2\text{O} + 3\text{UO}_2^{2+} \leftrightarrow (\text{UO}_2)_3(\text{OH})_4^{2+} + 4\text{H}^+$	-11.900
$(\text{UO}_2)_3(\text{OH})_5^+$	$5\text{H}_2\text{O} + 3\text{UO}_2^{2+} \leftrightarrow (\text{UO}_2)_3(\text{OH})_5^+ + 5\text{H}^+$	-15.550
$(\text{UO}_2)_3(\text{OH})_7^-$	$7\text{H}_2\text{O} + 3\text{UO}_2^{2+} \leftrightarrow (\text{UO}_2)_3(\text{OH})_7^- + 7\text{H}^+$	-32.200
$(\text{UO}_2)_4(\text{OH})_7^+$	$7\text{H}_2\text{O} + 4\text{UO}_2^{2+} \leftrightarrow (\text{UO}_2)_4(\text{OH})_7^+ + 7\text{H}^+$	-21.900
UCl^{3+}	$\text{Cl}^- + \text{U}^{4+} \leftrightarrow \text{UCl}^{3+}$	1.720
UO_2Cl^+	$\text{Cl}^- + \text{UO}_2^{2+} \leftrightarrow \text{UO}_2\text{Cl}^+$	0.170
$\text{UO}_2\text{Cl}_2(\text{aq})$	$2\text{Cl}^- + \text{UO}_2^{2+} \leftrightarrow \text{UO}_2\text{Cl}_2(\text{aq})$	-1.100

To elucidate the role of U(V) in the system, only the free UO_2^+ ion has been included in the calculations, as the only U(V) species critically reviewed by the NEA. For the modeling task, the code

Hydra/Medusa (Puigdomenech, 2004) has been applied. Note that the calculations are performed for equilibrium conditions without considering a solid phase. That is, the impact of a solid phase on the aqueous speciation by sorption or redox processes is omitted.

3.2.3 Results and Discussion

3.2.3.1 Solid Phase Characterization

Figure 3.9 depicts the measured XRD patterns for all mineral phases used throughout the study verifying that no additional mineral phase as the ones synthesized is present. Deviations between the magnetite and maghemite phases examined are visible in the range between 20° and 30° 2θ where the maghemite exhibits two additional peaks. This observation is in line with results presented by (Schwertmann and Cornell, 1991). BET N_2 -adsorption yielded a specific surface area of $19.7 \text{ m}^2\cdot\text{g}^{-1}$, $14.78 \text{ m}^2\cdot\text{g}^{-1}$ and $11.14 \text{ m}^2\cdot\text{g}^{-1}$ for the po-mag, fmag and mgh, respectively. Our values for both magnetite mineral phases are higher compared to e.g. (Missana et al., 2003b) who measured a value of $8.5 \text{ m}^2\cdot\text{g}^{-1}$ for their magnetite synthesized using the same approach as in this work. (Ilton et al., 2010) measured a value of $13.5 \text{ m}^2\cdot\text{g}^{-1}$ for their magnetite using a similar synthesis fitting quite well to our measurements. As shown in Figure 3.9 all mineral phases exhibit particle sizes around 100-300 nm as determined out of the SEM pictures in accordance with TEM investigations by Missana et al. (2003b). Derivation of the particle sizes by means of the Scherrer equation (Patterson, 1939) on basis of the XRD spectra yielded values around 30-60 nm. EDX spectra for the po-mag revealed only Fe and O with mean atomic concentrations of 31.2 % and 68.2 %, the fmag yields mean concentrations of 42.8 % to 56.8 % for Fe and O, respectively. Regarding mgh, the amount of Fe increased to a mean value of approximately 45 % while the amount of O decreases to 55% atomic percent. In a few samples, impurities of S and Si ($< 0.5 \text{ at.-%}$) were detected most likely as artifacts from the solid phase synthesis. Determination of the isoelectrical point (pH_{iep}) yielded values for fmag and po-mag of pH 5.5 and pH 6, respectively. Literature values for commercial, synthesized and natural magnetite range between $\text{pH} \sim 4$ and ~ 8 (Kosmulski, 2001; Illes and Tombacz, 2006; Mansour et al., 2009).

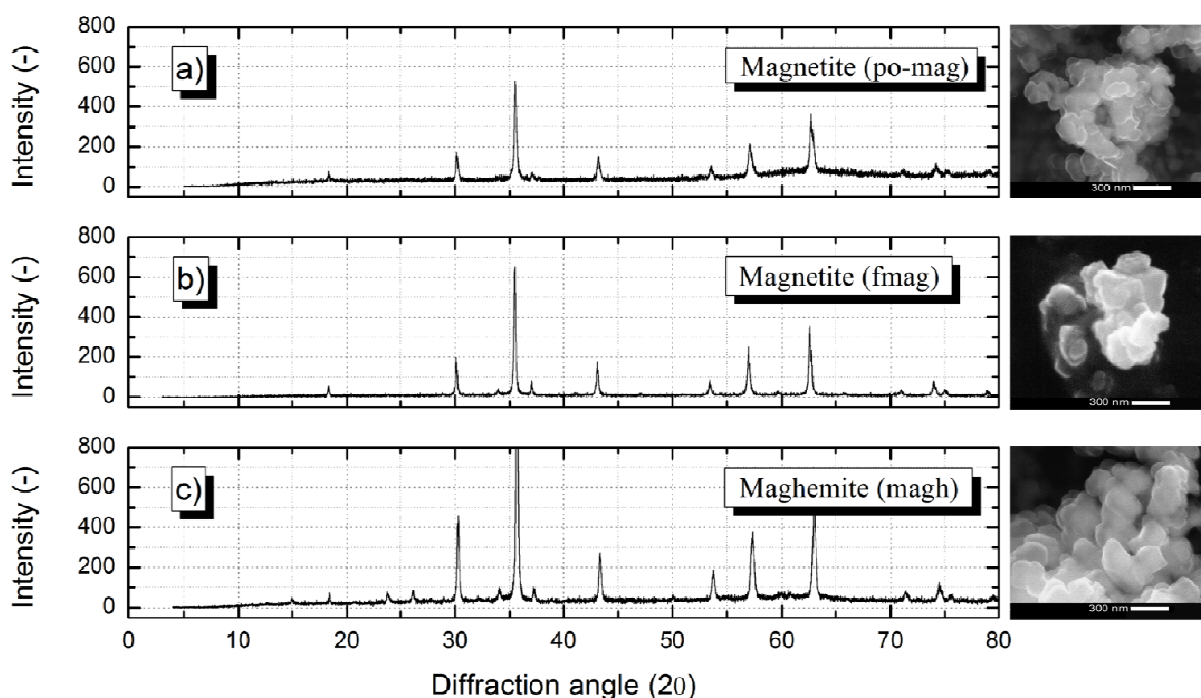


Figure 3.9: XRD patterns in conjunction with SEM pictures for all three solid phases used in the experiments. Scale bar 300 nm. a) Partly oxidized magnetite (po-mag) b) Non-oxidized magnetite (fmag) and c) Maghemite (mgh); enhanced view: max. peak intensity 1400 (-).

3.2.3.2 Thermodynamic modeling results and redox potential measurements

3.2.3.2.1 U Speciation

In Figure 3.10a and Figure 3.10b predominance diagrams for both U concentrations applied in the experiments are depicted. Regarding the results obtained for Series#2b shown in Figure 3.10a, above $E_h = 0$, the speciation is dominated by the free uranyl ion in the acidic pH range, by the first and second hydrolysis species, UO_2OH^+ and $(\text{UO}_2)_2(\text{OH})_2(\text{aq})$, in the circumneutral pH range (5 to 8) and by the third hydrolysis species $\text{UO}_2(\text{OH})_3^-$ above pH 8. Between $E_{h(\text{SHE})} = 0.1$ V and -0.1 V the pentavalent U species, UO_2^+ , dominates within a pH range of ~ 2 to 8, respectively. The borderline for U reduction lies slightly above $E_{h(\text{SHE})} = 0.1$ V at pH 2 to ~ 6 and continuously decreases afterwards to $E_{h(\text{SHE})} = \sim -0.45$ V at pH 12. Here, the amorphous tetravalent U species $\text{UO}_2(\text{am})$ prevails. Below pH 3 the dissolved U(IV) species, $\text{U}(\text{OH})^{3+}$, predominates in an $E_{h(\text{SHE})}$ range from ~ 0.05 V to below -0.5 V.

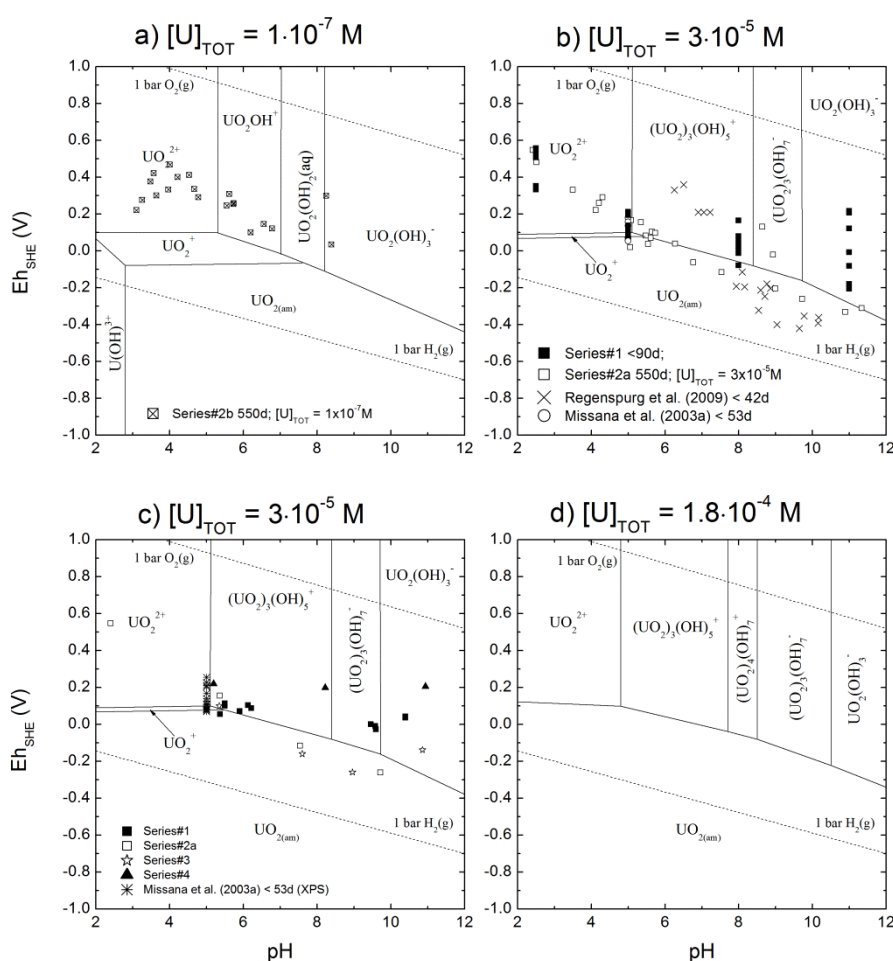


Figure 3.10: Predominance plots for the speciation of U calculated with the Hydra/Medusa code using NEA constants. a) $[\text{U}]_{\text{TOT}}: 1 \cdot 10^{-7}$ M. Additionally inserted are redox potentials obtained in this study. b) $[\text{U}]_{\text{TOT}}: 3 \cdot 10^{-5}$ M. Additionally inserted are redox potentials obtained in this study in comparison to literature data by Regenspurg et al. (2009) and Missana et al. (2003a). c) $[\text{U}]_{\text{TOT}}: 3 \cdot 10^{-5}$ M. Only samples measured by XPS are shown. d) $[\text{U}]_{\text{TOT}}: 1.8 \cdot 10^{-4}$ M as used in the experiments from Ilton et al. (2010).

Concerning thermodynamic calculations for Series#2a in Figure 3.10b, differences arise compared to the results of Series#2b. Generally speaking, polynuclear U species predominate due to the higher U concentrations applied. At acidic pH (2 to 5) above $E_{h(\text{SHE})} = 0.1$ V the free uranyl ion predominates followed by the polynuclear species $(\text{UO}_2)_3(\text{OH})_5^+$ from pH 5 to ~ 8 . Between pH ~ 8 and ~ 9.5 $(\text{UO}_2)_3(\text{OH})_7^-$ prevails. In contrast to the predominance diagram for $1 \cdot 10^{-7}$ M U concentration, the

pentavalent U species, UO_2^+ , dominates in a much smaller area between pH 2 and 5.5 for $E_{h(\text{SHE})}$ values within +0.1 V and $\sim +0.08$ V. Above pH ~ 9.5 the negatively charged third mononuclear hydrolysis species, $\text{UO}_2(\text{OH})_3^-$, becomes dominant. Between pH 2 to ~ 5 the borderline of U reduction is located at $E_{h(\text{SHE})} = \sim 0.09$ V and afterwards decreases to an $E_{h(\text{SHE})}$ of approximately -0.38 V at pH 12. Beneath the borderline, the amorphous U species, $\text{UO}_{2(\text{am})}$, dominates the speciation. At higher U concentration of $\sim 10^{-4}$ M (Figure 3.10d) as frequently used for spectroscopic investigations e.g. $1.8 \cdot 10^{-4}$ M (Ilton et al. 2010), $0.5 \cdot 10^{-4}$ M (O'Loughlin et al., 2010) or $1 \cdot 10^{-3}$ M (Vandenborre et al., 2007) thermodynamic calculations show the dominance of the polynuclear species $(\text{UO}_2)_4(\text{OH})_7^+$ at pH ~ 8 and the UO_2^+ field of pentavalent U diminishes. Though, it has to be stated, that U(V) species can still be present but to a minor fraction.

3.2.3.2.2 Redox Potential (Eh) Measurements

The aquatic chemistry of redox-sensible radionuclides like U is governed by the solution redox potential. Determination of the samples redox potential allows a more precise interpretation and analysis of the results. A literature review on the U-magnetite system revealed a substantial lack of experimentally determined redox potential data. This prevents not only a comparison between results presented by different authors for the same system studied but also hinders the interpretation of the results presented without thermodynamic calculations. It is therefore of utmost importance to conduct redox potential measurements, although it should be clearly stated that a systematical procedure for redox measurements is still not established in the literature (e.g. (Schüring, 2000)). Several authors dealt with the issue of redox potential determination both in synthetic and natural systems (see e.g. (Lindberg and Runnells, 1984; Grenthe et al., 1992) and references therein) concluding that severe uncertainties can sometimes be accompanied with redox potential measurements. Nonetheless, if the measurements are carried out in a consistent way they can at least be used in a qualitative way. The pH and Eh of the batch samples have been measured and compared to literature data using comparable synthesis protocols and U concentrations (Missana et al., 2003b; Regenspurg et al., 2009) (Figure 3.10b). Only the contact time of 550 d is considerably longer than in Regenspurg et al. (2009) (< 42 d) and Missana et al. (2003b) (< 53 d). For Series#1, between pH 2 to 4, the $E_{h(\text{SHE})}$ represent strongly oxidizing conditions with hexavalent U dominating the U speciation. Around pH 5 $E_{h(\text{SHE})}$ in this study and the data published by (Missana et al., 2003b) are comparable showing a range of +0.3 V down to +0.05 V. The values by Missana et al. (2003b) become lower with increasing contact time to a final value after 53 d of ~ 30 mV which is slightly lower than the values measured in this study. At this pH, $E_{h(\text{SHE})}$ continuously approach the calculated U(VI)/U(IV) borderline making U reduction thermodynamically feasible. At pH ~ 6 $E_{h(\text{SHE})}$ in this work are in the range of ~ 0.1 V which is ~ 0.2 V lower (more negative) than the data measured by Regenspurg et al. (2009), whereas in the neutral to slightly alkaline pH range both data sets show similar values in the range of $\sim +0.1$ V to ~ -0.1 V. In the alkaline pH regime from pH 8 to 10 our redox potentials measured for Series#2 are around -0.2 V which are slightly higher (more positive) compared to Regenspurg et al. (2009) with values down to -0.4 V. The $E_{h(\text{SHE})}$ for the short term kinetic experiments (Series#1) at pH ~ 5 and ~ 8 are more positive and subsequently decrease with time to redox conditions after 90 d comparable to values obtained in Series#2 and by Regenspurg et al. (2009). Again for Series#1, the same trend in the evolution of the $E_{h(\text{SHE})}$ can be observed for the samples at pH ~ 11 . This indicates that the $E_{h(\text{SHE})}$ values are a function of the contact time approaching after 90 d Eh conditions similar to the long term samples of Series#2. The $E_{h(\text{SHE})}$ values for maghemite (series#4 in Figure 3.10c) are independent of pH located in the range of $\sim +0.2$ V. Overall, the values obtained in this work and available literature data using comparable experimental conditions and similar magnetite phases fit satisfactorily well to each other regarding the uncertainties coupled to redox potential measurements as stated above.

3.2.3.3 Batch Experiment Results

In the next two chapters results for the batch experiment are presented. Firstly, the results of the short term kinetic studies (Series#1) and secondly, results for Series#2 (long term contact time / pH sorption edges) are presented. Both chapters only deal with the partly oxidized magnetite (po-mag).

3.2.3.3.1 Series#1 (Short Term (kinetic) studies)

In Figure 3.11a results of the kinetic batch experiments for U are depicted. Table 3.5 lists additional details about the results. All concentrations given represent mean values of the sample duplicates.

Regarding the samples at pH 2.5, U concentrations decrease slightly to $\sim 2.5 \cdot 10^{-5}$ M until 48 d and afterwards increase to a concentration of $\sim 3.17 \cdot 10^{-5}$ M after 90 d. The scatter in the data is referred to analytical uncertainties of the ICP-MS measurements. Moreover, precipitation of a U solid phase should not occur since the concentrations are below the solubility of e.g. schoepite for the pH conditions prevailing (Langmuir, 1978). A reduction to a tetravalent colloidal U phase cannot be excluded a priori (Neck and Kim, 2001) but is unlikely regarding the thermodynamic modeling results on basis of the measured redox potentials (+ 0.56 V).

Concerning the sample series at pH 5 a fast decrease in concentration of about one order of magnitude ($3.1 \cdot 10^{-6}$ M) is visible after 24 h. An ongoing decrease in U concentration is detectable until the end of the experiments with a final concentration after 90 d of $\sim 1.9 \cdot 10^{-7}$ M which is more than two orders of magnitude lower than the initial concentration. The scattering of the data at 6 d and 14 d is most probably related to slight fluctuations in pH and Eh. Regarding Eh/pH conditions given in Figure 3.10b the positively charged $(\text{UO}_2)_3(\text{OH})_5^+$ species and the amorphous tetravalent $\text{UO}_2(\text{am})$ species dominate at this pH, thus both sorption and/or reduction can be responsible for the U removal from solution. Moreover, regarding the solubility of hexavalent U, precipitation of a U containing mineral phase (U-oxide/hydroxide; Fe-U phase) like e.g. schoepite cannot be excluded which could as well explain the decrease in U concentration. On the other hand, the sample preparation procedure was chosen in a way to minimize precipitation. That is, after spiking of U to the suspension, the pH of the samples was around pH ~ 2.4 where no precipitation and only slight sorption should occur. Subsequently, pH was slowly adjusted by addition of small amounts of HCl and NaOH favoring sorption to the magnetite surface before a precipitation should occur. The fastest and most pronounced decrease in U concentration is observed for the pH 8 sample series. Here, after one day U concentration is almost 3 orders of magnitude lower ($\sim 5.2 \cdot 10^{-8}$ M) than the initial U concentration at the beginning of the experiments. In the course of the experiment a less pronounced decrease in U concentration is observed possibly indicating near equilibrium conditions after 90 d ($\sim 1.9 \cdot 10^{-8}$ M). Here, sorption of the hexavalent $(\text{UO}_2)_3(\text{OH})_5^+$ species to the negatively charged magnetite surface seems a reasonable explanation for the U removal. Moreover, besides a precipitation of a hexavalent U phase a reduction to the tetravalent $\text{UO}_2(\text{am})$ is thermodynamically feasible.

In case of the sample series at pH 11, an initial concentration decrease after 1 d of about 2 orders of magnitude ($\sim 2.1 \cdot 10^{-7}$ M) is measured which again is less pronounced in the further course of the experiment ($\sim 7.9 \cdot 10^{-8}$ M after 90 d) as it is the case for the series at pH 8. The calculated speciation for pH 11 yields the negatively charged $\text{UO}_2(\text{OH})_3^-$ species which may lead to a lesser pronounced sorption behaviour to the likewise negatively charged magnetite due to electrostatic effects. This circumstance may also explain the lower sorption compared to pH 8 where a positively charged U species prevails. In general, it can be stated that the processes responsible for the removal of the U

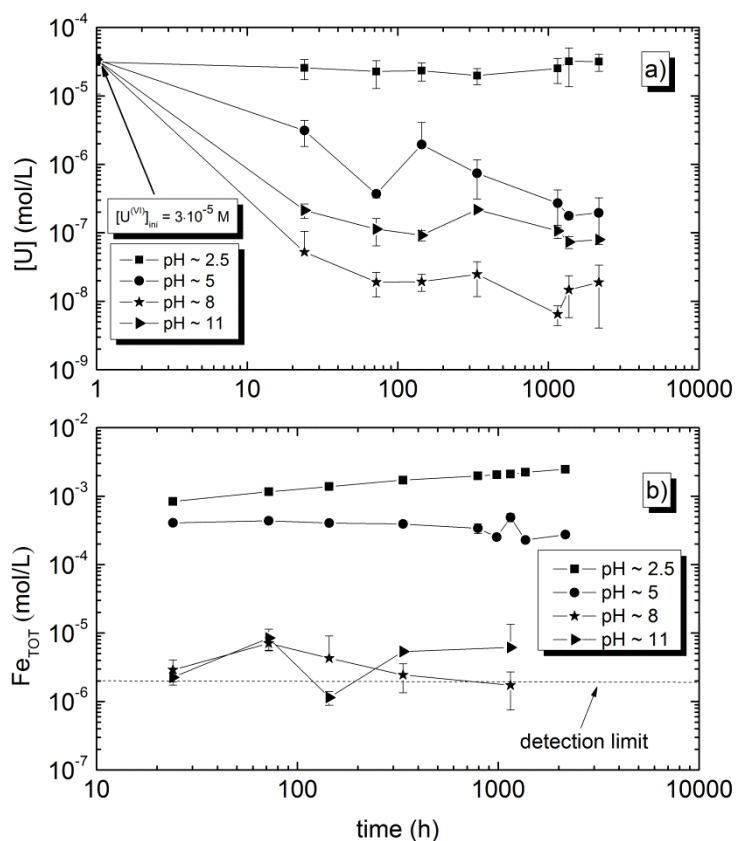


Figure 3.11: Results of the short term kinetic batch experiments using po-mag as solid phase. a) Aqueous U concentrations. The error bars for the sample series at pH 2.5 are in the order of the symbol size. b) Aqueous Fe_(TOT) concentrations.

from the solution (sorption, precipitation and/or reduction) show initially fast kinetics reaching near equilibrium conditions after 24 h. These results tally well to results presented by (Scott et al., 2005) for U interaction with natural magnetite single crystals at pH ~ 4.8 (U concentration = ~ 4·10⁻⁵ M and ~ 4.4·10⁻⁴ M) showing fast initial U removal (sorption) kinetics. Furthermore, the macroscopic batch kinetic results presented by Missana et al. (2003a) also show a U removal in the presence of magnetite of about 90 % after 1 d contact time for pH ~ 7 (U concentration = 4.4·10⁻⁷ M). Beside U, total iron concentrations have been determined in the Series#1 samples (Figure 3.11). At pH ~ 2.5 iron concentrations are in the range of 8.3·10⁻⁴ M after 24 h steadily increasing to 2.4·10⁻³ M at 90 d indicating a kinetically controlled magnetite dissolution. A slight time dependent decrease is observed for the samples at pH ~ 5.5. Here, the concentrations start at 4.1·10⁻⁴ M after 24 h and reach a final concentration of 2.7·10⁻⁴ M after 90 d showing slight fluctuations for the sample after 48 d. As expected, the total dissolved iron concentrations are much lower for the samples at pH ~ 8 and 11 following the known dissolution behaviour of magnetite which is more pronounced in the acidic pH range (see e.g. (Cornell and Schwertmann, 1996)). Measured total iron concentrations vary between 4.1·10⁻⁶ M and 1.1·10⁻⁶ M. This concentration range is near the detection limit of the ICP-MS

3 Influence of sorption and redox kinetics on radionuclide speciation

Table 3.5: Results of the short term kinetic batch experiments (Series#1).

Series #	Sample name	Contact time (d)	Ionic strength (M)	pH	Eh final (V)	U [initial] (M)	U [final] (M)	U removed (%)	Fe _{rot} [final] (M)	XPS/XAS
#1	po-mag#1	1	0.01	2.5	0.560	3·10 ⁻⁵	2.56·10 ⁻⁵	14.50	8.37·10 ⁻⁴	XPS
#1	po-mag#2	1	0.01	5	0.070	3·10 ⁻⁵	3.11·10 ⁻⁶	89.63	4.07·10 ⁻⁴	XPS
#1	po-mag#3	1	0.01	8	-0.028	3·10 ⁻⁵	5.25·10 ⁻⁸	99.83	2.90·10 ⁻⁶	XPS
#1	po-mag#4	1	0.01	11	-0.082	3·10 ⁻⁵	2.13·10 ⁻⁷	99.29	2.26·10 ⁻⁶	
#1	po-mag#5	3	0.01	2.5	0.533	3·10 ⁻⁵	2.27·10 ⁻⁵	24.06	1.16·10 ⁻³	
#1	po-mag#6	3	0.01	5	0.126	3·10 ⁻⁵	3.70·10 ⁻⁷	98.77	4.35·10 ⁻⁴	
#1	po-mag#7	3	0.01	8	0.029	3·10 ⁻⁵	1.91·10 ⁻⁸	99.94	7.09·10 ⁻⁶	
#1	po-mag#8	3	0.01	11	-0.181	3·10 ⁻⁵	1.13·10 ⁻⁷	99.62	8.49·10 ⁻⁶	
#1	po-mag#9	6	0.01	2.5	0.532	3·10 ⁻⁵	2.33·10 ⁻⁵	22.09	1.38·10 ⁻³	
#1	po-mag#10	6	0.01	5	0.106	3·10 ⁻⁵	1.94·10 ⁻⁶	93.52	4.06·10 ⁻⁴	
#1	po-mag#11	6	0.01	8	-0.014	3·10 ⁻⁵	1.93·10 ⁻⁸	99.94	4.28·10 ⁻⁶	
#1	po-mag#12	6	0.01	11	-0.206	3·10 ⁻⁵	9.20·10 ⁻⁸	99.69	1.15·10 ⁻⁶	
#1	po-mag#13	14	0.01	2.5	0.506	3·10 ⁻⁵	1.98·10 ⁻⁵	33.88	1.72·10 ⁻³	
#1	po-mag#14	14	0.01	5	0.111	3·10 ⁻⁵	7.39·10 ⁻⁷	97.54	3.92·10 ⁻⁴	
#1	po-mag#15	14	0.01	8	0.011	3·10 ⁻⁵	2.48·10 ⁻⁸	99.92	2.45·10 ⁻⁶	
#1	po-mag#16	14	0.01	11	0.216	3·10 ⁻⁵	1.09·10 ⁻⁷	99.64	8.48·10 ⁻⁴	
#1	po-mag#17	48	0.01	2.5	0.331	3·10 ⁻⁵	2.52·10 ⁻⁵	16.09	2.10·10 ⁻³	
#1	po-mag#18	48	0.01	5	0.085	3·10 ⁻⁵	2.72·10 ⁻⁷	99.09	4.88·10 ⁻⁴	
#1	po-mag#19	48	0.01	8	-0.079	3·10 ⁻⁵	6.50·10 ⁻⁹	99.98	1.73·10 ⁻⁶	
#1	po-mag#20	48	0.01	11	0.121	3·10 ⁻⁵	1.06·10 ⁻⁷	99.65	6.15·10 ⁻⁶	
#1	po-mag#21	57	0.01	2.5	0.349	3·10 ⁻⁵	3.18·10 ⁻⁵	0.00	2.23·10 ⁻³	
#1	po-mag#22	57	0.01	5	0.193	3·10 ⁻⁵	1.77·10 ⁻⁷	99.41	2.29·10 ⁻⁴	
#1	po-mag#23	57	0.01	8	0.049	3·10 ⁻⁵	1.47·10 ⁻⁸	99.95	< d.l.	
#1	po-mag#24	57	0.01	11	0.206	3·10 ⁻⁵	7.35·10 ⁻⁸	99.76	< d.l.	
#1	po-mag#25	90	0.01	2.5	0.352	3·10 ⁻⁵	3.17·10 ⁻⁵	0.00	2.47·10 ⁻³	
#1	po-mag#26	90	0.01	5	0.211	3·10 ⁻⁵	1.95·10 ⁻⁷	99.35	2.74·10 ⁻⁴	
#1	po-mag#27	90	0.01	8	0.078	3·10 ⁻⁵	1.89·10 ⁻⁸	99.94	< d.l.	
#1	po-mag#28	90	0.01	11	-0.009	3·10 ⁻⁵	7.98·10 ⁻⁸	99.73	< d.l.	
#1	po-mag#29	1	0.01	5.5	0.070	3·10 ⁻⁵	2.27·10 ⁻⁶	92.43	< d.l.	XPS
#1	po-mag#30	1	0.01	9.58	-0.028	3·10 ⁻⁵	3.76·10 ⁻⁶	87.45	< d.l.	XPS
#1	po-mag#31	1	0.01	5.37	0.112	3·10 ⁻⁵	n.m.	-	n.m.	XPS
#1	po-mag#32	1	0.01	9.46	-0.01	3·10 ⁻⁵	n.m.	-	n.m.	XPS
#1	po-mag#33	1	0.01	6.13	0.054	3·10 ⁻⁵	n.m.	-	n.m.	XPS
#1	po-mag#34	1	0.01	6.22	-0.001	3·10 ⁻⁵	n.m.	-	n.m.	XPS
#1	po-mag#35	1	0.01	10.4	-0.044	3·10 ⁻⁵	n.m.	-	n.m.	XPS
#1	po-mag#36	1	0.01	5.5	0.099	3·10 ⁻⁵	n.m.	-	n.m.	XPS
#1	po-mag#37	1	0.01	10.4	0.035	3·10 ⁻⁵	n.m.	-	n.m.	XPS

< d.l. = below detection limit; n.m. = not measured

($\sim 2 \cdot 10^{-6}$ M), thus considerable uncertainties are accompanied to these values. After 90 d, the total dissolved Fe concentrations are below the ICP-MS detection limit.

3.2.3.3.2 Series#2 (Long Term Studies)

In Figure 3.12a the effect of pH and total U concentration ($3 \cdot 10^{-5}$ M and $1 \cdot 10^{-7}$ M) on the interaction of U with a partly oxidized magnetite (po-mag) is depicted for a contact time of 550 days. Table 3.6 provides additional details concerning the experimental results. The pH adsorption edges are located in a narrow range within one to two pH units in case of Series#2b and Series#2a. No difference is visible in terms of the steepness of the adsorption edges. Regarding Series#2a, only a very slightly removal ($< 5\%$) of U can be detected below pH ~ 4 . At pH ~ 4 the sorption starts to increase and rises sharply to $\sim 100\%$ within one and a half pH unit. Above pH 5.5 the sorption remains at 100% until pH 11 which corroborates the absence of carbonate ions in solution which would weaken the sorption of U due to strong aqueous complexes.

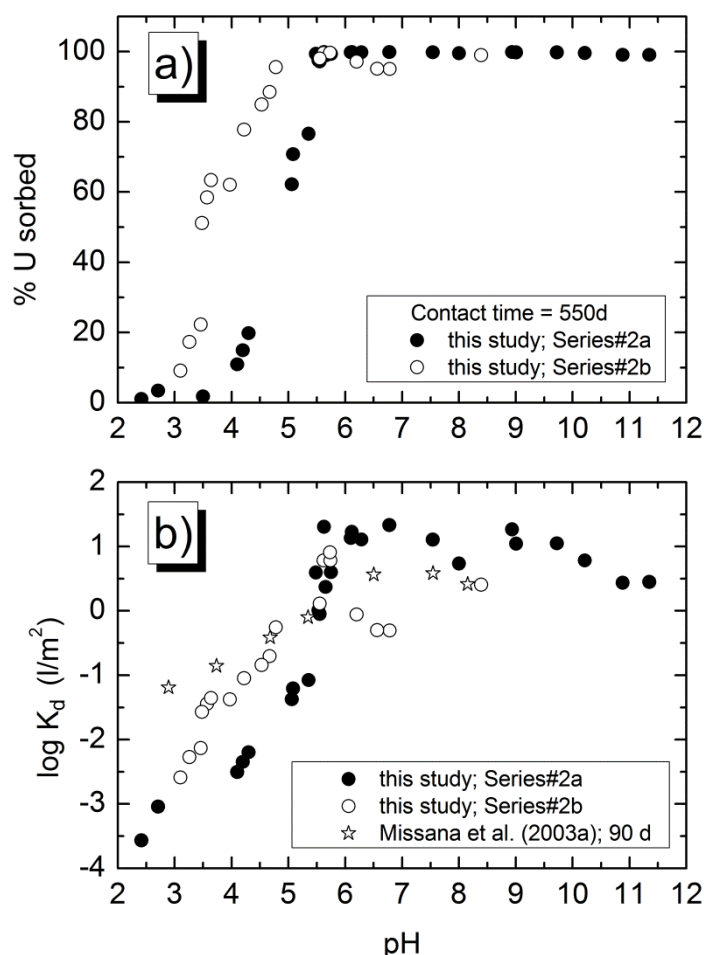


Figure 3.12: a) U pH edges (550 d contact time) of Series#2a ($3 \cdot 10^{-5}$ M U) and Series#2b ($1 \cdot 10^{-7}$ M U). b) Surface normalized log K_d values of Series#2a and Series#2b in comparison to literature data from Missana et al. (2003a). Regarding the aqueous concentrations applied, they used slightly higher amounts of U ($4.4 \cdot 10^{-7}$ M) as our lower concentration series.

Concerning the pH sorption edge for Series#2b ($3 \cdot 10^{-5}$ M U) showed in comparison to Series#2a, an edge shift to lower pH values is observed. This is a common observation in metal ion adsorption studies onto mineral phases (see e.g. (Dzombak and Morel, 1990; Appelo and Postma, 1996; Stumm and Morgan, 1996)). The sorption starts at \sim pH 3 and rises sharply to $\sim 100\%$ at pH 4. The sorption

remains at ~ 100 % until pH 8.4 in line with the results obtained for Series#2a and Series#1 further corroborating the absence of carbonate species as stated above.

Comparison between the batch results obtained in this study and work published by Missana et al. (2003a,b) with a contact time of 3 months using similar experimental conditions (same magnetite synthesis and solid to liquid ratio ($2 \text{ g}\cdot\text{L}^{-1}$), comparable ionic strengths and absence of CO_2) is presented in Figure 3.12b. For a consistent way of comparison, all data is shown as surface normalized distribution coefficient K_d ($\text{L}\cdot\text{m}^{-2}$) which can be expressed as:

$$K_d = \frac{\Gamma_U}{[U]_{aq}} = \frac{([U]_{TOT} - [U]_{aq})}{[U]_{aq}} / \phi m$$

where K_d is the distribution coefficient ($\text{L}\cdot\text{m}^{-2}$), Γ_U is the U concentration on the surface ($\text{mol}\cdot\text{m}^{-2}$), $[U]_{aq}$ is the dissolved U concentration ($\text{mol}\cdot\text{L}^{-1}$), $[U]_{TOT}$ is the total U concentration ($\text{mol}\cdot\text{L}^{-1}$), ϕ is the surface excess ($\text{m}^2\cdot\text{g}^{-1}$) and m is the solid phase concentration ($\text{g}\cdot\text{L}^{-1}$). One has to keep in mind that the distribution coefficient close to 100 % sorption is accompanied with a high uncertainty due to low U concentrations in solution. Furthermore, if the solution concentration is high (low pH conditions) the importance of the relative error increases (difference between two big numbers). The K_d values obtained in this study range from ~ -3.5 up to ~ 1.5. Scattering of about 1 K_d unit arises for the samples showing ~ 100 % sorption as mentioned above. Overall, the values by Missana et al. (2003a) coincide to our data. The K_d range covered (~ -1 up to ~ 0.5) is smaller compared to the samples obtained in this study. This discrepancy is visible in the pH range < 3. The data by Missana et al. (2003a) show a much higher K_d value (~ -1) corresponding to a decrease in U solution concentration between 50 to 70 % which is not the case for data obtained in our study (K_d ~ -3.5 to -2.5). The explanation for this observation given by (Missana et al., 2003a) is attributed to a reduction of hexavalent U to tetravalent U based on thermodynamic calculations. A predominance diagram for U (including the pentavalent U species UO_2^+) is depicted in Figure 2a which shows that reduction to $\text{UO}_{2(am)}$ is thermodynamic feasible at pH 3-4 for Eh values below ~ -0.09 V. However, no experimentally determined Eh values are given by Missana and co-workers for the samples at respective pH values which could corroborate their explanation and facilitate a direct comparison to our measured redox potentials. Nonetheless, in our study such low redox values were not measured in this pH range and therefore the calculated K_d values are in line with the thermodynamic calculations predicting U(VI) species under these conditions (Figure 3.10b, Table 3.4 and Table 3.5).

3.2.3.4 Spectroscopic Results

Since no conclusion about the U removal mechanism can be drawn solely on basis of the macroscopic batch results, spectroscopic measurements (XPS and XAS) are applied to reveal if sorption, reduction and/or precipitation are the mechanisms responsible for the decrease in aqueous U concentration. Both techniques are able to determine the valence state of U at the magnetite surface.

An important disadvantage of spectroscopic techniques is the need for sufficient high concentrations to obtain reliable measurements. Therefore, often significantly higher total concentrations are applied in XAS and/or XPS measurements as in the corresponding batch experiments hindering the comparison of batch data results to spectroscopic findings. It is questionable if the conclusion drawn for the conditions of the batch experiments can be transferred to the conditions of the samples

3 Influence of sorption and redox kinetics on radionuclide speciation

Table 3.6: Results of the long term batch experiments (Series#2) and the batch samples of Series#3 (fmag) and Series#4 (magh).

Series #	Sample name	Contact time (d)	Ionic strength (M)	pH	Eh (V)	U [initial] (M)	U [final] (M)	U removed (%)	Fe _{tot} (M)	XPS/XAS
#2a	po-mag#38	550	0.01	5.08	0.166	3·10 ⁻⁵	8.76·10 ⁻⁶	70.8	2.49·10 ⁻³	XPS
#2a	po-mag#39	550	0.01	5.35	0.155	3·10 ⁻⁵	7.02·10 ⁻⁶	76.6	1.29·10 ⁻³	XPS
#2a	po-mag#40	550	0.01	5.62	0.069	3·10 ⁻⁵	3.79·10 ⁻⁶	99.9	2.01·10 ⁻⁴	XPS
#2a	po-mag#41	550	0.01	5.65	0.103	3·10 ⁻⁵	3.23·10 ⁻⁷	98.9	2.22·10 ⁻⁴	XAS
#2a	po-mag#42	550	0.01	5.74	0.096	3·10 ⁻⁵	1.92·10 ⁻⁷	99.4	1.05·10 ⁻⁴	XAS
#2a	po-mag#43	550	0.01	6.28	0.038	3·10 ⁻⁵	5.98·10 ⁻⁸	99.8	1.06·10 ⁻⁵	XPS
#2a	po-mag#44	550	0.01	9.00	-0.205	3·10 ⁻⁵	6.95·10 ⁻⁸	99.8	< d.l.	XPS
#2a	po-mag#45	550	0.01	9.72	-0.262	3·10 ⁻⁵	6.87·10 ⁻⁸	99.8	1.46·10 ⁻⁵	XPS
#2a	po-mag#46	550	0.01	10.89	-0.332	3·10 ⁻⁵	2.79·10 ⁻⁷	99.1	< d.l.	XPS
#2a	po-mag#47	550	0.01	5.54	0.037	3·10 ⁻⁵	8.38·10 ⁻⁷	97.2	4.46·10 ⁻⁴	XPS
#2a	po-mag#48	550	0.01	6.77	-0.064	3·10 ⁻⁵	3.56·10 ⁻⁸	99.9	< d.l.	XPS
#2a	po-mag#49	550	0.01	7.54	-0.116	3·10 ⁻⁵	6.02·10 ⁻⁸	99.8	< d.l.	XPS
#2a	po-mag#50	550	0.01	11.34	-0.312	3·10 ⁻⁵	2.71·10 ⁻⁷	99.1	< d.l.	XPS
#2a	po-mag#51	550	0.01	2.41	0.546	3·10 ⁻⁵	2.97·10 ⁻⁵	1	1.45·10 ⁻³	XPS
#2a	po-mag#52	550	0.01	5.06	0.0189	3·10 ⁻⁵	1.13·10 ⁻⁵	62.2	3.13·10 ⁻³	XPS
#2a	po-mag#53	550	0.01	8.93	-0.021	3·10 ⁻⁵	4.17·10 ⁻⁸	99.9	< d.l.	XPS
#2a	po-mag#54	550	0.01	5.48	0.082	3·10 ⁻⁵	1.94·10 ⁻⁷	99.4	1.86·10 ⁻⁴	XPS
#2a	po-mag#55	550	0.01	8.64	0.131	3·10 ⁻⁵	4.03·10 ⁻¹⁰	99.9	3.77·10 ⁻⁴	XPS
#2a	po-mag#56	550	0.01	2.52	0.481	3·10 ⁻⁵	3.11·10 ⁻⁵	0	4.63·10 ⁻⁴	XPS
#2a	po-mag#57	550	0.01	4.12	0.22	3·10 ⁻⁵	2.67·10 ⁻⁵	10.8	5.77·10 ⁻⁴	XPS
#2a	po-mag#58	550	0.01	4.31	0.29	3·10 ⁻⁵	2.40·10 ⁻⁵	19.8	4.21·10 ⁻⁴	XPS
#2a	po-mag#59	550	0.01	4.21	0.26	3·10 ⁻⁵	2.55·10 ⁻⁵	14.9	4.64·10 ⁻⁴	XPS
#2a	po-mag#60	550	0.01	3.50	0.33	3·10 ⁻⁵	2.95·10 ⁻⁵	1.79	4.35·10 ⁻⁴	XPS
#2b	po-mag#61	550	0.01	4.01	0.468	1·10 ⁻⁷	7.88·10 ⁻¹⁰	99.2	2.43·10 ⁻⁴	XPS
#2b	po-mag#62	550	0.01	5.62	0.308	1·10 ⁻⁷	4.20·10 ⁻¹⁰	99.6	1.40·10 ⁻⁴	XPS
#2b	po-mag#63	550	0.01	5.74	0.258	1·10 ⁻⁷	4.20·10 ⁻¹⁰	99.6	1.42·10 ⁻⁴	XPS
#2b	po-mag#64	550	0.01	5.73	0.253	1·10 ⁻⁷	3.15·10 ⁻¹⁰	99.7	1.44·10 ⁻⁴	XPS
#2b	po-mag#65	550	0.01	5.55	0.245	1·10 ⁻⁷	1.94·10 ⁻⁹	98.1	6.96·10 ⁻⁵	XPS
#2b	po-mag#66	550	0.01	8.25	0.298	1·10 ⁻⁷	5.23·10 ⁻⁸	47.7	3.38·10 ⁻⁵	XPS
#2b	po-mag#67	550	0.01	3.10	0.220	1·10 ⁻⁷	9.09·10 ⁻⁸	9.14	2.26·10 ⁻⁴	XPS
#2b	po-mag#68	550	0.01	3.26	0.276	1·10 ⁻⁷	8.27·10 ⁻⁸	17.3	1.86·10 ⁻⁴	XPS
#2b	po-mag#69	550	0.01	3.97	0.332	1·10 ⁻⁷	3.79·10 ⁻⁸	62.1	1.32·10 ⁻⁴	XPS
#2b	po-mag#70	550	0.01	4.78	0.290	1·10 ⁻⁷	4.41·10 ⁻⁹	95.6	6.59·10 ⁻⁵	XPS
#2b	po-mag#71	550	0.01	4.67	0.335	1·10 ⁻⁷	1.15·10 ⁻⁸	88.5	6.18·10 ⁻⁵	XPS
#2b	po-mag#72	550	0.01	4.53	0.411	1·10 ⁻⁷	2.22·10 ⁻⁸	77.8	6.99·10 ⁻⁵	XPS
#2b	po-mag#73	550	0.01	4.22	0.399	1·10 ⁻⁷	4.9·10 ⁻⁹	95.1	9.32·10 ⁻⁵	XPS
#2b	po-mag#74	550	0.01	6.78	0.120	1·10 ⁻⁷	4.9·10 ⁻⁹	95.1	3.32·10 ⁻⁵	XPS
#2b	po-mag#75	550	0.01	6.56	0.145	1·10 ⁻⁷	1.0·10 ⁻⁹	99.0	3.31·10 ⁻⁵	XPS
#2b	po-mag#76	550	0.01	8.39	0.034	1·10 ⁻⁷	2.8·10 ⁻⁹	97.2	3.14·10 ⁻⁵	XPS
#2b	po-mag#77	550	0.01	6.20	0.099	1·10 ⁻⁷	4.15·10 ⁻⁸	58.5	3.30·10 ⁻⁵	XPS
#2b	po-mag#78	550	0.01	3.57	0.421	1·10 ⁻⁷	4.88·10 ⁻⁸	51.2	2.18·10 ⁻⁴	XPS
#2b	po-mag#79	550	0.01	3.48	0.376	1·10 ⁻⁷	3.66·10 ⁻⁸	63.4	2.29·10 ⁻⁴	XPS
#2b	po-mag#80	550	0.01	3.64	0.299	1·10 ⁻⁷	2.22·10 ⁻⁸	77.8	2.06·10 ⁻⁴	XPS
#3	fmag#1	13	0.01	7.6	-0.160	3·10 ⁻⁵	3.63·10 ⁻⁹	99.9	1.04·10 ⁻⁴	XPS
#3	fmag#2	13	0.01	10.86	-0.139	3·10 ⁻⁵	2.04·10 ⁻⁸	99.9	< d.l.	XPS
#3	fmag#3	13	0.01	5.35	0.099	3·10 ⁻⁵	9.50·10 ⁻⁶	96.8	1.05·10 ⁻³	XPS
#4	mgH#1	13	0.01	10.94	0.205	3·10 ⁻⁵	6.83·10 ⁻⁸	99.9	< d.l.	XPS
#4	mgH#2	13	0.01	8.22	0.198	3·10 ⁻⁵	2.01·10 ⁻⁹	99.9	< d.l.	XPS
#4	mgH#3	13	0.01	5.19	0.219	3·10 ⁻⁵	2.52·10 ⁻⁶	91.6	< d.l.	XPS

measured by XPS/XAS and vice versa, since e.g. (i) the aqueous equilibrium speciation depends on the total metal concentration, (ii) the borderline of U reduction is a function of the total U concentration and (iii) the precipitation of a U phase is very likely for higher U concentrations at higher pH (> pH 6). Compared to the used approach above frequently found in the literature, here the attempt was made to perform the spectroscopic studies under the same conditions as the macroscopic batch experiments.

3.2.3.4.1 XPS

3.2.3.4.1.1 Fe(II) speciation

Selected samples were analyzed to determine the Fe(II)/Fe_{TOT} ratios. Since Fe(II) is the only potential redox agent for U reduction present in the experiments, this information is crucial concerning their redox capacity. Several approaches determining the Fe(II) portion by XPS in iron oxides and compounds are reported. Examples are curve fits to Fe 3p spectra with functions assigned to Fe(II) and Fe(III) (McIntyre and Zetaruk, 1977; Raeburn et al., 1997a; Raeburn et al., 1997b; Aronniemi et al., 2005; Yamashita and Hayes, 2006; Yamashita and Hayes, 2008). However, Fe 3p spectra are less intense and more bulk sensitive than the Fe 2p main lines. Fitted calculated multiplet peaks to Fe 2p_{3/2} spectra of known Fe compounds were reported by (Grosvenor et al., 2004). If 2p spectra of Fe(II) and Fe(III) are used for evaluation of the Fe(II) portion, the result depends on the background function applied (Aronniemi et al., 2005).

In this work, the Fe 2p spectra are measured to estimate Fe(II)/Fe_{TOT} ratios on the mineral surfaces. More precisely, the intensity of the shoulder on lower binding energy side at the Fe 2p_{3/2} elemental line is representative for the amount of Fe(II) present. The intensity of the shoulder is determined within a band of 708.5 eV to 708.7 eV binding energy and set into relation to spectra of a freshly prepared magnetite and a hematite powder (Fe₂O₃ puratronic, Alfa Aesar) by use of normalized spectra (Figure 3.13a). Error in Fe(II) portion determination in this way is estimated to be about ± 5 %.

Table 3.7 lists the corresponding Fe(II)/Fe_{TOT} ratios after reaction with U for the samples measured. The Fe(II)/Fe_{TOT} ratio of the po-mag samples range between 10.9 % to 27.3 % with a mean value of 22 %, while the fmag samples range between 24.8 % to 33.2% with a mean value of 30.1 %. The mgh samples show values of only 0-2 % Fe(II)/Fe_{TOT} on the surface which is in the range of the analytical uncertainty. These results confirm a partly oxidization of the po-mag with roughly 30 % lower Fe(II) content than the fmag samples. In addition, the amount of Fe(II)/Fe_{TOT} is clearly a function of pH reflecting the preferential dissolution of Fe(II) out of the magnetite structure at low pH, since the amount of Fe(II)/Fe_{TOT} increases with increasing pH (Jolivet and Tronc, 1988; White et al., 1994). This trend follows the general curve of magnetite dissolution which is more pronounced in the acidic pH range. If U reduction occurs, an increase in Fe(III) (corresponding to a decrease in the Fe(II)/Fe_{TOT} ratio) should occur due to Fe(II) oxidization and the shoulder in the Fe 2p_{3/2} spectra should become less pronounced. However, the changes on the surface of the solid phases expected based on the U concentrations used before and after reaction are too small to be resolved by the analytical technique.

3.2.3.4.1.2 U speciation

The U 4f_{7/2} elemental line was used to determine the redox state of U in the selected batch samples of all three different series. Concerning different U valence states, a chemical shift is observed. A

separation between the bands for U(VI) to U(V) and U(V) to U(IV) is reported in the literature with values of 0.9 eV (Bera et al., 1998) and 0.6 eV (Schindler et al., 2009), respectively. Schindler et al. (2009) conducted XPS measurements using various U containing mineral phases and reported binding ranges for the different valence states as follows: U(VI) within 381.1 – 382.6 eV, U(V) within 380.5 – 381.2 eV and U(IV) within 380.2 – 380.7 eV, respectively. The range of values reflect the fact,

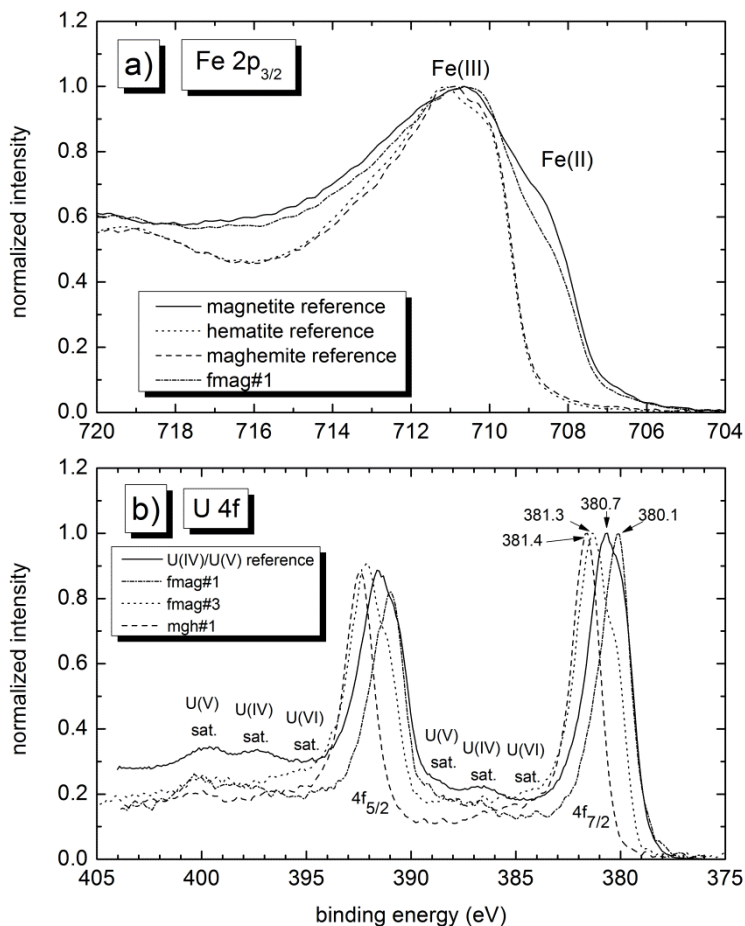


Figure 3.13: a) XPS $Fe\ 2p_{3/2}$ spectra for the magnetite reference, sample fmag#3, hematite reference and maghemite reference showing the amount of Fe(II) and Fe(III). B) XPS U 4f spectra of the UO_x -Pd film with U(IV,V), fmag#1 and fmag#3 samples. Additionally, the peak position of U(VI), U(V) and U(IV) are indicated in conjunction with their corresponding satellites of the U 4f peaks.

that the binding energies vary (chemical shift) as a function of compound chemical composition, crystal structure and type and number of nearest-neighbour ions. The binding energy ranges determined in the present study are for U(VI) and U(IV) 381.1 – 381.7 eV and 380.1 - 380.6 eV, respectively. In addition to the U 4f main peaks, small satellite peaks at higher binding energies are sometimes used for spectral interpretation (Keller and Jorgensen, 1975), (Ilton et al., 2010). These satellites are positioned (towards higher binding energies of the U 4f peaks) at 6-7 eV for U(IV), 7.8-8.5 eV for U(V) and 4 and 10 eV for U(VI), respectively. The shape of the U $4f_{7/2}$ peak and satellites are used for determination of the different valence states (Schindler et al., 2009). However, in the present work these satellite peaks are of low intensity due to low surface concentrations of U. That is, if the signal to noise ratio is low the intensities of the satellite peaks are within noise level and not resolved.

As a “reference” for U(IV) and U(V), we measured U 4f spectra of an oxidized UO_2 -Pd thin film vapour-deposited onto a semiconducting silicon wafer and stored in air (received from Institute of Transuranium Elements, JRC-ITU, Karlsruhe). The $4f_{7/2}$ spectrum consists of two main components

with binding energies at 379.9 eV, assigned to U(IV) and 380.9 eV assigned to U(V). Two satellites of the 4f spectrum are observed, one satellite with spacing of 6.5 eV to the 4f main lines assigned to U(IV) and a second satellite with spacing of 8.1 eV to the 4f main lines of U(V). Binding energies of $4f_{7/2}$ elemental lines and satellites spacings coincide with reported values (Ilton et al., 2010 in case of U(V); (Ilton et al., 2007) reports U(IV) satellites spacing between 6.3 to 6.8 eV) and thus confirm the appropriate assignments to the 4f main components concerning U valence in our study (Figure 3.13b). Satellites characteristic for U(VI) oxides are not detected in the $\text{UO}_2\text{-Pd}$ sample although U(VI) cannot be excluded to be present at low concentration on the outermost surface, since a curve fit to the U $4f_{7/2}$ spectrum indicates less than 8 % of U is U(VI). In case of U(VI), a binding energy of 381.4 eV was determined on basis of the sample magh#1 (maghemite; pH 10.94;) which showed only U(VI) on the mineral surface (Figure 3.14).

To estimate the amounts of the U valence states of U reacted magnetite, U $4f_{7/2}$ spectra are curve fitted by Gaussian-Lorentzian sum functions with same Gaussian fractions and FWHM. In contrast to reported values of 0.8 eV and 1.04 eV between U(IV) - U(V) and U(V) - U(VI), respectively (best fit derived from a single crystal annite; (Ilton et al., 2005)), in this study, curve fits yield spacing of about 1.1 eV for U(IV) - U(VI). One should keep in mind that U 4f spectra give no further insight how U interacts at the chosen U concentrations on the molecular scale with the magnetite surface.

Series#1 (po-mag; $\leq 90\text{d}$ contact time). In total 11 different batch samples have been measured after a contact time of 1 d (Figure 3.15a and Table 3.7). Two samples of Series#1 (po-mag#2 and po-mag#3) and additionally 9 samples (po-mag#29 to po-mag#37) using the same experimental conditions within a pH range of ~ 5 to ~ 10.5 to verify and gain confidence in the obtained results. The $\text{Fe(II)}/\text{Fe}_{\text{TOT}}$ ratios of all samples are located in the range between 21 % up to 27.3 %. For low $\text{Fe(II)}/\text{Fe}_{\text{TOT}}$ amounts (21 % to ~ 23 %), the U speciation determined by XPS is dominated by U(VI) with ~ 65 - 90 % and only about 10 % - 35% for U(IV). With increasing Fe(II) (up to 25 %), the amount of U(VI) decreases to ~ 50 % to 60 % and the amount of U(IV) increases to ~ 40 % - 45 %. Consequently, the sample with the highest $\text{Fe(II)}/\text{Fe}_{\text{TOT}}$ ratio (27.3 %) shows the highest amount of U(IV) (~ 52 %) and 48 % of U(VI). To sum up, Series#1 indicates that the reduction of U can be correlated to the available $\text{Fe(II)}/\text{Fe}_{\text{TOT}}$ ratio on the magnetite surface leading to an increase in U(IV) with rising $\text{Fe(II)}/\text{Fe}_{\text{TOT}}$ ratio.

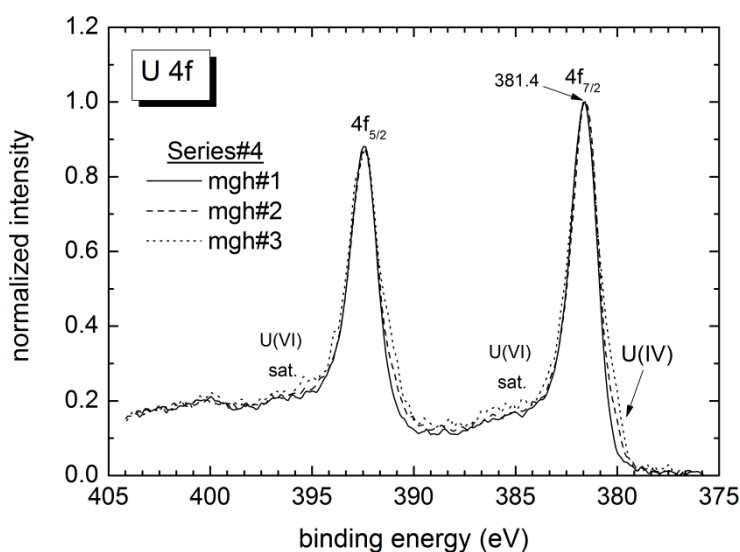


Figure 3.14: XPS U 4f spectra for Series#4 samples (maghemite; 13 d contact time) showing small portions of U(IV) in case of magh#2 and magh#3.

Series#2a (po-mag; 550 d contact time). XPS analyses of the long term samples have been conducted in comparison to the short-term kinetic XPS results to elucidate the effect of contact time on the U reduction. Results are shown in Figure 3.15b and Table 3.7. Four samples have been selected for XPS measurement at pH 2.5, 5.3, 7.5 and 9.7. The sample at pH ~ 2.5 revealed no U on the magnetite surface indicating that no sorption or precipitation occurred which is in accordance to the macroscopic results of the pH sorption edge and the batch kinetic experiments. This interpretation is furthermore corroborated by the measured redox potential (Eh = + 0.546 V) of the sample predicting no reduction as can be seen in the predominance diagram (Figure 3.10b and Figure 3.10c). This sample shows the lowest Fe(II)/Fe_{TOT} ratio of all samples analyzed (10.9 %) which can be explained both by the magnetite dissolution and the preferential dissolution of Fe(II) (White et al., 1994). This explanation may also hold in case of the other three samples measured since the Fe(II) content is considerably lower compared to Serie#1 ranging from only 17.3 % up to 20.2 %. Concerning the U speciation, differences arise compared to the results of Series#1. Here, the amount of U(IV) is clearly higher than for Series#1 ranging between 42 % up to 55 % and in case of U(VI) between 41.3 % up to 52.7 % despite the lower Fe(II)/Fe_{TOT} ratio. This deviation to Series#1 may be explained by the considerably longer contact time of Series#2 indicating that a fast partial U reduction to U(IV) occurs within the first day followed by a subsequent more slowly reduction kinetic with time. The fact that the hexavalent U is not quantitatively reduced to U(IV) after 550 d may again be referred to the lower Fe(II)/Fe_{TOT} ratio.

Table 3.7: Overview of all samples measured by XPS.

Series	sample name	contact time (d)	pH (-)	Eh (V)	Fe(II)/Fe _{TOT} (-)	U(IV) (%)	U(VI) (%)
#1	po-mag#2	1	5.9	0.07	25.4	43	57
#1	po-mag#3	1	9.6	-0.028	23.9	35	65
#1	po-mag#29	1	5.5	0.112	23.5	29	71
#1	po-mag#30	1	9.58	-0.01	22.9	19	81
#1	po-mag#31	1	5.37	0.054	23.1	30	70
#1	po-mag#32	1	9.46	-0.001	22.9	20	80
#1	po-mag#33	1	6.13	0.102	27.3	52	48
#1	po-mag#34	1	6.22	0.088	25	46	54
#1	po-mag#35	1	10.4	0.041	23.2	34	66
#1	po-mag#36	1	5.5	0.099	21	18	82
#1	Po-mag#37	1	10.4	0.035	21.5	11	89
#2a	po-mag#39	550	5.35	0.155	17.3	42	41
#2a	po-mag#45	550	9.72	-0.262	22	47	53
#2a	po-mag#49	550	7.54	-116.8	20.2	55	45
#2a	po-mag#51	550	2.41	546.4	10.9	0	0
#3	fmag#1	13	7.6	32.6	29	76	24
#3	fmag#2	13	10.86	48.1	33.2	78	22
#3	fmag#3	13	5.35	152.4	24.8	37	63
#4	magh#1	13	10.94	204.7	0	100	0
#4	magh#2	13	8.22	197.7	0	92	8
#4	magh#3	13	5.19	218.7	2	82	18

Series#3 (fmag; 13 d contact time). Three samples at pH ~ 5.3, ~ 7.6 and ~ 10.9 have been analyzed after a contact time of 13 days (Figure 3.15b and Table 3.7). The fmag#3 sample has a considerable lower Fe(II)/Fe_{TOT} ratio (24.8 %) as the fmag#1 and fmag#2 sample with ratios of 29 %

and 33.2 %, respectively. In consequence, the fmag#3 sample has the lowest U(IV) content (37%) compared to the fmag#1 and fmag#2 samples with ~ 76 % and ~ 78 %, respectively. Again, these findings further corroborate the trend that with increasing Fe(II)/Fe_{TOT} ratio the amount of U(IV) increases and in turn, the amount of U(VI) decreases as it has been observed in Series#1 and Series#2a.

Series#4 (magh). Identically to Series#3, three maghemite reacted uranium samples have been probed by XPS after a contact time of 13 d to determine both the Fe(II) content and the U speciation. The ratio of Fe(II)/Fe_{TOT} for all three samples is below ~ 2 % within the analytical uncertainty. The U 4f spectra for all maghemite samples are depicted in Figure 3.14. It can be seen that the magh#1 sample shows only U(VI) whereas for magh#2 and magh#3 about 4 and 8% U(IV) are measurable, respectively. A correlation of the amount of U(IV) on the maghemite surface with pH is obvious with decreasing U(IV) for increasing pH. This may indicate that a pronounced dissolution of maghemite at more acidic pH (magh#3 at pH 5.3) releases bulk Fe(II) which has not been fully oxidized in the synthesis step. This Fe(II) may become available for the sorbed U(VI) leading to a reduction of U(VI) to U(IV). Following this line of explanation, maghemite is more stable at higher pH (Cornell and Schwertmann, 1996) explaining the absence of Fe(II) at pH 10.94 (magh#3) where no U(IV) has been observed.

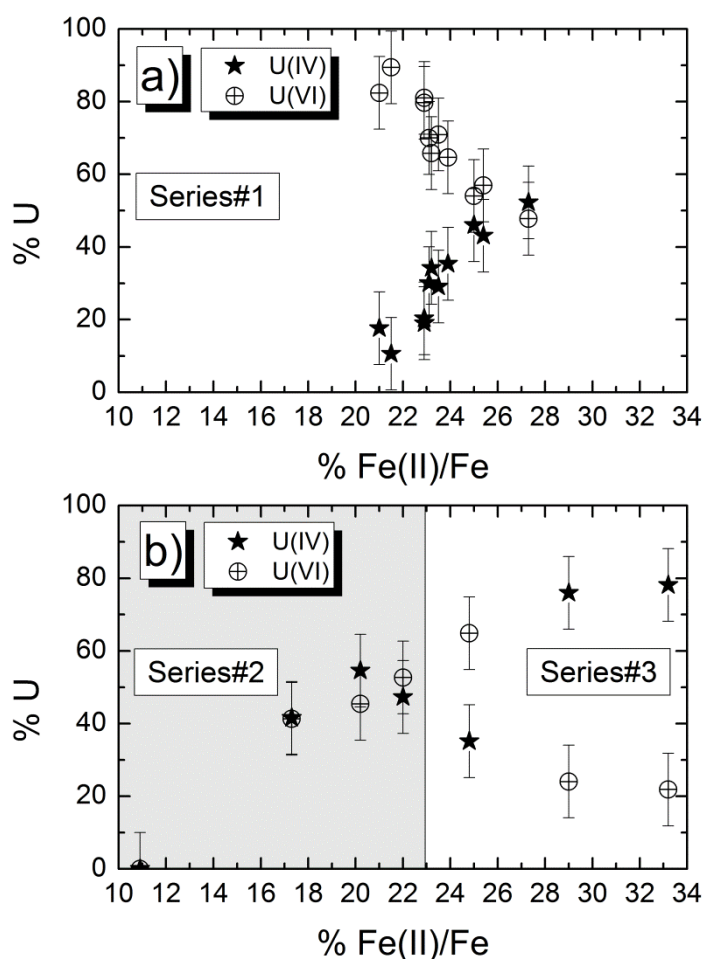


Figure 3.15: U speciation as function of Fe(II)/Fe_{TOT} content for all samples measured by XPS in the experiments. Note the trend in increasing U(IV) with increasing Fe(II)/Fe_{TOT} content and vice versa, the trend of decreasing U(V) and U(VI) with

increasing Fe(II)/Fe_{TOT} content, respectively in case of Series#1 and Series#3. a) Series#1 (po-mag; ≤ 90d contact time) b) Series#2a (grey area; po-mag; 550 d contact time) and Series#3 (fmag; 13 d contact time).

To sum up, the removal of U from solution can thus be explained only by sorption to the maghemite surface in case of magh#1 and, most likely to a much lesser extent, by precipitation of a hexavalent U phase. In case of magh#2 and magh#3, the main process of U removal can be again clearly attributed to sorption, but minor contributions of reduction to U(IV) are detectable as discussed above.

3.2.3.4.1.3 Comparison to literature data

This subchapter compares the XPS results obtained in this study to available literature data. XPS results presented by El Aamrani and co-workers yield no U(VI) reduction for contact times up to 85 d at acidic pH (~ 4.81) ([U]_{TOT} = 1.6·10⁻⁴ M) (El Aamrani, 1999). This finding is explained by the preferential release of Fe(II) out of the magnetite structure at acidic pH conditions. Furthermore, they found indications for a kinetically controlled U(VI) reduction to U(IV) in the presence of carbonate. These slow kinetics are in contrast to results presented in this study yielding much faster kinetics with ~ 50 % U(IV) after 1 d contact time (Series#1) and even ~ 80 % U(IV) for the freshly prepared magnetite after a contact time of 13 d (Series#3). These fast reduction kinetics are in good agreement to XPS results by Missana et al. (2003a) who found up to ~ 50 % U(IV) after 1 d contact time. However, they used considerably higher U concentrations in their XPS measurements (1·10⁻³ M) which may likely lead to precipitation of a U phase hindering a reasonable comparison to the results obtained in this study. Besides, a U(VI) reduction at pH ~ 3 as presented by Missana et al. (2003b), interpreted based on thermodynamic considerations, could not be verified in this study. Scott et al. (2005) presented XPS results on U(VI) interaction with magnetite single crystals. They found a kinetically controlled U(VI) to U(IV) reduction for contact times up to 7 d. These fast kinetics are again in line with our results. Using the same U concentrations and synthetic nanoparticulate magnetite as in the prevailing study, Regenspurg et al. (2009) found up to 52 % U(IV) on the magnetite surface for pH 6 to 10 and 27 d contact time. In contrast to the studies mentioned above, Ilton and co-workers did not observe U(IV) on the magnetite surface for contact times up to 52 d both by XPS and XAS (Ilton et al., 2010). Instead, they could verify the presence of U(V) based on the U 4f_{7/2} peak position and corresponding satellite peaks. As shown in Figure 3.13b and discussed in chapter 3.2.3.4.1, we were able to identify U(V) in a reference samples with our XPS set-up. The U(V) binding energies and corresponding U(V) satellite positions determined in this study for the reference compound are in good agreement to the values given by Ilton et al. (2010). The fact that no U(IV) was observed by Ilton et al. (2010) is referred to the absence of redox equilibrium in their system despite thermodynamic conditions which would allow a reduction to U(IV). Therefore, these authors explained the stability of U(V) due to incorporation into secondary Fe (oxy-hydr)oxide phases. As discussed earlier, we were not able to resolve U(V) in our batch samples due to the lower U concentrations used and therefore the lower signal-to-noise ratio of the U4f spectra in the XPS measurements. In consequence, no satellite peaks could be used for the verification of different U valence states on the magnetite surface. That is, we cannot exclude or verify the existence of U(V) in our experiments based on XPS analyses.

3.2.3.4.2 XAS

XPS is a surface sensitive technique, whereas XAS in standard transmission or fluorescence detection mode provides bulk information about the U oxidation state and its local coordination in magnetite. We studied with XAS one po-mag sample (po-mag#42 of Series#2a) to complement the results obtained with XPS.

The ARTEMIS program package (Ravel and Newville, 2005) was used for EXAFS analyses. The XAFS signal [$\chi(k)$] measured at the U L₃-edge, covering a k range from 2.7 to 10.5 Å⁻¹ was Fourier

transformed to R space using k weightings of 1, 2, and 3 and a Hanning window with window sills dk equal to 2. The ARTEMIS option for simultaneous fits with all three k weightings (1, 2, and 3) was used. The fit was performed in R space over a range from 1.0 to 3.4 Å. Four U-O/U-Fe single scattering paths (U-O at (ICSD 82477) 1.77, 2.68, (ICSD 26410) 1.89 Å and U-Fe at 3.48 Å) were used for the initial model of the po-mag#42 spectral fit. The amplitude reduction factor was held constant to 1.0 (S_0^2); the value was obtained from initial fits of the schoepite Fourier-transformed (FT) EXAFS spectrum measured under the same experimental conditions.

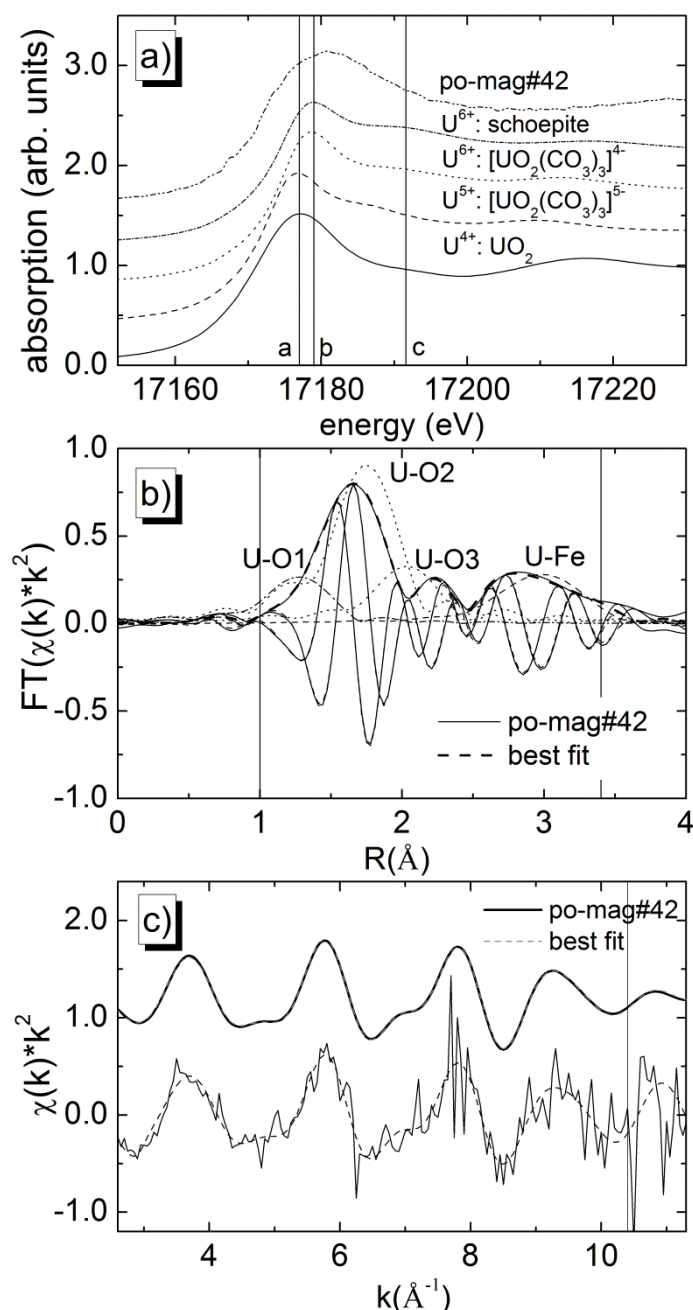


Figure 3.16: a) XANES spectra of the reference samples and the po-mag#42 sample. b) and c) EXAFS spectra of the po-mag#42 sample (in R (a) and k (b) space, the best fit and the used theoretical single scattering paths

The U L₃-edge XANES spectra of the U(IV), U(V), the two U(VI) references and the po-mag#42 sample (Series#2a) are plotted in Figure 3.16a. The energy position of the spectral WL maximum, which

describes mainly $2p \rightarrow 6d$ electronic transitions, shifts towards higher energies with the increase of the formal oxidation state of U (Denecke, 2006). However, its position can also be influenced by the degree of covalency of the U-O bond, i.e., U local symmetry, electronegativity of the U bonding partner and long range geometric structure of the material (Antonio and Sonderholm, 1994). For example, the U(VI) WL maximum is shifted to higher energies compared to the U(V) WL. The trend is preserved as U forms a short axial bond with two O atoms in the U(V) ($1.90 \pm 0.02 \text{ \AA}$) and U(VI) ($1.80 \pm 0.02 \text{ \AA}$) reference materials, i.e. uranyl species (Docrat et al., 1999). However, this short U-O bond also influences the energy position of the U(V) and U(VI) spectra causing overlap of the U(IV) and U(V) WL maxima; the U(IV) has different local symmetry than U(V) and U(VI) as it is bound to 8 O atoms at 2.36 \AA in UO_2 . The po-mag#42 WL exhibits an asymmetric shape. The energy position of its low energy part coincides with the energy positions of the U(IV) and U(V) WL, whereas its high energy part is positioned higher than the WLs of all reference spectra (see lines **a** and **b** in Figure 3.16a). The po-mag#42 WL broadening and its energy position indicate the presence of mixtures of U oxidation states as expected for the predominant reduction of U(VI) to U(IV). This implies the predominance of a geometric structure different than that of uranyl. We obtain further insights from the characteristic feature, marked with line **c**, which describes the multiple scattering of the photoelectron from the two axial O atoms (Antonio and Sonderholm, 1994; Denecke, 2006). The absence of this feature in the po-mag#42 spectrum suggests U-Os bond longer than about 2 \AA as confirmed by the EXAFS analysis. The po-mag#42 (A, C) EXAFS spectra in k and R space and their best fits are shown in Figure 3.16c and Figure 3.16b, respectively. The first coordination shell peak of the po-mag#42 EXAFS spectrum is fit with $0.5 \pm 0.1 \text{ O}$ at $1.77 \pm 0.01 \text{ \AA}$, $1.6 \pm 0.2 \text{ O}$ at $2.23 \pm 0.01 \text{ \AA}$ and $3.3 \pm 0.2 \text{ O}$ at $2.51 \pm 0.01 \text{ \AA}$ (Table 3.8). These results point out that most of the initial U(VI) in linear uranyl geometry reacted with the magnetite nanoparticles and was reduced to U(IV) forming a distorted octahedral oxygen coordination symmetry. Alternatively, the XANES and EXAFS spectra might reflect minor and major contributions of a U(VI)/U(V) and a U(IV) site, respectively. Notice that U(V) or U(VI) symmetries different than linear uranyl entities are rare (Antonio and Sonderholm, 1994), (Soldatov et al., 2007) and therefore, we do not consider them probable here. One possible reduction mechanism might take place at the Fe(II) octahedral sites of magnetite. One U(VI) reduces to U(IV) by oxidation of two Fe(II) atoms to Fe(III). The EXAFS fit yields at average $5.4 \pm 0.2 \text{ O}$ at $1.75\text{-}2.51 \text{ \AA}$ in the first coordination shell (FCS) and $5.7 \pm 1.5 \text{ Fe}$ atoms at $3.39 \pm 0.02 \text{ \AA}$ in the second coordination shell (SCS). Therefore incorporation of U in vacant Fe(II) (FCS: 6 O at 2.056 \AA , SCS: 6 Fe(II) at 2.97) sites in the bulk part of the particles is likely. Regarding U(V), we have to point out that a minor contribution of U(V) in the po-mag#42 sample previously detected (Ilton et al., 2010) cannot be excluded or confirmed on the basis of the present data.

Table 3.8: Results from the fit of the po-mag#41 EXAFS spectra.

Type of backscattering atom	Number of backscattering atoms (N)	Average distance (R(\AA))	Energy shift of the ionization potential (ΔE_0 (eV))	Debye –Waller factor (σ^2 (\AA^2))	Goodness of fit
U-O1	0.5 ± 0.1	1.75 ± 0.01	5.70 ± 0.9	0.001 ± 0.0003	0.003
U-O2	1.6 ± 0.2	2.23 ± 0.01	5.70 ± 0.9	0.001 ± 0.0003	0.003
U-O3	3.3 ± 0.2	2.51 ± 0.01	5.70 ± 0.9	0.001 ± 0.0003	0.003
U-Fe	5.7 ± 1.5	3.39 ± 0.02	3.77 ± 0.5	0.014 ± 0.001	0.003

3.2.4 Conclusion

The prevailing study confirmed the reduction of hexavalent U by nanoparticulate magnetite by means of XPS and XAS measurements at concentrations of max. $3 \cdot 10^{-5} \text{ M}$. As reduced species, tetravalent U was observed on the magnetite surface. A correlation between the Fe(II) content on the surface of magnetite and the amount of tetravalent U was found. Consequently, the highest

3 Influence of sorption and redox kinetics on radionuclide speciation

tetravalent U content was observed in case of the interaction with a freshly prepared magnetite which possesses the highest amount of Fe(II) on the surface underpinning the above mentioned correlation.

Removal processes show fast kinetics within 24 h with more than 90 % U associated to the magnetite surface. Specifically, a fast reduction was observed after 1 d contact time with up to 80 % reduced U on the magnetite surface. XANES results independently revealed the presence of tetravalent U in the magnetite particles. The presence of pentavalent U was not confirmed, though minor amounts cannot be excluded. Furthermore, EXAFS results suggest that U incorporates into vacant Fe(II) sites after contact time of 550 d and pH of 5.7. Overall, the results show that magnetite, both partly oxidized or “non-oxidized”, can effectively reduce hexavalent U, thus representing an effective retention pathway. The presence of pentavalent U, as previously reported in the literature cannot be confirmed or ruled out by XPS or XAS investigations under the experimental conditions.

3.3 *Removal of uranium(VI) from the aqueous phase by iron(II) minerals in presence of bicarbonate*

Uranium(VI) mobility in groundwater is strongly affected by sorption of mobile U(VI) species (e.g. uranyl, UO_2^{2+}) to mineral surfaces, precipitation of U(VI) compounds, such as schoepite ($\text{UO}_2)_4\text{O}(\text{OH})_6 \cdot 6\text{H}_2\text{O}$), and by reduction to U(IV), forming sparingly soluble phases (uraninite; UO_2). The latter pathway, in particular, would be very efficient for long-term immobilization of U. In nature, Fe(II) is an important reducing agent for U(VI) because it frequently occurs either dissolved in natural waters sorbed to matrix minerals or structurally bound in many minerals. Redox reactions between U(VI) and Fe(II) depend not only on the availability of Fe(II) in the environment, but also on the chemical conditions in the aqueous solution. Under natural groundwater conditions, U(VI) forms complexes with many anionic ligands, which strongly affect its speciation. Carbonate, in particular, is known to form stable complexes with uranium, raising the question if U(VI), when complexed by carbonate, can be reduced to UO_2 . The goal of this study was to find out if Fe(II) when structurally bound in a mineral (as magnetite, Fe_3O_4) or sorbed to a mineral surface (as corundum, Al_2O_3) can reduce U(VI) to U(IV) in presence of HCO_3^- . Batch experiments were conducted under anaerobic conditions to observe U removal from the aqueous phase by the two minerals depending on HCO_3^- addition (1 mM), U concentration (0.01-30 μM) and pH value (6-10). Immediately after the experiments, the mineral surfaces were analyzed by X-ray photoelectron spectroscopy (XPS) to obtain information on the redox state of uranium bound to the solid surfaces. XPS results gave evidence that U(VI) can be reduced both by magnetite and by corundum amended with Fe(II). In presence of HCO_3^- , the amount of reduced uranium on the mineral surfaces increased compared to carbonate-free solutions. This can be explained by the formation of Fe(II) carbonates on the mineral surfaces which represent an easily available Fe(II) pool for the U(VI) reduction. A facilitated U(VI) reduction is also considered possible when U is present as a carbonate complex compared to non-complexed U (e.g. uranyl).

Regenspurg, S., Schäfer T., Schild, D., Huber, F. and Malmström, M. E. (2009) Removal of uranium(VI) from the aqueous phase by iron(II) minerals in presence of bicarbonate. *Applied Geochemistry* (2009), <http://dx.doi.org/10.1016/j.apgeochem.2009.04.029>

3.3.1 Introduction

Uranium is a naturally occurring element that can be found in low levels within many rocks, sediments and soils. Due to its radioactivity and toxicity (carcinogenic for humans), uranium is a hazardous contaminant in the environment and the World Health Organization (WHO) recommends a drinking water limit of $0.015 \text{ mg}\cdot\text{L}^{-1}$ (WHO, 2004). The average U concentration in the earth crust is between 2 and 4 ppm, but it can be enriched in soil and groundwater by several anthropogenic activities, such as by the release from mill tailings of U mines, as a consequence of the use of depleted U for military devices (DU ammunition), or by agricultural application of phosphate fertilizers, which are often associated with U. The main use of U is as fuel in nuclear power plants and thus, it is a primary component of spent nuclear fuel and high level nuclear waste. Consequently it is of high concern for nuclear waste management. A thorough understanding of the interactions of U with geological materials and its behaviour in groundwater is of high relevance both for remediation strategies of contaminated sites and for the safety of final nuclear waste repositories.

Uranium mobility in groundwater is controlled by its redox, sorption and complexation behaviour. In oxic conditions, it occurs predominantly in the redox state of +VI (UO_2^{2+} or uranyl). Removal of U from the aqueous phase is possible by sorption to solid surfaces, precipitation as U(VI) mineral, such as schoepite ($(\text{UO}_2)_4\text{O}(\text{OH})_6\cdot 6\text{H}_2\text{O}$ or $\text{UO}_2(\text{OH})_2\cdot\text{H}_2\text{O}$), coffinite ($\text{U}(\text{SiO}_4)_{1-x}(\text{OH})_{4x}$), autunite ($\text{Ca}(\text{UO}_2)_2(\text{PO}_4)_2\cdot 10\text{-}12\text{H}_2\text{O}$) or sodium uranate $\text{Na}_2\text{O}(\text{UO}_3)_2\cdot 6\text{H}_2\text{O}$, or by reduction to U(IV) forming hardly soluble solid phases such as uraninite (UO_2), (U_3O_8), UO_{2+x} . Dissolved in natural water, aqueous U is prone to complexation with phosphate, silicate, sulphate, fluoride and especially with carbonate (Langmuir, 1978). Consequently, more than 42 dissolved U species, 89 U minerals and 368 inorganic crystal structures that contain essential U(VI) are known to date (Langmuir, 1978; Burns, 2005). Bicarbonate, especially, forms strong aqueous U-carbonate complexes (UO_2CO_3 , $\text{UO}_2(\text{CO}_3)_2^{2-}$ and $\text{UO}_2(\text{CO}_3)_3^{4-}$) and, thus, in the presence of CO_3^{2-} or HCO_3^- in water U(VI) is highly mobile (Grenthe et al., 1984; Nguyen Trung et al., 1992; Baborowski and Bozau, 2006).

Reduction of mobile U(VI) to sparingly soluble UO_2 can be induced for example by Fe(II) or sulphide - a process which is possible in the aqueous phase (Privalov et al., 2003), but enhanced in the presence of solid surfaces acting as catalysts (Jeon et al., 2005). Accordingly, it has been shown that sulphide or Fe(II) bearing minerals like pyrite (FeS_2), magnetite (Fe_3O_4) or biotite ($\text{K}(\text{Mg,Fe})_3\text{AlSi}_3\text{O}_{10}(\text{F,OH})_2$) can reduce U(VI) (Wersin et al., 1994; Ilton et al., 2004b; Scott et al., 2005; Ilton et al., 2006). Iron in the redox state of +II is an ubiquitous compound in all natural systems, occurring dissolved in water, structurally bound in many minerals and sorbed to mineral surfaces. The effect of Fe(II) containing minerals on the long term reduction of U(VI) is of high importance, due to the omnipresence of these minerals in the earth crust. In particular, for the construction of deep ground repositories for radioactive waste the interactions of radionuclides with the minerals in the backfill and in the surrounding bedrock have to be considered. For example, in Sweden the nuclear waste will potentially be stored in a repository hosted in granitic rock. The groundwater circulating in these granitic aquifers, which might react one day with the nuclear waste, contains, besides NaCl (ca. 10 mM) high concentration of NaHCO_3 (ca. 1 mM; (Metz et al., 2003)). Granite contains several Fe(II) minerals, such as pyrite, biotite or magnetite, which are responsible for an average FeO content in granite of 1.68 wt.-% (Blatt and Tracy, 1996). Previous studies have indicated that Fe(II) in all of the three minerals can reduce U(VI) to U(IV) (Wersin et al., 1994; Ilton et al., 2004a; Scott et al., 2005) but none of these studies considered the influence of HCO_3^- on the reduction. As mentioned above, carbonate is known to form very stable aqueous complexes with U(VI), a fact which is often used to prevent U(VI) mineral precipitation in experiments (Payne et al., 2002) or to extract U from soil (Zhou and Gu, 2005). However, U(VI) carbonate complexes are also known to sorb to mineral surfaces, thereby forming ternary surface complexes with Fe(III) as has been shown by infrared spectroscopy (Ho and Miller, 1986) and X-ray absorption spectroscopy on the hematite surface (Bargar et al., 2000).

To date, there are only few studies on the potential reduction of U(VI) by Fe(II) in the presence of (bi)carbonate in the scientific literature (Behrends and Van Cappellen, 2005). To the best of the author's knowledge, in none of them were spectroscopic methods applied to verify U reduction. The main goal of this study was to find out if U(VI), i.e. UO_2^{2+} can be reduced by Fe(II) which is either structurally bound in Fe(II) containing minerals or sorbed to a mineral surface. Moreover, it was aimed to find out to what extent HCO_3^- and the pH value affects this process. The experimental conditions in solution were held near to natural groundwater conditions.

3.3.2 Materials and Methods

Magnetite (Fe_3O_4) was prepared by reaction of 0.3 M FeSO_4 with 3.33 M KOH and 0.27 M KNO_3 (Cornell and Schwertmann, 1996). The mineral suspension was dialyzed against deionised water which was changed on a daily basis in a N_2 -atmosphere in a glove box until the electric conductivity was stable and below $10 \mu\text{S}\cdot\text{cm}^{-1}$ over 24 hours. Mineral composition was verified to consist solely of magnetite by powder X-ray diffraction. XRD patterns were recorded from $5^\circ - 80^\circ 2\theta$, using $0.01^\circ 2\theta$ steps, and a 2 s counting time per step with a Bruker AXS D8 powder diffractometer equipped with a BSI (Baltic Scientific Instrument) Si(Li) solid detector, and $\text{Cu K}\alpha$ radiation. Surface area of magnetite was determined by the BET method (5 step N_2 sorption of 0.08 g samples) into replicates. Suspensions of $2 \text{ g}\cdot\text{L}^{-1}$ magnetite with a specific surface area of $19.7 \text{ m}^2\cdot\text{g}^{-1}$ were used for the experiments. A synthetic corundum ($\alpha\text{-Al}_2\text{O}_3$) suspension (Krahn; purity > 99.99 %; particle size: 0.2 μm ; surface area: $14.5 \text{ m}^2\cdot\text{g}^{-1}$; specifications from the manufacturer) was diluted with MilliQ-water to obtain a final amount of $2 \text{ g}\cdot\text{L}^{-1}$ $\alpha\text{-Al}_2\text{O}_3$. The ionic strength was set to 0.01 M by adding NaCl to all mineral suspensions. Different chemical conditions were obtained by addition of NaHCO_3 (0 or 0.001 M) or FeCl_2 (0 or 0.001 M). Finally, the pH values were adjusted to 6, 8 or 10 (pH measured with a combined glass electrode) by addition of HCl and NaOH (Table 3.9). All solutions were purged for 1 h with N_2 gas before addition to the suspensions in an anaerobic glove box. Therein, samples were kept at room temperature during the experiment and anoxic conditions were assured.

Experiments were performed in polyethylene (PE) bottles containing 20 ml of suspension. The used chemicals (pro analysis) and gas (> 99.999 %) were of high purity.

After 24 h, U was added from a stock solution of $\text{UO}_2(\text{NO}_3)_2$ to the mineral suspensions to get final U concentrations between $3\cdot 10^{-7}$ M and $3\cdot 10^{-5}$ M. The pH was re-adjusted (6, 8, 10) immediately and again after 7 and 13 days. Table 1 gives an overview of all samples used in this batch. After a reaction time of 27 days, pH and redox potential (measured with a platinum electrode and Ag/AgCl reference electrode) were measured. 3 ml of all suspensions kept originally at pH 6 or 10 were ultra-centrifuged (90,000 rpm) to separate the dissolved Fe and U species from colloidal compounds. To prevent sample oxidation during centrifugation (outside the glovebox), samples were transferred in air-tight sealed PE centrifuge tubes. After centrifugation, the tubes were transferred back into the glove box. From the samples kept originally at pH 8 (the highest U concentration), only 0.5 mL were removed from the suspensions and filtered (0.22 μm). The pH in the remaining suspensions was adjusted to four by addition of HCl. The applied acid had been degassed and stored for several months in the permanently Ar filled glove box equipped with a gas purification system. After another 48 h, 3 ml of these acidified samples were again ultra-centrifuged (90,000 rpm) in air tight tubes and separated from the solids. In all supernatants and filtrates, the pH value were measured and the elemental composition was determined by inductively coupled plasma mass-spectrometry (ICP-MS), which has a detection limit for U of $0.006 \mu\text{g}\cdot\text{L}^{-1}$ and for Fe of $0.2 \mu\text{g}\cdot\text{L}^{-1}$. It was assumed that U in the aqueous phase exists predominantly in the redox state of +VI, because U(IV) would form solid precipitates (UO_2).

Theoretical U speciation and complexation in the different solutions were calculated with the HYDRA/MEDUSA software using the program internal database complex.db and complex.elb (Puigdomenech, 2004).

3.3.2.1 XPS analysis

After separation from the supernatant, selected samples of the solids were prepared in the glove box at inert gas (Ar) conditions for X-ray photoelectron spectroscopy (XPS) analysis. Portions of powder samples, dried at room temperature, were pressed onto indium foil and mounted on the sample holder. By means of an O-ring sealed vacuum transfer vessel (PHI model 04-110) samples were transported from inside the glovebox into the XPS instrument without air-contact. Within the following two days, samples were analyzed using a Physical Electronics Inc. (PHI) model 5600ci spectrometer equipped with Mg K_{α} , Al K_{α} , and monochromatic Al K_{α} x-ray sources. Electrons passing the spherical capacitor analyzer are detected by a 16-channel detector. Charging of isolating sample surfaces, due to emitting photo- and Auger electrons was compensated by a low-energy electron flood gun in case of monochromatic X-ray excitation.

Elemental lines of pure metals (Mg K_{α} : Cu $2p_{3/2}$ at 932.62 eV, Ag $3d_{5/2}$ at 368.22 eV, Au $4f_{7/2}$ at 83.95 eV) with well-established binding energies were used to calibrate the binding energy scale of the spectrometer following (Seah et al., 1998). Subsequently, these elemental lines were also measured by Al K_{α} and monochromatic Al K_{α} x-ray excitation. The determined standard deviations of binding energies were within ± 0.1 eV for conductors and within ± 0.2 eV for non-conducting samples. A linear regression between reference data and measured values of the calibration was used to correct measured binding energies of samples.

Surveys scans were recorded first by monochromatic Al K_{α} excitation, source power maximal 200 W, to identify the elements and to determine their atomic concentrations at sample surfaces. An area of about 1 mm in diameter was excited by the monochromatic Al K_{α} x-rays. Samples prepared had sizes of about 5 mm in diameter allowing multiple analyses at previously non-irradiated areas. Data analysis and curve fitting were performed using the PHI Multipak program. Narrow scans of the elemental lines were measured at 23.5 eV pass energy of the hemispherical analyzer. Elemental lines at the surface of magnetite showed a small shift due to charging relative to the conducting magnetite bulk, presumably due to formation of some isolating hydroxides at the surface. Therefore, U4f lines in magnetite as well as in all (isolating) corundum samples were charge referenced to the C 1s line of adventitious hydrocarbon (C_xH_y) at 284.4 eV. Solely for the elemental lines of Fe 2p and O 1s charge reference occurred at the O 1s binding energy reference of bulk Fe_3O_4 at 530.0 eV.

Potential beam reduced U(VI) reduction during XPS measurements was considered by recording narrow scans of the U 4f elemental lines of the samples by monochromatic Al K_{α} X-rays in combination with an electron flood gun as well as with the Al- K_{α} standard source equipped with an Al window. Besides different overall charging due to the different X-ray sources, the spectra of the elemental lines were similar and explicitly no further change at the U4f lines were observed during the measurement. Consequently, beam reduction of U(VI) can be considered as insignificant for the experiments.

With monochromatic Al K_{α} X-ray excitation, bremsstrahlung induced background intensity and X-ray satellites are absent, yielding a detection limit for U of about 0.02 wt.%. Moreover, thermal impact to the sample from the monochromatic X-ray source is prevented.

3.3.3 Results and discussion

3.3.3.1 Uranium immobilization – quantitative analysis

In all experimental mineral suspensions, U had been strongly removed from the aqueous solutions (58 to 99 % of initial uranium concentration) after 27 days (Table 3.9). For removal mechanisms, surface sorption of U(VI), precipitation of solid U(VI) phases and reduction and precipitation of U(IV) phases were considered. Additionally, the release of Fe from the minerals and precipitation of new Fe phases as Fe(II)- and Fe(III)-hydroxides or Fe(II)-carbonate and the sorption of U to these new

3 Influence of sorption and redox kinetics on radionuclide speciation

surfaces will be discussed. Results indicated that U removal from solution depends on the U concentration, the pH-value, the presence of HCO_3^- and the Fe(II) availability, i.e. the Fe(II) source. These factors will be discussed in the following sections.

3.3.3.1.1 Effect of initial uranium concentration

Conditions of oversaturation of the aqueous phase with respect to solid U(VI) compounds are easily established under experimental, carbonate-free suspensions. To determine differences between the U uptake from the aqueous phase in over and unsaturated solutions, the initial U concentration was varied in the magnetite suspensions (pH 6, 8 and 10) for final values of $2.9 \cdot 10^{-5}$ M, $8.9 \cdot 10^{-6}$ M and $9.9 \cdot 10^{-8}$ M (Table 3.9). Initial and final U concentrations were plotted into a predominance diagram (Figure 3.17a), which indicates that the predominant U species at higher U concentrations are the U(VI) minerals schoepite $\text{UO}_2(\text{OH})_2 \cdot \text{H}_2\text{O}$ and sodium uranate ($\text{Na}_2\text{U}_2\text{O}_7$). This observation implies that precipitation of solid phases must be considered for the two higher concentrated U suspensions. Only for the lowest initial uranium concentration ($9.9 \cdot 10^{-8}$ M), is the aqueous phase unsaturated with respect to U-containing solids, which implies that U can only be removed by sorption of U(VI) or reduction and precipitation as U(IV) species in these cases.

Table 3.9: Chemical properties of different mineral suspensions before (initial) and after (final) the reaction with U(VI) solution over 27 days. Fe(II) source (mineral), pH (6-10), HCO_3^- , and U(VI) concentration is indicated. Background electrolyte of all solutions was 10 mM NaCl.

Solid phase	NaHCO_3 (M)	FeCl_2 (M)	U _{initial} (M)	U _{final} (M)	U removed (%)	pH initial	pH final	E_{h_final} (mV)	Fe(II) _{final} (M)
Fe_3O_4	-	-	$2.95 \cdot 10^{-5}$	$2.581 \cdot 10^{-7}$	99.12	6	7.95	-193	$1.81 \cdot 10^{-5}$
	-	-	$2.96 \cdot 10^{-5}$	$1.24 \cdot 10^{-7}$	99.58	8	8.72	-247	$2.27 \cdot 10^{-5}$
	-	-	$2.95 \cdot 10^{-5}$	$4.04 \cdot 10^{-7}$	98.63	10	10.1	-385	$3.12 \cdot 10^{-5}$
	-	-	$8.94 \cdot 10^{-6}$	$2.24 \cdot 10^{-7}$	97.49	6	8.78	-173	$2.96 \cdot 10^{-5}$
	-	-	$8.91 \cdot 10^{-6}$	$1.08 \cdot 10^{-7}$	98.79	8	8.63	-211	$2.09 \cdot 10^{-5}$
	-	-	$8.93 \cdot 10^{-6}$	$2.63 \cdot 10^{-7}$	97.05	10	9.77	-355	$1.20 \cdot 10^{-5}$
	-	-	$9.96 \cdot 10^{-8}$	$3.22 \cdot 10^{-9}$	96.76	6	8.91	-208	$4.22 \cdot 10^{-5}$
	-	-	$9.95 \cdot 10^{-8}$	$2.19 \cdot 10^{-9}$	97.80	8	8.55	-320	$4.69 \cdot 10^{-5}$
	-	-	$9.94 \cdot 10^{-8}$	$1.52 \cdot 10^{-8}$	84.66	10	9.66	-416	$1.99 \cdot 10^{-4}$
	$1 \cdot 10^{-3}$	-	$2.94 \cdot 10^{-5}$	$7.04 \cdot 10^{-7}$	97.61	6	8.1	-117	$7.40 \cdot 10^{-5}$
	$1 \cdot 10^{-3}$	-	$2.96 \cdot 10^{-5}$	$2.32 \cdot 10^{-6}$	92.15	8	8.2	-197	$9.40 \cdot 10^{-6}$
	$1 \cdot 10^{-3}$	-	$2.96 \cdot 10^{-5}$	$1.23 \cdot 10^{-5}$	58.56	10	10.2	-362	$7.80 \cdot 10^{-6}$
Al_2O_3	-	$1 \cdot 10^{-3}$	$2.91 \cdot 10^{-5}$	$4.35 \cdot 10^{-6}$	85.04	6	6.14	-84	n.m.
	-	$1 \cdot 10^{-3}$	$2.88 \cdot 10^{-5}$	$2.23 \cdot 10^{-8}$	99.92	8	8.1	-143	$3.00 \cdot 10^{-5}$
	-	$1 \cdot 10^{-3}$	$2.58 \cdot 10^{-5}$	$1.48 \cdot 10^{-8}$	99.94	10	10.53	-403	$5.03 \cdot 10^{-6}$
	-	-	$2.80 \cdot 10^{-5}$	$1.87 \cdot 10^{-7}$	99.33	6	8.85	-291	$1.87 \cdot 10^{-7}$
	-	-	$2.80 \cdot 10^{-5}$	$2.88 \cdot 10^{-7}$	98.97	8	9.32	-208	$2.88 \cdot 10^{-7}$
	-	-	$2.94 \cdot 10^{-5}$	$2.53 \cdot 10^{-7}$	99.14	10	10.49	-412	$2.53 \cdot 10^{-7}$
	$1 \cdot 10^{-3}$	$1 \cdot 10^{-3}$	$2.89 \cdot 10^{-5}$	$2.44 \cdot 10^{-8*}$	99.92	6	7.43	-201	$3.70 \cdot 10^{-4}$
	$1 \cdot 10^{-3}$	$1 \cdot 10^{-3}$	$2.84 \cdot 10^{-5}$	$3.43 \cdot 10^{-8*}$	99.88	8	8.45	-265	$3.15 \cdot 10^{-6}$
	$1 \cdot 10^{-3}$	$1 \cdot 10^{-3}$	$2.65 \cdot 10^{-5}$	$6.65 \cdot 10^{-8*}$	99.75	10	10.46	-414	$5.60 \cdot 10^{-6}$

n.m. = not measured; * = Observation: color change (from white to black) in the end of the experiment.

Nevertheless, the highest U concentration ($2.95 \cdot 10^{-5}$ M) was used in most of the experiments, because the strong removal of U resulted in U concentrations close to the detection limit of ICP-MS. Also, XPS measurements require a relatively high U concentration on the mineral surfaces (0.02 at. %) to be detected and evaluated properly. Although no experimental evidence was ever observed for the formation of schoepite or sodium uranate, their possible precipitation and its effect of providing new surface sites for sorption needs to be considered in the obtained results.

3.3.3.1.2 Effect of pH values and redox conditions

Table 3.9 shows the pH values adjusted in the beginning and measured at the end of the experiment as well as the measured final redox potentials (Eh) in all experimental suspensions. Although the pH was re-adjusted to initial pH (6, 8, 10) twice during the experiments, a strong shift to higher values was observed at the end (Table 3.9). As the most probable reactions responsible for this pH increase, a slow surface protonation and possibly (at lower pH) mineral dissolution are the most likely.

Measured Eh data of all samples were between - 84 and - 416 mV and increased to negative values with increasing pH. Figure 2a shows the measured pH-, Eh data plotted in an Eh/pH stability diagram together with the redox equilibrium lines of the stability area of an Fe(II)/Fe(III) buffer, which was constructed using data from (Felmy et al., 1989) and (Rai et al., 2002), who worked with Fe powder. Thus, the lower line was obtained by the equation $pe + pH = 2$ (Felmy et al., 1989) and the upper line by $pe + pH = 4$ (Rai et al., 2002). All samples appear to be in equilibrium with the Fe(II)/Fe(III) couple - including the three corundum suspensions that have not had Fe added. Measured Fe concentrations of these Al_2O_3 -solutions revealed an Fe concentration of $3-6 \mu g \cdot L^{-1}$ ($= 5 \cdot 10^{-8} M$), which indicates some Fe-contamination of the corundum samples. According to manufacturer information, the Fe content in the corundum is below 20 ppm, corresponding to a maximum of $40 \mu g \cdot L^{-1}$ in each of the experimental suspensions (if corundum was completely dissolved). Thus, the apparent equilibrium with the Fe(II)/Fe(III) can be explained if both redox states are present in the contaminant Fe in corundum or if initially Fe(II) was reduced by U(VI). A similar observation as found in the present study for the U system, has been described for reductive dissolution of PuO_2 which is also strongly controlled by the Fe(II)/Fe(III) redox couple (Rai et al., 2002). Figure 3.18 further indicates that at the pH and redox conditions present as well as considering the Fe concentration in solution (given as $10 \mu M$ in the calculations), the solutions are oversaturated with respect to the formation of magnetite and hematite (Fe_2O_3). The measured total Fe concentration in the solutions is considered to be predominantly in the redox state +II, because at the given pH conditions (>3.5), the Fe(III), which potentially had formed by reduction of U(VI) would predominantly precipitate as Fe(III) hydroxide/oxide. The Fe(II) concentration in the magnetite suspensions usually increased with increasing pH (except in HCO_3^- -containing solutions, where siderite precipitation can be expected; Figure 3.18) and is between $1 \cdot 10^{-5}$ M and $2 \cdot 10^{-4}$ M (Table 3.9). In contrast to magnetite, the amount of dissolved Fe(II) decreased with increasing pH in Fe(II) amended corundum suspensions both, in the presence and absence of HCO_3^- .

In general, with increasing pH and increasing negative Eh, less U was removed from the solutions (Table 3.9). As shown in the two predominance diagrams of U(VI) in Figure 3.17, at higher pH values (> 7) negatively charged complexes (e.g. of $UO_2(OH)_3^-$ or $UO_2(CO_3)_2^{2-}$) are predominant in the aqueous phase. Therefore, less U sorption to negatively charged surfaces of oxide minerals can be expected (the point of zero charge (pH_{pzc}) of Al_2O_3 is 6.8-7.2; (Mustafa et al., 1998) and of Fe_3O_4 is 6.4-7.1; (Cornell and Schwertmann, 1996)). Clearly, the lowest U removal from solution (58 %) occurred for magnetite in presence of HCO_3^- at an initial pH of 10 (Table 3.9). This observation is explained by the competition of U complexes (e.g. $UO_2(OH)_3^-$) with carbonate for sorption sites on the negatively charged mineral surface.

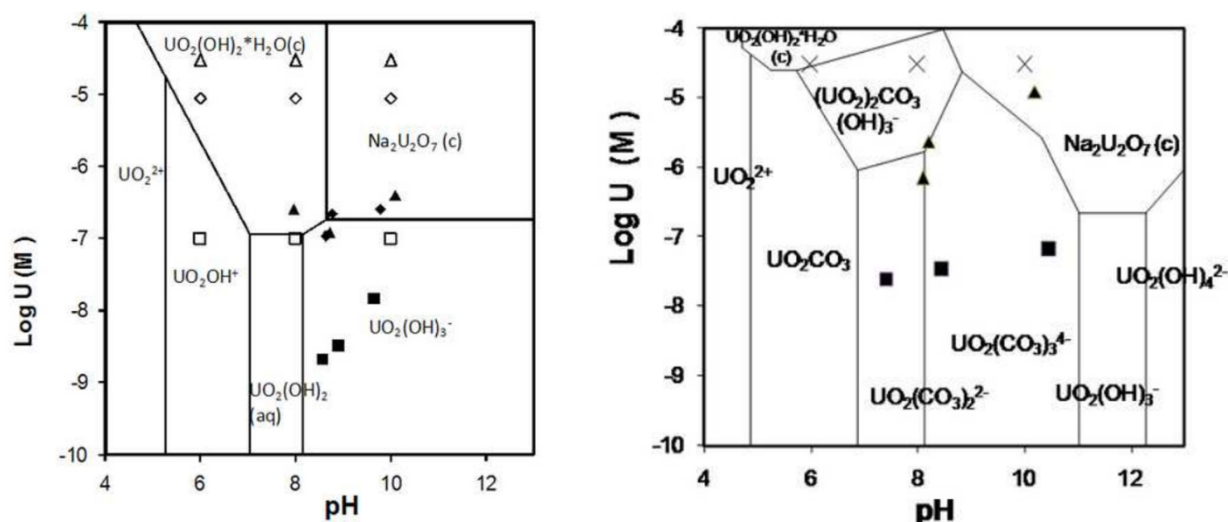


Figure 3.17: Left: Predominance diagram for uranium-mineral suspensions in 10 mM NaCl as calculated with Hydra/Medusa software (Puigdomenech, 2004). Data points represent measured values of pH and uranium concentration in different magnetite suspensions. Initial values (open symbols) are at pH 6, 8, 10 and at uranium concentration of $2.9 \cdot 10^{-5}$ M (triangles), $8.9 \cdot 10^{-6}$ M (diamonds) and $9.9 \cdot 10^{-8}$ M (squares). Filled symbols represent final measured data. Right: Predominance diagram for uranium-mineral suspensions containing 10 mM NaCl and 1 mM CO_3^{2-} as calculated with Hydra/Medusa software (Puigdomenech, 2004). Data points are measured values of pH and uranium concentration. Initial data (crosses) are at pH 6, 8, 10 and at uranium concentration of $2.9 \cdot 10^{-5}$ M. Filled symbols represent final concentration of uranium in corundum-Fe(II) amended suspensions (squares) and in magnetite suspensions (triangles).

3.3.3.1.2.1 Acidification to pH 4

After 27 days, mineral suspensions initially adjusted to pH 8 were acidified to pH 4. It was expected that at this pH, sorbed U(VI) and surface precipitates of U, e.g. schoepite ($\text{UO}_2(\text{OH})_2 \cdot \text{H}_2\text{O}$), would desorb and dissolve, respectively, and only the sparingly soluble, reduced form of uranium, i.e. UO_2 , would remain dominantly in the solid phase. Figure 3.19 compares the U concentrations measured in different suspensions before and after acidification. In case of Fe(II)-free corundum only 60 % of previously bound U was released to the aqueous phase (Table 3.9), indicating that a part of the formed surface precipitates or sorbed U(VI) species are quite stable against acidification because no, or only little uranium reduction (due to Fe(II) contamination) can be expected in these suspensions. The release of U in the Fe(II) amended corundum suspension was significantly lower (35 % of previously bound U), indicating that a considerable amount of U might have been reduced to less soluble UO_2 . In case of magnetite suspensions, only a relatively small fraction of pH 8 surface accumulated U was released by acidification to pH 4 (9.5 %; Figure 3.19) indicating that Fe(II) within magnetite also partly reduced the U(VI) to sparingly soluble U(IV). However, due to oxidation of Fe(II) to Fe(III) and probable subsequent precipitation of Fe-hydroxide (Figure 3.18) sorption or co-precipitation of U(VI) on these oxides cannot be excluded as an additional or alternative pathway (Duff et al., 2002). However, U associated with Fe(III) phases is unlikely to remain sorbed at the positively charged Fe(III)-hydroxide surface at low pH where the positively charged uranyl (UO_2^{2+}) dominates the aqueous speciation (Missana et al., 2003b), which is inconsistent with the observed low degree of U release upon acidification.

Although no change of the Fe(II)/Fe(III) redox equilibrium was expected at pH 4 (Rovira et al., 2007), a strong increase in the Fe(II) concentration was observed due to acidification (from $2.2 \cdot 10^{-5}$ M - $9.4 \cdot 10^{-6}$ M at pH 8-9 (Table 3.9) to $7.8 \cdot 10^{-5}$ - $9.5 \cdot 10^{-5}$ M at pH 4 (Table 3.10)). Clearly, the synthetic magnetite used is more reactive compared to commercially available magnetite (Rovira et al., 2007) which implicates either a desorption of sorbed Fe(II) or dissolution of weakly crystalline Fe species bound to the magnetite surface. Especially in the HCO_3^- suspensions the release of Fe at low pH values was very high, indicating dissolution of previously formed siderite (FeCO_3). Simultaneously U

concentration increased in this solution which is a consequence of desorption of siderite-surface bound U during siderite dissolution (Figure 3.19).

3.3.3.1.3 Effect of bicarbonate

Comparison of the predominance diagrams in Figure 3.17 show the strong effect of carbonate on U speciation in the aqueous phase. Instead of positively charged uranyl (UO_2^{2+}) species, which dominate under CO_2 -free conditions, the solutions in the presence of carbonate contain predominantly negatively charged $\text{UO}_2(\text{CO}_3)_2^{2-}$, or uncharged UO_2CO_3 complexes with different sorption properties. Uranium concentrations measured in this study in the presence and absence of HCO_3^- followed this behaviour. In general, more U was found in the aqueous solution in presence of HCO_3^- (Table 3.9). The concentration of U remaining in the aqueous phase also increased with increasing pH values (≥ 8) (Figure 3.19). This is consistent with the formation of (aqueous) U-carbonate complexes which sorb less than carbonate-free U species. Another effect of HCO_3^- addition at $\text{pH} \geq 8$ was a decrease in the aqueous Fe(II) concentration in both magnetite and corundum suspensions which can be explained by the formation of FeCO_3 precipitates (Figure 3.18) removing the Fe(II) from the aqueous phase. Acidification to $\text{pH} 4$ mobilized the Fe(II) again which is either due to desorption of surface bound Fe(II) or dissolution of siderite or Fe(III)hydroxides, formed by reduction of U(VI).

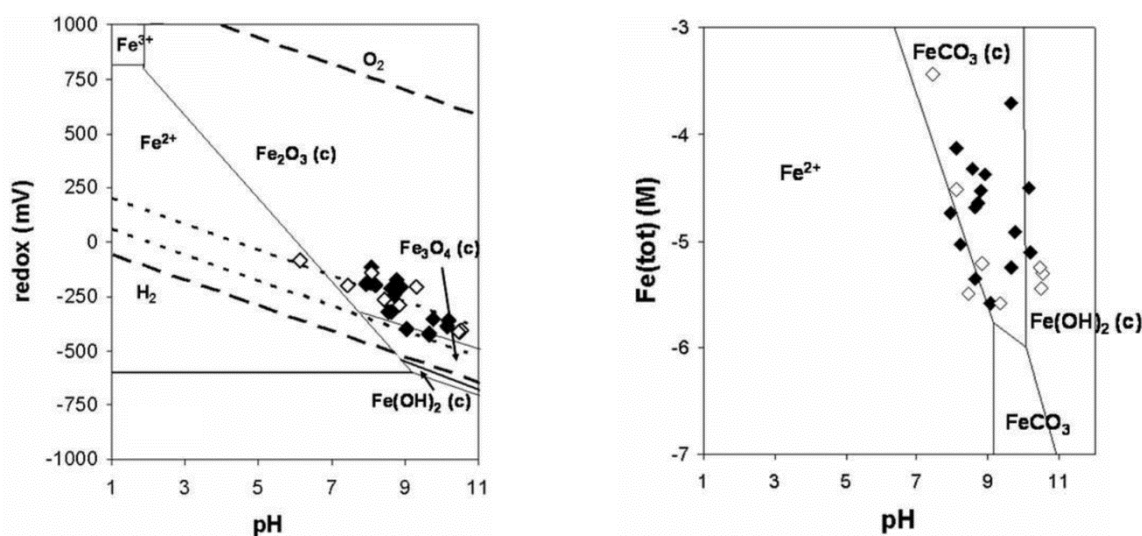


Figure 3.18: Left: Eh/pH diagram for the iron equilibrium system. Open diamonds represent corundum and black diamonds represent magnetite suspensions. Long-dashed lines give the stability line of H_2 and O_2 , respectively. The short-dashed line shows the equilibrium area of a solid Fe(II)-/Fe(III) buffer (Felmy et al., 1989; Rai et al., 2002). Other lines represent predominance areas of Fe(II) and Fe(III) species as calculated with Hydra/Medusa software with 1 mM CO_3^{2-} and a 0.01 mM Fe concentration. (“c” in the diagram indicates a solid phase. Right: Predominance diagram for Fe(II) species in a carbonate solution (1 mM). Data points represent measured iron concentrations and pH values of solutions reacted with corundum (open diamonds) and magnetite (black diamonds).

3.3.3.1.4 Effect of Fe(II) source

One of the central questions in this study was to find out whether the structural bound Fe(II) in a mineral (e.g. magnetite) is able to reduce U(VI) to U(IV) and to compare this ability with that of Fe(II) that is sorbed to a mineral surface (e.g. corundum). The total amount of Fe(II) in the magnetite suspensions is about 0.002 M as estimated according to (Missana et al., 2003a), who prepared magnetite under the same conditions as in the present study. Measured Fe(II) concentrations in our magnetite suspensions were around $4.3 \cdot 10^{-5} (\pm 5 \cdot 10^{-6}) \text{ M}$ independent of the pH (6-10), which is almost consistent with the low solubility of magnetite. In contrast, when Fe(II) was added to the corundum solutions (0.001 M), Fe(II) would bind to the mineral surface by sorption or in presence of

HCO_3^- also precipitate as siderite. The strong variation of the Fe concentration is consistent with the pH dependence of the sorption/ precipitation process ($3 \cdot 10^{-5}$ M to $5 \cdot 10^{-6}$ M at pH 8 and 10 respectively; Table 3.9).

Sorption reactions are controlled by the amount of surface sites and the kind of surface groups of the minerals used. Due to different surface areas of the two minerals used in our study (magnetite: $19.7 \text{ m}^2 \cdot \text{g}^{-1}$; corundum: $14.5 \text{ m}^2 \cdot \text{g}^{-1}$), in the following, surface area normalized U removal from the aqueous phase (for suspensions with $3 \cdot 10^{-5}$ M initial U concentration) are compared. The amount of surface area normalized U removed is slightly lower for magnetite ($7.6 \cdot 10^{-6} \pm 3.9 \cdot 10^{-8}$) compared to corundum ($1.0 \cdot 10^{-6} \pm 5.1 \cdot 10^{-9} \text{ mol} \cdot \text{m}^{-2}$, respectively; Table 3.11).

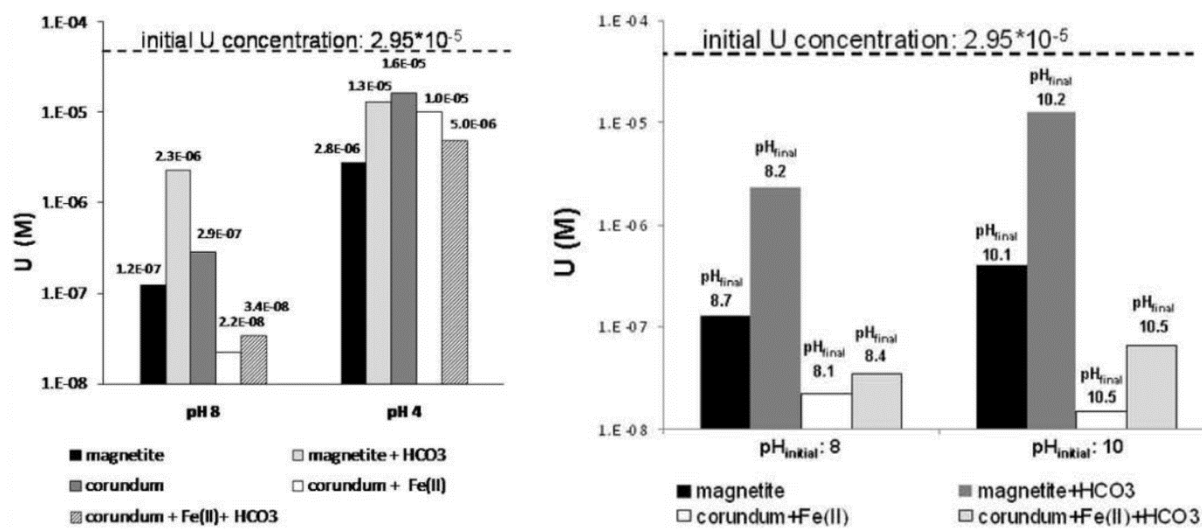


Figure 3.19: Left: Uranium concentration in solutions containing magnetite, magnetite amended with 1 mM HCO_3^- , corundum amended with 1 mM Fe(II) and corundum amended with each 1 mM Fe(II) and HCO_3^- , measured after the experiment at pH 8 (Table 1 and 2 indicate the final pH values) and after re-acidification to pH 4. Initial uranium concentration was $2.95 \cdot 10^{-5}$ M. Right: Uranium concentration in solutions containing magnetite, magnetite amended with 1 mM HCO_3^- , corundum amended with 1 mM Fe(II) and corundum amended with Fe(II) and HCO_3^- (each 1 mM), measured after the experiment at pH 8 and 10. Values above the columns indicate final pH values.

3.3.3.2 Surface analysis by XPS

The solid residues after centrifugation of magnetite and corundum suspensions treated at pH 8 before and after acidification to pH 4 in presence and absence of HCO_3^- and Fe(II) were analyzed by XPS. This technique allows not only determining quantitatively the elemental composition of solid surfaces but also their redox state.

3.3.3.2.1 Total elemental composition

The elemental composition of the mineral surfaces after reaction with HCO_3^- , U(VI), and Fe(II) were measured by XPS. Results are summarized in Table 3.11. High Na and Cl concentrations (0.2-2.5 at.%) result from the use of NaCl as inert electrolyte in all solutions. Occasionally, trace amounts of impurities of P, Si, K were found. The surface C content (2.6-8.9 at.%) does not correlate with the input of HCO_3^- , but derives from impurities of the minerals, solution reagents or from adventitious hydrocarbon. Uranium surface concentration ranges between 0.04 and 0.6 at.% and is clearly higher for magnetite compared to Fe(II) containing corundum samples (Table 3.11). This result differs from the surface area normalized U concentration as mentioned above, where the opposite effect was observed, but can be explained by the different measurement techniques: while BET measures the

sorption of gases on the whole surface area of a sample, XPS acquires elemental intensities on a constant 1 mm^2 of the geometric surface while penetrating to a certain depth beneath the surface (e.g. around 5 nm in the case of magnetite). The relatively high surface concentration as observed for the (Fe(II) and HCO_3^- -free) corundum suspension (0.6 at.%; Table 3.11) suggests that in this case U precipitated on the mineral surface (e.g. as schoepite).

Table 3.10: Chemical properties of different mineral suspensions originally adjusted to pH 8 with highest initial uranium concentration ($2.8 \cdot 10^{-5}$ - $2.9 \cdot 10^{-5}$ M; Table 3.9) measured 48 h after acidification to pH 4.

mineral	NaHCO_3 (M)	FeCl_2 (M)	U (M)	Fe(II) (M)	pH
Fe_3O_4	-	-	$2.81 \cdot 10^{-6}$	$7.79 \cdot 10^{-5}$	3.95
	x	-	$1.32 \cdot 10^{-5}$	$9.46 \cdot 10^{-5}$	3.93
Al_2O_3	-	x	$1.01 \cdot 10^{-5}$	$1.95 \cdot 10^{-5}$	3.78
	-	-	$1.65 \cdot 10^{-5}$	-	3.95
	x	x	$4.99 \cdot 10^{-5}$	$1.14 \cdot 10^{-4}$	4.12

x : compound was added initially; - : compound was not added

3.3.3.2.2 Redox state of uranium

XPS analyses were mainly performed to get evidence if U(VI) was removed from the solutions due to reduction by Fe(II) or due to U(VI) sorption or co-precipitation. Mostly, XPS elemental lines shift to lower binding energies with decreasing redox state. When comparing the XPS spectra of corundum with magnetite (Figure 3.20) it becomes obvious that the U peaks of corundum samples are much broader and exceed lower energies than the theoretical value of U 4f for U(IV), which is at 380 eV. This broadening can be explained by lateral differential surface charging of the isolating corundum due to emission of the electrons during the measurement. Therefore, corundum XPS spectra can only be compared to other corundum spectra and not directly to magnetite.

The corundum sample which was amended with Fe(II) (Figure 3.20, Spectrum b) shows a slight broadening of the U 4f peaks towards lower binding energy values compared to Fe(II)-free corundum indicating a slightly increased amount of reduced U (Figure 5 Spectrum a). This reduction is also optically visible by the formation of black precipitates, (which is the color of the mineral uraninite, UO_2), in the otherwise milky-whitish corundum suspension. In contrast, the Fe(II)-free corundum suspensions remained of whitish color during the experiment. In this latter sample, the U(IV) content was determined by XPS to be 11% of the U detected on the surface (Table 3.11), which might result from instrument error or from reduction of U(VI) by Fe(II) impurities contained within the corundum as mentioned above. The additional presence of HCO_3^- in the corundum suspension strongly increased the amount of reduced U species as the stronger shift of the U4f peaks to lower energies demonstrates (Figure 3.20, Spectrum d). This shift even exceeds the U(IV) elemental line, which could be explained by the presence of an element with lower Pauling's electronegativity than U (1.7) to be in the second shell of U(IV) like Na (0.9) or Al (1.5): U(IV)-O-Na or U(IV)-O-Al. However, the discussion of this phenomenon is beyond the scope of this paper. Since the amount of U bound to the corundum is very similar in HCO_3^- -free and in HCO_3^- -containing suspensions kept at pH 8 (99.2–99.8%; Table 3.9), this peak shift strongly indicates that in the presence of HCO_3^- more surface bound U(VI) has been reduced than in the absence of HCO_3^- .

3 Influence of sorption and redox kinetics on radionuclide speciation

Table 3.11: Elements determined by XPS (in at.%) in different samples. Initially, $2.95 \cdot 10^{-5}$ M U(VI) was added to all samples. Relative atomic concentrations results are typically within 10-20% error. Hydrogen is not measured by XPS.

sample	Al	Fe	O	C	Na	Cl	U	U(IV) /Fe	U(IV) (%U _{tot})
Al ₂ O ₃ ^{a,c}	32.87	---	57.83	5.55	0.64	0.64	0.61	---	11
Al ₂ O ₃ + Fe(II)	30.74	4.52	58.73	4.00	1.04	0.80	0.17	0.012	37
Al ₂ O ₃ + Fe(II); pH 4	26.55	8.92	57.71	4.56	1.41	0.81	0.04	0.004	100
Al ₂ O ₃ + Fe(II) + HCO ₃ ⁻	28.01	4.21	56.93	7.45	2.29	1.01	0.10	0.009	36 ^d
Al ₂ O ₃ + Fe(II) + HCO ₃ ⁻ ; pH 4	24.37	10.88	56.79	5.88	1.21	0.75	0.12	0.008	70
Fe ₃ O ₄	1.17	37.73	54.01	5.50	1.02	0.25	0.32	0.004	52
Fe ₃ O ₄ ; pH 4 ^b	---	33.62	52.95	8.93	2.44	1.04	0.36	0.001	5
Fe ₃ O ₄ + HCO ₃ ^{-a}	5.91	30.42	57.48	2.60	2.14	0.97	0.33	0.007	68
Fe ₃ O ₄ + HCO ₃ ⁻ ; pH 4 ^c	---	36.62	51.18	8.18	2.49	1.06	0.21	0.001	12

a Traces of K (< 0.15 atomic %); b Traces of P (0.66 atomic-%); c Traces of Si (< 0.4 atomic-%); d Potential occurrence of U species of lower redox state than U(IV).

A similar shift to lower energies was observed in XPS spectra of magnetite suspensions amended with HCO₃⁻ (Figure 3.20). The peak positions of carbonate-free treated magnetite samples were between the literature values for U(VI) and U(IV) oxides (U 4f_{7/2} at 380.8 eV (as UO₂) and 382.4 (as UO₃; (Wersin et al., 1994), indicating that both redox states of U are present in this sample. The finding of U(IV) in this sample implies that Fe(II) originating from magnetite is able to reduce U(VI) on the mineral surface. The ratio of U(IV) to Fe_(tot) as measured by XPS on the mineral surfaces is a measure of the availability of Fe(II) for U reduction inasmuch as one can assume that the higher this value is, the more available is the Fe(II) (Table 3.11). The U(IV)/Fe_(tot) ratio is quite similar for both minerals (0.004–0.01 at pH 8). However, due to different binding forms of Fe(II) in the minerals (structurally and adsorbed, respectively) the U(IV)/Fe ratio should be considered separately for magnetite and corundum. For both minerals the U(IV)/Fe_(tot) ratio increases in the presence of HCO₃⁻ indicating again better U reduction in the presence of HCO₃⁻.

XPS spectra were also obtained for pH 4 acidified corundum and magnetite samples (Figure 3.20). It was expected that the acidification would remove the weakly bound U(VI) species (sorbed or co-precipitated) from the surface, whereas the sparingly soluble UO₂ (U(IV)) would remain on the surface. However, experimental results in this line were obtained only for the corundum suspension, where the U(IV) content on the minerals was 100 % and 70 % of the total surface bound U. However, in HCO₃⁻-free, Fe(II) containing corundum suspensions, the U surface concentration decreased strongly (to 0.04 at.%; Table 3.11) indicating either re-oxidation of U(IV) (this could be possible by Fe(III), which could have been formed as a consequence of decreased pH and increased Eh conditions due to acidification) or that most U occurs in this sample as U(VI), which is desorbing at low pH. In the case of HCO₃⁻-amended corundum suspensions, the surface U content remained almost constant (0.1 and 0.12 at.%, respectively) indicating that reduced U–carbonate surface complexes are more resistant to acidification. In magnetite samples, the total U concentration at the mineral surfaces remained more or less constant during acidification. However, the U(IV) content drastically decreased (to 5% and 12% in the absence and presence of HCO₃⁻, respectively; Table 3.11). One possible explanation for this is that the reduced form of U is a weakly crystalline phase (e.g. amorphous UO₂ or U₄O₉) which dissolves more easily at low pH. The fact that the solubility of minerals changes depending on their crystallinity (the more amorphous a mineral is, the more easily it dissolves) is well known (Schindler et al., 1963) and explains why freshly formed uraninite dissolves more easily than aged uraninite. However, since most U remains on the mineral surface this explanation is not very likely. The other explanation is, as mentioned for the corundum samples, that

Fe(II) oxidizes at the low pH value to Fe(III) which in turn oxidizes U(IV) to U(VI) and desorbs from the surface.

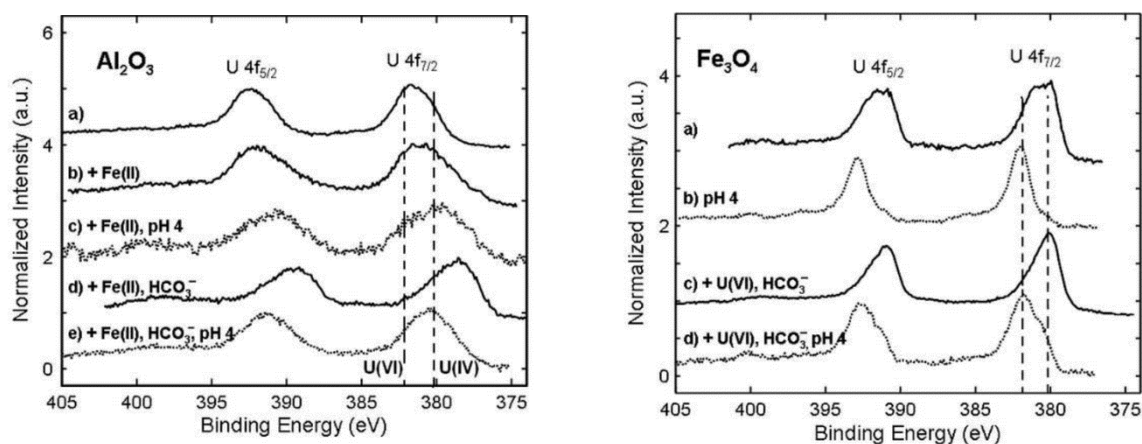


Figure 3.20: Left: XPS uranium 4f spectra on the surface of Al_2O_3 at various conditions: a) Corundum reacted with U(VI) at pH 8. b) Corundum reacted with U(VI) at pH 8 in presence of 1 mM Fe(II). c) Sample b) which was later acidified to pH 4. d) Corundum reacted with U(VI) at pH 8 in presence of each 1 mM HCO_3^- and Fe(II). e) Sample d) which was later acidified to pH 4. The dashed lines indicate the reference binding energies of U 4f_{7/2} for U(IV) in UO_2 and U(VI) in UO_3 , respectively. Right: XPS uranium 4f spectra on the surface of Fe_3O_4 at various conditions: a) Magnetite reacted with U(VI) at pH 8. b) Sample a) which was later acidified to pH 4. c) Magnetite reacted with U(VI) at pH 8 in presence of 1 mM HCO_3^- . d) Sample c) which was later acidified to pH 4. The dashed lines indicate the reference binding energies of U 4f_{7/2} for U(IV) in UO_2 and U(VI) in UO_3 , respectively.

3.3.3.2.3 Redox state of iron

In this study, Fe(II) is the only plausible reducing agent for U(VI). Consequently, the concentration of Fe(III) on the mineral surfaces should increase during reaction, because Fe(III) usually precipitates as an oxide or hydroxide phase at neutral to basic pH conditions. Thus the XPS Fe 2p spectra is expected to shift towards higher energies. However, compared to the bulk Fe, the change in Fe(III) surface concentration is too small to cause detectable changes in the spectra. Consequently, the Fe 2p spectra of all but one sample looked almost identical (Figure 3.21). The only exception was the HCO_3^- -amended magnetite sample: clearly, the amount of Fe(II) increased in this sample as compared to other samples (Figure 3.21). This observation suggests that a secondary Fe(II) phase, presumably siderite (FeCO_3), has formed on the magnetite surface. Additional support for siderite formation was obtained, by comparing the O 1s spectra, where the HCO_3^- -amended magnetite sample differed from the others. The peak is broadened towards higher binding energies (Figure 3.21), which is typical for a carbonate phase (Heuer and Stubbins, 1999). These observations are consistent with the suggested formation of a secondary Fe(II) carbonate phase on the magnetite surface already discussed in Section 3.3.3.1.3. Moreover, when acidifying this sample to pH 4 both, the O 1s and Fe 2p XPS spectra lose their previously described special features, indicating the re-dissolution of siderite.

The Fe 2p and O 1s spectra were measured also for the corundum samples containing Fe(II) and carbonate. However, the Fe 2p lines were quite broad thereby not allowing any interpretation of the data.

3.3.3.3 Uranium reduction processes

This study revealed that Fe(II) that is adsorbed to mineral surfaces (corundum) or structurally bound in a mineral (magnetite) is able to reduce U(VI) to U(IV). This ability is increased in HCO_3^- solutions (1 mM). However, the presence of HCO_3^- also increased the amount of dissolved U in the experiments. The latter effect was also observed by (Behrends and Van Cappellen, 2005), who concluded,

consequently, that U(VI) reduction is inhibited in the presence of HCO_3^- (45 mM). However, from microbiological studies it has also been found that U(VI) is more bio-available for microbial reduction when present as a carbonate complex (Behrends and Van Cappellen, 2005; Wall and Krumholz, 2006). By means of spectroscopic investigations (XPS), the study gives now for the first time direct evidence that U(VI) reduction is facilitated in dilute HCO_3^- solutions. Results obtained within the study indicate two pathways (potentially simultaneously) to be responsible for this effect: (i) in the presence of Fe(II), the formation of siderite is very probable, which accumulates on the solid surfaces where it acts as an easily available pool of Fe(II) with the solid surface simultaneously acting as a catalyst for U(VI) reduction. The redox- and pH conditions of the suspension control the siderite solubility, which dissolves with decreasing pH, simultaneously releasing the previously bound U.

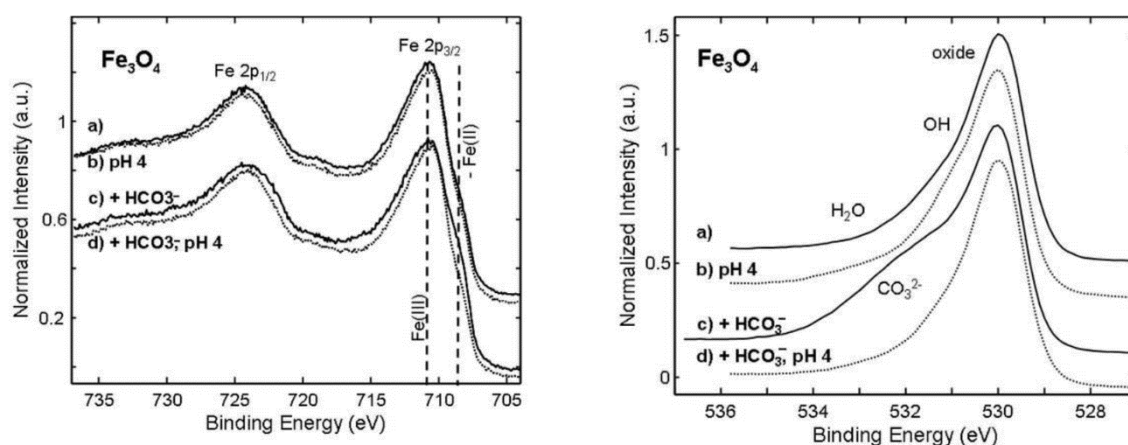


Figure 3.21: Left: XPS Fe 2p spectra on the surface of Fe_3O_4 at various conditions: a) Magnetite reacted with U(VI) at pH 8. b) Sample a) which was later acidified to pH 4. c) Magnetite reacted with U(VI) at pH 8 in presence of 1 mM HCO_3^- . d) Sample c) which was later acidified to pH 4. The dashed line indicates the reference binding energy of Fe $2p_{3/2}$ for Fe(III) and Fe(II). Right: XPS O 1s spectra on the surface of Fe_3O_4 at various conditions: a) Magnetite reacted with U(VI) at pH 8. b) Sample a) which was later acidified to pH 4. c) Magnetite reacted with U(VI) at pH 8 in presence of 1 mM HCO_3^- . d) Sample c) which was later acidified to pH 4. Positions of oxygen in oxides, water, carbonate and hydroxide are marked.

The other proposed pathway (ii) is independent from the presence of Fe(II) and relates to the reactivity of U(VI): results from the work in accordance with previous studies in the literature, gave evidence that U(VI) forms (relatively) stable complexes with carbonate anions (e.g. $\text{UO}_2(\text{CO}_3)_2^{2-}$ or UO_2CO_3), which predominantly remain dissolved as aqueous complexes. However, a considerable fraction of these complexes are also known to sorb to mineral surfaces and evidence of ternary surface complexes has been reported for the surface of hematite by a combination of different spectroscopic techniques (Fourier Transform infrared and X-ray absorption fine structure; (Ho and Miller, 1985)), as well as of measurements of the electrophoretic mobility of hematite–U–carbonate particles (Bargar et al., 2000). These studies described the structures of these negatively charged, ternary surface complexes as innersphere, metal bridged (hematite–U(VI)–carbonate) complexes with, depending on the pH, either monomeric or dimeric character (Ho and Miller, 1985; Bargar et al., 2000). It is proposed that these surface-attached, carbonate complexes can be more easily reduced to U(IV) than uncomplexed U(VI) species. Possibly, the reduction step of U(VI)–carbonate-complexes goes via an U(IV) carbonate species. The existence of U(IV) carbonate complexes ($\text{U}(\text{CO}_3)_4^{4-}$ and $\text{U}(\text{CO}_3)_6^{5-}$) was described by (Bruno et al., 1989), who also found small amounts of U(IV) in natural waters to be bound in such complexes, which supports the authors' second pathway for mediation of U(VI) reduction by HCO_3^- .

For the experiments in the HCO_3^- system one can assume that dissolved U(VI) first formed aqueous, carbonate complexes. They were partially sorbed to the mineral surfaces, where the Fe(II) reduced the U(VI) carbonates to U(IV) carbonates. In natural systems, it can be expected that over long time, these U(IV) carbonates age to form more stable U oxides, which are in the beginning less crystalline and more soluble, until finally the well-crystallized minerals UO_2 and U_3O_8 form. This hypothesis is

3 Influence of sorption and redox kinetics on radionuclide speciation

supported by the observation of the stability of the U surface complexes due to acidification. The U release from the mineral surfaces was strongest in the corundum suspension (with no Fe and HCO_3^-), where solely uranyl was expected to bind to the surface. Next strongest was the U release in corundum suspensions containing Fe(II) and HCO_3^- , followed by magnetite with HCO_3^- (the latter both would contain U(IV) carbonate complexes) and finally by HCO_3^- -free magnetite, where consequently hardly soluble UO_2 precipitation would be expected.

To summarize, within this study evidence was found on the catalyzing effect of dilute HCO_3^- solutions on the reduction of U(VI) by Fe(II). These results elucidate the role of carbonate ubiquitously present in groundwater on the migration of U.

4 Retardation by flow path heterogeneity: experiments versus modeling

We studied tracer (HTO) and nanoparticle (quantum dots) transport by means of column migration experiments and comparison to 3D CFD modeling. Concerning the modeling approach, a natural single fracture was scanned using micro computed tomography (μ CT) serving as direct input for the model generation. The 3D simulation does not incorporate any chemical processes besides the molecular diffusion coefficient solely reflecting the impact of fracture heterogeneity on mass transport. Complex fluid velocity distributions (flow channeling and flowpath heterogeneity) evolve as direct function of fracture geometry. Both experimental and simulated solute and colloidal breakthrough curves show heavy tailing (non-Fickian transport behaviour), respectively. Experimental breakthrough of the quantum dots always arrives faster than the solute tracer in line with the modeling results. Congruence of experimental and modeling results is better for the high flux experiments than for the low flux experiments. Besides processes like sorption or matrix diffusion, we show that fracture heterogeneity represents an important retardation mechanism for solutes and colloidal phases. Differences between the experimental results and the simulations are discussed with respect to uncertainties in the μ CT measurements and experimental and simulation boundary conditions, respectively.

Huber, F., Enzmann, F., Wenka, A., Bouby, M., Dentz, M., Schäfer T. Natural micro-scale heterogeneity induced solute and nanoparticle retardation in fractured crystalline rock. *Journal of Contaminant Hydrology* (under review).

4.1 Introduction

In highly impermeable rock like e.g. crystalline/igneous rock (basalt, granite) fractures represent the only pathways available for significant groundwater flow to take place. These discrete fracture planes often possess a complex overall geometry, fracture aperture variability and micro-scale roughness. The spatial heterogeneities directly impact the flow dynamics inside the fracture rendering complex velocity distributions. Typical characteristics of fracture flow fields are flow channeling in areas of strong fracture aperture variation and eddies or recirculation zones (Boutt et al., 2006) which can be accessible for solutes and/or solid particles by hydrodynamic dispersion and Brownian diffusion.

Since mass (solute and nanoparticle) transport is strongly coupled to the prevailing flow field it directly reflects the impact of heterogeneous flow velocity distributions on the transport behaviour. In general, mass transport in fractured media is prone to: hydrodynamic dispersion due to (i) the parabolic velocity profile between two no-slip walls (Taylor-Aris dispersion)(Taylor, 1953; Aris, 1956), (ii) the variability in fracture aperture leading to heterogeneous flowpath distributions (Bodin et al., 2003) and (iii) molecular diffusion as a result of concentration gradients. Molecular diffusion can lead both to a transport between different flow channels and into the porous matrix surrounding the fracture planes (matrix diffusion) (Grisak and Pickens, 1980). All these processes can cause non-Fickian mass transport behaviour leading to pronounced tailings in breakthrough curves (BTC) (Dentz et al., 2004).

A mechanistic process understanding of laboratory or field results is most often hindered due to the lack of detailed knowledge about the actual fracture geometry. Consequently, most experiments represent black box type situations. To circumvent the lack of actual fracture geometry information, modern laboratory techniques like e.g. computer tomography (CT) can be applied. This tool provides detailed spatial information which can be employed directly in numerical codes to conduct simulations on the measured scale. Several authors have coupled CT measurements data with numerical modeling in the past (Hirono et al., 2003) but unfortunately, most often 2D models are applied (Cardenas et al., 2009) and only rarely attempts have been made to compare the simulation results with experimentally data in the same system.

Nanoparticles are frequently defined as particles having one or more dimensions of the order of $\leq 100\text{nm}$. The upper size limit is thereby determined by the size, above which the properties of the particles are indistinguishable from those of the bulk material. This length scale of transition is the target of newly developed and designed so-called engineered nanomaterials (ENP) and has opened the broad field of nanoscience (Lieber, 2003). Possible undesirable results of these ENP capabilities are harmful interactions with biological systems and the environment, with the potential to generate toxicity (Nel et al., 2006; Nowack and Bucheli, 2007). Quantum dots (QD) made from semiconductor materials such as CdSe, CdTe or ZnS have attracted wide interest in areas such as molecular biology and medicine. Frequently, ENP as QP are functionalized being made hydrophilic for technical applications, which might change also drastically their mobility once released to the environment (Lecoanet et al., 2004). Drinking-water-treatment processes have been optimized for removal of bacteria and viruses (10–1000 nm), but their effectiveness in removing ENPs at the same time requires more investigations (Weinberg et al., 2011). Groundwater flow systems as karst environments or fractured rock are extremely vulnerable to colloid/nanoparticle migration (McCarthy and Shevenell, 1998) and therefore transport and possible retardation mechanisms are of paramount importance to predict contaminant mobility.

In the present study we have chosen the following approach to show the influence of fracture 3D geometry on fluid and nanoparticle transport: An over-cored natural fracture was characterized by means of μCT prior to migration experiments. Migration experiments were performed using both HTO and engineered nanoparticles (quantum dots) under variation of the flow velocity. 3D fluid flow and mass transport simulations on basis of the μCT data were conducted and compared with the experimental results. This study presents, for the first time, 3D CFD simulations on fluid flow and

mass transport on basis of μ CT data in a natural single fracture extending previous studies in 2D and investigations using purely synthetic or artificially induced fractures, respectively. Our model simulations aim to describe the experimental results solely by the effect of fracture heterogeneity neglecting any chemical processes.

4.2 Materials and Method

4.2.1 X-ray computed tomography

To gain information about fracture geometry, aperture and porosity distribution the drill core was scanned using a μ CT (Enzmann and Kersten, 2006). This method serves as a non-destructive tool to obtain information of internal structures and spatial characteristics of the specimen down to the micro-meter and even nano-meter scale. For further information about technical details of the method, see Dului et al. (1999). The drill core used in this study was obtained from the Äspö hard rock laboratory (HRL, Sweden) from the drill hole KOV 01 774.7-775.2. Prior to characterization by μ CT, the core was sealed on the outside by sticking it in a custom made Plexiglas column and equipped with devices and tubing for the migration experiments (Figure 4.1).

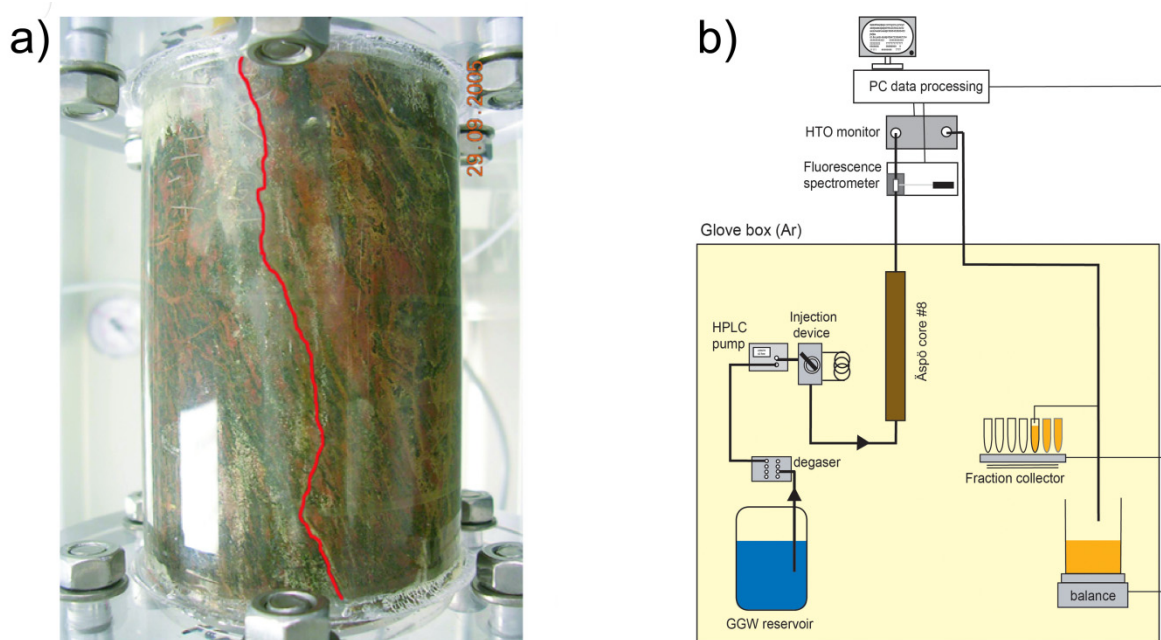


Figure 4.1: a) Drill core as installed in the laboratory. In red, the fracture suture is marked. b) A schematically sketch of the set-up as installed in the laboratory for use in the migration experiments.

4.2.2 Quantum dots

Engineered nanoparticles, namely quantum dots were applied to test their mobility in the drill core. This material consists of a CdSe/ZnS core with PEG lipid surface coating coupled to comb hair type carboxyl terminal groups, which were delivered as stable suspension in de-ionized water (Evident Technologies). The detection of this material can be performed by two ways, either through fluorescence detection with the setting of λ_{em} : 517 nm and λ_{exc} : 501 nm or via Asymmetrical Flow-Field-Flow Fractionation (AsFIFFF). The method is described in details elsewhere (Bouby et al., 2004).

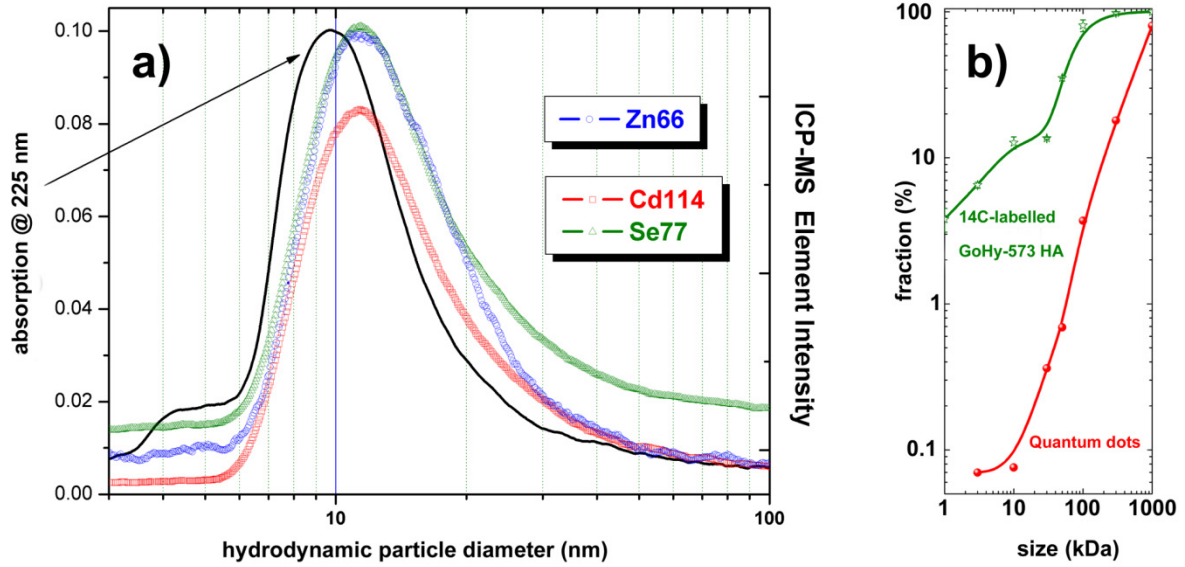


Figure 4.2: a) Absorbance and ICP-MS fractograms obtained after injection of 100 μL of a QD solution diluted at $1 \text{ mg}\cdot\text{L}^{-1}$ in the AsFIFFF eluent (ultrapure water + NaOH; pH 9.3). The system is calibrated prior to the QD size measurements by injection of a mixture of polystyrene sulfonate standard (PSS) salt and carboxylated polystyrene nanoparticles. b) Size distribution analysis via ultrafiltration (UF) of the QD in comparison to ^{14}C -labelled Gorleben humic acid (GoHy-573 HA) (Mansel and Kupsch, 2007).

4.2.3 Core migration experiments

In the laboratory core migration experiments a set-up comparable to (Schäfer et al., 2004) was used (Figure 4.1b). Via HPLC pump (Knauer Smartline 1000) the desired flow rates were established. The continuity of the pump flux was measured independently using a balance collecting the eluted fluid volume. A tracer cocktail was prepared using natural Grimsel groundwater (ionic strength 1.2 mM; pH 9.67) as background electrolyte (Table 3.2). The total activity of HTO in the cocktail was 400 kBq and a QD concentration of $12.5 \text{ mg}\cdot\text{L}^{-1}$ has been adjusted. HTO and QD concentrations were measured online using a HTO monitor (Raytest, MIRA-/GINASTAR) and a Luminescence spectrometer (AMINCO-Bowman Series 2), respectively. Injection of the tracer cocktail was applied using an injection valve (Upchurch Scientific) with a volume of 100 μL . Two different volume fluxes have been used in the experiments: 66.8 and 14.2 $\mu\text{L}\cdot\text{min}^{-1}$, respectively.

4.2.4 CFD modeling

The governing equations describing fluid flow through arbitrary geometries are the Navier-Stokes equations. For a steady state laminar flow of a single phase, incompressible Newtonian fluid with constant viscosity it can be expressed in vector form (eq. 4.1 and 4.2) as: (Batchelor, 1967)

$$\nabla \cdot \mathbf{v} = 0 \quad (4.1)$$

$$\nabla \cdot (\rho \mathbf{v} \mathbf{v}) = -\nabla p + \nabla \cdot (\boldsymbol{\tau}) \quad (4.2)$$

where ρ = fluid density ($\text{kg}\cdot\text{m}^{-3}$), p = static pressure (Pa), $\mathbf{v} = (v_x, v_y, v_z)$ velocity vector ($\text{m}\cdot\text{s}^{-1}$) and $\boldsymbol{\tau}$ = stress tensor (Pa). The assumption of an incompressible fluid holds for most of the fluids in the subsurface environment (Ertekin et al., 2001). Surface walls are treated as “no-slip” boundary

conditions constraining all velocity components to zero at the model walls. The inlet is defined as pressure inlet and pressure outlet boundary condition (prescribed gauge pressure = 0 Pa) are assigned at the outlet. In fluid mechanics, typically the Reynolds number (Re) is applied for characterization the type of flow. The Reynolds number provides a ratio of the inertia to the viscous forces or, in other words, the ratio of the velocity of convection to the diffusive velocity (Skjetne et al., 1999). The Reynolds number for fluid flow in a fracture can be described by eq. 4.3: (Cardenas et al., 2009)

$$Re = \frac{u \cdot a_m}{\eta} \quad (4.3)$$

where, u is a characteristic velocity (here, the volume averaged velocity magnitude; Table 4.1) ($m \cdot s^{-1}$), a_m is a characteristic length (here, the arithmetic average of fracture aperture is used) (m) and η = kinematic viscosity ($m^2 \cdot s^{-1}$).

Mass transport is modeled by the advection-diffusion equation (eq 4): (ANSYS, 2009)

$$\frac{\partial}{\partial t}(\rho Y_i) + \nabla \cdot (\rho v Y_i) = -\nabla \cdot J_i \quad (4.4)$$

with Y_i = mass fraction of i th species (-), t = time (s) and J_i = diffusive flux of species i ($1 \cdot m^{-2} \cdot s^{-1}$).

The influence of both hydrodynamic dispersion and diffusion on the transport behaviour is generally expressed by the Peclet number (Pe) (eq. 5): (Detwiler et al., 2000)

$$Pe = \frac{u \cdot b}{D_m} \quad (4.5)$$

where b = mean aperture (m) and D_m = molecular diffusion coefficient ($m^2 \cdot s^{-1}$). It describes the ratio between advection and molecular diffusion. For high Pe numbers ($Pe > \sim 50$) advection dominates whereas low Peclet numbers ($Pe < \sim 1$) indicate dominance of molecular diffusion.

The 3D model applied in this study is generated using the μ CT measurements. The μ CT scan resulted in 1691 stacked 2D slices transformed into a 3D model representation of the drill core. The obtained μ CT dataset was pre-processed using different computational tools for data artifact reduction facilitating the segmentation of the fracture planes. Care was taken to accurately capture the fracture geometry. Subsequently, 3D triangulated surfaces of the fracture (in STL format) were produced out of the full resolution segmented raw μ CT data. The 3D STL data was imported in the software ICEM CFD (ANSYS, 2009) for further processing. First, re-meshing of the surfaces has been conducted constrained to user defined surface element size and quality resulting in a 3D surface mesh with ~ 1.1 million elements. Regarding the volume mesh generation, four boundary layers on every fracture surface using prismatic elements have been generated to better resolve near-wall flow and transport dynamics. With this type of mesh elements it was furthermore assured that even in areas where the aperture is very small sufficient elements are present to resolve the flow and mass transport dynamics. The remaining fracture interior was filled with tetrahedral elements. The final 3D mesh of the fracture consists of ~ 10.5 million elements (3156334 nodes).

Flow and mass transport simulations were modeled using the finite volume CFD software FLUENT (ANSYS, 2009). The flow was calculated using the steady state, double precision, implicit, pressure

based solver. As solution method the SIMPLE algorithm was chosen for Pressure-Velocity coupling. Pressure and momentum were solved applying a 2nd order and 3rd order MUSCL scheme, respectively. As convergence criteria 10^{-7} was used for the continuity equation as absolute solution residuals. Mass was introduced as a classical step input boundary condition. Initial concentration is defined as zero in the whole computational domain (eq. 4.6):

$$C = 0 \quad [-\infty \leq x \leq +\infty; 0 \leq y \leq +\infty; 0 \leq z \leq +\infty; t = 0] \quad (4.6)$$

At the inlet (eq. 4.7):

$$C = 1 \quad \text{for } t > 0 \quad (4.7)$$

A molecular diffusion coefficient for HTO of $2.5 \cdot 10^{-9} \text{ m}^2 \cdot \text{s}^{-1}$ was applied. The molecular diffusion coefficient of $4.2 \cdot 10^{-11} \text{ m}^2 \cdot \text{s}^{-1}$ for the QD was calculated based on their hydrodynamic diameter (12 nm) using the Stokes-Einstein equation (eq. 4.8):

$$D_m = \frac{k \cdot T}{3 \cdot \pi \cdot \eta \cdot d_p} \quad (4.8)$$

where k = Boltzmann's constant ($\text{J} \cdot \text{K}^{-1}$), d_p = particle diameter (m) and T = absolute temperature (K). By derivation of the BTCs calculated with step input functions residence time distributions are obtained. Calculations were carried out on the Karlsruhe Institute of Technology (KIT) high performance cluster HP XC3000.

4.3 Results and Discussion

4.3.1 Core analysis by x-ray computed tomography

A thorough mineralogical and chemical analysis of the Äspö diorite can be found in the literature (Byegård et al., 1998). Here, only the most important features are summarized. The Äspö diorite can be classified as a medium-grained and porphyritic quartz monzodiorite/granodiorite with K-feldspar phenocrysts (1-2 cm) (Byegård et al., 1998). It comprises of plagioclase, K-feldspar, biotite and calcite as major minerals and of muscovite, titanite, apatite, fluorite, zircon and opaque phases (mostly Fe-containing phases, e.g. magnetite) as accessory components (Byegård et al., 1998).

The spatial dimensions of the core are 0.1352 m in length and 0.05048 m in diameter. With the μ CT setup a voxel resolution of 80 μm was achieved. By utilization of the complete μ CT dataset a connected porosity of 0.68 % and an aperture distribution of the core could be derived. As expected for a natural fracture, it possesses a complex 3D spatial geometry and fracture surface morphology (Figure 4.3). Zones where two fracture planes intersect each other (asperities) are visible heterogeneously distributed throughout the fracture. Especially in the upper third of the fracture a big asperity is visible in an area where the fracture is folded $\sim 90^\circ$ perpendicular to the z direction. One side of the core shows a relatively sharp border, while the other side has a very irregular boundary. The fracture exhibits a wedge-shaped geometry resulting in higher apertures at the more open regular left boundary and smaller apertures in the vicinity of the irregular boundary on the right side of the fracture. A possible presence of porous media (porous fracture filling material and

microcracks lower than 80 μm) at the right fracture boundary is impossible to resolve on basis of these μCT data, but cannot be excluded. This circumstance would directly impact the total volume of the fracture and thus the flow and mass transport dynamics. Additionally, the fracture walls could possess a porosity facilitating solute matrix diffusion. Since no unambiguous decision can be drawn it was decided to treat the fracture as fully open without the presence of porous media and the fracture walls were considered as impermeable for both flow and mass transport. An overview of the aperture distribution is depicted in Figure 4.3b. A mean aperture of 0.45 mm and a maximum aperture of 1.5308 mm can be derived. Approximately 56 % of the aperture values are in the range between 0.42 mm and 0.56 mm, 14% are in the range between 0.56 mm and the maximum aperture of 1.5308 mm and 28 % are distributed in the range between 0.42 mm to 0 mm (Figure 4.3b).

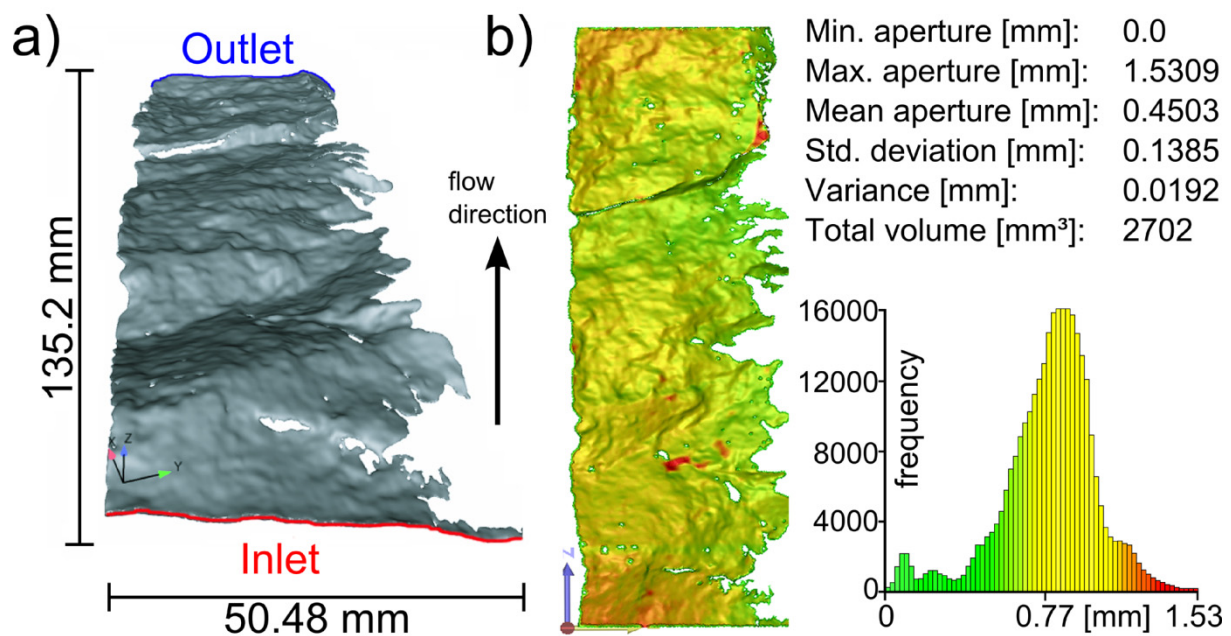


Figure 4.3: a) Rendered view of the fracture on basis of the μXCT data set showing the complex fracture geometry and morphology together with the spatial dimensions. b) Fracture aperture distribution in conjunction with a histogram of aperture and several statistical parameters of the fracture.

4.3.2 Quantum dots characterization by AsFIFFF

According to the calibration with polystyrene sulfonate standard (PSS) salt and carboxylated polystyrene nanoparticles, the hydrodynamic diameter of the QD is 11.4 ± 0.5 nm as deduced from the peak maxima position of the Cd, Se and Zn- ICP-MS fractograms which are the fingerprints of the QD core and superimpose as expected very well (Figure 4.2). A slight shift is observed for the UV-Vis fractogram recorded at 225 nm with a peak maximum position at 9.6 nm. As the UV-Vis detection be more related and affected by lipid surface coating with eventual interaction with the AsFIFFF membrane, the hydrodynamic size obtained by considering the elements constituting the core of the QD is preferred and is the value presently considered.

4.3.3 Flow modeling

Figure 4.4a shows a volume rendering plot of the simulated normalized velocity magnitude for the core. Generally speaking, the simulated 3D flow field reflects the spatial complexity of the fracture

geometry. The resulting flow field is a combination of four spatial fracture characteristics: (a) the wedge-shaped nature of the fracture, (b) the aperture variability, (c) the asperities and (d) the irregular right fracture boundary. The influence of the asperities leads to flow channeling which is obvious, e.g. in the upper third model domain where the fracture is closed to a high extent. Here, flow velocities strongly increase to its maximum value as a result of the narrowing of the flow cross sectional area. High flow velocities (red colors in Figure 4.4a) always occur in the vicinity of asperities indicating their paramount impact on the flow field. The very irregular right fracture boundary is characterized by low velocities (blue colors in Figure 4.4a) in contrast to the middle and left part of the fracture where the apertures are larger and thus higher flow velocities can be observed (green and yellow colors in Figure 4.4a). To enhance the visualization of the flow dynamics, snapshots of particle traces are presented in Figure 4.4b for three different travel times. The particles are purely

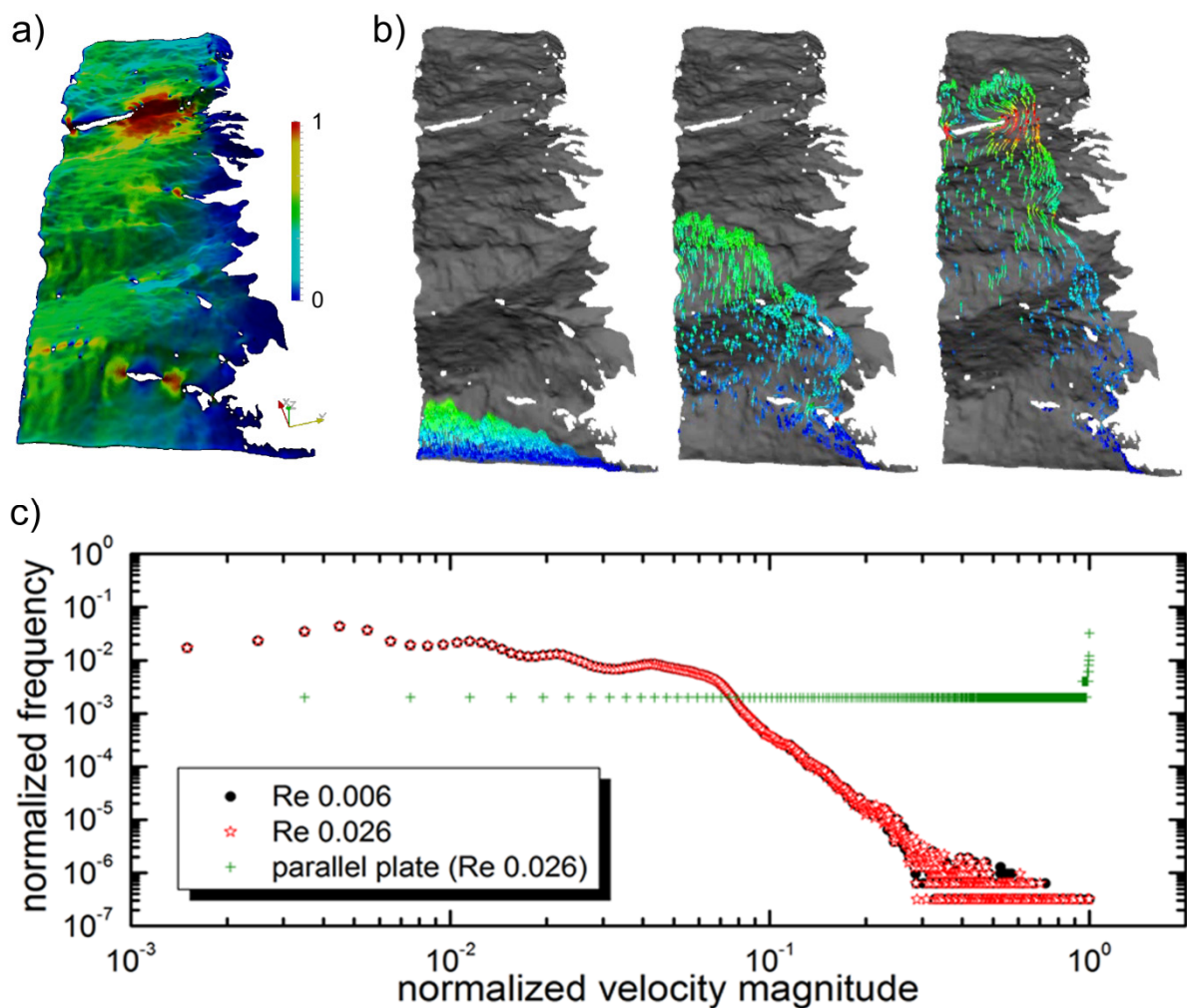


Figure 4.4: a) Normalized volume rendering plot of the flow field as calculated on basis of the μ CT data. b) Particle traces snapshots showing the heterogeneous particle spreading due to flow velocity variability. c) Normalized histogram of the flow velocities for both Re numbers. Number of bins are 1000. Frequency is normalized to total number of frequencies; velocity magnitude normalized by the maximum velocity magnitude.

transported by advection and do not exhibit any molecular diffusion. Uniformly introduced at the inlet surface the particles spread out heterogeneously due to flow velocity variability and are constraint by the flow path heterogeneity on their way through the fracture. Particles starting near the right irregular boundary where low flow velocities prevail are delayed compared to particles travelling in the middle and left part of the fracture. These low speed particles creep along the right fracture boundary and reach the outlet at much later times than the overall particle ensemble. Flow

velocity distributions are shown in Figure 4.4c as a log-log histogram for both Re numbers applied. Additionally inserted in Figure 4c, the velocity distribution for a 3D parallel plate model (3DPPM) using the mean fracture aperture is shown. While the 3DPPM exhibits a homogeneous distribution due to geometry uniformity, the distribution of the real fracture directly reflects the complex fracture geometry. The normalized frequency maximum represents the highest flow velocities in case of the 3DPPM. This is in distinct contrast to the histogram of the real 3D fracture. Here most of the flow velocities are low flow velocities and only a very small amount represents high flow velocities. By comparison of both Re numbers applied for the real fracture, it is obvious that only very little variations for the highest flow velocities occur. That is, the flow field linearly correlates to the applied pressure gradient (Darcy-type).

4.3.4 Core migration experiment

Figure 4.5 depicts the experimental breakthrough curves for both runs in conjunction with the mass transport simulation results. Table 4.1 lists further details about experimental and model parameters and results. For simplification, in the following Run#1 represents the high flux experiment ($Re = 0.026$) and Run#2 stands for the low flux experiments ($Re = 0.0058$), respectively.

4.3.4.1 Run#1

In general, both the experimental HTO and QD BTC show a pronounced tailing (Figure 4.5). The shapes of both BTCs differ from each other in such that QD show a Δt between first arrival and peak maximum of 470 s compared to a Δt of 600 s for HTO indicating a sharper leading edge for the QD's. The tailing of the HTO BTC can be approximated fairly well by fitting to a power law of $t^{-3/2}$. This type of power law is often referred to as matrix diffusion and has been observed both in field and laboratory studies (Carrera et al., 1998). Considering the Re numbers prevailing, the occurrence of matrix diffusion seems reasonable to some extent. In contrast to the HTO BTC, the QD residence time distribution is much more broadened but also characterized by a pronounced tailing. As expected for colloidal transport, the QD peak maximum arrives faster than the HTO peak maximum which is a frequent observation in both field and laboratory experiments (Geckeis et al., 2004; Schäfer et al., 2004). The calculated experimental retardation factor (R_f) for the QD peak is 0.94 based on the positions of the peak maximum time of HTO and QD (Table 4.1). This finding can be explained by the different chemical properties and physical transport behaviour of the colloids compared to solutes. In consequence, the QD BTC tailing cannot be described by the empirical matrix diffusion power law. This observation can be expected since the diffusion coefficient of the QD is almost two orders of magnitude lower than it is the case for HTO which is further reflected in the Pe number of 607 for the QD and only 10 for HTO, respectively. This indicates that the QD are more strongly influenced by advection whereas HTO exhibits a much higher impact of molecular diffusion facilitating matrix diffusion. Matrix diffusion coefficients for colloids range between $7 \cdot 10^{-18} \text{ m}^2 \cdot \text{s}^{-1}$ for 2nm to $1.5 \cdot 10^{-18} \text{ m}^2 \cdot \text{s}^{-1}$ for 100 nm colloids, respectively (Alonso et al., 2007b). Moreover, the QD are likely to be effectively hindered to diffuse into a possible porous fracture wall matrix due to other processes like e.g. size exclusion effects.

4.3.4.2 Run#2

The HTO BTC is again characterized by a sharper increase in concentration and peak maximum compared to the QD BTC. The QD BTC shows a Δt between first arrival and peak maximum of 1740 s compared to a Δt of 1370 s for HTO indicating this time a sharper leading edge for the HTO compared to the QD BTC. The tailing of the HTO can be approximated by the empirical matrix diffusion power law in line with the BTC from Run#1. The Pe number for HTO in Run#2 is 2 indicating an even

stronger impact of molecular diffusion on the transport behaviour. Consequently, the prevailing flow and transport conditions even more facilitate a diffusion of the HTO into a possible core matrix. Recoveries of HTO are within analytical uncertainty quantitative both for Run#1 and Run#2 and decrease for the QD with decreasing flow velocities from 88% in Run#1 to 68% in Run#2, respectively. This leads to the conclusion of a more pronounced interaction of the QD with the fracture surfaces in terms of sorption or filtration processes with decreasing flow velocity explaining the observed difference in the rising edge of the BTCs. Similar to Run#1, the QD BTC shows an earlier first arrival time than the HTO peak. The position of the peak maximum between the QD and HTO BTCs are almost identical (R_f QD = 0.99) showing that the mean residence times approach each other with decreasing flow velocity.

4.3.5 Transport modeling (Run#1 & Run#2)

Regarding the first arrival of the modeled BTCs, the QD BTCs for both flow velocities show an earlier arrival times compared to the HTO BTCs in line with the experimental findings. Furthermore, the position of the QD peak maximum is also shifted to earlier times compared to the HTO BTC. Again, this observation fits to the experimental findings. The overall modeled BTC positions are shifted to

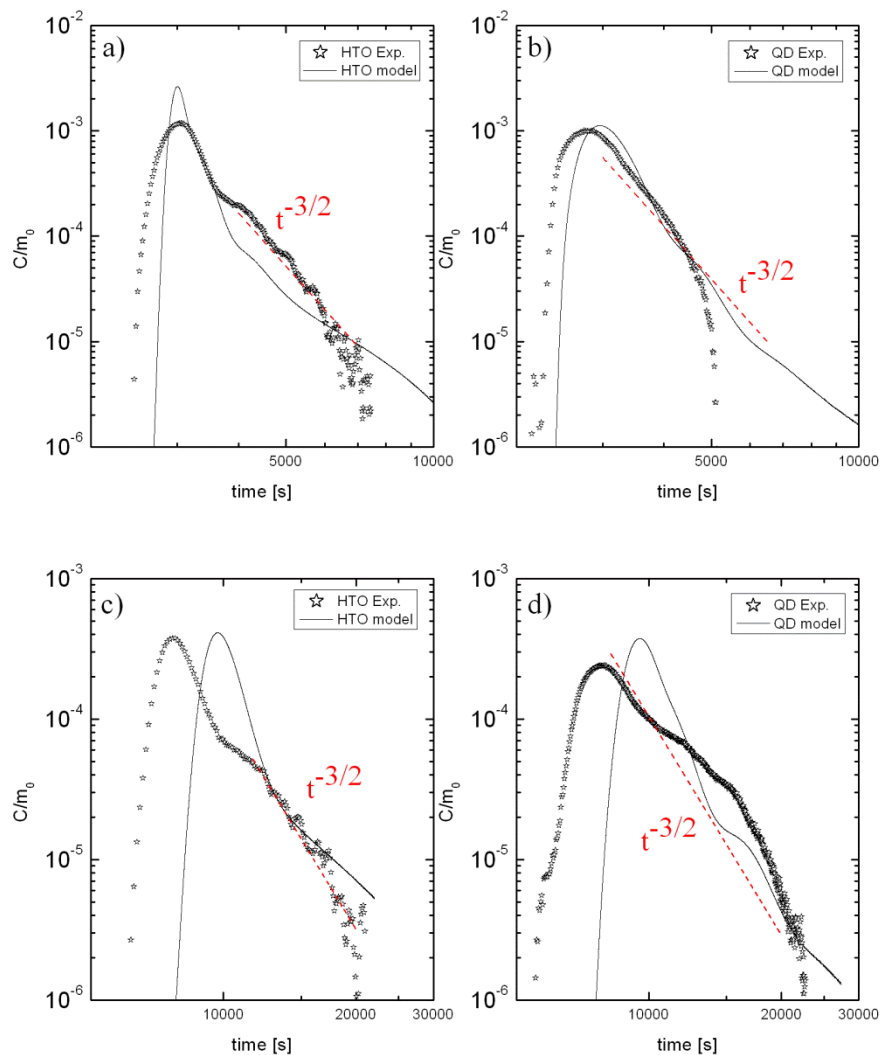


Figure 4.5: Experimentally derived BTCs (open stars) in comparison to simulated BTCs (black lines). a) HTO BTCs for Run#1 b) QD BTCs for Run#1 c) HTO BTCs for Run#2 and d) QD BTCs for Run#2. Red lines in a) and b) represents the empirical power law for matrix diffusion ($t^{-3/2}$), respectively.

later times for the lower flow velocity (Run#2) compared to the experimental BTCs, whereas for Run#1 the positions are almost comparable. Though, the R_f value of 0.98 for the simulated QD peak is slightly higher than the experimental QD R_f (0.94) in Run#1, whereas the QD R_f value of 0.99 is equal to the experimental QD R_f value (0.99). Concerning HTO, the modeled BTC (Run#1) describes the peak maximum position quite good though over-predicts the maximum normalized concentration. The modeled HTO BTC of Run#2 can reproduce the experimental maximum concentration very well and also the overall peak shape of the BTC fits satisfactorily to the experimental BTC though shifted to much later times.

In contrast, the simulated QD BTC of Run#1 describes the normalized concentration of the experimental BTC very good, but is shifted to later times as stated above. The modeled QD BTC of Run#2 shows in addition to the time shift also a higher peak maximum and the agreement to the experimental BTC in terms of predicted maximum concentrations and overall peak shape is rather poor. Here, the model exhibits a much sharper peak shape than the experimental QD BTC. The deviation in Run#2 can be explained with the observed decrease in QD recovery (Table 4.1), which would dampen the peak maximum and influence through retardation the shape of the BTC tailing.

Table 4.1: Conditions and results from migration experiments and CFD simulations.

	Run #1	Run #2
Flux [$\mu\text{l}\cdot\text{min}^{-1}$]	66.8	14.2
Re [-]	0.026	0.0058
Pe HTO[-]	10	2
Pe QD [-]	607	135
max. velocity magnitude [$\text{m}\cdot\text{s}^{-1}$]	$1.3\cdot 10^{-3}$	$2.9\cdot 10^{-4}$
volume averaged velocity magn. [$\text{m}\cdot\text{s}^{-1}$]	$5.67\cdot 10^{-5}$	$1.26\cdot 10^{-5}$
R_p (Peak max. exp. HTO) [min]	51	129
R_p (Peak max. exp. QD) [min]	48	128
R_p (Peak max. model. HTO) [min]	50	161
R_p (Peak max. model. QD) [min]	49	159
R_f exp. [-]	0.94	0.99
R_f model [-]	0.98	0.99
Recovery HTO	96%	99%
Recovery QD	88%	68%

R_p = peak elution time; R_f = retardation factor ($R_f = R_p[\text{QD}] / R_p[\text{HTO}]$)

Overall, as in the case for the experimental BTCs, the simulated residence time distributions show pronounced tailings. Since the model does not include matrix diffusion the tailing cannot be fitted to a power law of $t^{-3/2}$. Generally speaking, the observed heavy tailings in the simulated breakthrough curves can be clearly attributed solely to dispersion due to the fracture geometry and confirms the proposal made by Kosakowski (2004) that tailing of the colloids is mainly caused by the structure of the flow field and that for colloid/nanoparticle transport, matrix diffusion is of minor importance (Kosakowski, 2004).

4.3.6 Uncertainties in μCT analysis and boundary conditions

As stated above a voxel resolution of 80 μm has been achieved in the μCT analysis. In consequence, spatial features (microcracks) smaller than this threshold resolution remain unresolved and therefore excluded in the model. Moreover, the right fracture boundary may represent a porous media (porous

fracture filling) type material but is treated as open space in the model resulting in a higher void volume compared to the drill core. If this would be the case, applying the same pressure gradient in both experiments and simulations would cause higher flow velocities in the experiment due to the smaller total volume resulting in a faster arrival of the experimental BTCs. For this, more systematic simulations with varying boundary conditions and changing spatial features (erosion and dilatation of fracture surface, means adding/subtracting volume) are necessary to understand the impact of available volume in the computing domain. Furthermore, a possible matrix porosity in the vicinity of the fracture walls are not visible in the CT data and thus not taken into account in the modeling exercise. For testing this, a coupling of the transport simulations with a dual porosity approach would be useful. The experimental BTCs for HTO may indicate matrix diffusion since the tailings can be approximated with the empirical power law of $t^{-3/2}$. Assuming matrix diffusion present in the experiments would lead to a broadening of the HTO BTC compared to the calculated HTO BTC due to the lack of fracture wall porosity in the model. This deviation between the model and the experiment could explain the smaller normalized maximum concentrations in the experimental data.

Much effort has been spent to generate the best possible computational grid in terms of mesh resolution and computational resources and times, respectively. Mesh resolution studies using 1.5, 3, 5.5, 7.5, 9, 10.5 and 14 Mio. elements revealed that the mesh resolution of 10.5 Mio elements applied is sufficiently detailed to capture the flow and mass transport dynamics. Numerical diffusion/dispersion was minimized using appropriate small time steps (0.1 s) fulfilling the Courant and Neumann criterion, respectively.

Concerning boundary conditions it cannot be excluded that conditions set in the flow and transport simulation do not match exactly the conditions prevailing in the experiments. The application of a pressure inlet boundary condition correctly takes into account the influence of inlet surface geometry on fluid flow resulting in a heterogeneous velocity distribution along the inlet surface. On the other hand, a perfect uniformly introduced tracer in the simulations may not represent the real experimental conditions prevailing. It is likely that the tracer is introduced more concentrated in terms of surface area in the experiments (point source type). This circumstance should result in a narrower BTC since the tracer would not map all the fracture volume. In contrast, the experimental BTCs are always broadened compared to the simulated BTCs. Here, the occurrence of matrix diffusion could be the responsible process for HTO leading to the broadening of the experimental BTCs. In case of the QD, interaction with the fracture surfaces would cause a broadening of the BTC which should be more pronounced in the low flow experiments.

4.4 Conclusions

Overall, our study clearly shows the mobility of the ENP's (hydrophilic QDs) in a natural single fracture under natural Grimsel groundwater conditions representing glacial melt water-type hydrogeochemistry. Concerning the core migration experiments, a decrease in QD recovery is observed with lower flow velocity ($1.5 \text{ m}\cdot\text{d}^{-1}$) indicating a possible sorption/retardation to the fracture wall or filtration effects. Simulated HTO and QD breakthrough curves exhibit heavy tailing reflecting univocally the influence of fracture heterogeneity on flow velocity distributions and on mass transport. The additional differences observed in the experimental HTO BTCs may be attributed to matrix diffusion. Despite the higher computational and technical effort in creating a 3D model on basis of μCT data, the results provide a step forward towards a more fundamental understanding of the processes governing fluid flow and mass transport in real single fractures. Furthermore, this approach facilitates the interpretation and analysis of migration experiments which most often represent black box type experiments.

5 Major conclusions

Regarding the main goals of the prevailing thesis to enhance the understanding of the effect of kinetically controlled retardation and retention processes like sorption and reduction as well as flow path heterogeneity on radionuclide migration, one can draw the following major conclusions.

- The process of sorptive reduction of U(VI) to sparingly soluble tetravalent uranium by structural bound Fe(II) in magnetite shows fast kinetics (hours to a few days contact time). A clear correlation between the Fe(II) content on the magnetite surface and the amount of U(VI) was observed, that is, increasing U(IV) with increasing Fe(II). Moreover, a congruency between the measured $E_{h(SHE)}$ and the U valence state can partly be derived within the analytical uncertainties of the redox potential measurements. That is, a prediction of uranium oxidation states based on thermodynamics is feasible. Thus, secondary phases as the stainless steel corrosion product magnetite can have beneficial effects on radionuclide migration as an effective retardation pathway for redox sensitive radionuclides. Beside, the studies on U(VI) maghemite sorption show that oxidized surfaces can possess long-term reduction capacities further enhancing radionuclide retention.
- Concerning the colloid-facilitated radionuclide transport, the batch sorption reversibility studies revealed the significance of kinetically controlled radionuclide desorption from the colloidal phase and subsequent sorption to the fracture filling materials (independent of the mineralogy and/or size fraction). By this process, initially colloidal associated radionuclides like the tri- and tetravalent radionuclides Th, Pu and Am are effectively retarded leading to an increase in the residence time. These reversibility results need to be included in codes for simulating colloid-facilitated radionuclide transport to reduce the conservatism and degree of uncertainties in input parameters leading to an improvement in the quality of the simulation results. Beyond, colloid-facilitated transport is of no concern for U(VI), Np(V) and Tc(VII) under the chosen experimental conditions which showed no attachment to montmorillonite colloids.
- The effect of flow path heterogeneity/fracture geometry on fluid flow and solute transport has been investigated using 3D CFD simulations under the application of a μ CT dataset of a single fracture in a diorite drill core. Due to the fracture geometry, CFD simulations predict the evolution of a complex flow field with a widespread flow velocity distribution. As a consequence simulated HTO and QD breakthrough curves exhibit heavy tailings reflecting univocally the influence of fracture heterogeneity on flow velocity distribution and mass transport. Thus, it can be clearly shown, that fracture geometry can effectively lead to retardation of solutes and colloidal phases solely on basis of hydrodynamic processes without considering physicochemical processes like matrix diffusion, sorption or reduction. The core migration studies using engineered nanoparticles (quantum dots (QD)) show a colloidal mobility under the given hydraulic and geochemical conditions in the fractured core from Äspö (Sweden). A decrease in QD recovery with lower flow velocity indicates a possible sorption/retardation to the fracture surface or filtration effects. In contrast, it could be shown that Febex bentonite colloids and associated Am, Th and Pu are almost immobile (< 5% recovery) under geochemical conditions favoring the stability of colloids in solution. The immobility of bentonite colloids is currently explained by a diffusive leaching of the core matrix pore water having still the original Äspö KXTT4 chemical signature to the fracture surface, providing a divalent cation pool resulting in high bentonite colloid fracture surface attachment probability/collision efficiency α . This explanation indicates the importance of geochemical disequilibrium conditions in contrast to equilibrium conditions which are most often assumed for simplicity. Tc(VII) is transported comparable to HTO consistent with the pe/pH conditions whereas Np shows retardation most likely due to interaction with the fracture surface. The results highlight that additional detailed studies have to be launched in

5 Major conclusions

order to investigate this colloid retention process under glacial melt water conditions and also the potential impact of this divalent cation source on bentonite erosion.

6 Open questions and future directions of research

- Bentonite sorption reversibility studies

The laboratory experiments on the bentonite sorption reversibility revealed desorption kinetics for the colloid associated tri- and tetravalent radionuclides Th, Pu and Am. Unfortunately, there are relatively high uncertainties in the analytical determination (ICP-MS) of the Al concentrations as indicator for the structural Al of the bentonite colloids, as well as the dissolved Al concentration in the Grimsel groundwater applied. A promising approach to circumvent these uncertainties lies in the application of Zn (and/or Ni)-labeled montmorillonite where Zn (Ni) substitutes the Mg in the octahedral layers of the clay mineral. Therefore, experiments using the same conditions as presented in the present thesis exchanging the FEBEX bentonite colloids with Zn-labeled colloids could reduce the uncertainties in the presented results.

Moreover, the results obtained in this study show that the reversibility kinetics determined critically depend on the experimental duration. An expansion of the dataset to longer contact times (residence time) would provide more confidence in the kinetic rates obtained.

- Sorptive reduction of uranium

Since pentavalent U could not be verified doubtlessly further experiments under environmentally relevant total uranium concentrations are needed to elucidate the presence and stability of U(V) and thus gain information on the longterm relevance of U(V) and their implications. The application of an in-situ redox cell for XAS measurements may provide additional insights into the process of uranium reduction (sorptive reduction) and kinetics involved. If applicable, EXAFS analysis may shed light on the chemical structure of the pentavalent uranium to distinguish between a sorbed U(V) species or a precipitated and incorporated U-Fe mineral phase.

- Core migration experiments

Results of the migration experiments using a drill core from Äspö (Sweden) showed a high mobility of especially Tc and to a minor extent Np, whereas U showed no mobility at all. The formation/precipitation of a Ca-U solid phase (e.g. Ca-Uranate) is postulated as explanation for this immobility due to the fact that Ca may still leach from the core matrix into the fracture indicating non-equilibrium of the core matrix with the Grimsel groundwater applied. Furthermore, these higher Ca concentrations may lead to an increase in the attachment probability of the bentonite colloids explaining their immobility (and thus the immobility of the bentonite associated radionuclides Th, Pu and Am). Therefore it seems that longer times (> several months) are needed to establish equilibrium conditions between the core matrix and the groundwater.

Moreover, the application of longer residence times (lower flow velocities) in the migration experiments are necessary to directly compare the results of the bentonite sorption reversibility experiments to the migration studies evaluating their influence in real dynamic systems.

Further experiments under the application of anoxic obtained drill cores would enlighten the influence of redox conditions on the migration of redox sensitive radionuclides like Tc, U or Np. Though the experiments presented in this thesis have been carried out under Ar atmosphere no

attempts have been undertaken to avoid oxygen contact to the drill core before the start of the experiments. Thus, the redox capacity of the drill core was likely minimized.

Additionally, to elucidate the role of fracture roughness and surface charge heterogeneity on colloid retention, the available μ CT dataset of the natural fracture in the drill core can be used for the realization of a fracture replica in polyethylene by means of rapid-prototyping techniques. Besides, migration experiments on this replica could be used to study the impact of matrix diffusion when compared to the real drill core where matrix porosity and porous media (fracture filling material) has to be taken into account.

- Modeling

The modeling study using a 3D model on basis of μ CT data clearly revealed the influence of fracture heterogeneity on flow and mass transport. The comparison between the simulations and the migration experiments showed some discrepancies which can be referred to uncertainties in the μ CT measurements and the boundary conditions in both the model and the experiments. Here a modified experimental and simulation setup could reduce these uncertainties and enhance their comparison.

The application of Discrete Phase Models (DPM) to simulate colloidal particles would be a step forward towards a more realistic treatment of their transport dynamics (particle tracking; calculation of particle trajectories in a Lagrangian frame). These kinds of models allow, among others, the incorporation of particle attachment possibilities, that is, reversible/irreversible sorption of the particles to surfaces can be taken into account. Furthermore, particle tracking along single streamlines may be used for a simplified reactive transport modeling approach.

Since the transport simulations carried out in this thesis are purely non-reactive, an extension to reactive transport simulations is the next step. Here, coupling of the simulated flow field to an external geochemical code (e.g. CHEPROO (Bea et al., 2009)) would allow the simulation of reactive transport. A drawback would be the high computational resources needed to carry out reactive transport calculations on a computational mesh consisting of several million of elements. This circumstance highlights the need of upscaling of the simulations to a lesser spatial resolution, e.g. into 2D or even 1D.

In terms of safety assessment of a nuclear waste disposal and strictly speaking, the stability of the bentonite barrier the presented 3D flow field in a natural single fracture realized in this thesis would allow the possibility to simulate bentonite erosion of a virtual clay plug in comparison to results obtained with 2D/cubic law simplifications of the 3D flow field. This would facilitated the evaluation of the impact on the bentonite erosion for uncertainty analysis

7 References

- Albarran N., Missana T., Alonso U., Garcia-Gutierrez M., and Lopez-Torrubia T. (2009) Dynamic study of bentonite colloid retention in a smooth granite fracture under unfavorable electrostatic conditions. In: Buckau, G., Kienzler, B., Duro, L., Montoya, V., and Delos, A. Eds.) *4th Annual Workshop Proceeding of integrated project "Fundamental processes of Radionuclide Migration" - 6th EC FP IP FUNMIG, FZKA report 7461.*
- Alonso U., Missana T., and Garcia-Gutierrez M. (2008) Experimental approach to study the bentonite colloid generation source term in different geochemical conditions. In: Buckau, G., Kienzler, B., Duro, L., Montoya, V., and Delos, A. Eds.) *3rd Annual workshop Proceedings of IP FUNMIG, NDA report.* Nuclear Decommissioning Authority (NDA), Edinburgh (Scotland).
- Alonso U., Missana T., Patelli A., Ceccato D., Albarran N., Garcia-Gutierrez M., Lopez-Torrubia T., and Rigato V. (2009) Quantification of Au nanoparticles retention on a heterogeneous rock surface. *Colloids and Surfaces a-Physicochemical and Engineering Aspects* **347**, 230-238.
- Alonso U., Missana T., Patelli A., and Rigato V. (2007a) Bentonite colloid diffusion through the host rock of a deep geological repository. *Physics and Chemistry of the Earth* **32**, 469-476.
- Alonso U., Missana T., Patelli A., Rigato V., and Ravagnan J. (2007b) Colloid diffusion in crystalline rock: An experimental methodology to measure diffusion coefficients and evaluate colloid size dependence. *Earth. Planet. Sci. Lett.* **259**, 372-383.
- Altmann S. (2009) RTD Component 3. In: Buckau, G., Kienzler, B., Duro, L., Montoya, V., and Delos, A. Eds.) *4th Annual Workshop Proceeding of integrated project "Fundamental processes of Radionuclide Migration" - 6th EC FP IP FUNMIG, FZKA report 7461.*
- Ansys (2009) ANSYS FLUENT 12.1.4 User Guide.
- Antonio M. R. and Sonderholm L. (1994) *The Chemistry of the Actinides and Transactinide Elements.* Springer, New York.
- Appelo C. a. J. and Postma D. (1996) *Geochemistry, groundwater and pollution.* A.A. Balkema, Rotterdam.
- Aris R. (1956) On the dispersion of a solute in a fluid flowing through a tube. *Proceedings of the Royal Society of London Series a-Mathematical and Physical Sciences* **235**, 67-77.
- Arnold T. and Baumann N. (2009) Boltwoodite $[K(UO_2)(SiO_3OH)(H_2O)_{1.5}]_2[(UO_2)_3O^{2-}(OH)_3]_2 \cdot 7H_2O$ characterized by laser fluorescence spectroscopy. *Spectrochimica Acta Part a-Molecular and Biomolecular Spectroscopy* **71**, 1964-1968.
- Aronniemi M., Sainio J., and Lahtinen J. (2005) Chemical state quantification of iron and chromium oxides using XPS: the effect of the background subtraction method. *Surf. Sci.* **578**, 108-123.
- Artinger R., Marquardt C. M., Kim J. I., Seibert A., Trautmann N., and Kratz J. V. (2000) Humic colloid-borne Np migration: influence of the oxidation state. *Radiochim. Acta* **88**, 609-612.
- Artinger R., Schuessler W., Schäfer T., and Kim J. I. (2002) A kinetic study of Am(III)/humic colloid interactions. *Environ. Sci. Technol.* **36**, 4358-4363.
- Baborowski M. and Bozau E. (2006) Impact of former mining activities on the uranium distribution in the River Saale (Germany). *Appl. Geochem.* **21**, 1073-1082.
- Backhus D. A., Ryan J. N., Groher D. M., Macfarlane J. K., and Gschwend P. M. (1993) Sampling colloids and colloid associated contaminants in groundwater. *Ground Water* **31**, 466-479.
- Baik M. H., Cho W. J., and Hahn P. S. (2007) Erosion of bentonite particles at the in-terface of a compacted bentonite and a fractured granite. *Engineering Geology* **91**, 229-239.
- Baik M. H., Lee S. Y., Lee J. K., Kim S. S., Park C. K., and Choi J. W. (2008) Review and Compilation of Data on Radionuclide Migration and Retardation for the Performance Assessment of a HLW Repository in Korea. *Nuclear Engineering and Technology* **40**, 593-606.
- Barcelona M. J., Varljen M. D., Puls R. W., and Kaminski D. (2005) Groundwater-purging and sampling methods: History vs. hysteria. *Ground Water Monit. Rem.* **25**, 52-62.

- Bargar J. R., Reitmeyer R., Lenhart J. J., and Davis J. A. (2000) Characterization of U(VI)-carbonato ternary complexes on hematite: EXAFS and electrophoretic mobility measurements. *Geochim. Cosmochim. Acta* **64**, 2737-2749.
- Barnett M. O., Jardine P. M., Brooks S. C., and Selim H. M. (2000) Adsorption and transport of uranium(VI) in subsurface media. *Soil Sci. Soc. Am. J.* **64**, 908-917.
- Batchelor G. K. (1967) *An Introduction to Fluid Dynamics*. Cambridge University Press, Cambridge.
- Bates J. K., Bradley J. P., Teetsov A., Bradley C. R., and Tenbrink M. B. (1992) Colloid Formation During Waste Form Reaction - Implications for Nuclear Waste-Disposal. *Science* **256**, 649-651.
- Bathe K. J., Zhang H., and Ji S. H. (1999) Finite element analysis of fluid flows fully coupled with structural interactions. *Computers & Structures* **72**, 1-16.
- Bea S. A., Carrera J., Ayora C., Batlle F., and Saaltink M. W. (2009) CHEPROO: A Fortran 90 object-oriented module to solve chemical processes in Earth Science models. *Computers & Geosciences* **35**, 1098-1112.
- Behrends T. and Van Cappellen P. (2005) Competition between enzymatic and abiotic reduction of uranium(VI) under iron reducing conditions. *Chem. Geol.* **220**, 315-327.
- Bekhit H. M. and Hassan A. E. (2005) Stochastic modeling of colloid-contaminant transport in physically and geochemically heterogeneous porous media. *Water Resour. Res.* **41**.
- Bekhit H. M. and Hassan A. E. (2007) Subsurface contaminant transport in the presence of colloids: Effect of nonlinear and nonequilibrium interactions. *Water Resour. Res.* **43**.
- Bellenger J.-P. and Staunton S. (2008) Adsorption and desorption of ⁸⁵Sr and ¹³⁷Cs on reference minerals, with and without inorganic and organic surface coatings. *J. Environ. Radioact.* **99**, 831-840.
- Bera S., Sali S. K., Sampath S., Narasimhan S. V., and Venugopal V. (1998) Oxidation state of uranium: an XPS study of alkali and alkaline earth uranates. *J. Nucl. Mater.* **255**, 26-33.
- Blatt H. and Tracy R. J. (1996) *Petrology*. Freeman, New York.
- Bodin J., Delay F., and De Marsily G. (2003) Solute transport in a single fracture with negligible matrix permeability: 1. fundamental mechanisms. *Hydrogeology Journal* **11**, 418-433.
- Bosshard E., Zimmerli B., and Schlatter C. (1992) Uranium in the diet - Risk Assessment of its nephrotoxicity and radiotoxicity. *Chemosphere* **24**, 309-321.
- Bouby M., Filby A., Geckeis H., Geyer F., Götz R., Hauser W., Huber F., Kienzler B., Kunze P., Küntzel M., Lützenkirchen J., Noseck U., Plaschke M., Pudewills A., Schäfer T., Seher H., and Walther C. (2010) Colloid/ Nanoparticle formation and mobility in the context of deep geological nuclear waste disposal (Project KOLLORADO-1; Final report). In: Schäfer, T. and Noseck, U. Eds.) *FZKA report 7515*. Forschungszentrum Karlsruhe, Karlsruhe.
- Bouby M., Geckeis H., Lützenkirchen J., Mihai S., and Schäfer T. (2009) Interaction of bentonite colloids with Eu and Th in presence of humic acid: A Flow Field- Flow Fractionation study. In: Buckau, G., Kienzler, B., Duro, L., Montoya, V., and Delos, A. Eds.) *4th Annual Workshop Proceeding of integrated project "Fundamental processes of Radionuclide Migration" - 6th EC FP IP FUNMIG*, FZKA report 7461.
- Bouby M., Geckeis H., Manh T. N., Yun J. I., Dardenne K., Schäfer T., Walther C., and Kim J. I. (2004) Laser-induced breakdown detection combined with asymmetrical flow field-flow fractionation: application to iron oxi/hydroxide colloid characterization. *J. Chromatogr. A* **1040**, 97-104.
- Boutt D. F., Grasselli G., Fredrich J. T., Cook B. K., and Williams J. R. (2006) Trapping zones: The effect of fracture roughness on the directional anisotropy of fluid flow and colloid transport in a single fracture. *Geophys. Res. Lett.* **33**.
- Brevet J., Claret F., and Reiller P. E. (2009) Spectral and temporal luminescent properties of Eu(III) in humic substance solutions from different origins. *Spectrochimica Acta Part a-Molecular and Biomolecular Spectroscopy* **74**, 446-453.
- Bruggeman C., Maes A., and Vancluysen J. (2007) The interaction of dissolved Boom Clay and Gorleben humic substances with selenium oxyanions (selenite and selenate). *Appl. Geochem.* **22**, 1371-1379.

- Bruggeman C., Maes A., Vancluysen J., and Vandenmussele P. (2005) Selenite reduction in Boom clay: Effect of FeS₂, clay minerals and dissolved organic matter. *Environ. Pollut.* **137**, 209-221.
- Bruno J., Grenthe I., and Robouch P. (1989) Studies of metal carbonate equilibria. 20. Formation of tetra(carbonato)uranium(IV) ion, U(CO₃)₄⁴⁻, in hydrogen carbonate solutions. *Inorg. Chim. Acta* **158**, 221-226.
- Buck E. C. and Bates J. K. (1999) Microanalysis of colloids and suspended particles from nuclear waste glass alteration. *Appl. Geochem.* **14**, 635-653.
- Buck E. C., Finn P. A., and Bates J. K. (2004) Electron energy-loss spectroscopy of anomalous plutonium behaviour in nuclear waste materials. *Micron* **35**, 235-243.
- Buck E. C. and Wittman R. S. (2009) The Formation and Modeling of Colloids From the Corrosion of Nuclear Waste Forms. *Scientific Basis for Nuclear Waste Management XXXII* **1124**, 509-518.
- Buckau G. (2004) Humic substances in performance assessment of nuclear waste disposal: actinide and iodine migration in the far-field : 2nd technical progress report Forschungszentrum Karlsruhe, Karlsruhe.
- Buckau G. (2005) Origin, stability and mobility of humic colloids in Äspö groundwater: Feasibility study. In: Laaksoharju, M. and S., W. Eds.) *The Colloid investigations conducted at the Äspö Hard Rock laboratory during the years 2000-2004*. SKB report, Appendix #4.
- Burns P. C. (2005) U⁶⁺ minerals and inorganic compounds: Insights into an expanded structural hierarchy of crystal structures. *Can. Mineral.* **43**, 1839-1894.
- Buzzi O., Boulon M., Deleruyelle F., and Besnus F. (2008) Hydromechanical behaviour of rock-bentonite interfaces under compression. *Rock Mechanics and Rock Engineering* **41**, 343-371.
- Byegård J., Johansson H., Skålberg M., and Tullborg E.-L. (1998) The interaction of sorbing and non-sorbing tracers with different Äspö rock types. Sorption and diffusion experiments in the laboratory scale. SKB Technical report TR-98-18. Svensk Kärnbränslehantering AB, Stockholm, Sweden.
- Cardenas M. B., Slottke D. T., Ketcham R. A., and Sharp J. M., Jr. (2009) Effects of inertia and directionality on flow and transport in a rough asymmetric fracture. *J. Geophys. Res.* **114**, B06204.
- Carrera J., Sánchez-Vila X., Benet I., Medina A., Galarza G., and Guimerà J. (1998) On matrix diffusion: formulations, solution methods and qualitative effects. *Hydrogeology Journal* **6**, 178-190.
- Chapuis R. P. (2002) The 2000 R.M. Hardy Lecture: Full-scale hydraulic performance of soil-bentonite and compacted clay liners. *Canadian Geotechnical Journal* **39**, 417-439.
- Chernyshova I. V., Hochella Jr M. F., and Madden A. S. (2007) Size-dependent structural transformations of hematite nanoparticles. 1. Phase transition. *PCCP* **9**, 1736-1750.
- Chheda P., Grasso D., and Van Oss C. J. (1992) Impact of ozone on the stability of montmorillonite suspensions. *J. Colloid Interface Sci.* **153**, 226-236.
- Chrysikopoulos C. V. and Abdel-Salam A. (1997) Modeling colloid transport and deposition in saturated fractures. *Colloids Surf., A* **121**, 189 - 202.
- Claret F., Schäfer T., Brevet J., and Reiller P. E. (2008) Fractionation of Suwannee River Fulvic Acid and Aldrich Humic Acid on α -Al₂O₃: Spectroscopic Evidence. *Environ. Sci. Technol.* **42**, 8809-8815.
- Claret F., Schäfer T., Rabung T., Wolf M., Bauer A., and Buckau G. (2005) Differences in properties and Cm(III) complexation behaviour of isolated humic and fulvic acid derived from Opalinus clay and Callovo-Oxfordian argillite. *Appl. Geochem.* **20**, 1158-1168.
- Comans R. N. J. (1987) Adsorption, desorption and isotopic exchange of cadmium on illite: evidence for complete reversibility. *Water Res.* **21**, 1573-1576.
- Comans R. N. J., Haller M., and Depreter P. (1991) Sorption of Cesium on Illite - Nonequilibrium Behaviour and Reversibility. *Geochim. Cosmochim. Acta* **55**, 433-440.
- Contardi J. S., Turner D. R., and Ahn T. M. (2001) Modeling colloid transport for performance assessment. *J. Contam. Hydrol.* **47**, 323-333.
- Coppin F., Castet S., Berger G., and Loubet M. (2003) Microscopic reversibility of Sm and Yb sorption onto smectite and kaolinite: Experimental evidence. *Geochim. Cosmochim. Acta* **67**, 2515-2527.

- Corapcioglu M. Y. and Jiang S. (1993) Colloid-Facilitated Groundwater Contaminant Transport. *Water Resour. Res.* **29**, 7, 2215 - 2226.
- Cornell R. M. and Schwertmann U. (1996) *The Iron Oxides -structure, properties, reactions, occurrence and uses-*. VCH-Verlag, Weinheim.
- Courdouan A., Christl I., Meylan S., Wersin P., and Kretzschmar R. (2007a) Characterization of dissolved organic matter in anoxic rock extracts and in-situ pore water of the Opalinus Clay. *Appl. Geochem.* **22**, 2926-2939.
- Courdouan A., Christl I., Meylan S., Wersin P., and Kretzschmar R. (2007b) Isolation and characterization of dissolved organic matter from the Callovo-Oxfordian formation. *Appl. Geochem.* **22**, 1537-1548.
- Courdouan A., Christl I., Rabung T., Wersin P., and Kretzschmar R. (2008) Proton and Trivalent Metal Cation Binding by Dissolved Organic Matter in the Opalinus Clay and the Callovo-Oxfordian Formation. *Environ. Sci. Technol.* **42**, 5985-5991.
- Davis C. J., Eschenazi E., and Papadopoulos K. D. (2002) Combined effects of Ca²⁺ and humic acid on colloid transport through porous media. *Colloid. Polym. Sci.* **280**, 52-58.
- Davis J. A., Meece D. E., Kohler M., and Curtis G. P. (2004) Approaches to surface complexation modeling of uranium(VI) adsorption on aquifer sediments. *Geochim. Cosmochim. Acta* **68**, 3621-3641.
- De Koning A. and Comans R. N. J. (2004) Reversibility of radiocaesium sorption on illite. *Geochim. Cosmochim. Acta* **68**, 2815-2823.
- Degueldre C., Aeberhard P., Kunze P., and Bessho K. (2009) Colloid generation/elimination dynamic processes: Toward a pseudo-equilibrium? *Colloids and Surfaces a-Physicochemical and Engineering Aspects* **337**, 117-126.
- Degueldre C., Pfeiffer H.-R., Alexander W., Wernli B., and Bruetsch R. (1996) Colloid properties in granitic groundwater systems. I: Sampling and characterisation. *Appl. Geochem.* **11**, 677-695.
- Degueldre C., Scholtis A., and Thomas B. (1998) Opalinus clay groundwaters and colloids. A sampling exercise at Mt. Terri (June/July 1997). Analytical results.
- Delos A., Walther C., Schäfer T., and Buchner S. (2008) Size dispersion and colloid mediated radionuclide transport in a synthetic porous media. *J. Colloid Interface Sci.* **324**, 212-215.
- Denecke M. A. (2006) Actinide speciation using X-ray absorption fine structure spectroscopy. *Coord. Chem. Rev.* **250**, 730-754.
- Denovio N. M., Saiers J. E., and Ryan J. N. (2004) Colloid movement in unsaturated porous media: recent advances and future directions. *Vadose Zone Journal* **3**, 338-351.
- Dentz M., Cortis A., Scher H., and Berkowitz B. (2004) Time behaviour of solute transport in heterogeneous media: transition from anomalous to normal transport. *Advances in Water Resources* **27**, 155-173.
- Derjaguin B. V. and Landau L. (1941) *Acta Physicochim. URSS* **14**, 633.
- Desbois G., Urai J. L., and Kukla P. A. (2009) Morphology of the pore space in claystones - evidence from BIB/FIB ion beam sectioning and cryo-SEM observations. *eEarth* **4**, 15-22.
- Detwiler R. L., Rajaram H., and Glass R. J. (2000) Solute transport in variable-aperture fractures: An investigation of the relative importance of Taylor dispersion and macrodispersion. *Water Resour. Res.* **36**, 1611-1625.
- Docrat T. I., Mosselmans J. F. W., Charnock J. M., Whiteley M. W., Collison D., Livens F. R., Jones C., and Edmiston M. J. (1999) X-ray absorption spectroscopy of tricarbonatodioxouranate(V), UO₂(CO₃)₃⁵⁻, in aqueous solution. *Inorg. Chem.* **38**, 1879-1882.
- Duff M. C. and Amrhein C. (1996) Uranium(VI) adsorption on goethite and soil in carbonate solutions. *Soil Sci. Soc. Am. J.* **60**, 1393-1400.
- Duff M. C., Coughlin J. U., and Hunter D. B. (2002) Uranium co-precipitation with iron oxide minerals. *Geochim. Cosmochim. Acta* **66**, 3533-3547.
- Dzombak D. A. and Morel F. M. M. (1990) *Surface complexation modeling - hydrous ferric oxide*. Wiley & Sons, New York.

- EFSA (2009) Scientific Opinion of the Panel on Contaminants in the Food Chain on a request from German
- Federal Institute for Risk Assessment (BfR) on uranium in foodstuff, in particular mineral water. *The EFSA Journal* **1018**, 1-59.
- El Aamrani F. C., T.; De Pablo, J. (1999) Experimental and modeling study of the interaction between uranium(VI) and magnetite - TR-99-21. SKB.
- Enzmann F. and Kersten M. (2006) X-ray computed micro tomography (μ -XRT) results of a granitic drill core. In: Reiller, P., Buckau, G., Kienzler, B., and Duro, L. Eds.), *1st Annual workshop Proceedings of IP FUNMIG, report CEA R-6122*. Commissariat a l'energie atomique (CEA), Gif sur Yvette (France).
- EPA (2011) <www.epa.gov/radiation/radionuclides/uranium.html>.
- Ertekin T., Abou-Kaseem J. H., and King G. R. (2001) *Basic Applied Reservoir Simulation; SPE Text Book Series Vol. 7*, Richardson, Texas.
- Felmy A. R., Rai D., Schramke J. A., and Ryan J. L. (1989) The Solubility of Plutonium Hydroxide in Dilute-Solution and in High-Ionic-Strength Chloride Brines. *Radiochimica Acta* **48**, 29-35.
- Filby A. (2009) Interaction of colloids with mineral surfaces: a microscopical and nanoscopical approach. PhD thesis, Universität Fridericiana Karlsruhe (TH).
- Filby A., Plaschke M., Geckeis H., and Bosbach D. (2009a) Interaction of carboxylated latex colloids with mineral surfaces studied by AFM force spectroscopy. *Geochim. Cosmochim. Acta* **73**, A375-A375.
- Filby A., Plaschke M., Geckeis H., and Bosbach D. (2009b) Interaction of latex colloids with mineral surfaces and Grimsel granodiorite. In: Buckau, G., Kienzler, B., Duro, L., Montoya, V., and Delos, A. Eds.) *4th Annual Workshop Proceeding of integrated project "Fundamental processes of Radionuclide Migration" - 6th EC FP IP FUNMIG, FZKA report 7461*.
- Filby A., Plaschke M., Geckeis H., and Fanghänel T. (2008) Interaction of latex colloids with mineral surfaces and Grimsel granodiorite. *J. Contam. Hydrol.* **102**, 273-284.
- Flügge J., Küntzel M., Schäfer T., Gaus I., and Noseck U. (2010) Modeling colloid-bound radionuclide transport at the Grimsel Test Site *International Groundwater Symposium by IAHR, Valencia (Spain)*.
- Galunin E., Alba M. D., Aviles M. A., Santos M. J., and Vidal M. (2009) Reversibility of La and Lu sorption onto smectites: Implications for the design of engineered barriers in deep geological repositories. *J. Hazard. Mater.* **172**, 1198-1205.
- Galunin E., Alba M. D., Avilés M. A., Santos M. J., and Vidal M. Reversibility of La and Lu sorption onto smectites: Implications for the design of engineered barriers in deep geological repositories. *J. Haz. Materials* In Press, Corrected Proof.
- Gates W. P., Bouazza A., and Churchman G. J. (2009) Bentonite Clay Keeps Pollutants at Bay. *Elements* **5**, 105-110.
- Geckeis H. and Rabung T. (2008) Actinide geochemistry: From the molecular level to the real system. *J. Contam. Hydrol.* **102**, 187-195.
- Geckeis H., Schäfer T., Hauser W., Rabung T., Missana T., Deguedre C., Möri A., Eikenberg J., Fierz T., and Alexander W. R. (2004) Results of the Colloid and Radionuclide Retention experiment (CRR) at the Grimsel Test Site (GTS), Switzerland -Impact of reaction kinetics and speciation on radionuclide migration-. *Radiochimica Acta* **92**, 765-774.
- Glaus M. A., Baeyens B., Lauber M., Rabung T., and Van Loon L. R. (2005) Influence of water-extractable organic matter from Opalinus Clay on the sorption and speciation of Ni(II), Eu(III) and Th(IV). *Appl. Geochem.* **20**, 443-451.
- Grambow B., Smailos E., Geckeis H., Müller R., and Hentschel H. (1996) Sorption and reduction of uranium(VI) on iron corrosion products under reducing saline conditions. *Radiochimica Acta* **74**, 149-154.
- Grasso D., Subramaniam K., Butkus M., Strevett K., and Bergendahl J. (2002) A review of non-DLVO interactions in environmental colloidal systems. *Re/Views in Environmental Science & Bio/Technology* **1**, 17-38.

- Grenthe I., Ferri D., Salvatore F., and Riccio G. (1984) Studies on metal carbonate equilibria .10. A solubility study of the complex-formation in the uranium(VI) water carbon-dioxide (G) system at 25-degrees-C. *Journal of the Chemical Society-Dalton Transactions*, 2439-2443.
- Grenthe I., Stumm W., Laaksuharju M., Nilsson A. C., and Wikberg P. (1992) Redox potentials and redox reactions in deep groundwater systems. *Chem. Geol.* **98**, 131-150.
- Grisak G. E. and Pickens J. F. (1980) Solute transport through fractured media. 1. The effect of matrix diffusion. *Water Resour. Res.* **16**, 719-730.
- Grosvenor A. P., Kobe B. A., Biesinger M. C., and McIntyre N. S. (2004) Investigation of multiplet splitting of Fe 2p XPS spectra and bonding in iron compounds. *Surf. Interface Anal.* **36**, 1564-1574.
- Guillaumont R., Fanghänel T., Fuger J., Grenthe I., Neck V., Palmer D. A., and Rand M. H. (2003) *Update on the chemical thermodynamics of uranium, neptunium, plutonium, americium and technetium*. Elsevier B.V., Amsterdam, The Netherlands.
- Hauser W., Geckeis H., Kim J. I., and Fierz T. (2002) A mobile laser-induced breakdown detection system and its application for the in-situ-monitoring of colloid migration. *Colloids and Surfaces a-Physicochemical and Engineering Aspects* **203**, 37-45.
- Heidmann I., Christl I., and Kretzschmar R. (2005) Sorption of Cu and Pb to kaolinite-fulvic acid colloids: Assessment of sorbent interactions. *Geochim. Cosmochim. Acta* **69**, 1675-1686.
- Hetzel F. and Doner H. E. (1993) Some Colloidal Properties of Beidellite - Comparison with Low and High Charge Montmorillonites. *Clays Clay Miner.* **41**, 453-460.
- Heuer J. K. and Stubbins J. F. (1999) An XPS characterization of FeCO₃ films from CO₂ corrosion. *Corros. Sci.* **41**, 1231-1243.
- Hirono T., Takahashi M., and Nakashima S. (2003) In-situ visualization of fluid flow image within deformed rock by X-ray CT. *Engineering Geology* **70**, 37-46.
- Ho C. H. and Miller N. H. (1985) Effect of humic-acid on uranium uptake by hematite particles. *J. Colloid Interface Sci.* **106**, 281-288.
- Ho C. H. and Miller N. H. (1986) Adsorption of uranyl species from bicarbonate solution onto hematite particles. *J. Colloid Interface Sci.* **110**, 165-171.
- Hochella M. F., Lower S. K., Maurice P. A., Penn R. L., Sahai N., Sparks D. L., and Twining B. S. (2008) Nanominerals, mineral nanoparticles, and Earth systems. *Science* **319**, 1631-1635.
- Hoek E. M. V. and Agarwal G. K. (2006) Extended DLVO interactions between spherical particles and rough surfaces. *J. Colloid Interface Sci.* **298**, 50-58.
- Hoek E. M. V., Bhattacharjee S., and Elimelech M. (2003) Effect of membrane surface roughness on colloid-membrane DLVO interactions. *Langmuir* **19**, 4836-4847.
- Holzer L. and Münch B. (2009) Toward Reproducible Three-Dimensional Microstructure Analysis of Granular Materials and Complex Suspensions. *Microsc. Microanal.* **15**, 130-146.
- Holzer L., Münch B., Rizzi M., Wepf R., Marschall P., and Graule T. (2010, in press) 3D-microstructure analysis of hydrated bentonite with cryo-stabilized pore water. *Applied Clay Science* doi:10.1016/j.clay.2009.11.045.
- Honeyman B. D. (1999) Colloidal culprits in contamination. *Nature* **397**, 23-24.
- Huber F., Kunze P., Geckeis H., and Schäfer T. (2010, in review) Sorption and reversibility studies on the interaction of radionuclides with FEBEX bentonite under Grimsel groundwater conditions in the presence of Äspö and Grimsel fracture filling material. *Appl. Geochem.*
- Huber F. and Lützenkirchen J. (2009) Uranyl retention on quartz - New experimental data and blind prediction using an existing surface complexation model. *Aquatic Geochemistry* **15**, 443-456.
- Huber F., Pudewills A., Enzmann F., and Schäfer T. (2009) Finite element modeling of flow and transport in a single fracture from the Äspö HRL (Sweden). In: Buckau, G., Kienzler, B., Duro, L., Montoya, V., and Delos, A. Eds.)^{4th} *Annual Workshop Proceeding of integrated project "Fundamental processes of Radionuclide Migration" - 6th EC FP IP FUNMIG, FZKA report 7461*.
- Hummel W. (2008) Radioactive contaminants in the subsurface: the influence of complexing ligands on trace metal speciation. *Monatsh. Chem.* **139**, 459-480.

- Ibaraki M. and Sudicky E. A. (1995) Colloid-facilitated contaminant transport in discretely fractured porous media .1. Numerical formulation and sensitivity analysis. *Water Resour. Res.* **31**, 2945-2960.
- Illes E. and Tombacz E. (2006) The effect of humic acid adsorption on pH-dependent surface charging and aggregation of magnetite nanoparticles. *J. Colloid Interface Sci.* **295**, 115-123.
- Ilton E. S., Boily J.-F. O., Buck E. C., Skomurski F. N., Rosso K. M., Cahill C. L., Bargar J. R., and Felmy A. R. (2010) Influence of dynamical conditions on the reduction of U(VI) at the magnetite solution interface. *Environ. Sci. Technol.* **44**, 170-176.
- Ilton E. S., Boily J. F., and Bagus P. S. (2007) Beam induced reduction of U(VI) during X-ray photoelectron spectroscopy: The utility of the U4f satellite structure for identifying uranium oxidation states in mixed valence uranium oxides. *Surf. Sci.* **601**, 908-916.
- Ilton E. S., Haiduc A., Moses C. O., Heald S. M., Elbert D. C., and Veblen D. R. (2004a) Heterogeneous reduction of uranyl by micas: Crystal chemical and solution controls. *Geochim. Cosmochim. Acta* **68**, 2417-2435.
- Ilton E. S., Haiduc A., Cahill C. L., and Felmy A. R. (2005) Mica surfaces stabilize pentavalent uranium. *Inorg. Chem.* **44**, 2986-2988.
- Ilton E. S., Haiduc A., Moses C. O., Heald S. M., Elbert D. C., and Veblen D. R. (2004b) Heterogeneous reduction of uranyl by micas: Crystal chemical and solution controls. *Geochim. Cosmochim. Acta* **68**, 2417-2435.
- Ilton E. S., Heald S. M., Smith S. C., Elbert D., and Liu C. X. (2006) Reduction of uranyl in the interlayer region of low iron micas under anoxic and aerobic conditions. *Environ. Sci. Technol.* **40**, 5003-5009.
- Ionescu A., Maes N., and Mallants D. (2008) Modelling transport of C-14-labelled Natural Organic Matter (NOM) in Boom Clay. *Scientific Basis for Nuclear Waste Management Xxxi* **1107**, 629-636.
- Jakob A., Mazurek M., and Heer W. (2003) Solute transport in crystalline rocks at Äspö - II: Blind predictions, inverse modelling and lessons learnt from test STT1. *J. Contam. Hydrol.* **61**, 175-190.
- Jeon B. H., Dempsey B. A., Burgos W. D., Barnett M. O., and Roden E. E. (2005) Chemical reduction of U(VI) by Fe(II) at the solid-water interface using natural and synthetic Fe(III) oxides. *Environ. Sci. Technol.* **39**, 5642-5649.
- Jolivet J. P. and Tronc E. (1988) Interfacial Electron-transfer in colloidal spinel iron-oxide - Conversion of Fe₃O₄-gamma-Fe₂O₃ in aqueous medium. *J. Colloid Interface Sci.* **125**, 688-701.
- Kaminski M. D., Dimitrijevic N. M., Mertz C. J., and Goldberg M. M. (2005a) Colloids from the aqueous corrosion of uranium nuclear fuel. *J. Nucl. Mater.* **347**, 77-87.
- Kaminski M. D., Goldberg M. M., and Mertz C. J. (2005b) Colloids from the aqueous corrosion of aluminium-based nuclear fuel. *J. Nucl. Mater.* **347**, 88-93.
- Kaoser S., Barrington S., Elektorowicz M., and Ayadat T. (2006) The Influence of Hydraulic Gradient and Rate of Erosion on Hydraulic Conductivity of Sand-Bentonite Mixtures. *Soil and Sediment Contamination: An International Journal* **15**, 481-496.
- Keller C. and Jorgensen C. K. (1975) Photoelectron-spectra of uranium(V) in mixed oxides showing characteristic satellite signals. *Chem. Phys. Lett.* **32**, 397-400.
- Kelokaski M., Siitari-Kauppi M., Sardini P., Mori A., and Hellmuth K. H. (2006) Characterisation of pore space geometry by C-14-PMMA impregnation - development work for in-situ studies. *Journal of Geochemical Exploration* **90**, 45-52.
- Kemps J. a. L. and Bhattacharjee S. (2009) Particle Tracking Model for Colloid Transport near Planar Surfaces Covered with Spherical Asperities. *Langmuir* **25**, 6887-6897.
- Kersting A. B., Efurud D. W., Finnegan D. L., Rokop D. J., Smith D. K., and Thompson J. L. (1999) Migration of plutonium in groundwater at the Nevada Test Site. *Nature* **397**, 56-59.
- Kienzler B., Vejmelka P., Romer J., Fanghänel E., Jansson M., Eriksen T. E., and Wikberg P. (2003) Swedish-German actinide migration experiment at ASPO hard rock laboratory. *J. Contam. Hydrol.* **61**, 219-233.

- Kim J. I. (1994) Actinide colloids in natural aquifer systems. *Mat. Res. Soc. Bull.* **19**, 47-53.
- Kim J. I., Buckau G., Baumgärtner F., Moon H., and Lux D. (1984) Colloid generation and the actinide migration in Gorleben groundwaters. *Mater. Res. Soc. Symp. Proc.* **26**, 31-40.
- Kim J. I., Buckau G., Li G. H., Duschner H., and Psarros N. (1990) Characterization of Humic and Fulvic-Acids from Gorleben Groundwater. *Fresenius J. Anal. Chem.* **338**, 245-252.
- Kim M. A., Panak P. J., Breban D. C., Priemyshev A., Yun J. I., Mansel A., and Kim J. I. (2007) Interaction of actinides(III) with aluminosilicate colloids. Part IV. Influence of humic acid. *Colloids and Surfaces a-Physicochemical and Engineering Aspects* **296**, 206-215.
- Kim M. A., Panak P. J., Yun J. I., Priemyshev A., and Kim J. I. (2005) Interaction of actinides(III) with aluminosilicate colloids in "statu nascendi" Part III. Colloid formation from monosilanol and polysilanol. *Colloids and Surfaces a-Physicochemical and Engineering Aspects* **254**, 137-145.
- Konstantinou M., Kolokassidou K., and Pashalidis I. (2009) Studies on the interaction of olive cake and its hydrophylic extracts with polyvalent metal ions (Cu(II), Eu(III)) in aqueous solutions. *J. Hazard. Mater.* **166**, 1169-1173.
- Korichi S. and Bensmaili A. (2009) Sorption of uranium (VI) on homoionic sodium smectite experimental study and surface complexation modeling. *J. Hazard. Mater.* **169**, 780-793.
- Kosakowski G. (2004) Anomalous transport of colloids and solutes in a shear zone. *J. Contam. Hydrol.* **72**, 23-46.
- Kosmulski M. (2001) *Chemical properties of material surfaces*. Dekker, New York.
- Kretzschmar R. and Schäfer T. (2005) Metal retention and transport on colloidal particles in the environment. *Elements* **1**, 205-210.
- Kulenkampff J., Grundig M., Richter M., and Enzmann F. (2008) Evaluation of positron-emission-tomography for visualisation of migration processes in geomaterials. *Physics and Chemistry of the Earth* **33**, 937-942.
- Kumke M. U., Eidner S., and Kruger T. (2005) Fluorescence quenching and luminescence sensitization in complexes of Tb³⁺ and Eu³⁺ with humic substances. *Environ. Sci. Technol.* **39**, 9528-9533.
- Kunze P., Seher H., Hauser W., Panak P., Geckeis H., and Schäfer T. (2008a) Radionuclide speciation in the Grimsel granite groundwater Febex bentonite pore water mixing zone In: Buckau, G., Kienzler, B., Duro, L., Montoya, V., and Delos, A. Eds.) *3rd Annual workshop Proceedings of IP FUNMIG, NDA report*. Nuclear Decommissioning Authority (NDA), Edinburgh (Scotland).
- Kunze P., Seher H., Hauser W., Panak P. J., Geckeis H., Fanghänel T., and Schäfer T. (2008b) The influence of colloid formation in a granite groundwater bentonite pore water mixing zone on radionuclide speciation. *J. Contam. Hydrol.* **102**, 263-272.
- Kurosawa S., Tanaka S., James S. C., and Yui M. (2006) The effect of montmorillonite partial density on the role of colloid filtration by a bentonite buffer. *J. Nucl. Sci. Technol.* **43**, 605-609.
- Kurosawa S. and Ueta S. (2001) Effect of colloids on radionuclide migration for performance assessment of HLW disposal in Japan. *Pure Appl. Chem.* **73**, 2027-2037.
- Lagaly G. and Ziesmer S. (2003) Colloid chemistry of clay minerals: the coagulation of montmorillonite dispersions. *Adv. Colloid Interface Sci.* **100-102**, 105-128.
- Langmuir D. (1978) Uranium solution-mineral equilibria at low temperatures with applications to sedimentary ore deposits. *Geochim Cosmochim Acta* **42**, 547 - 569.
- Latrille C., Ly J., and Herbette M. (2006) Retention of Sn(IV) and Pu(IV) onto four argillites from the Callovo-Oxfordian level at Bure (France) from eight equilibrated sedimentary waters. *Radiochimica Acta* **94**, 421-427.
- Lead J. R. and Wilkinson K. J. (2006) Aquatic colloids and nanoparticles: Current knowledge and future trends. *Environmental Chemistry* **3**, 159-171.
- Lecoanet H. F., Bottero J. Y., and Wiesner M. R. (2004) Laboratory assessment of the mobility of nanomaterials in porous media. *Environ. Sci. Technol.* **38**, 5164-5169.
- Lemonnier M., Collet O., Depautex C., Esteva J. M., and Raoux D. (1978) High-vacuum 2 crystal soft-X-ray monochromator. *Nuclear Instruments & Methods* **152**, 109-111.

- Leskinen A., Penttinen L., Siitari-Kauppi M., Alanso U., Garcia-Gutierrez M., Missana T., and Patelli A. (2007) Determination of granites' mineral specific porosities by PMMA method and FESEM/EDAX. *Scientific Basis for Nuclear Waste Management XXX* **985**, 599-604.
- Lieber C. M. (2003) Nanoscale science and technology: Building a big future from small things. *MRS Bull.* **28**, 486-491.
- Liger E., Charlet L., and Van C. P. (1999) Surface catalysis of uranium(VI) reduction by iron(II). *Geochim. Cosmochim. Acta* **63**, 2939.
- Lindberg R. D. and Runnells D. D. (1984) Groundwater redox reactions: An analysis of equilibrium state applied to Eh measurements and geochemical modeling. *Science* **225**, 925 - 927.
- Liu D. J., Bruggeman C., and Maes N. (2008) The influence of natural organic matter on the speciation and solubility of Eu in Boom Clay porewater. *Radiochimica Acta* **96**, 711-720.
- Liu J. and Neretnieks I. (2006) Physical and chemical stability of the bentonite buffer. SKB Technical Report 06-103, Svensk Kärnbränslehantering AG, Stockholm, Sweden, .
- Liu J., Xu Z., and Masliyah J. (2004) Role of fine clays in bitumen extraction from oil sands. *AIChE J.* **50**, 1917-1927.
- Liu J., Xu Z., and Masliyah J. (2005) Interaction forces in bitumen extraction from oil sands. *J. Colloid Interface Sci.* **287**, 507-520.
- Liu L., Moreno L., and Neretnieks I. (2009a) A Dynamic Force Balance Model for Colloidal Expansion and Its DLVO-Based Application. *Langmuir* **25**, 679-687.
- Liu L., Moreno L., and Neretnieks I. (2009b) A Novel Approach to Determine the Critical Coagulation Concentration of a Colloidal Dispersion with Plate-like Particles. *Langmuir* **25**, 688-697.
- Lovley D. R., Phillips E. J. P., Gorby Y. A., and Landa E. R. (1991) Microbial reduction of uranium. *Nature* **350**, 413-416.
- Lührmann L. (1999) Modellierung des kolloidgetragenen Schadstofftransports mit dem Rechenprogramm TRAPIC. Gesellschaft für Anlagen- und Reaktorsicherheit (GRS) mbH, Braunschweig.
- Lützenkirchen J. (2009) Summary of studies on (ad)sorption as a “well-established” process within FUNMIG activities. *Appl. Geochem.* (under review).
- Madden A. S. and Hochella Jr M. F. (2005) A test of geochemical reactivity as a function of mineral size: Manganese oxidation promoted by hematite nanoparticles. *Geochim. Cosmochim. Acta* **69**, 389-398.
- Maes N., Wang L., Hicks T., Bennett D., Warwick P., Hall T., Walker G., and Dierckx A. (2006) The role of natural organic matter in the migration behaviour of americium in the Boom Clay - Part I: Migration experiments. *Physics and Chemistry of the Earth, Parts A/B/C* **31**, 541-547.
- Mahmood A., Amirtharajah T., Sturm W., and Denett K. E. (2001) A micromechanics approach for attachment and detachment of asymmetric colloidal particles. *Colloids and Surfaces A: Physicochemical and Engineering Aspects* **177**, 99-110.
- Mansel A. and Kupsch H. (2007) Radiolabelling of humic substances with C-14 by azo coupling C-14 phenyldiazonium ions. *Appl. Radiat. Isot.* **65**, 793-797.
- Mansour C., Lefevre G., Pavageau E. M., Catalette H., Fedoroff M., and Zanna S. (2009) Sorption of sulfate ions onto magnetite. *J. Colloid Interface Sci.* **331**, 77-82.
- Marang L., Eidner S., Kumke M. U., Benedetti M. F., and Reiller P. (2008) Combining spectroscopic and potentiometric approaches to characterize competitive binding to humic substances. In: Buckau, G., Kienzler, B., Duro, L., Montoya, V., and Delos, A. Eds.) *3rd Annual workshop Proceedings of IP FUNMIG, NDA report*. Nuclear Decommissioning Authority (NDA), Edinburgh (Scotland).
- Marang L., Eidner S., Kumke M. U., Benedetti M. F., and Reiller P. E. (2009) Spectroscopic characterization of the competitive binding of Eu(III), Ca(II), and Cu(II) to a sedimentary originated humic acid. *Chem. Geol.* **264**, 154-161.
- Marang L., Reiller P., Pepe M., and Benedetti M. F. (2006) Donnan membrane approach: From equilibrium to dynamic speciation. *Environ. Sci. Technol.* **40**, 5496-5501.

- Mccarthy J. F. and Mckay L. D. (2004) Colloid transport in the subsurface: past, present, and future challenges. *Vadose Zone Journal* **3**, 326-337.
- Mccarthy J. F., Mckay L. D., and Bruner D. D. (2002) Influence of Ionic Strength and Cation Charge on Transport of Colloidal Particles in Fractured Shale Saprolite. *Environ. Sci. Technol.* **36**, 3735-3743.
- Mccarthy J. F. and Shevenell L. (1998) Processes controlling colloid composition in a fractured and karstic aquifer in eastern Tennessee, USA. *Journal of Hydrology* **206**, 191-218.
- Mccarthy J. F. and Zachara J. M. (1989) Subsurface transport of contaminants: Mobile colloids in the subsurface environment may alter the transport of contaminants. *Environ. Sci. Technol.* **23**, 497-502.
- McIntyre N. S. and Zetaruk D. G. (1977) X-ray photoelectron spectroscopic studies of iron-oxides. *Anal. Chem.* **49**, 1521-1529.
- Metz V., Kienzler B., and Schussler W. (2003) Geochemical evaluation of different groundwater-host rock systems for radioactive waste disposal. *J. Contam. Hydrol.* **61**, 265-279.
- Missana T., Alonso U., Albarran N., Gomez P., Buil B., Schäfer T., Hauser W., Seher H., and Garralon A. (2008a) Bentonite colloid generation from a deep geological repository in granite: An in-situ study. *Geochim. Cosmochim. Acta* **72**, A635-A635.
- Missana T., Alonso U., Garcia-Gutierrez M., and Mingarro M. (2008b) Role of bentonite colloids on europium and plutonium migration in a granite fracture. *Appl. Geochem.* **23**, 1484-1497.
- Missana T., Garcia-Gutierrez M., and Fernandez V. (2003a) Uranium(VI) sorption on colloidal magnetite under anoxic environment: Experimental study and surface complexation modelling. *Geochim. Cosmochim. Acta* **67**, 2543-2550.
- Missana T., Maffiotte U., and Garcia-Gutierrez M. (2003b) Surface reactions kinetics between nanocrystalline magnetite and uranyl. *J. Colloid Interface Sci.* **261**, 154-160.
- Möri A., Alexander W. R., Geckeis H., Hauser W., Schäfer T., Eikenberg J., Fierz T., Degueldre C., and Missana T. (2003) The colloid and radionuclide retardation experiment at the Grimsel Test Site: influence of bentonite colloids on radionuclide migration in a fractured rock. *Colloids and Surfaces a-Physicochemical and Engineering Aspects* **217**, 33-47.
- Möri A., Geckeis H., Fierz T., Eikenberg J., Degueldre C., Hauser W., Geyer F. W., and Schäfer T. (2004) Grimsel Test Site - Investigation Phase V "The CRR final project report series I: Description of the Field Phase - Methodologies and Raw Data". Nagra, Wettingen, Switzerland.
- Moulder J. F., Stickle W. F., Sobol P. E., and Bomben K. D. (1992) Handbook of X-ray Photoelectron Spectroscopy. In: Chastain, J. (Ed.). Perkin Elmer Corporation, Physical Electronics Division, Minnesota, USA.
- Mustafa S., Dilara B., Neelofer Z., Naeem A., and Tasleem S. (1998) Temperature effect on the surface charge properties of gamma-Al₂O₃. *J. Colloid Interface Sci.* **204**, 284-293.
- Nagra (2002) Stability and mobility of colloids in Opalinus Clay. In: Voegelin, A. and Kretzschmar, R. Eds.). Nagra, Wettingen (Switzerland).
- Nagra (2006) Grimsel Test Site Investigation Phase V, The CRR Final Report Series II: Supporting laboratory experiments with radionuclides and bentonite colloids. Nagra Technical Report NTB 03-02. In: Missana, T., Mingarro, M., Gutierrez, M. G., Alonso, U., Geckeis, H., Schäfer, T., Rabung, T., Vejmelka, P., and Marquardt, C. Eds.). Nagra, Wettingen, Switzerland.
- Nagra (in press) GTS Phase V (CRR Experiment): Supporting laboratory experiments with radionuclides and bentonite colloids. Nagra Technical Report NTB 03-02. In: Missana, T., Mingarro, M., Gutierrez, M. G., Alonso, U., Geckeis, H., Schäfer, T., Rabung, T., Vejmelka, P., and Marquardt, C. Eds.). Nagra, Wettingen, Switzerland.
- NEA (2009) Natural tracer profiles across argillaceous formations: the CLAYTRAC project. NEA-OECD (Nuclear Energy Agency - Organisation for Economic Co-Operation and Development), Paris.
- Neck V., Altmaier M., and Fanghänel T. (2007a) Solubility of plutonium hydroxides/hydrous oxides under reducing conditions and in the presence of oxygen. *C.R. Chimie* **10**, 959-977.
- Neck V., Altmaier M., Fellhauer D., Runke J., and Fanghänel T. (2009) Quantification of the redox potential for the reduction of Np(V) in non-complexing aqueous solutions at pH 5-10. In:

- Buckau, G., Duro, L., Montoya, V., and Delos, A. Eds.) *1st Annual Workshop Proceedings 7th EC FP – Recosy CP, Barcelona 10-12th February 2009*.
- Neck V., Altmaier M., Seibert A., Yun J. I., Marquardt C. M., and Fanghänel T. (2007b) Solubility and redox reactions of Pu(IV) hydrous oxide: Evidence for the formation of PuO₂+x(s, hyd). *Radiochimica Acta* **95**, 193-207.
- Neck V. and Kim J. I. (2001) Solubility and hydrolysis of tetravalent actinides. *Radiochim. Acta* **89**, 1-16.
- Nel A., Xia T., Madler L., and Li N. (2006) Toxic potential of materials at the nanolevel. *Science* **311**, 622-627.
- Neretnieks I. (1980) Diffusion in the rock matrix - An important factor in radionuclide retardation. *Journal of Geophysical Research* **85**, 4379-4397.
- Neretnieks I. (2002) A stochastic multi-channel model for solute transport--analysis of tracer tests in fractured rock. *J. Contam. Hydrol.* **55**, 175-211.
- Nguyentrung C., Begun G. M., and Palmer D. A. (1992) Aqueous uranium complexes. 2. Raman-spectroscopic study of the complex-formation of the dioxouranium(VI) ion with a variety of inorganic and organic ligands. *Inorg. Chem.* **31**, 5280-5287.
- Nilsson A. C., Hedqvist I., and Degueldre C. (2008) Granitic groundwater colloids sampling and characterisation: the strategy for artefact elimination. *Anal. Bioanal. Chem.* **391**, 1327-1333.
- Noseck U. and Klotz D. (2002) Modelling of colloid-facilitated contaminant transport with the computer code TRAPIC: Theoretical basis and application. *Radionuclide Retention in Geologic Media, Workshop Proceedings*, 231-239.
- Noseck U., Rozanski K., Dulinski M., Havlova V., Sracek O., Brassler T., Hercik M., and Buckau G. (2009) Carbon chemistry and groundwater dynamics at natural analogue site Ruprechtov, Czech Republic: Insights from environmental isotopes. *Appl. Geochem.* **24**, 1765-1776.
- Novikov A. P., Kalmykov S. N., Utsunomiya S., Ewing R. C., Horreard F., Merkulov A., Clark S. B., Tkachev V. V., and Myasoedov B. F. (2006) Colloid Transport of Plutonium in the Far-Field of the Mayak Production Association, Russia. *Science* **314**, 638-641.
- Nowack B. and Bucheli T. D. (2007) Occurrence, behaviour and effects of nanoparticles in the environment. *Environ. Pollut.* **150**, 5-22.
- O'Loughlin E. J., Kelly S. D., and Kemner K. M. (2010) XAFS Investigation of the Interactions of U(VI) with Secondary Mineralization Products from the Bioreduction of Fe(III) Oxides. *Environ. Sci. Technol.* **44**, 1656-1661.
- Opel K., Weiss S., Hubener S., Zanker H., and Bernhard G. (2007) Study of the solubility of amorphous and crystalline uranium dioxide by combined spectroscopic methods. *Radiochimica Acta* **95**, 143-149.
- Panak P. J., Kim M. A., Klenze R., Kim J. I., and Fanghänel T. (2005) Complexation of Cm(III) with aqueous silicic acid. *Radiochimica Acta* **93**, 133-139.
- Patterson A. L. (1939) The Scherrer Formula for X-Ray Particle Size Determination. *Physical Review* **56**, 978.
- Payne R. B., Gentry D. A., Rapp-Giles B. J., Casalot L., and Wall J. D. (2002) Uranium reduction by *Desulfovibrio desulfuricans* strain G20 and a cytochrome c3 mutant. *Appl. Environ. Microbiol.* **68**, 3129-3132.
- Privalov T., Schimmelpfennig B., Wahlgren U., and Grenthe I. (2003) Reduction of uranyl(VI) by iron(II) in solutions: An ab initio study. *J. Phys. Chem. A* **107**, 587-592.
- Puigdomenech I. (2004) HYDRA and MEDUSA chemical equilibrium software. Software and documentation. <http://web.telia.com/~u15651596/>.
- Puls R. W. (1995) Use of low-flow or passive sampling techniques for sampling groundwater. *Ground Water Sampling- A Workshop Summary*. U.S.E.P.A. United States Environmental Protection Agency, report number: EPA/600/R-94/205, Dallas, Texas.
- Rabung T. and Geckeis H. (2009) Influence of pH and metal ion loading on the Cm(III) humate complexation: a time resolved laser fluorescence spectroscopy study. *Radiochimica Acta* **97**, 265-271.

- Rabung T., Pierret M. C., Bauer A., Geckeis H., Bradbury M. H., and Baeyens B. (2005) Sorption of Eu(III)/Cm(III) on Ca-montmorillonite and Na-illite. Part 1: Batch sorption and time-resolved laser fluorescence spectroscopy experiments. *Geochim. Cosmochim. Acta* **69**, 5393-5402.
- Raeburn S. P., Ilton E. S., and Veblen D. R. (1997a) Quantitative determination of the oxidation state of iron in biotite using X-ray photoelectron spectroscopy: I. Calibration. *Geochim. Cosmochim. Acta* **61**, 4519-4530.
- Raeburn S. P., Ilton E. S., and Veblen D. R. (1997b) Quantitative determination of the oxidation state of iron in biotite using X-ray photoelectron spectroscopy: II. In-situ analyses. *Geochim. Cosmochim. Acta* **61**, 4531-4537.
- Rai D., Gorby Y. A., Fredrickson J. K., Moore D. A., and Yui M. (2002) Reductive dissolution of PuO₂(am): The effect of Fe(II) and hydroquinone. *J. Solution Chem.* **31**, 433-453.
- Rajagopalan R. and Tien C. (1976) Trajectory analysis of deep-bed filtration with the sphere-in-cell porous media model. *Am. Inst. Chem. Eng. J. AIChE* **22**, 523-533.
- Ravel B. and Newville M. (2005) ATHENA and ARTEMIS: Interactive graphical data analysis using IFEFFIT. *Phys. Scr.* **T115**, 1007-1010.
- Regenspurg S., Schild D., Schäfer T., Huber F., and Malmström M. E. (2009) Removal of uranium(VI) from the aqueous phase by iron(II) minerals in presence of bicarbonate. *Appl. Geochem.* **24**, 1617-1625.
- Reiller P. E., Evans N. D. M., and Szabo G. (2008) Complexation parameters for the actinides(IV)-humic acid system: a search for consistency and application to laboratory and field observations. *Radiochimica Acta* **96**, 345-358.
- Robinson B. A., Li C. H., and Ho C. K. (2003) Performance assessment model development and analysis of radionuclide transport in the unsaturated zone, Yucca Mountain, Nevada. *J. Contam. Hydrol.* **62-3**, 249-268.
- Rovira M., El Aamrani S., Duro L., Giménez J., De Pablo J., and Bruno J. (2007) Interaction of uranium with in-situ anoxically generated magnetite on steel. *J. Hazard. Mater.* **147**, 726-731.
- Ryan J. N. and Gschwend P. M. (1994) Effects of Ionic Strength and Flow Rate on Colloid Release - Relating Kinetics to Intersurface Potential Energy. *J. Colloid Interface Sci.* **164**, 21-34.
- Sardini P., Siitari-Kauppi M., Beaufort D., and Hellmuth K. H. (2006) On the connected porosity of mineral aggregates in crystalline rocks. *Am. Mineral.* **91**, 1069-1080.
- Schäfer T., Chanudet V., Claret F., and Filella M. (2007) Spectromicroscopy mapping of colloidal/particulate organic matter in Lake Brienz, Switzerland. *Environ. Sci. Technol.* **41**, 7864-7869.
- Schäfer T., Geckeis H., Bouby M., and Fanghänel T. (2004) U, Th, Eu and colloid mobility in a granite fracture under near-natural flow conditions. *Radiochimica Acta* **92**, 731-737.
- Schäfer T. and Reiller P. (2008) Summary of the 3rd Topical Session: Influence of organics on radionuclide migration processes. In: Buckau, G., Kienzler, B., Duro, L., Montoya, V., and Delos, A. Eds.) *3rd Annual workshop Proceedings of IP FUNMIG, NDA report*. Nuclear Decommissioning Authority (NDA), Edinburgh (Scotland).
- Schäfer T., Seher H., Hauser W., Walther C., Degueldre C., Yamada M., Suzuki M., Missana T., Alonso U., Trick T., and Blechschmidt I. (2009) The Colloid Formation and Migration (CFM) project at the Grimsel Test Site (Switzerland): Results from the homologue tests. *Geochim. Cosmochim. Acta* **73**, A1168-A1168.
- Schindler M., Hawthorne F. C., Freund M. S., and Burns P. C. (2009) XPS spectra of uranyl minerals and synthetic uranyl compounds. I: The U 4f spectrum. *Geochim. Cosmochim. Acta* **73**, 2471-2487.
- Schindler P., Michaelis W., and Feitknecht W. (1963) Löslichkeitsprodukte von Metalloxiden und -hydroxiden. 8. Die Löslichkeit gealterter Eisen(III)-hydroxidfällungen. *Helv. Chim. Acta* **46**, 444-8.
- Schüring J. S., H.D.; Fischer, W.R.; Böttcher, J.; Duijnsveld, W.H.M. (Eds.) (2000) Redox - Fundamentals, Processes and Applications. Springer, Berlin.

- Schwertmann U. and Cornell R. M. (1991) *Iron Oxides in the Laboratory (Preparation and Characterization)*. VCH Verlagsgesellschaft mbH, Weinheim.
- Scott T. B., Allen G. C., Heard P. J., and Randell M. G. (2005) Reduction of U(VI) to U(IV) on the surface of magnetite. *Geochim. Cosmochim. Acta* **69**, 5639-5646.
- Seah M. P., Gilmore I. S., and Spencer S. J. (1998) XPS: Binding energy calibration of electron spectrometers 4 - Assessment of effects for different x-ray sources, analyser resolutions, angles of emission and overall uncertainties. *Surf. Interface Anal.* **26**, 617-641.
- Seher H., Albarran N., Hauser W., Götz R., Missana T., Geckeis H., Fanghänel T., and Schäfer T. (2009) Colloid generation by erosion of compacted bentonite under different geochemical conditions. In: Buckau, G., Kienzler, B., Duro, L., Montoya, V., and Delos, A. Eds.) *4th Annual Workshop Proceeding of integrated project "Fundamental processes of Radionuclide Migration" - 6th EC FP IP FUNMIG, FZKA report 7461*.
- Seher H., Hauser W., Geckeis H., Fanghänel T., and Schäfer T. (2010, in prep.) Bentonite nanoparticle stability and effect of fulvic acids: experiments and modelling. *Colloids Surf., A*.
- Seher H., Schäfer T., Geckeis H., and Fanghänel E. (2006) FEBEX bentonite colloid stability in groundwater. In: Buckau, G., Kienzler, B., Duro, L., and Montoya, V. Eds.) *2nd Annual Workshop Proceedings of the Integrated Project "Fundamental Processes of Radionuclide Migration"- 6th EC FP IP FUNMIG*. SKB Technical Report TR-07-05, Stockholm.
- Sen T. K. and Khilar K. C. (2006) Review on subsurface colloids and colloid-associated contaminant transport in saturated porous media. *Adv. Colloid Interface Sci.* **119**, 71-96.
- Severino G., Cvetkovic V., and Coppola A. (2007) Spatial moments for colloid-enhanced radionuclide transport in heterogeneous aquifers. *Advances in Water Resources* **30**, 101-112.
- Sjöblom R., Kalbantner P., Bjurström H., and Pusch R. (1999) Application of the general microstructural model to erosion phenomena -- mechanisms for the chemical-hydrodynamic conversion of bentonite to a pumpable slurry in conjunction with retrieval. *Engineering Geology* **54**, 109-116.
- SKB (2005a) The colloid investigations conducted at the Äspö Hard Rock Laboratory during 2000–2004, Technical report TR-05-20. In: Laaksoharju, M. and Wold, S. (Eds.). Svensk Kärnbränslehantering AB, Stockholm, Sweden.
- SKB (2005b) RETROCK Project (Treatment of geosphere retention phenomena in safety assessment models). SKB report R-04-48, Sweden.
- SKB (2006a) Buffer and backfill process report for the safety assessment SR-Can. Svensk Kärnbränslehantering AB, Stockholm, Sweden.
- SKB (2006b) Long-term safety for KBS-3 repositories at Forsmark and Laxemar - a first evaluation; Main report of the SR-Can project. SKB Technical report TR-06-09. Svensk Kärnbränslehantering AB, Stockholm, Sweden.
- SKB (2008) Oskarshamn site investigation - Detecting the near surface redox front in crystalline rock - Results from drill cores KLX09B-G and KLX11B-F. In: Drake, H. and Tullborg, E.-L. Eds.). Svensk Kärnbränslehantering AB, Stockholm, Sweden.
- Skjetne E., Hansen A., and Gudmundsson J. S. (1999) High-velocity flow in a rough fracture. *J. Fluid Mech.* **383**, 1-28.
- Soldatov A. V., Lamoën D., Konstantinovic M. J., Van Den Berghe S., Scheinost A. C., and Verwerft M. (2007) Local structure and oxidation state of uranium in some ternary oxides: X-ray absorption analysis. *J. Solid State Chem.* **180**, 54-61.
- Stumm W. and Morgan J. J. (1996) *Aquatic Chemistry*. John Wiley & Sons, New York.
- Szabo G., Guczi J., Reiller P., Geckeis H., and Bulman R. A. (2006) Investigation of complexation of thorium by humic acid using chemically immobilized humic acid on silica gel. *Radiochimica Acta* **94**, 553-557.
- Taylor G. (1953) Dispersion of soluble matter in solvent flowing slowly through a tube. *Proceedings of the Royal Society of London Series a-Mathematical and Physical Sciences* **219**, 186-203.
- Tombácz E., Abraham I., Gilde M., and Szanto F. (1990) The pH dependent colloidal stability of aqueous montmorillonite suspensions. *Colloids and Surfaces* **49**, 71- 78.

- Tombácz E. and Szekeres M. (2004) Colloidal behaviour of aqueous montmorillonite suspensions: the specific role of pH in the presence of indifferent electrolytes. *Applied Clay Science* **27**.
- Traexler K. A., Utsunomiya S., Kersting A. B., and Ewing R. C. (2004) Colloid transport of radionuclides: Yucca mountain performance assessment. *Scientific Basis for Nuclear Waste Management XXVII* **807**, 653-658.
- Tufenkji N. and Elimelech M. (2004a) Correlation equation for predicting single-collector efficiency in physicochemical filtration in saturated porous media. *Environ. Sci. Technol.* **38**, 529-536.
- Tufenkji N. and Elimelech M. (2004b) Deviation from the classical colloid filtration theory in the presence of repulsive DLVO interactions. *Langmuir* **20**, 10818-10828.
- Tufenkji N. and Elimelech M. (2005) Breakdown of colloid filtration theory: Role of the secondary energy minimum and surface charge heterogeneities. *Langmuir* **21**, 841-852.
- Tullborg E.-L. and Gustafsson E. (1999) ¹⁴C in bicarbonate and dissolved organics--a useful tracer? *Applied Geochemistry* **14**, 927-938.
- Turner N. B., Ryan J. N., and Saiers J. E. (2006) Effect of desorption kinetics on colloid-facilitated transport of contaminants: Cesium, strontium, and illite colloids. *Water Resour. Res.* **42**.
- Tushar K. S. and Khilar K. C. (2006) Review on subsurface colloids and colloid-associated contaminant transport in saturated porous media. *Adv. Colloid Interface Sci.* **119**, 71-96.
- Utsunomiya S., Kersting A. B., and Ewing R. C. (2009) Groundwater Nanoparticles in the Far-Field at the Nevada Test Site: Mechanism for Radionuclide Transport. *Environ. Sci. Technol.* **43**, 1293-1298.
- Vandenborre J., Drot R., and Simoni E. (2007) Interaction mechanisms between uranium(VI) and rutile titanium dioxide: From single crystal to powder. *Inorg. Chem.* **46**, 1291-1296.
- Velegol D., Holtzer G. L., Radovic-Moreno A. F., and Cuppett J. D. (2007) Force measurements between sub-100 nm colloidal particles. *Langmuir* **23**, 1275-1280.
- Verwey E. J. W. and Overbeek J. T. G. (1948) *Theory of the stability of lyophobic colloids*. Elsevier, Amsterdam.
- Vilks P. and Bachinski D. B. (1996a) Characterization of organics in whiteshell research area groundwater and the implications for radionuclide transport. *Appl. Geochem.* **11**, 387-402.
- Vilks P. and Bachinski D. B. (1996b) Colloid and suspended particle migration experiments in a granite fracture. *J. Contam. Hydrol.* **21**, 269-279.
- Vilks P., Frost L. H., and Bachinski D. B. (1997) Field-Scale colloid migration experiments in a granite fracture. *J. Contam. Hydrol.* **26**, 203-214.
- Villar M. V., Martin P. L., Pelayo M., Ruiz B., Rivas P., Alonso E., Lloret A., Pintado X., Gens A., Linares J., Huertas F., Caballero E., Jimenez De Cisneros C., Obis J., Perez A., and Velasco J. (1998) FEBEX bentonite: origin, properties and fabrication of blocks (full-scale engineered barriers experiment in crystalline host rock). Enresa (empresa nacional de residuos radiactivos, s.a.), Madrid, Spain.
- Voutilainen M., Lamminmaki S., Timonen J., Siitari-Kauppi M., and Breitner D. (2009) Physical Rock Matrix Characterization: Structural and Mineralogical Heterogeneities in Granite. *Scientific Basis for Nuclear Waste Management XXXII* **1124**, 555-560.
- Waite T. D., Davis J. A., Payne T. E., Waychunas G. A., and Xu N. (1994) Uranium(VI) adsorption to ferrihydrite - Application of a surface complexation model. *Geochim. Cosmochim. Acta* **58**, 5465-5478.
- Wall J. D. and Krumholz L. R. (2006) Uranium reduction. *Annu. Rev. Microbiol.* **60**, 149-166.
- Walther C., Buchner S., Filella M., and Chanudet V. (2006) Probing particle size distributions in natural surface waters from 15 nm to 2 μm by a combination of LIBD and single-particle counting. *J. Colloid Interface Sci.* **301**, 532-537.
- Walz J. Y. and Sharma A. (1994) Effect of Long Range Interactions on the Depletion Force between Colloidal Particles. *J. Colloid Interface Sci.* **168**, 485-496.
- Weinberg H., Galyean A., and Leopold M. (2011) Evaluating engineered nanoparticles in natural waters. *TrAC, Trends Anal. Chem.* **30**, 72-83.

- Weng L. P., Van Riemsdijk W. H., and Hiemstra T. (2007) Adsorption of humic acids onto goethite: Effects of molar mass, pH and ionic strength. *J. Colloid Interface Sci.* **314**, 107-118.
- Wersin P., Hochella M. F., Persson P., Redden G., Leckie J. O., and Harris D. W. (1994) Interaction between aqueous uranium (VI) and sulfide minerals: Spectroscopic evidence for sorption and reduction. *Geochim Cosmochim Acta* **58**, 2829 - 2843.
- White A. F., Peterson M. L., and Hochella M. F. (1994) Electrochemistry and dissolution kinetics of magnetite and ilmenite. *Geochim. Cosmochim. Acta* **58**, 1859-1875.
- WHO (2004) Uranium in drinking water. Chemical Fact Sheets of WHO Guidelines for Drinking-water Quality.
- Wickham S. M., Bennett D. G., and Higgo J. J. W. (2000) Evaluation of Colloid Transport Issues and Recommendations for SKI Performance Assessments. SKI (The Swedish Nuclear Power Inspectorate), Stockholm, Sweden.
- Wigginton N. S., Haus K. L., and Hochella M. F. (2007) Aquatic environmental nanoparticles. *J. Environ. Monit.* **9**, 1306-1316.
- Wilkinson K. J. and Lead J. R. (2006) Environmental Colloids and Particles Behaviour, Separation and Characterisation. *IUPAC Series on Analytical and Physical Chemistry of Environmental Systems*. John Wiley & Sons, New York.
- Wold S. and Eriksen T. (2007) Diffusion of humic colloids in compacted bentonite. *Physics and Chemistry of the Earth* **32**, 477-484.
- Wold S. and Eriksen T. E. (2003) Diffusion of lignosulfonate colloids in compacted bentonite. *Applied Clay Science* **23**, 43-50.
- Yamashita T. and Hayes P. (2006) Effect of curve fitting parameters on quantitative analysis of Fe_{0.94}O and Fe₂O₃ using XPS. *J. Electron. Spectrosc. Relat. Phenom.* **152**, 6-11.
- Yamashita T. and Hayes P. (2008) Analysis of XPS spectra of Fe²⁺ and Fe³⁺ ions in oxide materials. *Appl. Surf. Sci.* **254**, 2441-2449.
- Zhou P. and Gu B. H. (2005) Extraction of oxidized and reduced forms of uranium from contaminated soils: Effects of carbonate concentration and pH. *Environ. Sci. Technol.* **39**, 4435-4440.
- Zhuang J., McCarthy J. F., Tyner J. S., Perfect E., and Flury M. (2007) In-situ colloid mobilization in hanford sediments under unsaturated transient flow conditions: Effect of irrigation pattern. *Environ. Sci. Technol.* **41**, 3199-3204.
- Zvikelsky O., Weisbrod N., and Dody A. (2008) A comparison of clay colloid and artificial microsphere transport in natural discrete fractures. *J. Colloid Interface Sci.* **323**, 286-292.

8 APPENDIX A: Sorption reversibility kinetics: The Äspö system

Additional experiments using fracture filling material from Äspö, Sweden under the same experimental conditions as presented in Chapter 3.1 have been performed. Due to this similarity the following results for the Äspö system are discussed in comparison to the results obtained for the Grimsel system (see Chapter 3.1).

The case of mono- and divalent cations (Na, Cs, Ba)

The data presented in Figure A1 for both the Äspö and Grimsel FFM system are single point measurements, therefore no error bars are given in the diagrams of Figure A1. In the case of the monovalent sodium (^{22}Na) the concentration in both batch-systems (Äspö and Grimsel FFM) decreases within the first two hours and remains constant at $1.0 \pm 0.1 \cdot 10^{-9}\text{M}$ over the experimental duration analyzed. These results give confidence that potential evaporation of liquid from the batch Zinsser vials in the glove box can be excluded. A colloid bound Na fraction cannot be determined within the analytical uncertainty of the data ($\pm 5\text{-}10\%$).

In the case of ^{137}Cs a concentration decrease by more than two orders of magnitude can be observed over the duration of 1000 h, whereas the initial concentration decrease (2 h sample) for both ^{137}Cs and ^{133}Ba might be explained by a matrix diffusion process into the fracture filling material. This is indicated in Figure A1 by the additional inserted dashed line illustrating the $t^{-3/2}$ -dependency of concentration decrease frequently used as an indicator for matrix diffusion processes (Jakob et al., 2003) and for further discussions see also (Kosakowski, 2004)). However the matrix in the case of this batch-type study on the 1-2 mm FFM fraction is limited and the diffusion length L_D can be predicted based on the equation (A1):

$$L_D = \sqrt{2D_w\tau} \quad (\text{A1})$$

where D_w is the Stokes-Einstein diffusion coefficient in water [$\text{m}^2 \cdot \text{s}^{-1}$] and τ the time interval [s] (Zvikelsky et al., 2008).

Based on the diffusivity in the water phase (D_w) published (Byegård et al., 1998; Neretnieks, 2002) for different cations ($2.0 \cdot 10^{-9} \text{m}^2 \cdot \text{s}^{-1}$ for Cs^+ , $1.33 \cdot 10^{-9} \text{m}^2 \cdot \text{s}^{-1}$ for Na^+ and $0.83 \cdot 10^{-9} \text{m}^2 \cdot \text{s}^{-1}$ for Ba^{2+}) one can estimate the diffusion length for the different cations investigated based on a 2h time interval, which is 5.4 mm (Cs^+), 4.5 mm (Na^+) and 3.5 mm (Ba^{2+}), respectively. This simple estimation shows that the two hours are already sufficient for a full through diffusion of the FFM size fraction used throughout this experiments. Future evaluation of the data will include an application of a homogeneous diffusion-sorption model (Byegård et al., 1998). Comparing the data of the ultracentrifugated with the not ultracentrifugated samples gives an estimate of the bentonite colloid associated fraction. For the cocktail equilibrated with bentonite prior to the addition of fracture filling material, the colloid bound ^{22}Na fraction of 0-6 % is within the analytical uncertainty of the C_0 concentration measurements, whereas approximately 7-11 % colloid associated ^{137}Cs and 12-22 % colloid associated ^{133}Ba could be quantified. The colloid-bound ^{133}Ba - and ^{137}Cs - fraction shows no clear tendency of decrease throughout the experimental duration of the batch-type study and remains for ^{137}Cs at $43 \pm 11\%$ colloid bond (Äspö FFM) and $44 \pm 19\%$ colloid bond (Grimsel FFM), whereas these values are slightly lower in the case of ^{133}Ba with $25 \pm 15\%$ colloid bond (Äspö FFM) and $16 \pm 9\%$ colloid bond (Grimsel FFM) fraction. From this data a full reversibility of bentonite ^{137}Cs sorption under the given observation period (1000 h) cannot be concluded.

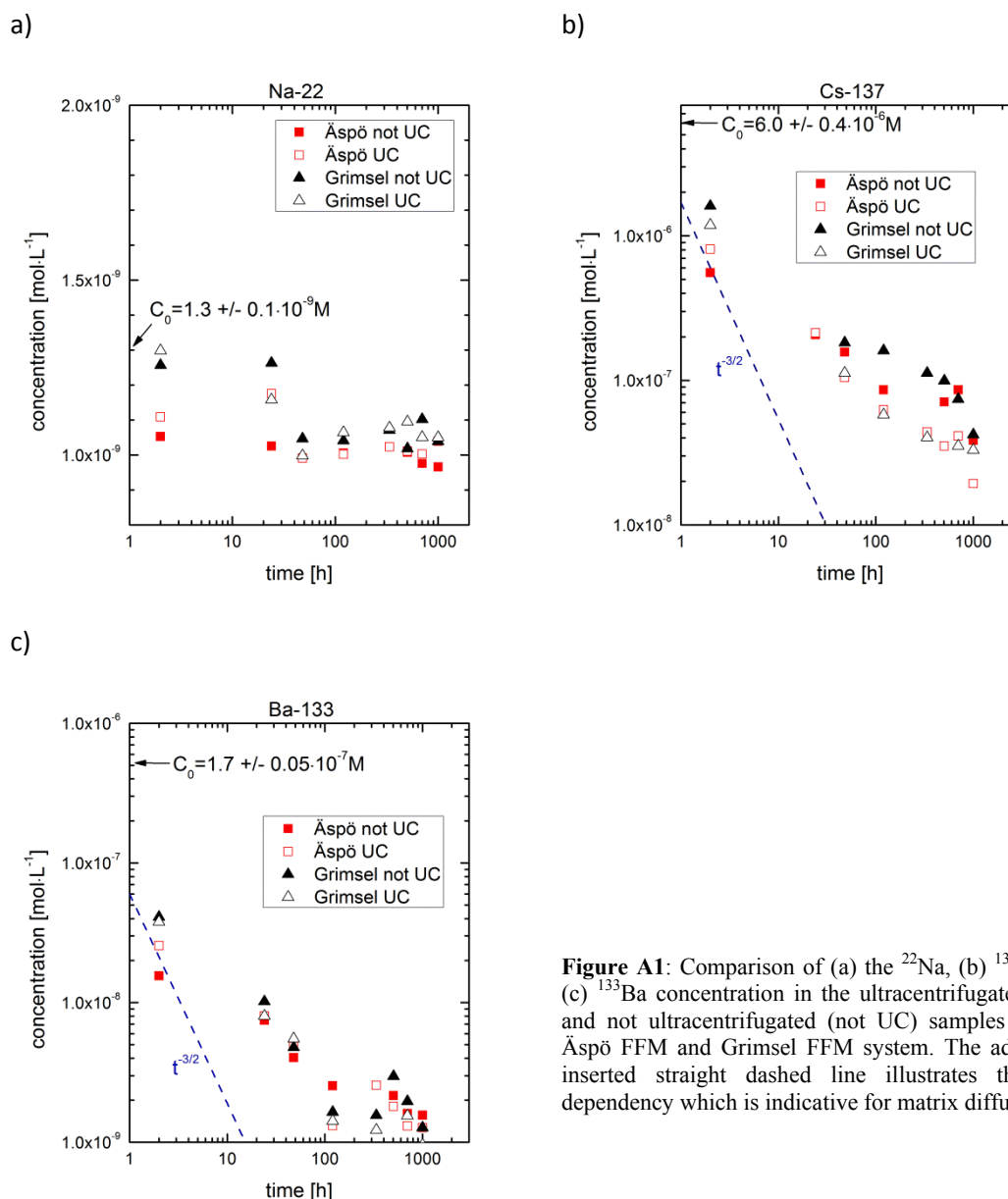


Figure A1: Comparison of (a) the ^{22}Na , (b) ^{137}Cs and (c) ^{133}Ba concentration in the ultracentrifugated (UC) and not ultracentrifugated (not UC) samples for the Äspö FFM and Grimsel FFM system. The additional inserted straight dashed line illustrates the $t^{-3/2}$ -dependency which is indicative for matrix diffusion.

The case of tri- and tetravalent actinides (^{243}Am , ^{242}Pu and ^{232}Th)

The tri- and tetravalent elements ^{232}Th , ^{242}Pu and ^{243}Am are clearly colloid associated which can be derived through a comparison between the UC and the not UC samples. The differences in radionuclide concentration are 1-2 orders of magnitude which also reflect the effective separation of the colloids through the experimental procedure.

This is furthermore documented in the Al ICP-MS signal, which gives information on the structural alumina of the Febex bentonite colloids. As shown in Figure A2 the Al concentration after UC is also reduced by around two orders of magnitude providing further confidence in the laboratory procedure to separate bentonite colloids from aqueous solution species.

To study the influence of RN concentration on sorption and reversibility two series with the 1-2 mm Grimsel FFM size fraction have been prepared applying two different $^{237}\text{Np(V)}$, $^{242}\text{Pu(IV)}$ and $^{243}\text{Am(III)}$ concentrations. In both sample sets the same solid to solution ratio ($1:4 \text{ g}\cdot\text{mL}^{-1}$) has been used. For the experiments with higher radionuclide concentration two samples have been prepared for long

term measurements after 7500 h. In addition to Pu(IV), Th(IV) was chosen as a homologue for tetravalent actinides.

Figure B3 shows the results of $^{242}\text{Pu(IV)}$ and $^{243}\text{Am(III)}$ concentrations with time. Additionally inserted in Figure B3 are calculated concentration margins for the ternary system based on batch sorption data derived partitioning coefficients of the binary systems “bentonite colloids – radionuclide” ($K_{d, coll}$) and “FFM – radionuclide” ($K_{d, FFM}$) (published in Tab. 4.7 and 4.9 (Nagra, 2006)).

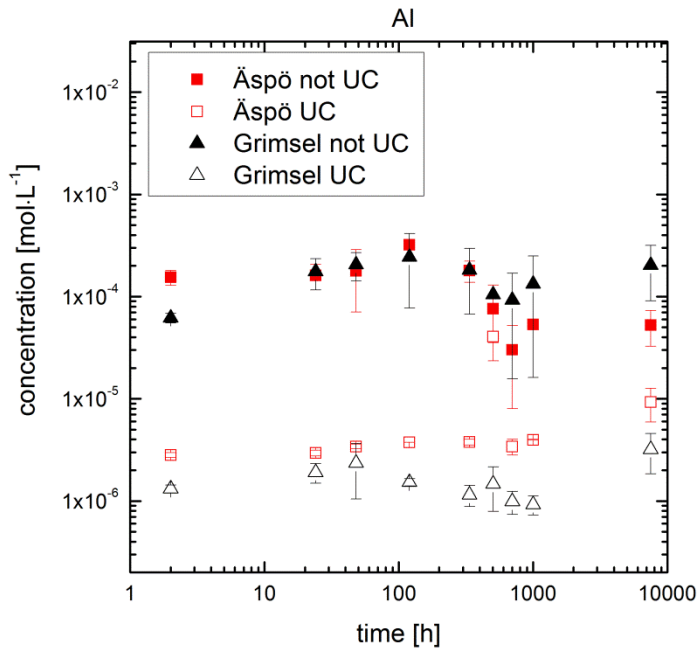


Figure A2: Comparison of the Al concentration in the ultracentrifugated (UC) and not ultracentrifugated (not UC) samples for the Äspö FFM and Grimsel FFM system.

The almost stable aluminium concentration measured throughout the experimental period (Figure A2) infers that the interaction of colloids with the fracture filling material can be neglected ($K_{d, coll-FFM} = 0$) and therefore the following equation (eq. A2) can be applied (Lührmann, 1999):

$$R_{d, tot} = \frac{K_{d, FFM}}{1 + C_c \cdot K_{d, coll}} \quad (\text{A2})$$

where C_c is the bentonite colloid concentration in solution. From the calculated distribution coefficient $R_{d, tot}$ the solution concentration for individual radionuclides in the ternary system C_f is derived by (eq. A3):

$$C_f = \frac{C_0}{\left(\frac{m}{V} \cdot R_{d, tot} + 1\right)} \quad (\text{A3})$$

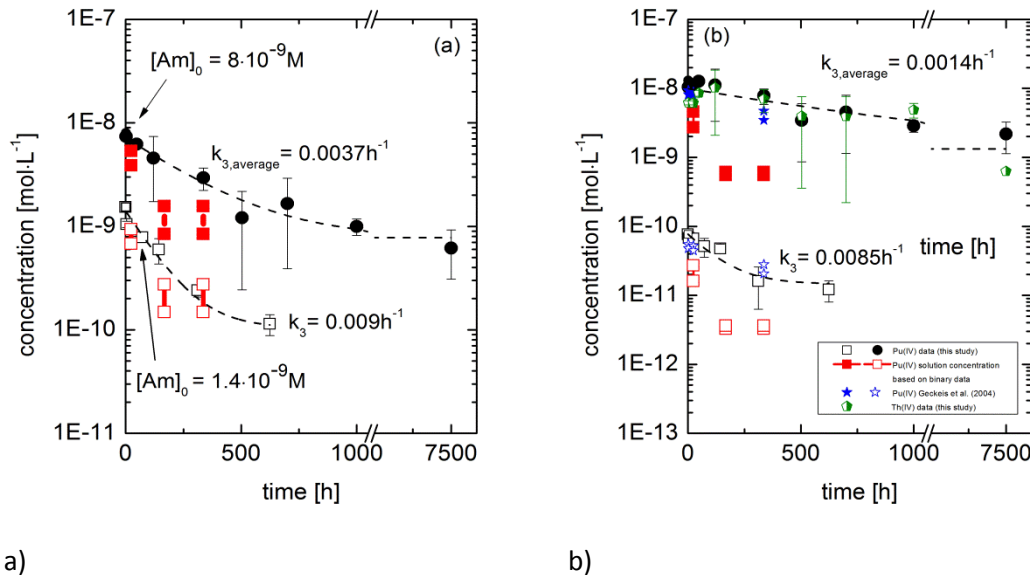


Figure A3: Time dependent radionuclide concentration change in the ternary system RN-fracture filling material (FFM)-bentonite colloids. The time-dependent concentration margins given in red squares (filled or open) represent predictions of the ternary system based on the binary system sorption data: (i) bentonite colloids – RN and (ii) fracture filling material – RN as published in (Nagra, 2006). (a) Initial Am(III) concentrations $8 \cdot 10^{-9} \text{ mol}\cdot\text{L}^{-1}$ (filled circles) and $1.4 \cdot 10^{-9} \text{ mol}\cdot\text{L}^{-1}$ (open black squares). The dashed lines are first order rate law fitting curves using a desorption rate k_3 of 0.009 h^{-1} as presented in (Flügge et al., 2010) and the desorption rate $k_{3,average}$ of 0.0037 h^{-1} as determined for the long-term desorption data. (b) Initial Pu(IV) concentrations $1.3 \cdot 10^{-8} \text{ mol}\cdot\text{L}^{-1}$ (filled circles) and $7.7 \cdot 10^{-11} \text{ mol}\cdot\text{L}^{-1}$ (open black squares). The dashed lines are first order rate law fitting curves using a desorption rate k_3 of 0.0085 h^{-1} as presented in (Flügge et al., 2010) and the desorption rate $k_{3,average}$ of 0.0014 h^{-1} as determined for the long-term desorption data averaged from the Pu(IV) and Th(IV) desorption experiments. Additionally inserted are the back calculated Pu(IV) solution concentrations based on the ternary Rd values published in (Nagra, 2006) (blue stars).

²⁴³Am(III)

Results for the ²⁴³Am(III) ternary system as a function of concentration ($1.4 \cdot 10^{-9} \text{ mol}\cdot\text{L}^{-1}$ and $8 \cdot 10^{-9} \text{ mol}\cdot\text{L}^{-1}$) feature an exponential concentration decrease in the log-linear visualization (Figure A3). The time-dependent concentration margins given in red squares (filled or open) of $K_{d, coll}$ and $K_{d, FFM}$. The additionally inserted dashed lines are first order rate law best-fit curves using a desorption rate k_3 of 0.009 h^{-1} as taken in (Flügge et al., 2010) under the assumption that equilibrium in the sorption systems has been reached after 624 h. The long-term desorption experiment however yielded a significantly lower desorption rate $k_{3,average}$ of 0.0037 h^{-1} . Comparison of the predicted solution concentration based on the binary systems with those of the ternary system data shows a systematically lower predicted solution concentration (Figure A3). The reason is the clear difference between the bentonite colloid – radionuclide desorption rate k_3 and the bentonite colloid – radionuclide sorption rate K_3 of 0.123 h^{-1} as determined after 24 h contact time. Therefore, Am(III) desorption from the initially almost quantitatively bentonite colloid associated Am(III) (94.8 %) is the overall rate limiting step in our ternary system and clearly determines the radionuclide solution concentration. Between 1000 h and 7500 h desorption time only a small decrease in ²⁴³Am(III) concentration can be detected, indicating that either the system has reached equilibrium conditions or the kinetics of the reversibility process are becoming very slow, which could have a significant impact on colloid-mediated radionuclide migration. Further samplings at longer observation periods are in work to elucidate this open issue.

$^{242}\text{Pu(IV)}$ and $^{232}\text{Th(IV)}$

$^{242}\text{Pu(IV)}$ is initially colloidal associated to 84.1 %, whereas $^{232}\text{Th(IV)}$ is quantitatively colloidal associated (99.7 %) after spiking to the groundwater with bentonite colloids and 24 h equilibration time. ^{242}Pu samples with $7.0 \cdot 10^{-11} \text{ mol} \cdot \text{L}^{-1}$ and $1.3 \cdot 10^{-8} \text{ mol} \cdot \text{L}^{-1}$ have been prepared. Geochemical calculations show that Pu is in the tetravalent oxidation state under the given conditions. Figure A3 shows the time dependent concentration decrease for both Pu sample sets. The series with the lower $^{242}\text{Pu(IV)}$ concentration shows a slightly steeper decrease in concentration starting after approximately 125 h compared to the set with higher $^{242}\text{Pu(IV)}$ concentration. Final Pu(IV) concentrations after 624 h (equilibrium assumption in (Flügge et al., 2010)) for the high and the low Pu(IV) concentration series are $1.21 \cdot 10^{-11} \text{ mol} \cdot \text{L}^{-1}$ and $4.53 \cdot 10^{-9} \text{ mol} \cdot \text{L}^{-1}$, respectively. Pu(IV) concentration for the long term sample after 7500 h is $2.18 \cdot 10^{-9} \text{ mol} \cdot \text{L}^{-1}$. Like $^{242}\text{Pu(IV)}$, a time dependent concentration decrease (from initially $7.3 \cdot 10^{-9} \text{ mol} \cdot \text{L}^{-1}$ to $6.2 \cdot 10^{-10} \text{ mol} \cdot \text{L}^{-1}$) has been observed for $^{232}\text{Th(IV)}$. The additionally inserted dashed lines in Figure A3 are again first order rate law best-fit curves using a desorption rate k_3 of 0.0085 h^{-1} as taken in (Flügge et al., 2010) under the assumption that equilibrium in the sorption systems has been reached after 624 h. The long-term desorption experiment however yielded a significantly lower desorption rate averaged over both the Pu(IV) and Th(IV) data sets with $k_{3,\text{average}}$ of 0.0014 h^{-1} . In comparison to $^{243}\text{Am(III)}$, both $^{242}\text{Pu(IV)}$ and $^{232}\text{Th(IV)}$ obviously exhibits a slower reversibility kinetic. Similar slow desorption kinetics from bentonite colloids have been observed by (Bouby et al., 2010).

A straightforward interpretation of the presented Pu results is hindered by the complex Pu(IV) aquatic chemistry and the fact that due to low metal concentrations used no spectroscopic technique can be applied to gain further insights into the prevailing Pu(IV) speciation. Therefore, the following discussion is based on macroscopic/phenomenological observations and supporting thermodynamic calculations. Recalling the results from the thermodynamic calculations presented above, the $\text{Pu(OH)}_4(\text{am})$ solid phase (also termed $\text{PuO}_2 \cdot x\text{H}_2\text{O}(\text{am})$ or $\text{PuO}_2(\text{am,hyd})$) is oversaturated in case of the high Pu(IV) concentration series (but not in case of the low Pu(IV) concentrations series) and the $\text{Th(OH)}_4(\text{am})$ is undersaturated in the experiments presented. However, no immediate removal of Pu(IV) from solution due to precipitation can be observed in the experimental data, since the $^{242}\text{Pu(IV)}$ (and Th(IV)) concentration remains constant for more than 100 hours after spiking to the radionuclide cocktail and the sample batches, respectively. Under the given experimental conditions the precipitation of a Pu(IV) solid phase starts with the formation of nanocrystalline Pu(IV) oxyhydroxide species, also called polymeric $\text{Pu(IV)O}_n(\text{OH})_{4-2n}$ "eigencolloids". Colloidal Pu(IV) species are known to be quite stable in aqueous solution in equilibrium with a Pu(IV) solid phase and considered part of the overall thermodynamic equilibrium system (Neck et al., 2007a). It is reasonable to assume that the neutrally charged polymeric $\text{Pu(IV)O}_n(\text{OH})_{4-2n}$ "eigencolloids" possess very similar chemical and sorption properties like the neutrally charged monomeric aquatic Pu(IV) hydrolysis complex $\text{Pu(IV)OH}_4(\text{aq})$. Therefore, it is not possible on the basis of the available experimental evidences to differentiate if Pu(IV) is present as a monomeric hydrolysis complex or an "eigencolloid" species. Following this line of reasoning, both types of Pu(IV)/Th(IV) species should be equally prone to sorption onto the bentonite colloids. A similar chemical behaviour of both types of Pu(IV)/Th(IV) species would also corroborate the observation of the quite likewise desorption kinetics for both Pu(IV) concentrations series (due to the absence of Pu(IV) "eigencolloids" for the low concentration series). The results presented by (Geckeis et al., 2004) under similar experimental conditions to the prevailing study reported a Pu(IV) "eigencolloid" fraction between 5 to 55 % (in absence of bentonite colloids) for Pu(IV) concentrations of $9.94 \cdot 10^{-9} \text{ mol} \cdot \text{L}^{-1}$ and approximately 84 % colloid associated Pu(IV) in presence of $20 \text{ mg} \cdot \text{L}^{-1}$ bentonite colloids for Pu(IV) concentrations of $6.7 \cdot 10^{-9} \text{ mol} \cdot \text{L}^{-1}$. Thus, the concentration decrease is explainable by desorption of colloid bound $^{242}\text{Pu(IV)}/^{232}\text{Th(IV)}$, either as a monomeric or an "eigencolloid" species and subsequent sorption on the FFM.

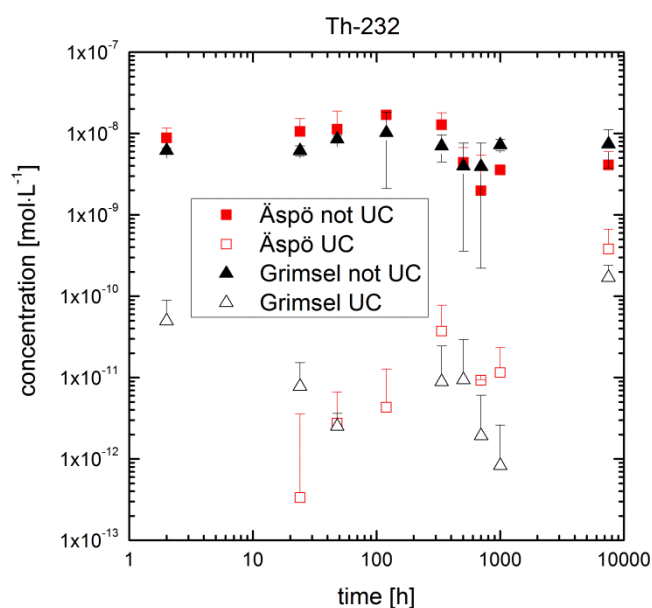


Figure A4: Time dependent ^{232}Th evolution of radionuclide concentration for the Äspö (red symbols) and Grimsel FFM (black symbols) experiments. Values are given both for ultracentrifugated (UC) samples and for not ultracentrifugated (not UC) samples.

$^{237}\text{Np(V)}$

Figure A5 shows the temporal evolution of ^{99}Tc , ^{233}U and ^{237}Np both for ultracentrifugated (UC) and not ultracentrifugated (not UC) samples. From a comparison of ultracentrifugated with not ultracentrifugated samples it is obvious that ^{237}Np as well as ^{99}Tc and ^{233}U are not colloidal associated. ^{237}Np concentration decreases after ~ 100 h in both systems which could either be explained by sorption to the fracture filling material or by a slow reduction to Np(IV). The borderline of Np reduction is around -60 mV (50 % reduced Np), which is slightly lower than our measured Eh values of -50 mV for the Äspö system and $+25$ mV in the Grimsel system. Due to uncertainties in redox measurements these values are likely in the range of the borderline for reduction. The fact that the decrease in concentration first occurs after 100 h corroborates the hypothesis of reduction because a concentration decrease due to adsorption should onset at earlier times. The reduction itself is known to be kinetically controlled and the experimental data obtained so far shows that the time frame is insufficient to reach equilibrium conditions. A partial reduction at shorter contact times might occur, but cannot be resolved within the analytical uncertainties. Calculating the pe based on the values given above results in the borderline for 50% Np(V) reduction at $pe = \sim -1$ as given in Figure A6. This calculated pe is not far away from the measured pe values in the batch experiments, therefore a partial reduction of Np(V) on the FFM surface can be assumed.

$^{99}\text{Tc(VII)}$ and $^{233}\text{U(VI)}$

The concentrations of $^{99}\text{Tc(VII)}$ and $^{233}\text{U(VI)}$ remains almost constant over the experimental period with $1.3 \cdot 10^{-8} \pm 1.4 \cdot 10^{-9} \text{ mol}\cdot\text{L}^{-1}$ and $5 \cdot 10^{-7} \pm 3 \cdot 10^{-8} \text{ mol}\cdot\text{L}^{-1}$, respectively indicating the absence of sorption to fracture filling material or reduction within the analytical uncertainty in both investigated systems. In case of the Grimsel system after 7500 h contact time, a slight decrease in ^{99}Tc concentration is visible which is even more pronounced for the UC sample. This might indicate that $^{99}\text{Tc(VII)}$ is reduced to colloidal $^{99}\text{Tc(IV)}$. Both elements show no interaction with the FEBEX colloids which is evidenced by the comparison between UC and not UC samples in Figure A5. A K_d value of ~ 0.87 for $^{99}\text{Tc(VII)}$ and ~ 1.74 for $^{233}\text{U(VI)}$ could be determined. These K_d values are comparable to data of K_d $^{99}\text{Tc(VII)} = 0.38 \pm 0.10$ and K_d $^{233}\text{U(VI)} = 1.81 \pm 0.19$ obtained after one week contact time for fracture filling material fraction $< 1160\mu\text{m}$ published in (Nagra, in press), but significantly lower than

K_d $^{99}\text{Tc(VII)} = 2.5 \pm 0.10$ and K_d $^{233}\text{U(VI)} = 10.4 \pm 0.10$ obtained after five weeks contact time. Interestingly, the uranium in-situ K_d simply calculated based on the given FFM uranium concentration (Table 3.1) and the groundwater uranium concentration (Table 3.2) is orders of magnitude higher with $K_d \approx 3800$ which clearly indicates that a large part of the natural uranium pool present in the FFM does not interact with the groundwater.

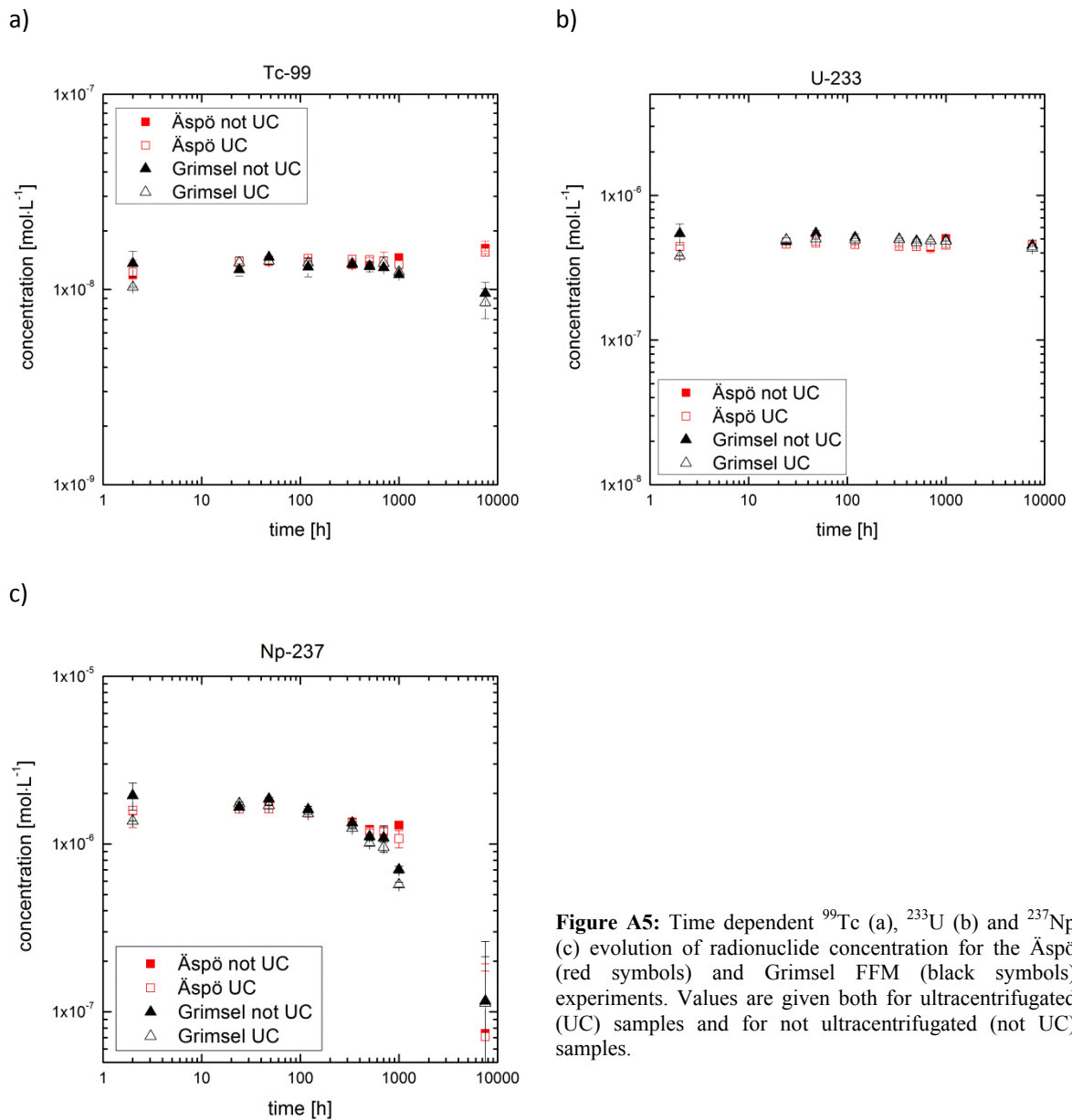


Figure A5: Time dependent ^{99}Tc (a), ^{233}U (b) and ^{237}Np (c) evolution of radionuclide concentration for the Äspö (red symbols) and Grimsel FFM (black symbols) experiments. Values are given both for ultracentrifugated (UC) samples and for not ultracentrifugated (not UC) samples.

For comparison, $^{232}\text{Th(IV)}$ in-situ K_d show even higher values with $\sim 1.6 \cdot 10^5$. But again these so-called in-situ K_d values do not provide information on “sorption” behaviour. They rather reflect a general measure for element mobilities in the geosphere. It is well known that U mobility is higher than Th mobility mainly due to its redox chemistry.

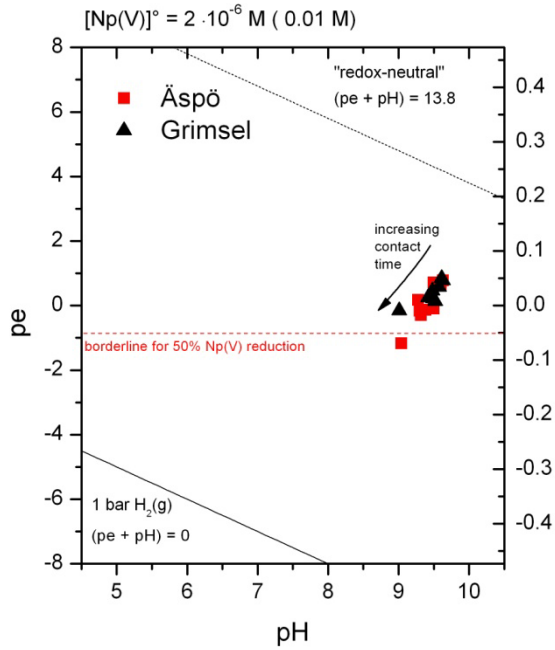


Figure A 6: pe/pH diagram for the batch experiments showing the experimental pe/pH range and the pe borderline for 50% Np reduction. (black: Grimsel FFM; red: Äspö FFM)

Effect of available surface area on sorption reversibility of Np, Am and Pu

Three different FFM grain sizes have been used to study the influence of available surface area on sorption reversibility for $^{237}\text{Np(V)}$, $^{242}\text{Pu(IV)}$ and $^{243}\text{Am(III)}$, namely 0.25-0.5 mm, 0.5-1 mm and 1-2 mm. Specific surface area measurements (BET) of the three Grimsel size fractions yielded values of $0.238 \text{ m}^2\cdot\text{g}^{-1}$, $0.187 \text{ m}^2\cdot\text{g}^{-1}$ and $0.153\text{-}0.166 \text{ m}^2\cdot\text{g}^{-1}$ for 0.25-0.5 mm, 0.5-1 mm and 1-2 mm size fraction, respectively. Concerning the 1-2 mm size fraction, sample sets with two different RN concentrations have been examined.

Results are depicted in Figure A7 and presented as surface area normalized distribution coefficients, calculated according to equation A4:

$$R_d = \frac{\Gamma_{RN}}{[RN]} = \frac{TOTRN - [RN]}{[RN]} / \varphi m = \left(\frac{TOTRN}{[RN]} - 1 \right) / \varphi m \quad (\text{A4})$$

with R_d = distribution coefficient [$\text{L}\cdot\text{m}^{-2}$]; Γ_{RN} = surface excess of [RN] [$\text{mol}\cdot\text{m}^{-2}$]; [RN] = dissolved [RN] concentration [$\text{mol}\cdot\text{L}^{-1}$]; $TOTRN$ = total [RN] concentration [$\text{mol}\cdot\text{L}^{-1}$]; φ = surface area [$\text{m}^2\cdot\text{g}^{-1}$]; m = solid concentration [$\text{g}\cdot\text{L}^{-1}$].

$^{237}\text{Np(V)}$ shows lower R_d values (~ 0.5 orders of magnitude) for the 1-2 mm system with higher $^{237}\text{Np(V)}$ concentration compared to the same size fraction with lower concentrations. All data sets show an increase in R_d values of about one order of magnitude with time. This time dependent trend of increasing $^{237}\text{Np(V)}$ R_d values was not observed in earlier studies (Geckeis et al., 2004).

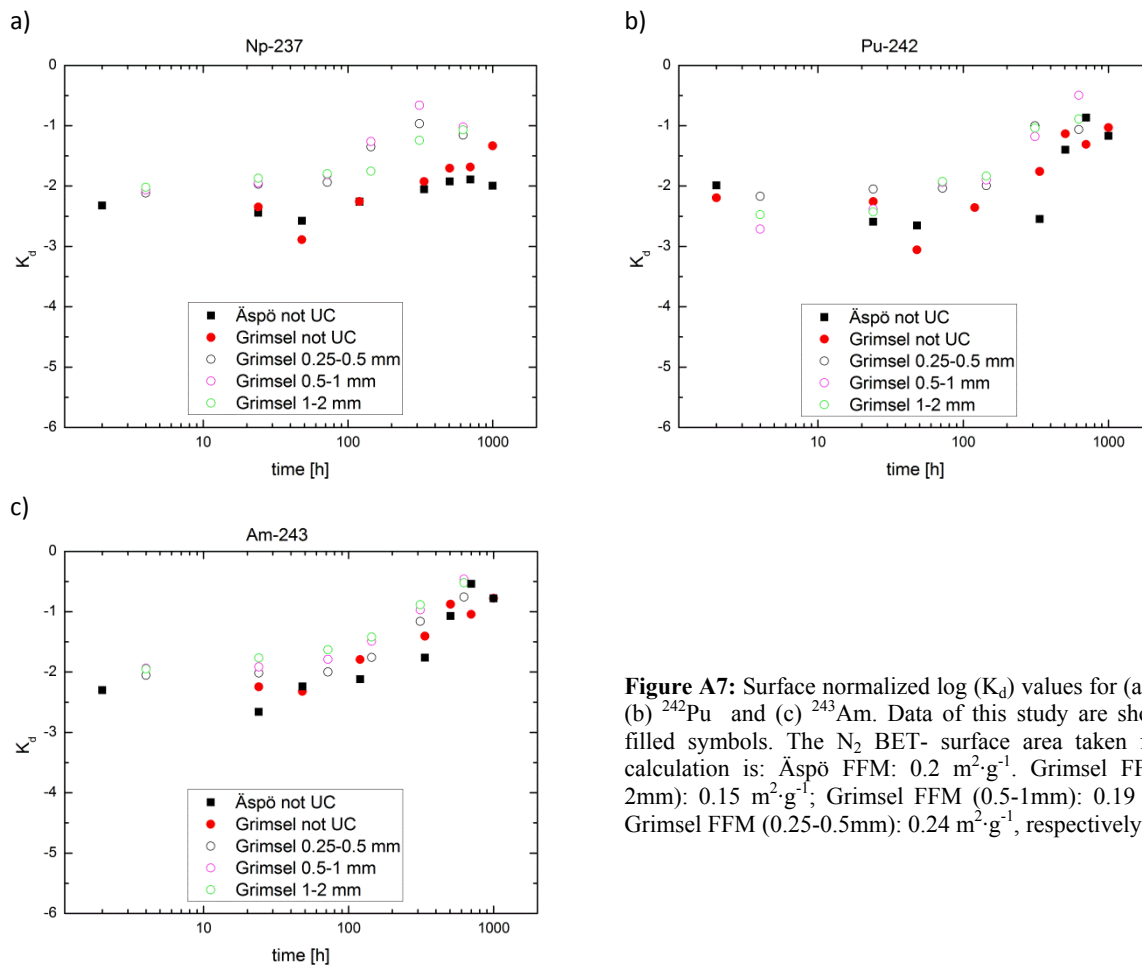


Figure A7: Surface normalized $\log(K_d)$ values for (a) ^{237}Np (b) ^{242}Pu and (c) ^{243}Am . Data of this study are shown as filled symbols. The N_2 BET- surface area taken for the calculation is: Äspö FFM: $0.2 \text{ m}^2\cdot\text{g}^{-1}$. Grimsel FFM (1-2mm): $0.15 \text{ m}^2\cdot\text{g}^{-1}$; Grimsel FFM (0.5-1mm): $0.19 \text{ m}^2\cdot\text{g}^{-1}$, Grimsel FFM (0.25-0.5mm): $0.24 \text{ m}^2\cdot\text{g}^{-1}$, respectively.

R_d values for $^{242}\text{Pu}(\text{IV})$ and $^{243}\text{Am}(\text{III})$ show a rise from $R_d \sim -2.5$ up to $-0.5 \text{ L}\cdot\text{m}^{-2}$. This increase in R_d can be explained by the kinetics of desorption and the subsequent sorption to the fracture filling material, whereas the observed trend in the $^{237}\text{Np}(\text{V})$ R_d values reflects most likely a combined effect of reduction and sorption. In general, R_d values for the three samples series with higher metal concentration are always lower than R_d values for the three samples series with lower metal concentration. This observation maybe reflect the sorption reversibility in terms of a slower desorption in case of the higher concentration series. The scatter of the data presented in Figure A7 give an uncertainty margin for the kinetics of actinide dissociation form FEBEX bentonite colloid that can be used in reactive transport modeling (Noseck and Klotz, 2002).

The surface normalized R_d values reflect no systematic trend in terms of the available surface area and/or the mineralogy of the FFM. The latter observation is expected since the mineralogical composition of the three different FFM size fractions is very similar to each other based on the XRD results stated above.

Overall, the results show that the desorption kinetics from bentonite colloids are rather independent from the FFM used and also from the grain size of the investigated material, at least in the size fraction range 0.25-2 mm.

9 APPENDIX B: Core migration experiments

Besides the HTO and QD more migration studies presented in chapter 4, additional column migration studies applying the radionuclide cocktail presented in Chapter 2.2 have been performed.

Chemical characterization of contact water evolution

Prior to the experiments the core was equilibrated with Grimsel groundwater. During the equilibration phase secondary phase formation could be observed on the outer surface of the core (Figure B1). Detailed SEM-EDX analysis revealed a precipitation of most probably Al-oxide-hydroxide phases. Taking into account the pH perturbation induced by the exchange from Äspö groundwater (pH 7.5) to Grimsel GW (pH 9.6) a higher Al concentration in solution and the dissolution of Al-oxide-hydroxides within the drill core can be expected. This is also documented in the contact water analysis of the drill core (Table B1), where a significant higher Al concentration could be found. During the equilibration stagnant porewater conditions were established and small pH drifts during these stagnant phases might have forced these Al-precipitates. The migration experiments have been started after the milestone of $[Me^{2+}] < 1 \text{ mM}$ to ensure bentonite colloid stability was reached.

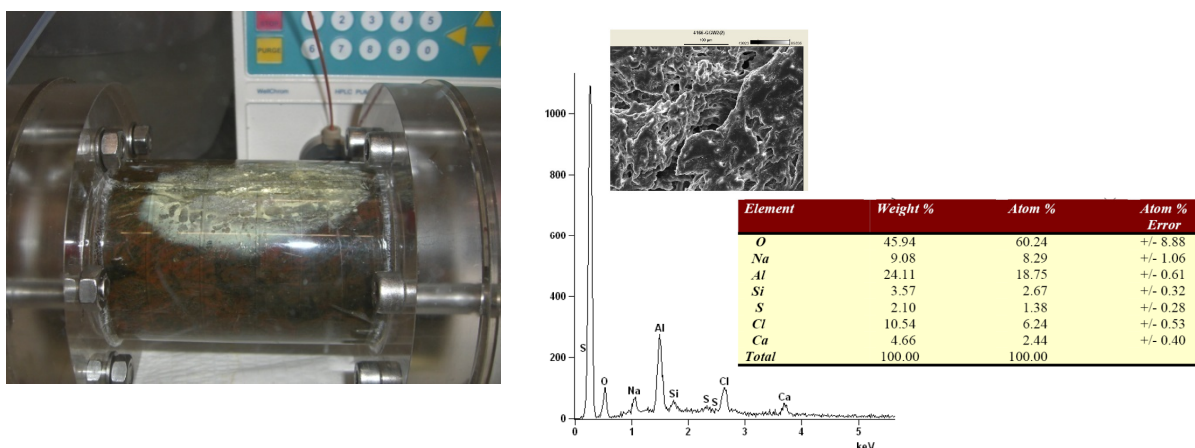


Figure B1: (left) Picture taken from white precipitate observed after stagnant phase in core #8. (right) SEM-EDX characterization of the white precipitate observed during the change from Äspö GW to Grimsel GW.

Run#1

A first pulse injection experiment using only a small volume of cocktail (0.1 mL) under a flow rate of $50 \mu\text{L}\cdot\text{min}^{-1}$ was conducted. A breakthrough of the HTO and some of the injected radionuclides can be observed (see Figure B1), but taking into account the sample volume needed to fully characterize each fraction for all radionuclides injected the sampling resolution is quite limited. It was therefore decided to change for the migration experiments to continue with a considerable higher injection volume. The results of the pulse injection experiment however show a mobility of Am and Pu with the peak maximum running ahead of the conservative tracer as expected for colloid mediated transport of tri- and tetravalent actinides. Surprisingly, also the uranium shows a colloid associated transport and no retarded breakthrough of dissolved U(VI) could be observed. In earlier studies on Grimsel granite cores from the migration shearzone (Schäfer et al., 2004) a retardation factor R_f of 14.6-20 depending on the flow rate was observed for U(VI) and a small U fraction associated with bentonite colloids could be resolved by Asymmetrical Flow Field Flow Fractionation (AsFIFFF).

9 APPENDIX B: Core migration experiments

Table B1: Chemical composition of the Äspö groundwater (TRUE-1 site, Feature A, KXTT4), the Grimsel groundwater (GGW) as well as the chemical evolution of GGW during contact with Äspö core #8 and after stop-flow (to observe the influence of matrix porewater).

	Äspö GW	Grimsel GW (barrel #3) (MI shearzone)	Grimsel GW (sample CFMH1- 0c) (MI shearzone)	Grimsel GW Contact core #8	Grimsel GW Contact core #8	Grimsel GW Contact core #8 Stop flow 25d
	Sep.-Nov. 2007	22. May 2007	12. Febr. 2008	4. March 2008	1. April 2008	12.2.-6.3.2010
pH	7.5 ± 0.1	9.6	9.67	9.89	9.8	9.5
E _{h(SHE)}	~ 62 mV	-170 mV	n.d.	~ +50mV	~ 0mV	~ 200mV
[Mg ²⁺]	76.4 mg·L ⁻¹	14.1 µg·L ⁻¹	12.6 µg·L ⁻¹	36.3µg·L ⁻¹	46.7 µg·L ⁻¹	133.5 ± 8.0 µg·L ⁻¹
[Ca ²⁺]	0.87 g·L ⁻¹	5.4 mg·L ⁻¹	5.3 mg·L ⁻¹	9.0 mg·L ⁻¹	9.4 mg·L ⁻¹	5.6 ± 0.2 mg·L ⁻¹
[Fe ^{2+,3+}]	< D.L.	< D.L.	< D.L.	< D.L.	< D.L.	68.6 ± 3.5 µg·L ⁻¹
[Mn ²⁺]	532 µg·L ⁻¹	23.2 µg·L ⁻¹	< D.L.	2.86µg·L ⁻¹	1.25 µg·L ⁻¹	7.9 ± 0.2 µg·L ⁻¹
[Sr ²⁺]	15.4 mg·L ⁻¹	197 µg·L ⁻¹	181.5µg·L ⁻¹	285.1µg·L ⁻¹	290.2 µg·L ⁻¹	114.7 ± 0.6 µg·L ⁻¹
[Cs ⁺]	3.5 µg·L ⁻¹	n.d.	0.79µg·L ⁻¹	0.64µg·L ⁻¹	0.31 µg·L ⁻¹	0.46 ± 0.01 µg·L ⁻¹
[La ³⁺]	0.03 µg·L ⁻¹	n.d.	< D.L.	< D.L.	< D.L.	0.024 ± 0.017 µg·L ⁻¹
[U]	0.35 µg·L ⁻¹	n.d.	n.d.	0.098µg·L ⁻¹	0.128 µg·L ⁻¹	0.071 ± 0.006 µg·L ⁻¹
[Al ³⁺]	9.2 µg·L ⁻¹	126.8 µg·L ⁻¹	42.9 µg·L ⁻¹	29.9µg·L ⁻¹	64.7 µg·L ⁻¹	32.4 ± 3.6 µg·L ⁻¹
[Na ⁺]	1.2 g·L ⁻¹	12.9 mg·L ⁻¹	14.7 mg·L ⁻¹	50.3 mg·L ⁻¹	53.7 mg·L ⁻¹	49.2 ± 1.4 mg·L ⁻¹
[Cl ⁻]	4.9 g·L ⁻¹	5.3 mg·L ⁻¹	6.7 mg·L ⁻¹	n.d.	10.6 mg·L ⁻¹	53.4 ± 16.3 mg·L ⁻¹
[Si]	4.9 mg·L ⁻¹	4.2 mg·L ⁻¹	5.6 mg·L ⁻¹	8.9 mg·L ⁻¹	9.3 mg·L ⁻¹	7.1 ± 0.2 mg·L ⁻¹
[SO ₄ ²⁻]	268 mg·L ⁻¹	5.0 mg·L ⁻¹	5.8 mg·L ⁻¹	n.d.	8.8 mg·L ⁻¹	n.d.
[F ⁻]	1.3 mg·L ⁻¹	5.9 mg·L ⁻¹	6.3 mg·L ⁻¹	n.d.	10.3 mg·L ⁻¹	n.d.
[Br ⁻]	n.d.	n.d.	n.d.	n.d.	n.d.	n.d.
[NO ₃ ²⁻]	< D.L.	< D.L.	< D.L.	n.d.	< D.L.	n.d.
[HCO ₃ ⁻]	125.6 mg·L ⁻¹	4.5 mg·L ⁻¹	3.0 mg·L ⁻¹	n.d.	n.d.	n.d.

n.d.: not determined. D.L.: detection limit

The Np breakthrough shows a double peak feature with a small fraction running again slightly ahead of the conservative tracer, which might indicate a small colloid associated fraction of Np, whereas a retarded Np breakthrough was additionally observed. The Np breakthrough showed a retarded double peak feature with approximated R_f values of 3.25 and 6.5.

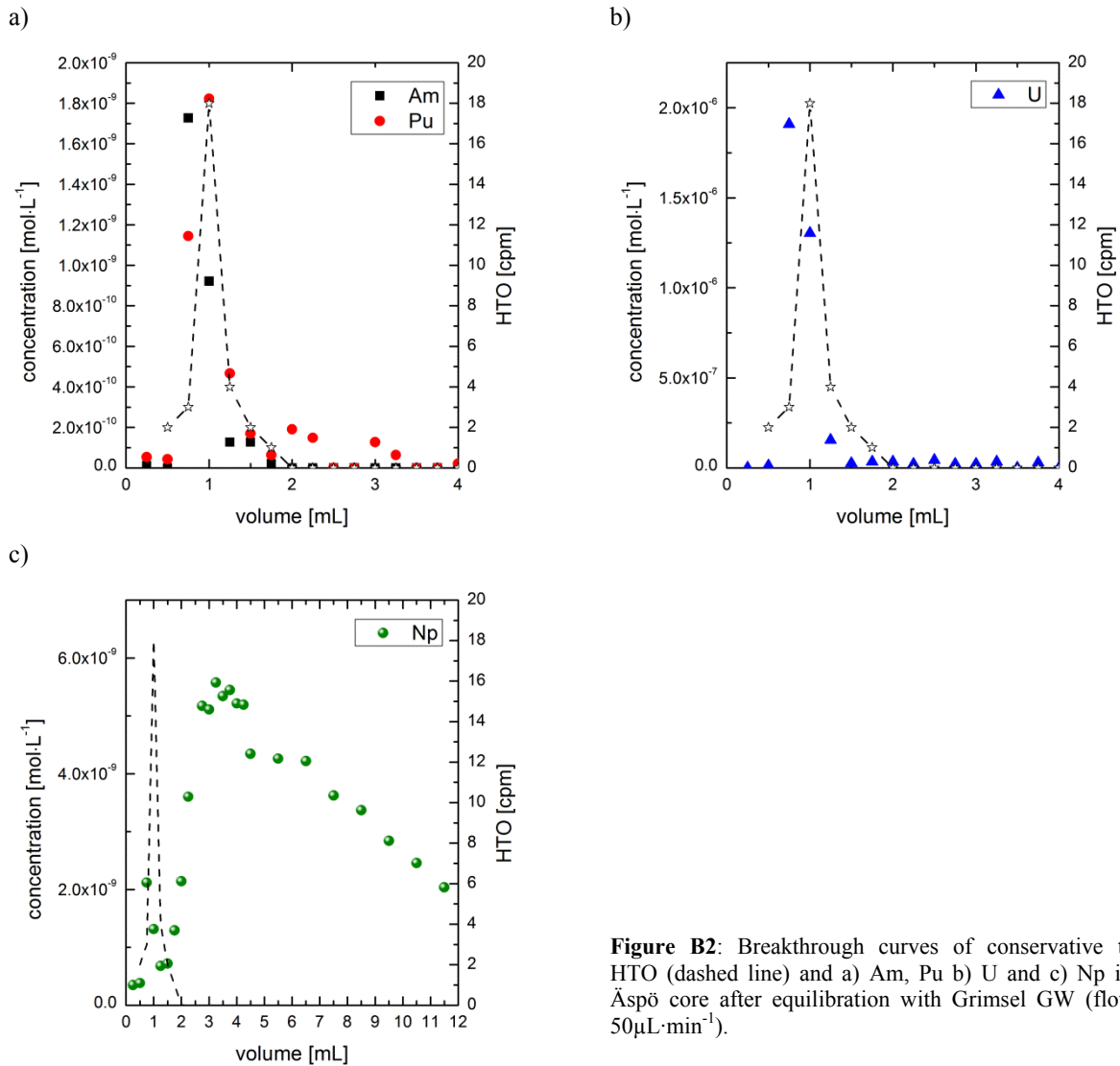


Figure B2: Breakthrough curves of conservative tracer HTO (dashed line) and a) Am, Pu b) U and c) Np in the Äspö core after equilibration with Grimsel GW (flowrate 50 $\mu\text{L}\cdot\text{min}^{-1}$).

Run#2 and Run#3

Due to the analytical problems mentioned above additional experiments under the same hydraulic conditions were conducted using a ten times increased injection volume of 1000 μL and the same cocktail composition. The experimental results obtained were rather surprising, namely colloid associated tri- and tetravalent radionuclides (Th initially 99.7 % bentonite colloid bond, Am initially 94.8 % bentonite colloid bond and Pu initially 84.1 % bentonite colloid bond) were only to a minor fraction (<5 %) mobile under the chosen hydraulic conditions (50 $\mu\text{L}\cdot\text{min}^{-1}$ corresponding to $\sim 3 \text{ m}\cdot\text{d}^{-1}$); see Table B2. The recovery of the tri- and tetravalent radionuclides is in accordance with the Al recovery, which is used as the indicator element for the bentonite colloids; see Table B1.

In order to reconfirm these results and estimate the reproducibility of the recoveries obtained, the migration experiment was conducted twice (Run#2 & Run#3) under the same hydraulic conditions. The results show good reproducibility and provide general confidence in the experimental set-up as well as in the observed bentonite colloid-retention under the given geochemical conditions (glacial melt water). The current explanation for the observed colloid retention is a diffusive leaching of the core matrix pore water having still the Äspö KXTT4 chemical signature to the fracture surface, providing a divalent cation pool resulting in a high bentonite colloid fracture surface attachment

probability/collision efficiency α . The effect of divalent cations on the colloid attachment probability has been frequently observed in porous media (Davis et al., 2002) and in AFM studies on mineral phases frequently found in granite fracture filling material using force-distance measurements (Filby, 2009; Filby et al., 2009b).

Table B2: Summary of the radionuclide migration studies in presence of Febex bentonite colloids in the Äspö drill core under Grimsel groundwater conditions. Colloid associated elements are given in bold letters.

	Injected mass (mol)	Colloid associated (%)	Recovery (%)	R_p (min)	R_f (-)	Recovery (%)	R_p (min)	R_f (-)
				Run#2			Run#3	
HTO	-	0	98	61	1	96.8	67	1
Al	$9.0 \cdot 10^{-5}$	100%	0.9	-	-	4.3	-	-
^{99}Tc	$1.5 \cdot 10^{-11}$	0.9	79	53	0.87	100	67	1
^{232}Th	$1.7 \cdot 10^{-11}$	99.7	2.1	-	-	3.5	-	-
^{233}U	$8.0 \cdot 10^{-10}$	1.6	0.2	-	-	1	-	-
^{237}Np	$1.8 \cdot 10^{-9}$	0.1	76	102/185	1.67/3	72	237/562	3.5/8
^{242}Pu	$3.0 \cdot 10^{-11}$	84.1	3.9	-	-	4.7	-	-
^{243}Am	$8.0 \cdot 10^{-9}$	94.8	0.01	-	-	0.01	-	-

R_p = peak elution time; R_f = retardation factor ($R_f = R_p[\text{RN}]/R_p[\text{HTO}]$)

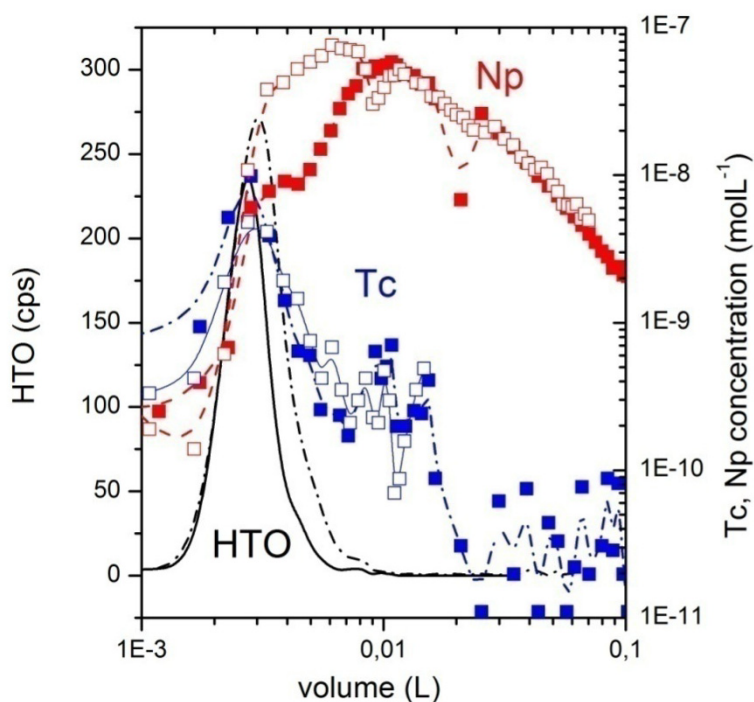


Figure B3: Breakthrough curves of Tc and Np (Run#2 & Run#3) together with the conservative tracer HTO.

Tc introduced in the cocktail as pertechnetate (TcO_4^-) shows the peak maximum coinciding with the conservative tracer tritium, but exhibits a pronounced tailing compared to HTO (Figure B3). The

recovery is high ranging between 79-100 %. Taking the pe/pH conditions established in the core (see Table B1) a reduction of Tc(VII) is either kinetically hindered or not expected under the experimental conditions. One has to state clearly that the core used throughout this study has neither been drilled under anoxic conditions nor stored preventing oxidation prior to the transfer into the Ar glove box. Therefore, establishing strongly reducing conditions with Grimsel groundwater having low reduction capacity might take a considerable period.

Der Lebenslauf ist in der Online-Version aus Gründen des Datenschutzes nicht enthalten!

Der Lebenslauf ist in der Online-Version aus Gründen des Datenschutzes nicht enthalten!